Tuning the dimensionality and interactions in transition metal oxides: a μSR study

Peter James Baker
Balliol College

A thesis submitted for the degree of
Doctor of Philosophy
at the
University of Oxford
Michaelmas Term 2007

Tuning the dimensionality and interactions in transition metal oxides: a μSR study

Peter James Baker
Balliol College, Oxford University
Michaelmas Term 2007

Abstract of Thesis Submitted for the Degree of Doctor of Philosophy

This thesis is concerned with how the physical properties of transition metal oxides change due to chemical substitution or intercalation. Experiments using the muon-spin relaxation and rotation (μSR) techniques were carried out at the ISIS Facility (UK) and the Paul Scherrer Institute (CH). In conjunction with the μSR results, the results of heat capacity and magnetic susceptibility experiments are used to provide complementary information on the same samples.

Investigations of the properties of the layered triangular lattice magnets $NaNiO_2$ and $LiNiO_2$ are presented. For $NaNiO_2$, all three experimental techniques are used to provide a full survey of the thermodynamic and magnetic properties of this compound. For $LiNiO_2$, μSR studies of notionally stoichiometric and Mg-doped samples were carried out. These showed that Mg doping causes a significant change in the magnetic dynamics of the material, but neither sample exhibits long-range magnetic order.

The magnetic ordering of the extensively studied perovskite compounds $LaTiO_3$ and $YTiO_3$ is investigated using μSR. The results were in agreement with previous neutron diffraction studies of the two compounds, but clarified the orientation of the magnetic moments in $LaTiO_3$. It was also possible to make a detailed comparison between the μSR results and those of dipole field calculations of the magnetic field at possible muon stopping sites, allowing these to be deduced and compared with results in other well characterized transition metal oxides.

The two titanium chain compounds $NaTiSi_2O_6$ and TiOCl exhibit spin gap formation at unusually high temperatures due to unconventional dimerization mechanisms. A model allowing the comparison of X-ray diffraction data, dimerization, and the magnitude of the spin gap is proposed. This is tested against both magnetic susceptibility and μSR data for both compounds. For $NaTiSi_2O_6$ both experimental techniques are in reasonable agreement, whereas in TiOCl the results are conclusively different. The origin of this disparity in TiOCl is explored.

The intercalation of organic chain molecules into Bi based high-temperature superconductors has previously been demonstrated to extend the interlayer spacing by a factor of up to three without changing the superconducting transition temperature. μSR is used to investigate the London penetration depth, as a function of interlayer spacing, of two series of such samples. The results show a simple trend corresponding to a constant density of superconducting electron pairs in each layer. The consequences of this result are discussed in the context of previously identified scaling relations between superconducting parameters. Results of experiments excluding the possibility of magnetic order and muon-organic radical formation in these samples are presented, as well a preliminary study of the field distributions in a mosaic of intercalated crystallites.

For my family

For unlike the nuclear or elementary particle physicist, we know what our particles are, and what are the forces between them, but we must use all our intelligence and insight to understand the consequences of this interaction.

D. Pines, Elementary Excitations in Solids

The principle of science, the definition, almost, is the following: The test of all knowledge is experiment. Experiment is the sole judge of scientific "truth."

R. P. Feynman, The Feynman Lectures on Physics, Volume 1

Acknowledgements

I am greatly indebted to the following people and institutions, and I wish to thank them:
Those in Oxford:

- Steve Blundell for his wise guidance, patience, and good humour as supervisor of this thesis, assistance with certain experiments, allowing me use and develop certain programs he had written, and acting as a reliable chauffeur to ISIS.
- Bill Hayes for suggesting that experiments should be performed on, and then obtaining, most of the magnetic samples discussed herein, and also for helpful readings of the manuscripts that resulted from these experiments and make up those parts of this thesis.
- Tom Lancaster for obtaining μSR data on $NaNiO_2$ and $LaTiO_3$, the analysis of which forms part of this thesis, and advising on the analysis and interpretation of my results.
- Francis Pratt for developing WiMDA so that it can analyse the broad variety of experimental data used herein, for help and advice concerning μSR experiments, and his insights into superconductor phenomenology.
- Mick Brooks for helpful advice on LaTeX, C++ programming, and for help with some of my earlier attempts at data analysis and experiments, as well as lifts to ISIS for experiments.
- Prabhakaran for making the samples of $NaNiO_2$ and for his help with heat capacity and magnetic susceptibility measurements.
- More generally: Paul Goddard for carrying out high-field magnetization measurements and helping me interpret the results, Olivier Rival for suggesting an interesting experiment, Heather Lewtas and Russell Ewings for assistance with a variety of experiments, Elisa Wheeler for discussions on $AgNiO_2$ and more broadly on neutron scattering, Sophie Oldham for the collaboration on $FeMo_4Ge_3$, and all the others who assisted in many ways.

Those at μSR facilities:

- Philip King, Adrian Hillier, Steve Cottrell, and James Lord for technical assistance at ISIS.
- Alex Amato, Chris Baines, Robert Scheuermann, and Hubertus Luetkens for technical assistance at PSI.

Those who provided samples:

- Michael Holzapfel and Sophie de Brion for their collaboration on $LiNiO_2$ and discussions on $NaNiO_2$.
- Markus Hoinkis for helpful advice and comments on my work on TiOCl, as well as the groups of Professors Horn and Claessen who provided the samples.
- Masahiko Isobe for providing the samples of $NaTiSi_2O_6$ and $MgTi_2O_4$ and helpful discussions on the literature on these compounds.
- Soon-Jae Kwon and his collaborators for the series of intercalated superconductor samples.
- Professor Itoh who provided the sample of $LaTiO_3$ and Professor Akimitsu who provided the samples of $YTiO_3$, and their research groups.
- Mo Kurmoo for providing a wide selection of samples for heat capacity measurements and Jamie Manson likewise for magnetic susceptibility measurements.

My family, to whom this work is dedicated, and those friends whom I have not mentioned so far, particularly Halim, Heather, and Jenn, who have supported me in many different ways and offered many amusing diversions during my project.

I am indebted to the Engineering and Physical Sciences Research Council and the Rutherford Appleton Laboratory for financial support during my research studies, and to Balliol College, which has been my home for the last 7 years, for financially supporting conference attendances.

Contents

List of Figures

Chapter 1

Introduction

1.1 Introductory remarks

Condensed matter physics may be considered the study of collections of atoms which exhibit some form of order, such that it can be described in terms of an order parameter. Examples of these include the crystallization of a material into a regular structure, the nematic order observed in liquid crystals, or superfluidity in liquid helium [Chai95, Kitt96]. Experimentally, the aim is to measure the order parameter associated with the phenomenon in question, characterize transitions between phases with different order parameters or from order to disorder, or investigate fluctuations within the system, while controlling the material by changing thermodynamic variables such as temperature or volume. These properties can often be predicted theoretically, since condensed matter phenomena provide examples of both single particle and many body problems, and provide an opportunity to experimentally probe theories, which is not always true in other areas of theoretical physics [Pine63, Ande84]. The combination of condensed matter physics, chemistry, and materials science has also led to technological applications, examples being magnetic information storage or medical MRI scanners. These examples also demonstrate the success of combining these approaches in magnetism and superconductivity - two active areas of experimental, theoretical, and technological research.

Since the physical properties of solid and liquid phases are largely governed by the interactions of electrons, particularly true in the cases of magnetism and superconductivity, investigating these properties requires techniques that probe the collective behaviour of electrons. Heat capacity measurements provide a direct

probe of the entropy of a material, and a window into how the thermally available states change as a function of thermodynamic variables such as temperature, magnetic field, or pressure [Whit79]. Magnetic susceptibility is another approach to measuring the bulk properties of a magnetic or superconducting system, and another response function that can be predicted theoretically [Blun01]. As well as thermodynamic and magnetic measurements, fundamental particles have long been used to study solids, and more recently liquids and colloids. Both X-rays and neutrons are well established as probes of the atomic structure of materials, and, in addition, their magnetic properties [Squi78, Love84, Balc89, AlsN01]. Both of these techniques give information about the bulk properties of the system being studied, and this can be a significant limit to the information that can be discovered about systems which have a mixture of phases or do not possess long-range order. In such situations, local probes that can investigate materials on an atomic scale are needed.

The use of the muon, heavier counterpart to the electron, as a local probe in investigations of solids be traced back as far as the experiments made by Garwin *et al.* [Garw57], looking for parity violation in muon decay. With the advent of meson factories, such as TRIUMF in Vancouver and PSI near Zürich, sufficient quantities of muons became available to allow new information about materials to be deduced. This technique is now known as μSR (muon-spin-rotation/relaxation/resonance), since the experiment is similar to Nuclear Magnetic Resonance [Abra61, Hore95] or Electron Spin Resonance [Abra70]. μSR has primarily been used in the fields of magnetism and superconductivity because the large magnetic moment of the muon allows sensitive measurements of magnetic fields, with or without the application of an external field. I will go on to discuss this form of experiment in far more detail in section 2.2.

Examples of the uses of μSR include the detection of magnetic order in almost one-dimensional magnetic chains [Lanc06]; demonstrating that a magnetic field spontaneously appears below the superconducting transition temperature in Sr_2RuO_4, breaking time-reversal symmetry [Luke98]; and finding trends in high temperature superconductors that may give an indication of the so far unidentified origin of superconductivity in these materials [Uemu89, Uemu91, Prat05].

Combining these different techniques offers the possibility of probing the physical properties of materials on different timescales and length scales, gaining information from each technique that cannot be obtained from others. This com-

plementarity is an approach I exploit at several points within this thesis.

Transition metal oxides [Cox92, Rao98] have long been the subject of human interest and enquiry, examples being the optical properties of gemstones such as ruby or emerald, or the magnetic properties of lodestone. Because this class of materials encompasses a great chemical variety, its members exhibit most of the electronic phases available to solid matter. This allows all the degrees of freedom accessible to correlated electrons to be investigated; spin, charge, and orbital interactions all contribute to the physical properties of these materials. The chemical variety also allows the effect of substitution, disorder, and doping to be probed in a controlled manner. This can be seen in the Colossal Magneto-Resistance compounds [Rami97] or the superconducting analogues of La_2CuO_4 [Bedn86]. We can also see analogues of other physical systems in transition metal oxides: spins obeying Pauling's ice rules in pyrochlores [Snyd01] or the nematic electronic phase encountered in $Sr_3Ru_2O_7$ [Borz07]. In this thesis I investigate some examples of transition metal oxide systems where the physical properties are changed by controlled chemical alteration.

1.2 Plan of the thesis

This thesis covers three principle topics within magnetism and superconductivity, magnetic order, spin gap formation in spin chains, and the effect of changing layer spacing on a high temperature superconductor. These are all investigated using different forms of the μSR technique, and information from other experimental techniques is included as appropriate. While exhibiting a diverse range of physical properties, these materials all share the property of being spin-1/2 transition metal oxides. Beyond this, we see the effects of changing the effective dimensionality of magnetically ordered systems and the contrast in the properties of Ti^{3+} ions arranged in chains rather than in a more isotropic structure. Together, these represent a demonstration of the broad applicability of the μSR technique, and also show some of its limits.

The plan of this thesis is as follows:

- In Chapter 2, I explain the methodology of the μSR, magnetic susceptibility, and heat capacity measurements used to obtain the experimental results discussed in subsequent chapters, and give some illustrative examples of

data recorded using each technique.

- Chapter 3 considers layered triangular-lattice magnets of general formula $X\mathrm{NiO_2}$, comprising a study of the thermodynamic and magnetic properties of the A-type antiferromagnet $\mathrm{NaNiO_2}$ and a μSR study of the sister compound $\mathrm{LiNiO_2}$, including an investigation of the effects of doping this compound with Mg. In these compounds we see the effect of changing ionic radius and its influence on the chemical disorder in the material.

- In Chapter 4, I present the results of a μSR investigation of the magnetic properties of the orthorhombic perovskite compounds $\mathrm{LaTiO_3}$ and $\mathrm{YTiO_3}$, together with calculations deriving the expected results from the results of previous neutron diffraction measurements. While they have a similar structure, the magnetic properties are dramatically altered by the different radii of the La and Y ions.

- Chapter 5 considers the effect of dimerization on the magnetic properties of two spin-1/2 $\mathrm{Ti^{3+}}$ chain compounds, $\mathrm{NaTiSi_2O_6}$ and TiOCl, where the dimerization processes are rather unusual. A model relating the structural dimerization to the magnetic properties is developed and tested against magnetic susceptibility and μSR results.

- Finally, Chapter 6 reports the results of a systematic study of the effect on the properties of cuprate superconductors of changing their layer spacing by the intercalation of organic molecules. The possibility of magnetic order or muonic radical formation is tested, superfluid densities for each sample are extracted, and the results are put in the context of scaling relations between superconducting parameters, allowing straightforward comparison with literature data on a wide range of superconducting materials.

The lists of references for all the chapters and a list of publications are at the end of this thesis.

Chapter 2

Experimental methods

Contents

2.1 Introduction

In this chapter I introduce the experimental techniques used in the rest of this thesis. This is done through an explanation of the principles underlying each type of experiment, a description of the experimental apparatus and methodology, and examples of the form of the results. The techniques used here can be separated into the microscopic technique of μSR, which investigates the environment local to an implanted muon, and the bulk techniques of magnetic susceptibility and heat capacity measurements, where the signal is determined by the response of the whole sample to an external stimulus. Since μSR is the primary technique used in this thesis, I begin with a description of μSR in section 2.2. Further information about some of the samples used for μSR experiments was obtained using magnetic susceptibility and heat capacity measurements, and these are described in sections 2.3 and 2.4 respectively.

2.2 μSR

Studying the precession of muon spins within solids can be considered to have started about fifty years ago with the experiments of Garwin *et al.* looking for parity violation in the muon decay [Garw57]. Such experiments, examining the physical properties of muons continue to this day and still provide information that challenges theoretical models of particle physics [Jami06, Chit07]. Using muons to investigate the properties of the material they are implanted into is somewhat more recent, and about thirty years ago Yamazaki, Nagamine, Crowe, and Brewer coined the adjective μSR (Muon Spin Rotation, Relaxation, and Resonance) to describe the general technique, drawing on the analogy between these methods and those of techniques such as Nuclear Magnetic Resonance (NMR) and Electron Spin Resonance (ESR) [Brew94]. That the R in μSR needed to remain ambiguous highlights the variety of experimental methods that can be employed using muons, investigating topics in solid state physics, chemistry, soft condensed matter, and even biophysics [Naga03].

That muons are useful in investigating these subjects is determined by the physical properties of the muon, given in Table 2.1. Firstly, the particle physics leading to muon production by proton spallation leads to an almost ideally spin polarized beam of muons (processes 2.1 & 2.2), the short pion lifetime also being

Table 2.1: The properties of muons. Data taken from Refs [Part06, Chit07].

Mass (m_μ)	105.658369(9) MeV/c^2
	$= 206.7683\ m_\mathrm{e}$
	$\approx 1/9\ m_\mathrm{p}$
Charge	$\pm e$
Spin	1/2
Magnetic moment μ	$1.0011659208(9)e\hbar/2m_\mu$
Lifetime	2.197019(21) μs

an advantage for a pulsed muon source. Secondly, the muon decay preferentially emits the positron along the direction of the muon spin at the moment of decay (process 2.3). These two facts allow information about how the orientation of the muon spin has changed while it is in the sample to be extracted, underpinning the technique. For positive muons the relevant particle physics processes are:

$$p + p \rightarrow \pi^+ + p + n, \quad \text{or} \quad p + n \rightarrow \pi^+ + n + n, \tag{2.1}$$

$$\pi^+ \rightarrow \mu^+ + \nu_\mu, \tag{2.2}$$

$$\mu^+ \rightarrow e^+ + \nu_e + \bar{\nu}_\mu. \tag{2.3}$$

Other quantities favourable for the μSR technique are:

- The lifetime of 2.2 μs is long compared with many condensed matter processes, and allows timescales around 10^{-12}-10^{-4} s, intermediate between those investigated by NMR (10^{2}-10^{-5} s) or ac susceptibility measurements (1-10^{-4} s) and neutron scattering ($< 10^{-9}$ s), to be investigated [Sche85].

- The gyromagnetic ratio $\gamma_\mu/2\pi = 135.55342$ MHzT^{-1}, proportional to the magnetic moment, is intermediate between those of electrons and nuclei, meaning the technique is sensitive to magnetic fields as small as $\sim 10^{-5}$ T.

- The spin-1/2 nature of the muon means that quadrupolar coupling to its environment does not occur, which can complicate NMR experiments.

More detailed general descriptions of the μSR technique are given in books by Schenck [Sche85], the contributors to the 1991 Scottish Universities Summer School in Physics [Lee99], and Nagamine [Naga03], and in review articles by, among others, Cox [Cox87], Dalmas de Reotier [Dalm97], and Blundell [Blun99].

I now go on to describe the specific details of the muon techniques required for the experiments described in this thesis. These may be conveniently grouped into three varieties: zero-field (ZF) experiments, longitudinal-field (LF) experiments where a magnetic field is applied parallel to the initial muon spin orientation, and transverse-field (TF) experiments where the applied magnetic field is perpendicular to the initial muon spin orientation. Before coming to the specifics of these experiments, however, I outline the process by which muons are produced and are implanted into the sample, and the general method of a μSR experiment.

Muon production through the processes 2.1 and 2.2 requires a source of protons with an energy above around 500 MeV. The proton beam is incident on a stationary target of a light element, typically graphite, and pions are produced. If only positive muons of relatively low momentum are required the pions decaying at rest within the target produce 'surface muons'. This approach is used, for example, at the ISIS Pulsed Muon Facility. If both positive and negative muons are required then the pions produced are allowed to decay in flight, leading to higher momenta muons suitable for applied pressure experiments where a longer stopping range is required. This produces what are referred to as 'decay muons', and is used at the RIKEN-RAL facility, among others. Pions also decay into positrons, with a smaller branching ratio, and these and any other charged particles need to be removed from the beam of muons before it reaches the sample. This can be achieved using beam steering and the charged particle contamination can be reduced significantly. Positive muons produced by the process 2.2 have their spins antiparallel to their direction of travel (due to neutrino helicity conservation) and for certain experiments it is desirable to change this (e.g. more favourable magnet orientation). This is done using a spin rotator, which consists of electric and magnetic fields aligned perpendicular to each other and to the muon direction of travel. This approach can rotate the muon spin by 90° [Eato99]. The beam of muons arrives in the sample and stops within ~ 1 ns, and has a typical stopping range of 0.11 g/cm^2 for surface muons [Eato99] or 0.13 g/cm^2 for decay muons at PSI [Amat06].

Schematic descriptions of μSR experiments are shown in Figure 2.1. The experimental clock starts at continuous muon sources when the muons pass a trigger detector and at pulsed muon sources a signal from the particle accelerator is used as the start time. Useful data cannot be extracted until a short time after the start time, details of which will be discussed below. The muon interacts in

Figure 2.1: Schematic depictions of the two types of μSR experiments used within this thesis. (a) A transverse field (TF) experiment. (b) A zero-field (ZF) experiment. The longitudinal field (LF) experiments have the same arrangement of the apparatus, but a magnetic field is applied along the direction of the initial muon spin polarization. Figures taken from Ref. [Soni02].

some way with its environment until it decays. The positron emitted according to process 2.3 is most likely to be emitted along the instantaneous direction of the muon spin at the time of the decay, with an angular distribution about the spin orientation of:

$$N(\theta) = N_0 \left(1 + a \cos\theta\right), \tag{2.4}$$

where $a = 1$ for the maximum possible emitted positron energy of 52.83 MeV/c and averages to 1/3 considering all positron energies. The positron is counted by a scintillating detector and the light emitted from the scintillator is recorded using a photomultiplier tube, stopping the experimental clock. Recording the decays of many muons, typically 10^7 per experimental step, allows a picture of the time evolution of the muon spin to be built up.

To gain any information from the muons decaying in the sample we need to be able to determine how their spin polarization changes as a function of time. The simplest apparatus one could consider for such a time-differential μSR experiment consists of two detectors placed on opposite sides of the sample. To get this information we define an asymmetry, $A(t)$, between the count rates $N_{\mathrm{F}}(t)$ and

$N_B(t)$ in the two detectors [F(orward) and B(ackward)] as:

$$A(t) = \frac{N_F(t) - \alpha N_B(t)}{N_F(t) + \alpha N_B(t)}, \tag{2.5}$$

where α is a parameter describing the inequivalency of the two detectors. In reality, corrections for background counts and deadtimes in each detector are made as described below. If our hypothetical detectors are arranged symmetrically around the muon decay position, as depicted in Figure 2.1(b), we would expect an asymmetry in the number of muons counted in the forward and backward detectors of 1/3, if the polarization is ideally maintained, this being the energy averaged asymmetry in equation 2.4. In reality, the detectors are not ideally symmetric about the sample position and are likely to have some difference in their count rate, such as different solid angle coverage. This means that we need to determine the parameter α experimentally. α is determined by measuring a sample in its paramagnetic phase in a weak transverse field, typically 20 or 50 G (2 or 5 mT). The form of the data obtained is shown in Figure 2.3(a), with a TF data set obtained on a sample of CoGly [Prat07]. The data from the two opposing detectors are added together bin by bin with a variable scaling factor depending only on α, and the correct value of α is obtained by ensuring that the cancellation between the counts in the opposing detectors is exact and independent of time.

Several different μSR spectrometers were used in the course of this thesis, MuSR and EMU at the ISIS pulsed muon facility, and ARGUS at RIKEN-RAL, both situated at the Rutherford Appleton Laboratory, United Kingdom, and GPS and DOLLY at the Paul Scherrer Institute (PSI), Switzerland. Since the majority of the data presented below was recorded on the MuSR, GPS, and DOLLY spectrometers, and DOLLY is a clone of GPS, I will only describe MuSR and GPS here. Figure 2.2 shows both spectrometers in panels (a) and (b) respectively.

While the experiments done in these spectrometers are essentially the same and they have similar capabilities, the differences between the pulsed muon source at ISIS and the continuous source at PSI necessitate certain differences in the setup of the spectrometers. At ISIS the proton accelerator is a synchrotron that produces a double pulse of protons (FWHM = 70 ns, separation = 330 ns) fifty times per second [Eato99]. Using a kicker the two pulses are separated and the pulse is also sliced before the muons reach MuSR. Around 4000 muons arrive at the spectrometer in each pulse and because detectors have a finite 'dead time'

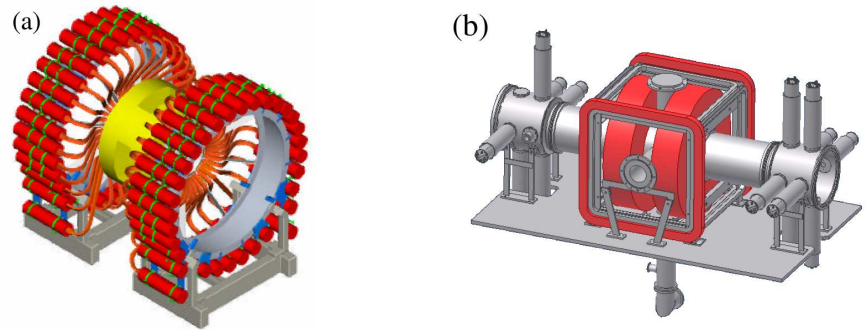

Figure 2.2: (a) The MuSR spectrometer at ISIS [Hill05]. ZF & LF experiments have the muon beam arriving from the top left of the figure, TF experiments involve rotating the apparatus so the beam arrives from the top right. The CCR cryostat is inserted from the side, other cryostats are inserted from the top. The two rings of photomultiplier tubes and light guides leading from the scintillating detectors are visible. (b) The GPS spectrometer at PSI [Amat06]. The beam enters from the right hand side and the flow cryostat used is fixed to the side port shown. Experimental magnets are seen around the sample space in the centre of the spectrometer.

between being able to detect positrons, the detector array is highly segmented into 64 elements so each detector covers a smaller solid angle and therefore counts fewer positrons. Having muons arriving in pulses allows a much higher count rate for the experiment, but the width of the pulse provides a limit to the muon precession frequencies or relaxation rate ($\sim$ 10 MHz) that can be measured [MuSRWeb]. Cryostats are interchangeable and those used will be described as appropriate. At PSI the proton accelerator is a cyclotron and supplies a continuous beam of protons. Muons arrive at the apparatus about once every 10 μs. There should therefore be only one muon in the apparatus at any given time, controlled by the Muons On REquest system that prevents a second muon entering the spectrometer until the first muon has decayed [Abel99, Amat06]. This limits the rate available but the time resolution is only limited by the detector electronics, to around 1 ns. This is sufficient for measurements on almost all transition metal oxide compounds. With only one muon in the sample at any time, GPS needs only five separate detectors, to allow for both LF and TF geometries, and magnetic fields up to 0.6 T can be applied [GPSWeb]. GPS has a fixed ^{4}He flow cryostat that operates between room temperature and 1.8 K.

That the experimental clock for a μSR experiment starts slightly before the muons enter the sample can be used to advantage. Before the muon or pulse of

muons arrive the only contribution to the counts in each detector will be from the positron background. This is found to be approximately constant in time (small at pulsed sources) and can be used as the background count rate, when producing corrected count rates to use in equation 2.5. When muons arrive in the sample the count rate rises to a maximum. The midpoint of this rise, which lasts for approximately the pulse width (zero at a continuous source such as PSI), is used to define the zero of time for the experiment, t_0. The maximum constitutes the earliest useful data point, t_{good}. These values are generally known from calibration runs, although they can be fitted from the raw data. Because detectors have a 'dead time' after detecting a positron of $\tau_d \sim 10$ ns, the relaxation of muon spins in a substance, such as Ag, which does not depolarize them significantly will be non-exponential. Making high statistics calibration runs on Ag mounted in the sample position allows this effect to be measured and appropriate corrections to the count rate. The true count r varies with the observed count rate r_{ob} as:

$$r = r_{\mathrm{ob}}/(1 - r_{\mathrm{ob}}\tau_d), \tag{2.6}$$

and this correction has been included in all the data sets recorded at pulsed muon sources presented in this thesis.

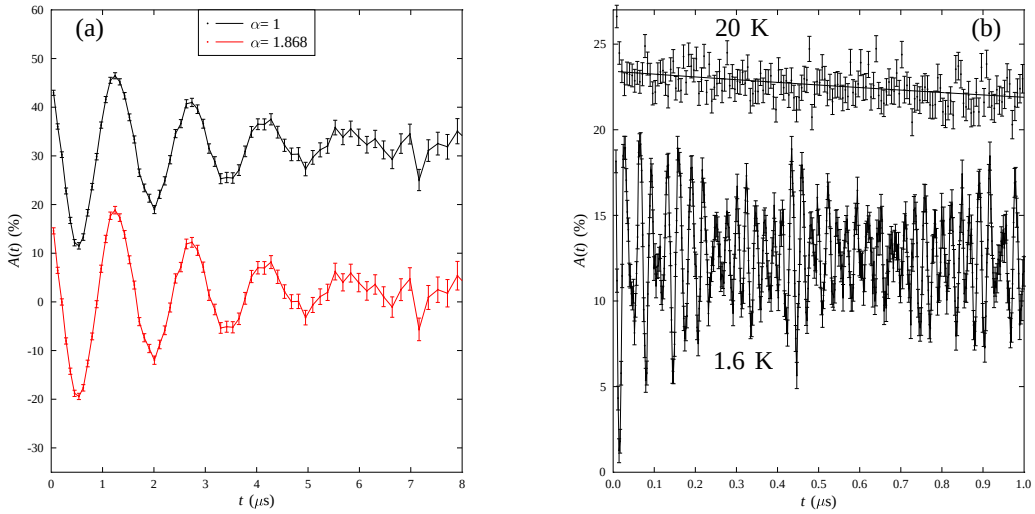

Figure 2.3: (a) Transverse field data from a TF50 run on CoGly [Prat07]. Variable length time bins have been used to correct for the poorer counting statistics at longer times. (b) Zero-field data recorded for $AgNiO_2$. After Ref. [Lanc08]

Examples of the raw data are shown in Figure 2.3. Panel (a) shows a weak transverse field run recorded to determine the α parameter in CoGly [Prat07], and panel (b) shows two data sets recorded for $AgNiO_2$, discussed in Chapter 3. The former shows the weak exponential relaxation of the precessing signal observed in a typical paramagnetic material when a weak magnetic field is applied perpendicular to the initial muon spin orientation, and the importance of determining α. The zero-field data shows the difference between the signals observed in the paramagnetic phase above T_N and the magnetically ordered phase below T_N. $AgNiO_2$ is particularly interesting because six distinct precession frequencies are observed below T_N, pointing to a complex magnetic structure.

The analysis of muon data considered within this thesis was carried out using the WiMDA program written by Dr F. L. Pratt, versions 1.158-1.181 [Prat00].

An important issue concerning a μSR experiment is the question of where the implanted muon comes to rest within the sample. This is particularly true in the studies of ordered magnetic systems, since the local field at the muon site could depend strongly on the location of the muon relative to the magnetic moments. Naively, one would expect the positive muon to implant at sites of the greatest electronegativity, such as near negative fluoride or oxygen ions. In the case of fluoride compounds this can lead to F-μ^+-F states and quantitative analysis of the characteristic signal arising from this process can be used to gain considerable information about the muon site [Brew86, Lanc07]. In oxides, such as those considered in this thesis, the muon remains in a diamagnetic state and far less information can be obtained from the signal above the magnetic ordering transition. Instead, the dipolar fields $B_{\rm dip}$ arising from the alignment of the magnetic ions, which dominate the local field at the muon site, can be calculated for possible magnetic structures. This is done by calculating, over around 10^4 unit cells, the function:

$$B_{\rm dip}(\mathbf{r}_\mu) = \frac{\mu_0}{4\pi} \sum_i \frac{3(\mu_i \cdot \hat{\mathbf{n}}_i)\hat{\mathbf{n}}_i - \mu_i}{|\mathbf{r}_\mu - \mathbf{r}_i|^3}, \tag{2.7}$$

where $\mathbf{r}_\mu$ is the muon site, $\mathbf{r}_i$ is the position of the i th magnetic ion, μ_i is the ordered magnetic moment of the i th magnetic ion, and $\hat{\mathbf{n}}_i (= (\mathbf{r}_\mu - \mathbf{r}_i)/|\mathbf{r}_\mu - \mathbf{r}_i|)$ is the unit vector between the muon and magnetic ion sites. This approach is sufficient for insulating antiferromagnets, but for insulating ferromagnets the Lorentz field and the demagnetizing field may be relevant. Other contributions to the local field at the muon sites, except the diamagnetic field within a superconductor, are

outside the scope of this thesis. Comparison between the calculated fields and the observed precession frequencies allows muon stopping sites to be deduced, giving a means of testing proposed structures [Dalm97].

2.3 Magnetic susceptibility and magnetization

Magnetic susceptibility measurements provide the simplest way of characterizing the magnetic properties of most samples. Information about the average magnetic moments of ions, whether the coupling between ions is primarily antiferromagnetic or ferromagnetic, concentrations of magnetic impurities, and the temperatures of any magnetic transitions are generally straightforward to determine. It is normally also one of the easiest quantities to calculate from a theoretical model, and so provides a direct comparison between experiment and theory.

The majority of magnetic susceptibility measurements presented in this thesis were carried out using a Quantum Design MPMS-XL SQUID magnetometer [MPMS90], the exception being the high field magnetization measurements done by Dr P. A. Goddard included in section 3.3.2. The MPMS system provides an integrated SQUID, cryostat (1.8-400 K), 7 T superconducting magnet, and sample transport, together with a data acquisition system. Three schemes of measurement are used below, DC measurements of the susceptibility and magnetization, and ac susceptibility measurements. Given that the difference between the DC measurements is only whether T or B is changed between measurements, I explain them together in section 2.3.1, and explain ac susceptibility measurements in section 2.3.2. Details common to both sections are included below.

To obtain the correct value of the magnetic susceptibility the sample must be placed in the correct position relative to the detection coils of the magnetometer. This is usually carried out in the paramagnetic phase with a field applied to the sample to induce a sufficient magnetic moment to measure with the detection coils. In an automated process the sample is moved through the detection coils with measurements taken at various positions along the magnet axis. As a function of position, the response takes the form $\sin(x)/x$. Correct alignment for the MPMS system requires that the primary maximum of this function, at $x = 0$, corresponds to the position of the detection coils. While a superconducting magnet provides a significantly larger field range for measurements, it has the concomitant disadvantage that magnetic flux can be trapped within the bore, or in the shielding

around the magnet, so that while the current applied to the superconducting coil may be zero, the magnetic field at the sample position is not zero. This problem is overcome by 'degaussing' the magnet after it has been used to generate a field over 5 T. The process works by rapidly cycling through alternating positive and negative field values decreasing from 1T to 0.1T, such that any remenant fields are expelled. Measurements using standard samples suggest that this process successfully decreased the remenant field to less than 1 G (0.1 mT).

2.3.1 DC magnetic susceptibility measurements

The DC measurements carried out during the course of this thesis were carried out using the Reciprocating Sample Option (RSO) [MPMS99] of the MPMS apparatus described above. This is a quasi-DC measurement, since the sample is oscillated up and down at a frequency of only a few Hz. If done carefully this produces results consistent with a full DC measurement where the magnetization is measured at a number of positions relative to the detection coils, and this approach collects the data at a significantly faster rate. Magnetic susceptibility measurements using this method actually measure the magnetization at a fixed field, and the susceptibility values presented below are extracted under the linear, small field assumption: $\chi = \mu_0 M/H$. The magnetization measurements are also measured in fixed fields, changing the field in small steps at constant temperature.

Two forms of DC susceptibility measurements are referred to below: zero field cooled (ZFC) and field cooled (FC). For a ZFC measurement the sample is cooled from room temperature in as close to zero field as the apparatus allows, and once the base temperature for the measurements is reached the measurement field is applied. The data is recorded while warming the sample through a series of temperatures, stabilizing the temperature for each measurement. If a series of these measurements is carried out, the sample is warmed well above any ordering temperatures before being cooled again in zero field. FC measurements mean that the measurement field was applied to the sample at high temperature and then cooled in that field. These data can be collected either on warming or cooling, as specified.

The example data sets shown in Figure 2.4 come from a series of measurements on polycrystalline samples of planar organic magnets containing Cu^{2+} ions. The compound shown here, $Cu(pyz)_2(HF_2)(PF_6)$ [Mans07], is a layered transition

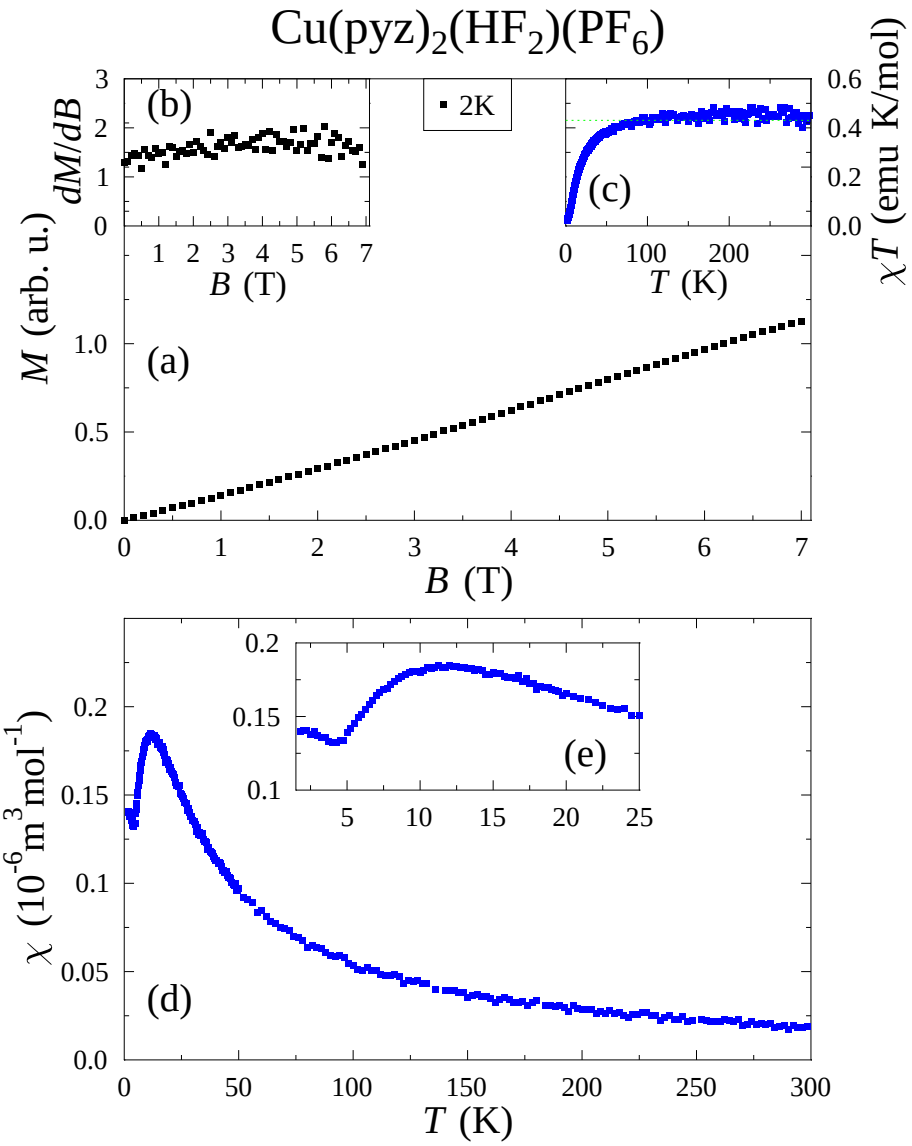

Figure 2.4: DC magnetic susceptibility data measured on polycrystalline samples of $\mathrm{Cu(pyz)_2(HF_2)(PF_6)}$ [Mans07]. (a) Magnetization M as a function of applied magnetic field B. (b) Field derivative of the magnetization, dM/dB. (c) Product of the magnetic susceptibility shown in panel (d) and temperature, χT. (d) Magnetic susceptibility measured in an applied field of 1 T. (e) Magnetic susceptiblity around the peak at 6 K. The methodology is discussed in detail in the text. The author is grateful to J. L. Manson for providing the sample.

metal complex where the organic groups co-ordinated around the Cu^{2+} ion have been chosen to control the magnetic properties. Panel (a) shows magnetization measurements as a function of applied field. Panel (b) shows the field derivative of the magnetization, calculated as the difference between the magnetization values at successive steps. Neither panel shows any significant features that might suggest metamagnetic transitions or going from long-range order to paramagnetism. Panel (c) shows the product of the magnetic susceptibility and temperature, χT, which tends to a constant value at higher temperature, giving the size of the magnetic moments in the sample and also suggesting antiferromagnetic interactions dominate at low temperature. The value suggests $\mu_{\text{eff}}/\mu_{\text{B}} = 1.86(2)$. Panel (e) is an inset showing the magnetic susceptibility data at low temperature.

2.3.2 AC magnetic susceptibility measurements

Measurements of the ac susceptibility of a magnetic specimen are used to investigate slow dynamic fluctuations of the magnetic moments present. In superconductors, the technique gives a clear signal of the onset of superconductivity. The experiment involves applying a small alternating magnetic field to the sample, passing an alternating current of known frequency, amplitude, and phase, through drive coils wound around the sample position. Measurement coils placed close to the sample measure the magnetic moment of the sample as an induced current. The ac susceptibility has two components, one in phase with the drive current (the real part χ'), and one out of phase with the drive current (the imaginary part χ''), with the phase difference ϕ usually referred to as the loss angle. We can write this as:

$$\chi_{\text{ac}} \exp i(\omega t + \phi) = \chi' \cos(\omega t) + \chi'' \sin(\omega t), \tag{2.8}$$

where ω is the measurement frequency. This approach gives more experimental parameters to vary compared with the DC measurements described in section 2.3.1 above. The experiments described below were carried out using a constant amplitude of the drive field, constant applied DC field (generally zero), and measuring at a series of frequencies as a function of temperature. The drive field is typically less than 10 Oe (0.1 mT), as opposed to the typical DC field used for DC susceptibility measurements of around 1000 Oe (100 mT), allowing behaviour that varies strongly at very small fields to be probed. Two consequences of this are that the approximation that the magnetization reported by the apparatus is even

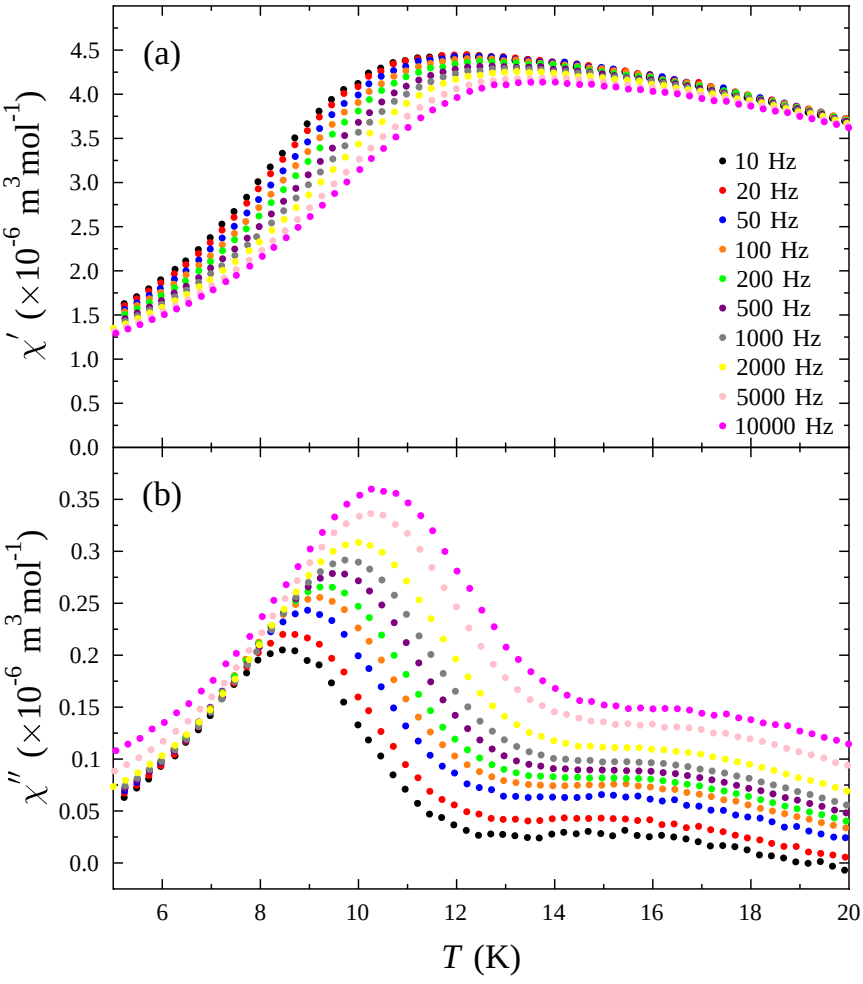

Figure 2.5: AC susceptibility data recorded on the intermetallic spin glass $FeMo_4Ge_3$ using the ACMS option of a PPMS. (a) Real part of the ac susceptibility, χ'. (b) Imaginary part of the ac susceptibility, χ''. The author is grateful to S. E. Oldham for providing the sample and H. J. Lewtas for assistance with these measurements.

further within the range where $\mu_0 M = \chi H$ and also that zeroing the DC field within the apparatus is far more important, because the drive field is so small. The example data sets shown in Figure 2.5 were recorded using the ACMS option of the PPMS [PPMS00] apparatus described below. This is similar to the ac susceptibility apparatus within the MPMS system, but has a lower sensitivity. The sample used was the intermetallic spin glass $FeMo_4Ge_3$ [Bake08]. While it was intended to carry out these measurements in zero applied DC field, the large superconducting magnet within the PPMS had not been correctly zeroed, with a remenant field of around 100 Oe (10 mT) (verified by repeating a subset of these measurements in an MPMS using known applied DC fields). The peak in χ' around 12 K can be seen to increase in temperature as the measurement frequency was increased, a feature characteristic of spin glasses. Details necessary to analyse ac susceptibility data will be introduced as necessary in the experimental sections below.

2.4 Heat capacity

Heat capacity measurements provide another straightforward measurement that can be used to characterize the properties of samples. They provide a means of probing how the entropy of a sample changes as a function of temperature (or other experimental parameters such as magnetic field). This gives a clear way of observing phase transitions in most materials. To measure the heat capacity, the temperature of the sample is measured as heat is applied to the sample in a known and controlled way. For the experiments discussed below, this is done using a technique referred to as the 'two-tau' method, implemented within the Heat Capacity option of a Quantum Design Physical Properties Measurement System (PPMS) [Hwan97, PPMS00]. The apparatus allows measurements in the temperature range 0.4-400 K. To explain this approach I follow the discussion given by Lashley *et al.* [Lash03] in their critical investigation of the effectiveness of this apparatus for measurements of heat capacities in different situations.

We are interested in the unknown heat capacity C_s of the sample being measured at a temperature T_s. The sample is attached to a 3×3 mm thin alumina platform using Apiezon grease, with a thermal conductance K_2 to the sample. The platform has a thermometer attached to it measuring a temperature T_p and has a heat capacity C_a, referred to as the addendum and measured over the whole

temperature range of interest without a sample mounted on the platform. The platform has a thin-film heater evaporated onto the bottom of it which supplies the heat pulse used in the experiment. The platform is connected to a copper heat sink held at a constant temperature T_0 through four thin wires that provide a thermal conductance K_1 and also the electrical connections to the heater and thermometer on the platform. This entire setup is enclosed within a puck that can be inserted into the standard electrical connections of the PPMS.

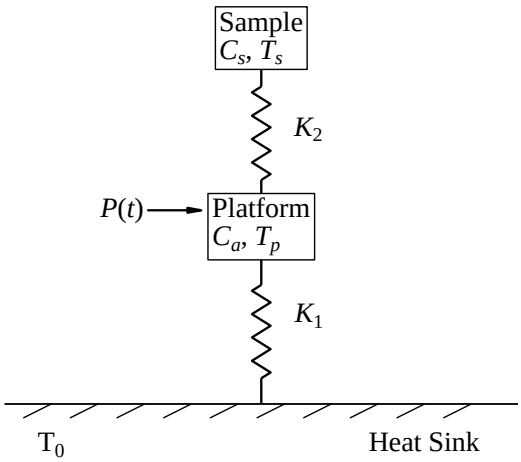

Figure 2.6: Schematic diagram describing the experimental arrangement for a 'two-tau' heat capacity measurement after Refs. [Schw75, Hwan97, Lash03]. The parameters shown are those in Equations 2.9 & 2.10.

With a power $P(t)$ applied to the platform using the thin-film heater the coupled differential equations describing the heat-balance conditions for the system depicted in Figure 2.6 are:

$$P(t) = C_a \frac{\mathrm{d}T_p}{\mathrm{d}t} + K_2(T_p(t) - T_s(t)) + K_1(T_p(t) - T_0), \tag{2.9}$$

$$0 = C_s \frac{\mathrm{d}T_s}{\mathrm{d}t} + K_2(T_s(t) - T_p(t)). \tag{2.10}$$

Since the sample-platform thermal link is not necessarily sufficient to ensure that $K_2 \gg K_1$ the sample temperature will not equal the platform temperature. In this case the platform temperature falls as:

$$T_p = T_0 + A\exp(-t/\tau_1) + B\exp(-t/\tau_2), \tag{2.11}$$

with τ_2 normally much shorter than τ_1. The former describes the sample to platform thermal link and the latter describes the link between the heat sink and the sample and platform combined.

The experimental scheme is to apply a constant heat pulse of duration $\sim \tau_1$ and then measure the platform temperature during this heat pulse and for an equal time afterwards while the temperature falls. The value of P is chosen to raise the sample temperature by a specified amount controlled by the user, typically of order 1 % of the measurement temperature, within a certain tolerance. The temperature is fitted to equations of the form 2.11 for both heating and cooling parts of the temperature trace, and to extract the sample heat capacity C_s the method described by Hwang *et al.* [Hwan97] is used. A data set is recorded as a sequence of these measurements repeated at each value of the experimental variable, stabilizing the initial temperature before each heat pulse is applied.

The systematic investigation of the accuracy of the PPMS Heat Capacity option made by Lashley *et al.* [Lash03] found that the standard measurement approach works very well for metallic conductors with an uncertainty of ± 2 % for $5 \leq T \leq 300$ K, and around ± 5 % for $T \leq 5$ K. Results can differ significantly from reference values if the sample heat capacity becomes small compared to the addendum heat capacity, a problem particularly for insulators, or for any sample in the vicinity of a first-order phase transition, due to the latent heat.

The example heat capacity data sets shown in Figure 2.7 (from my own work and to be presented elsewhere) use each of the two approaches used later in this thesis. Figure 2.7(a) shows the results of measurements as a function of temperature on a series of $Co_{1-x}Zn_xGly$ samples, where Gly is the organic group glycerolate. CoGly has interesting critical properties [Prat07] and the magnetic ordering at $T_N = 35$ K is evident in the sharp peak in the heat capacity. Measuring the heat capacity of ZnGly allows the lattice contribution to the heat capacity to be estimated. The remaining magnetic heat capacity in the Co containing samples is composed of contributions from magnetic ordering and the excitations between crystal field levels, both of which change with the Co concentration. Figure 2.7(b) shows measurements of the heat capacity of the heterometallic wheel molecular magnet Cr_7Ni [Lars03, Evan06] as a function of magnetic field at a constant temperature of 0.5 K. This compound has a complicated series of energy levels which change as a function of magnetic field. Measuring the heat capacity as a function of field shows peaks where the measurement temperature is comparable with

the separation between energy levels (Schottky anomalies for $\Delta \sim 2.4 k_B T$), and falling close to zero when energy levels cross [Evan06]. Evidence for anti-crossing of levels would be seen as a higher heat capacity contribution away from the peaks.

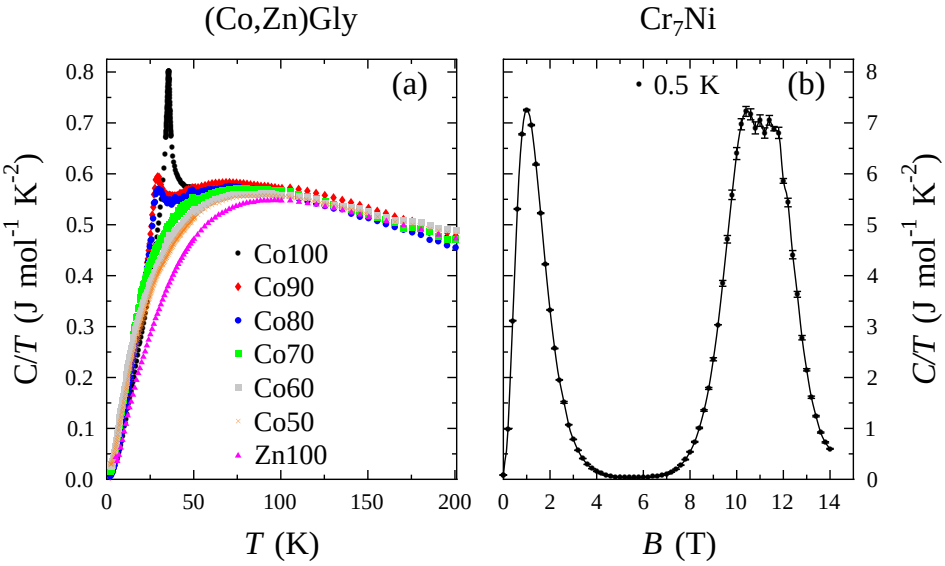

Figure 2.7: (a) Zero field heat capacity of various $(\mathrm{Co,Zn})\mathrm{Gly}$ samples measured as a function of temperature. The author is grateful to Dr M. Kurmoo for providing these samples. (b) Heat capacity of the heterometallic wheel magnet $\mathrm{Cr_7Ni}$ [Lars03] measured as a function of magnetic field at a constant temperature of 0.5 K. The author thanks O. Rival for suggesting this experiment and supplying a sample.

2.5 Conclusion

In this chapter I have discussed the techniques that will be used on a range of samples in the remainder of this thesis. Each has its own strengths and weaknesses, but combining the techniques gives a more complete picture of the properties of the sample under investigation.

Chapter 3

Layered triangular lattice magnets: $NaNiO_2$ and $LiNiO_2$

Contents

3.1 Introduction

Triangular lattice antiferromagnets exhibit a rich variety of ordering phenomena related to geometrical frustration [Coll97]. When the triangles forming the lattice are distorted from equilateral to isosceles there is a partial release of the geometrical frustration, which can lead to more unusual forms of magnetic order exemplified in the fractional spin-liquid in Cs_2CuCl_4 [Cold03], the spin-density wave in $Na_{0.75}CoO_2$ [Sale04], and the rich B–T phase diagram of $CoNb_2O_6$ [Koba00].

The series of triangular lattice magnets $LiNiO_2$, $AgNiO_2$, and $NaNiO_2$, seems to offer the possibility of tuning the release of the geometrical frustration by changing the exchange parameters, allowing models describing these systems [Daré03, Vern04, Reit05] to be tested experimentally. The first synthesis of $NaNiO_2$ and $LiNiO_2$ in near stoichiometric form was reported by Dyer *et al.* [Dyer54]. Interest in the magnetic properties of these compounds began with the proposal by Hirakawa *et al.* [Hira85] that $LiNiO_2$ might be a physical realization of the $S = 1/2$ resonating valence bond ground state proposed by Anderson [Ande73]. Studies of $LiNiO_2$ have suffered from the high lithium ion mobility [Good58] that makes the compound an excellent ionic conductor, but leads to non-stoichiometry when lithium and nickel ions substitute with one another. A discussion of the literature on $LiNiO_2$ is given by Reynaud *et al.* [Reyn01], highlighting the variety of sample dependent results observed. The analogous compound $NaNiO_2$ has proved more straightforward to characterize because it can be produced in stoichiometric form. More recently, the hexagonal form of $AgNiO_2$ (leading to better defined magnetic properties) and Ag_2NiO_2 have been synthesized [Sörg05, Schr02] and are beginning to be characterized [Wawr07, Lanc08, Yosh06, Sugi06].

In this chapter I present a thermodynamic and magnetic study of $NaNiO_2$ in sections 3.2-3.7, the results of μSR experiments on notionally stoichiometric $LiNiO_2$ and 5 % Mg-doped $LiNiO_2$ in sections 3.8-3.10, and in section 3.11 conclude by relating these results to similar work on the analogous compounds $AgNiO_2$ and Ag_2NiO_2, as well as water intercalated $NaNiO_2$.

The majority of the work presented here on $NaNiO_2$ has already been published [Bake05, Bake06], as well as in [Godd05]. The work in section 3.9 is being prepared for publication in conjunction with an ESR and magnetic susceptibility study investigating the effects of Mg-doping on $LiNiO_2$ [Bond08].

3.2 Thermodynamic and magnetic properties of $NaNiO_2$

Above 480 K the space group of $NaNiO_2$ is rhombohedral ($R\bar{3}m$) [Figure 3.1 (Left)] and there is a cooperative Jahn-Teller transition to a low temperature monoclinic ($C2/m$) phase [Figure 3.1 (Right)] below this temperature [Chap00b]. The low-temperature structure can be considered to be layers of NiO_6 octahedra in the ab plane, with a trigonal distortion lengthening the Ni-O bonds in the ac plane along an axis at 41° to the c-axis of the crystal. This gives a lattice of isosceles triangles of Ni^{3+} ions. Each Ni^{3+} ($3d^7$) ion is in the low spin state ($t_{2g}^6 e_g^1$, $S = 1/2$), so the ground state is a singly-occupied $|3z^2 - r^2\rangle$ orbital with z along the axis of the Jahn-Teller induced trigonal distortion [Chap00b].

Figure 3.1: Structure of $NaNiO_2$. (Left) High temperature $R\bar{3}m$ phase shared by $LiNiO_2$. Figure from [Mesk04]. (Right) Low temperature $C2/m$ phase relevant to the magnetic phase of $NaNiO_2$ discussed below. Figure from [Chap00b].

A peak in the magnetic susceptibility interpreted as the Néel temperature, T_N, has been observed around 20 K [Bong66, Kemp90, Chap00a]. Darie *et al.* [Dari05] find the ordering of the magnetic moments at 4 K to be a slight modification of the A-type antiferromagnetic ordering previously proposed [Bong66]. The magnetic moments were found to be aligned at an angle of 100(2)° to the a-axis in the ac plane with no moment along the b-axis. This magnetic structure is shown in

Figure 3.13(a). The Curie-Weiss constant, $\theta_{CW} = +36$ K [Chap00a], shows the presence of ferromagnetic interactions above T_N.

The intralayer and interlayer exchange constants of $NaNiO_2$, $J_{\parallel} = -13.3$ K and $J_{\perp} = 1.3$ K, have been determined from a model assuming an A-type antiferromagnetic ordering in the presence of anisotropy [Holz04]; the layers are sufficiently strongly coupled to permit long range magnetic order below T_N. The Ni-O-Ni bond angles are $\approx 95°$ at room temperature [Chap00b]. An undistorted 90° geometry favours weak ferromagnetic superexchange, while a large deviation from a 90° bond angle can reverse the sign of this exchange coupling [Torn99]. In $NaNiO_2$ it appears that despite the distortion, in-plane ferromagnetic coupling prevails, though the precise nature of the spin and orbital ordering remains under discussion [Daré03, Vern04, Reit05].

Despite the consistency in the value of T_N deduced in magnetic measurements [Bong66, Kemp90, Chap00a] a recent neutron powder diffraction study found Bragg peaks corresponding to A-type antiferromagnetic ordering extending up to $T_N \sim 23$ K [Lewi05]. The peaks did not follow a simple power law near the transition as might be expected for a magnetic order parameter. This study also found a bifurcation between the low temperature field cooled and zero field cooled susceptibility which suggested some form of glassy behaviour, despite the magnetic Bragg peaks persisting to low temperature. This leaves two major questions regarding the magnetic properties of $NaNiO_2$. Firstly, what is the value of T_N and why is there a disparity between the results of magnetic measurements and neutron powder diffraction? Secondly, is the system glassy at low temperature, and if so, what causes this?

The polycrystalline sample of $NaNiO_2$ used in this study was prepared by Dr. D. Prabhakaran following the method outlined by Kemp *et al.* [Kemp90]. Powdered Na_2O_2 and NiO were heated together at 700° C for 100 hours under pure oxygen flow, with intermediate grinding. X-ray powder diffraction showed that the impurity concentration was below the 2 % resolution limit of the apparatus.

The magnetic measurements used to further characterize the sample are explained in section 3.3, heat capacity measurements are described in section 3.4, the B–T phase diagram resulting from these measurements is given in section 3.5, and the μSR measurements are presented in section 3.6.

3.3 Magnetic measurements on $NaNiO_2$

3.3.1 DC susceptibility

Magnetic susceptibility data were recorded as a function of temperature in a number of different applied fields. The methodology used is discussed in section 2.3.1 and the results are shown in Figure 3.2, with temperatures T_{sf} derived from ac susceptibility measurements (section 3.3.3) and T_N from the μSR measurements (section 3.6).

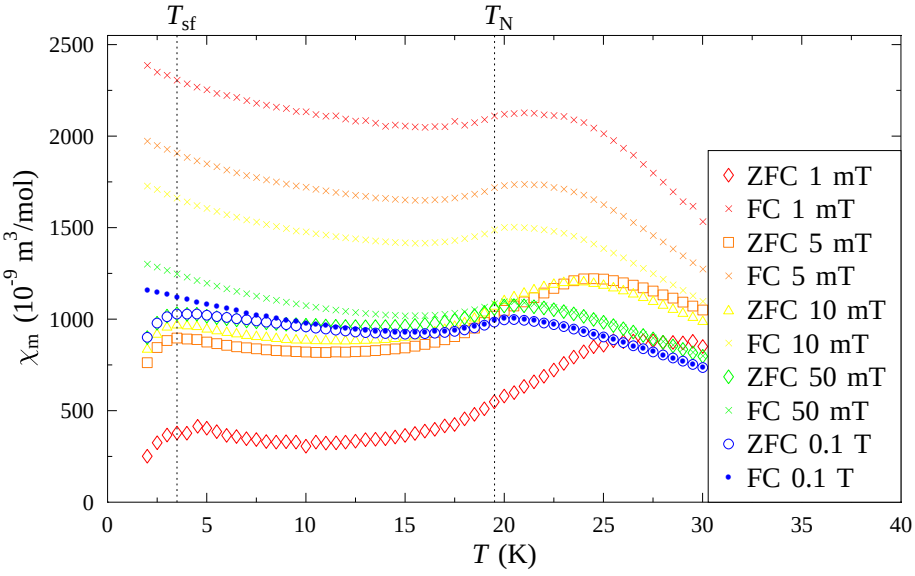

Figure 3.2: Magnetic susceptibility curves for both zero field cooled (ZFC) and field cooled (FC) measurements showing the variation with field of the susceptibility, and the variation of the peak shape near T_N. The temperature at which bifurcation between ZFC and FC measurements occurs decreases with increasing magnetic field, strongly suggesting either glassiness or clustering.

The field dependence is consistent with the magnetization curves presented in section 3.3.2 but the measurements show a bifurcation between field cooled and zero field cooled susceptibilities at temperatures varying with the applied field. This has previously been taken to be evidence for glassiness in this material [Lewi05], and the results presented in that study look very similar to our 0.1 T data. The temperature at which bifurcation occurs is not easily quantifiable since at low fields it can be seen to occur at temperatures well above T_N and as

the field is increased this falls to around T_N, and there is a dramatic increase in the separation between the field cooled and zero field cooled values near T_{sf}.

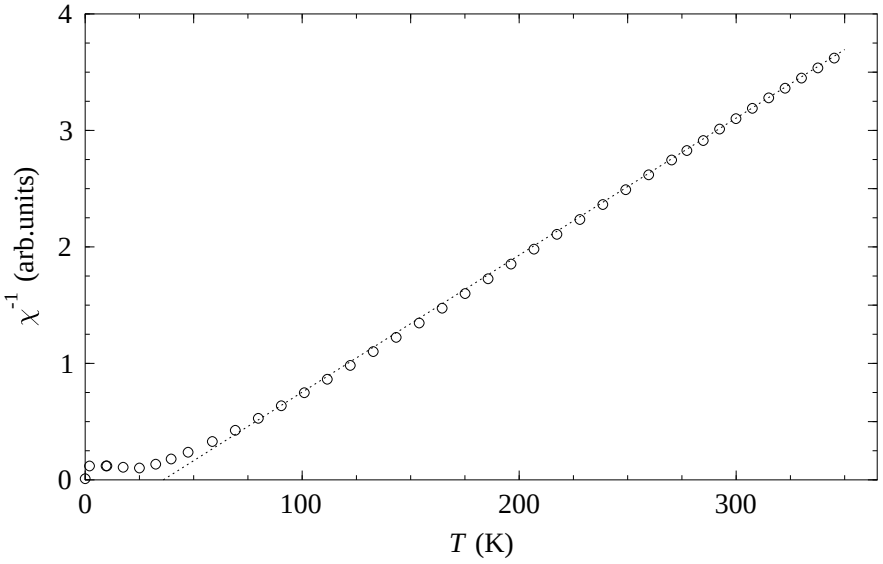

Figure 3.3: Inverse of the dc magnetic susceptibility with a linear fit to the data above 50 K using the literature value of $\theta_{CW} = +36$ K [Chap00a].

To check that the Curie-Weiss constant was consistent with the literature value, $\theta_{CW} = +36$ K [Chap00a], high temperature dc susceptibility measurements were made. The inverse of the susceptibility is presented in Figure 3.3, showing the linear behaviour above around 50 K and the positive Curie-Weiss constant.

3.3.2 Magnetization

To elucidate the phase diagram of $NaNiO_2$, magnetization curves (2.3.1) were measured using a Quantum Design MPMS SQUID magnetometer in Oxford and torque magnetometry at Los Alamos National Laboratory. The first report on the magnetic properties of $NaNiO_2$ [Bong66] used a small single crystal to measure a spin-flop transition at 1.8 T. No studies using single crystals have been reported since then. Chappel *et al.* [Chap00a] and Holzapfel *et al.* [Holz04] have made high field magnetization studies on polycrystalline samples more recently. The measurements presented here are both self-consistent and consistent with the results previously reported, as well as providing better field resolution.

The measurements made using the SQUID magnetometer are presented in Figure 3.4, with the M vs. B data in panel (a) and the derivative with respect to the field in panel (b). Peaks in the derivative indicate spin reorientations or phase boundaries.

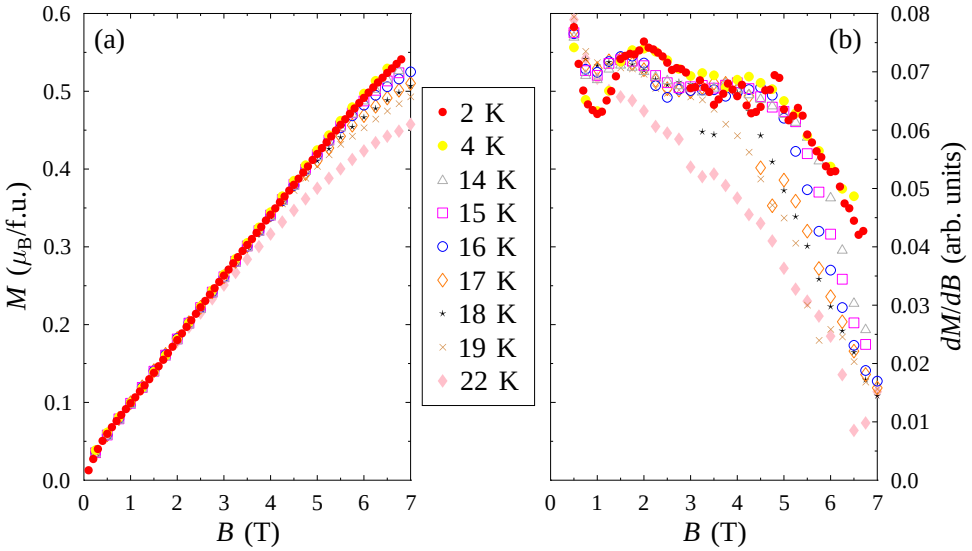

Figure 3.4: Magnetization data taken using a Quantum Design MPMS SQUID magnetometer. (a) The magnetization M as a function of the applied magnetic field B. (b) Derivative dM/dB.

A similar experiment was carried out by Dr. P. A. Goddard, on a sample of $NaNiO_2$ from the same batch, using the inductive-coil magnetometers at the Los Alamos National Laboratory [Godd05]. This method has the advantage of an increased field range, but cannot provide absolute values of the magnetization without low field calibration, such as that described above. These measurements also provided better field resolution than the SQUID measurements. The data are presented in Figure 3.5. The increased resolution shows the susceptibility features in considerably greater detail and the features labelled A, B, C, and D will be discussed in section 3.5.

3.3.3 AC susceptibility

Since the low temperature feature seen in Figure 3.2 had previously been associated with glassiness [Lewi05], ac magnetic susceptibility measurements explained

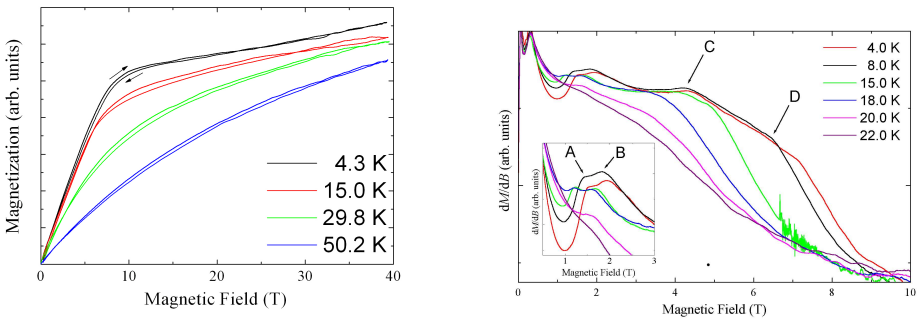

Figure 3.5: Magnetization data taken using high field torque magnetometry. (Left) Magnetization data at four representative temperatures. (Right) Derivative dM/dB in the low field region where the magnetic transitions are observed. The features A, B, C, and D are discussed in section 3.5. (Data provided by Dr P.A. Goddard [Godd05].)

in section 2.3.2 were performed to investigate this hypothesis.

Having degaussed the shielding around the magnet at high temperature, the sample was cooled to 2 K without an applied field (the degaussing process generally achieves a field at the sample position less than 0.1 mT). The ac susceptibility measurements were made while warming the sample in 0.5 K steps using an oscillating magnetic field of 0.35 mT at frequencies f between 1 and 1000 Hz. Measurements were made up to 50 K where the frequency dependence was weak and the magnitude of the susceptibility was in good agreement with the dc susceptibility data shown in Figure 3.2.

The real (χ') and imaginary (χ'') parts of the ac susceptibility data are shown in Figure 3.6. The magnitude of the real part of the ac susceptibility data is very similar to the low field magnetic susceptibility data shown in Figure 3.2. There is a clear frequency dependence at low temperature, $T \sim T_{\rm sf}$, and above $T_{\rm N}$. The peak in χ' above $T_{\rm sf}$ occurs at temperatures matching the steepest gradient of the fall in χ'' at the same measurement frequency, which is characteristic of glassy behaviour. Above $T_{\rm N}$ the features in χ' and χ'' occur at very similar temperatures suggesting they have a different origin to the low temperature peak.

More detailed measurements were made around the peak in χ' near $T_{\rm sf}$ at a greater number of frequencies and with smaller temperature steps. From these data sets, peak temperatures, T_p, were derived by fitting a quadratic polynomial of the form:

$$\chi' = A + B(T - T_p)^2, \tag{3.1}$$

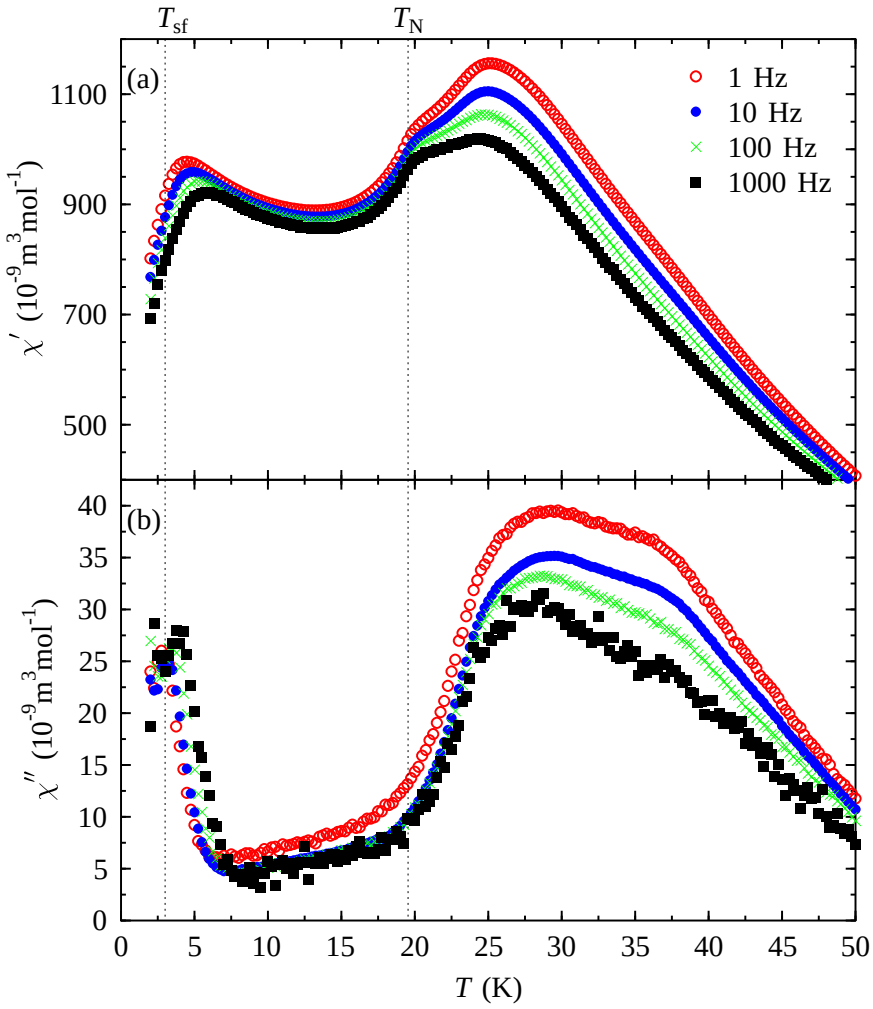

Figure 3.6: The panels correspond to: (a) Real part, χ', of the ac magnetic susceptibility. (b) Imaginary part, χ'', of the ac magnetic susceptibility.

to the five data points nearest the peak as judged by eye. The peak temperatures obtained from this fitting are shown in Figure 3.7 with error bars based on the error in T_p. T_p shows a smooth increase in the as the frequency is increased, as is conventional for glassy magnetic behaviour.

To gain some insight into the origin of the feature seen in χ' above T_{sf} we examine the frequency dependence of T_p. A crude parametrization useful in the classification of glassy systems is the fractional change in T_p per decade in frequency [Mydo93]:

$$\frac{\Delta T_p}{T_p \Delta \log_{10}(\omega)}. \tag{3.2}$$

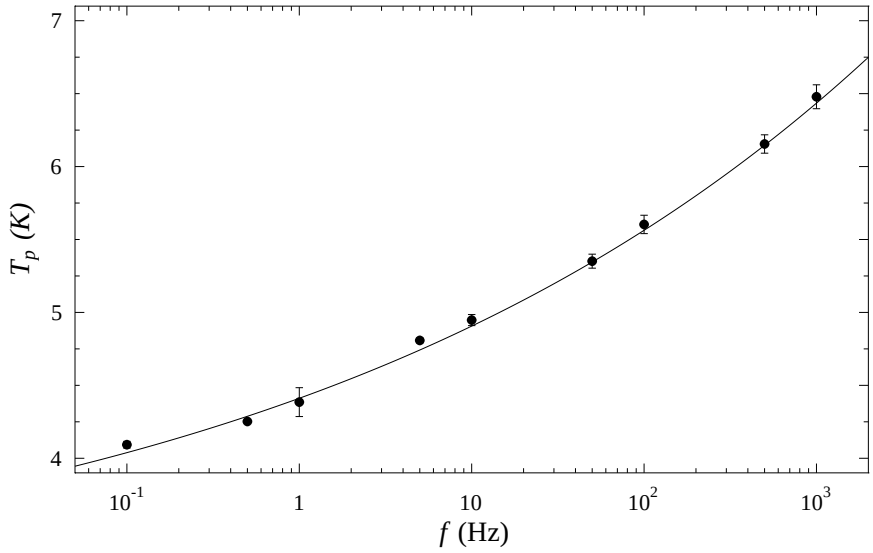

Figure 3.7: Scaling of the temperature T_p of the peak in the real part of the ac susceptibility χ' associated with $T_{\rm sf}$ plotted against the frequency of the applied magnetic field. The line plotted is a fit to a linear dynamic scaling formula (Equation 3.2).

Typical values of this parameter are: 0.005 for the metallic spin glass $Cu_{1-x}Mn_x$, 0.05 for the insulating spin glass $Eu_xSr_{1-x}S$, and 0.28 for the superparamagnetic system $a-(Ho_2O_3)(B_2O_3)$ [Mydo93]. For $NaNiO_2$ we find that this parameter has a value of approximately 0.1, but plotting T_p vs. $\log_{10}(f)$ (Figure 3.7) shows that the trend does not fit on the straight line that Equation 3.2 would suggest. A more sophisticated analysis assumes linear dynamic scaling [Hohe77] and gives a frequency dependence of T_p:

$$T_p = T_{\rm sf}[1 + (f\tau_0)^{1/z\nu_c}], \tag{3.3}$$

where $T_{\rm sf}$ is a finite temperature phase transition, f is the measurement frequency, τ_0 is a characteristic time of the system, z is a dynamic exponent and ν_c is a critical exponent. Fitting to the T_p values plotted in Figure 3.7 gives values of $T_{\rm sf} = 3\pm0.2$ K, $\tau_0 = (5.4\pm0.2)\times10^{-3}$ s, and $z\nu_c = 8.1\pm0.4$. The value of $T_{\rm sf}$ seems consistent with the peak observed in the dc susceptibility data (Figure 3.2) and the value of $z\nu_c$ is within the typical range found in spin glasses, both experimentally and theoretically [Ogie85, Mydo93].

A similarly detailed set of ac susceptibility measurements were taken to probe the temperature dependence of the features around T_N and 25 K, but these were found to have negligible temperature dependence. The timescale for formation of long range order at T_N is well outside the range of ac susceptibility measurements so no frequency dependence would be expected. The origin of the feature at 25 K remains uncertain and will be discussed in section 3.7.

3.4 Heat capacity measurements on $NaNiO_2$

Heat capacity data measured in magnetic fields between 0 and 14 T, taken with a Quantum Design PPMS, are shown in Figure 3.8. The general methodology for these measurements is discussed in section 2.4. A 25 mg pressed pellet was affixed to the measurement stage with a small amount of Apiezon N-grease and measurements were made on cooling. The sample was warmed to a temperature well above T_N for each successive field. In zero field the transition at $T_N = 19.5$ K is seen as a rather broad peak, and there is no evidence for other phase transitions below 300 K. With increasing magnetic field the temperature of this peak decreases to about 14 K (see Figure 3.8). It is interesting that the heat capacity appears to be nearly field independent around 25 K, where features occur in both the ac susceptibility data (section 3.3.3) and the μSR data (section 3.6). The origin of the features at this temperature is not clear, particularly in relation to the heat capacity, and the behaviour above T_N is discussed in section 3.7. The high temperature data shown in the inset to Figure 3.8 show that there is a magnetic contribution to the heat capacity up to around 100 K.

Constant temperature heat capacity data with varying magnetic field are presented in Figure 3.9. These measurements are taken in the same way as those above, with the magnetic field held fixed while each point is measured. Except for the data taken at 22 K, a peak is observed which corresponds to the field labelled H_{C1} in the magnetization data previously reported [Holz04]. This suggests that this marks the upper field boundary of A-type antiferromagnetic order. At 22 K the heat capacity decreases with increasing field, consistent with short-range order.

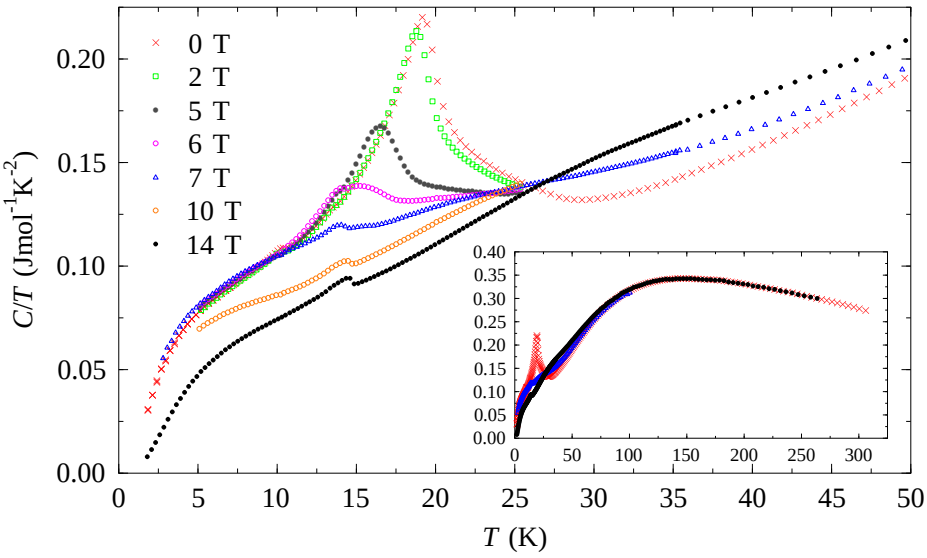

Figure 3.8: Heat capacity divided by temperature in fields between 0 and 14 T for temperatures below 50 K. The inset shows data between 0 and 300 K in a reduced number of fields.

3.5 Phase diagram of $NaNiO_2$

Using the peaks in dM/dB (Figures 3.4 and 3.5), and the peaks in the heat capacity data (Figures 3.8 and 3.9), it is possible to plot the B–T phase diagram shown in Figure 3.10.

From the heat capacity measurements in constant magnetic fields we can plot the high temperature boundary of the ordered phase. This shows a smooth field dependence from 0 to 5.5 T, and then becomes almost independent of field to 14 T. Because this upper region does not show any variation with field it is not apparent in either of the magnetization measurements.

The magnetization measurements are far more instructive in resolving the field dependent features that appear almost vertical in Figure 3.10. Bongers and Enz [Bong66] found a spin flop transition in their single crystal sample at 1.8 T at 4 K. This appears to correspond to features A and B in the pulsed field magnetization data. The origin of the separation between A and B is not clear, although it may result from the random orientation of the crystalline axes relative to the magnetic field direction, inherent in using a polycrystalline sample. Surprisingly, features A and B appear to persist above T_N, which may be related to the short

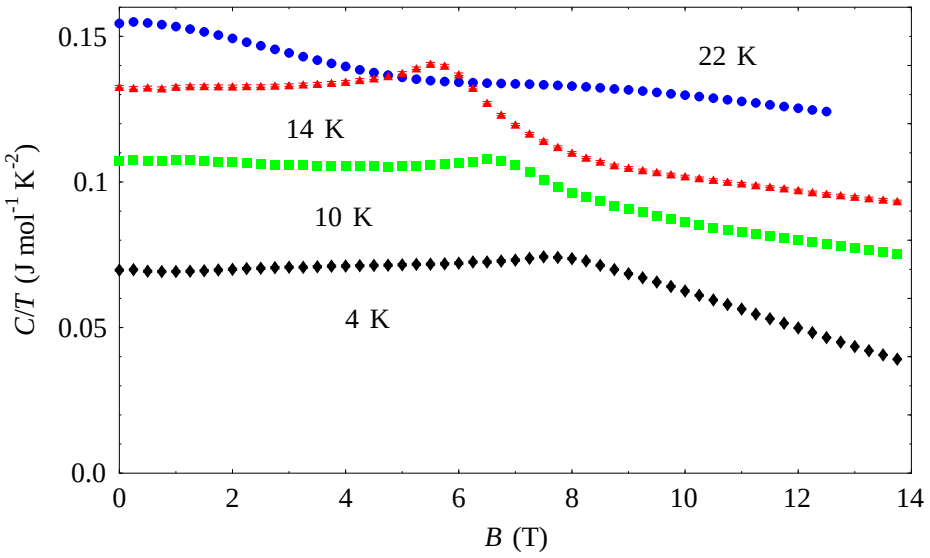

Figure 3.9: Constant temperature heat capacity field scans at four different temperatures. Small shoulders are observed at the boundary of the AF ordered phase.

range order apparent in the ac susceptibility measurements (section 3.3.3) and the μSR data (section 3.6). Feature C has not been reported previously and seems to be some sort of spin reorientation. Feature D appears in both magnetization and heat capacity measurements at constant temperature, and probably marks the AF to FM (saturated) boundary previously referred to as H_{C1} [Holz04]. Pulsed field magnetization experiments on a single crystal sample are planned, with the aim of understanding features A and B around the spin flop transition and identifying the origin of feature C.

3.6 μSR measurements on $NaNiO_2$

Our zero-field μSR experiments were carried out using the DOLLY instrument at the Paul Scherrer Institute (PSI), Villigen, Switzerland, on polycrystalline $NaNiO_2$. This spectrometer is equivalent to GPS and the treatment of the raw data was as discussed in section 2.2.

The asymmetry data were fitted to Equation 3.4 [Dalm97] below T_N, and to

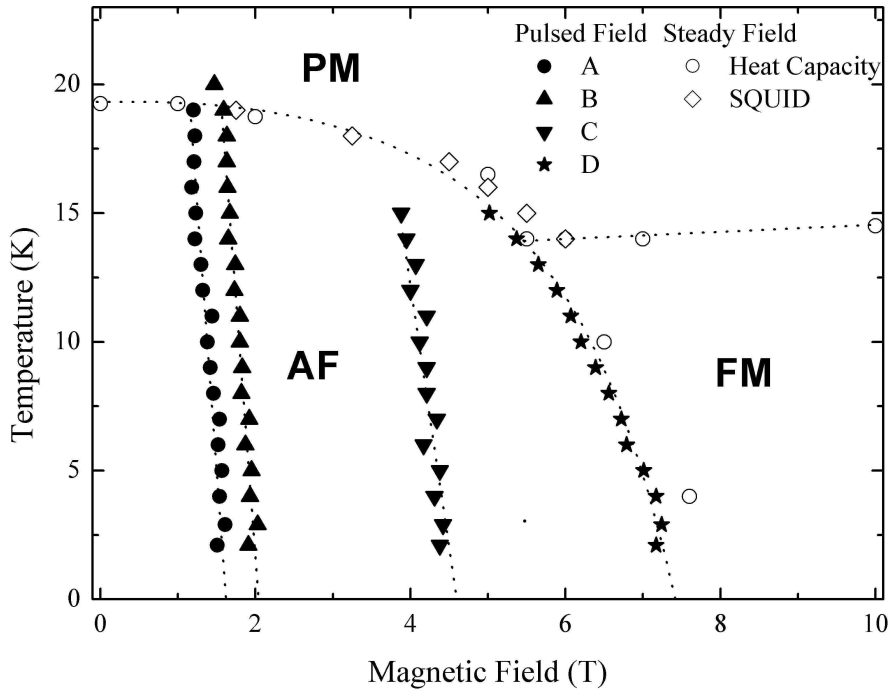

Figure 3.10: Phase diagram derived from the combination of heat capacity and magnetization measurements. The steady field heat capacity data are shown in Figure 3.8 and Figure 3.9. The steady field magnetization data are shown in Figure 3.4. The pulsed field magnetization data and the features corresponding to the marked phase boundaries are shown in Figure 3.5. Lines are guides to the eye. (Figure provided by Dr P.A. Goddard from [Godd05]).

Equation 3.5 above T_N:

$$A(t) = A(0)\left(P_1 e^{-\lambda_1 t} + P_2 e^{-\lambda_2 t}\cos\left(2\pi\nu_\mu t + \phi_0\right)\right), \quad (3.4)$$

$$A(t) = A(0)\left(P_f e^{-\lambda_f t} + P_s e^{-\lambda_s t}\right), \quad (3.5)$$

where $A(0)$ is the initial asymmetry.

P_1 and P_2 are respectively the longitudinal and transverse components of the muon polarization, and $P_1 + P_2 = 1$. The exponential relaxation associated with P_1 reflects the dynamical fluctuations of the fields being probed. The P_2 term describes muon precession with a distribution of local fields dephasing the muon spins. In a fully magnetically ordered polycrystalline sample we expect $P_2/P_1 = 2$. Coherent muon precession will be observed if long range order is present within

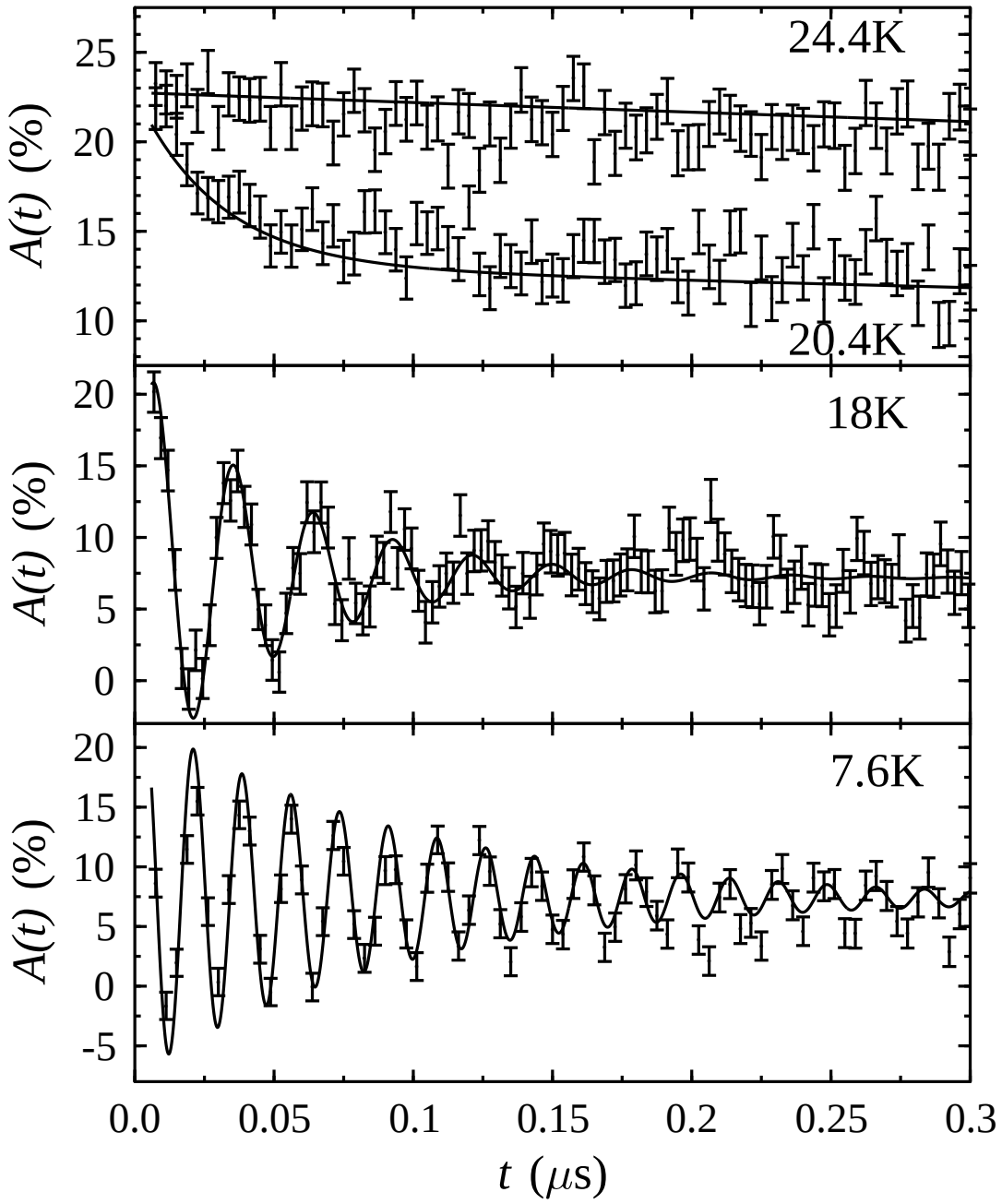

Figure 3.11: Muon decay asymmetry in $NaNiO_2$ plotted at different temperatures. The solid lines are fits of the data to Equations 3.4 & 3.5 with the parameters shown in Figure 3.12.

the sample. P_s and P_f describe slow and fast dynamic fluctuations respectively. A small initial phase offset, ϕ_0, was observed below T_N, larger than could be attributed to errors in determining the time that the muons enter the sample. This could be produced by a small magnetic inequivalency in the position of muons stopped within the sample, consistent with an asymmetric peak seen in Fourier transforms of the data. In the fitting procedure, data were fitted in the time range $0 < t < 8\,\mu$s, where the effect of background counts could be reliably subtracted. Rapid dynamic fluctuations lead to $\lambda_1 \propto {\gamma_\mu}^2(\Delta B)^2/\nu$, where ΔB is the amplitude of the fluctuating local field and ν is the fluctuation rate [Dalm97].

Spectra measured at four temperatures are shown in Figure 3.11. There are three distinct temperature regions apparent from the muon asymmetry spectra. At low temperatures ($T \leq 19.5$ K) there are clear oscillations in the asymmetry showing that long range magnetic order exists and the observed ratio of $P_2 : P_1 \approx 2$ (see Figure 3.12(b)) indicates that the sample is magnetic over its entire volume. The values of λ_2 & λ_s are much larger than those of λ_1 & λ_f (see Figure 3.12(c) & (d)), so at short times only the effects of λ_2 & λ_s are seen in Figure 3.11. An intermediate temperature range ($19.5 < T < 24$ K) gives no oscillations, and the relaxation is modelled with the two exponential components of Equation 3.5, with the amplitude of the faster relaxing component decreasing with increasing temperature. Above 24 K the relaxation is well described by a single exponential, $P_f\exp(-\lambda_f t)$, consistent with fast fluctuations of paramagnetic moments characterized by a single correlation time in the muon time window.

The temperature dependence of the parameters derived from fitting Equations 3.4 & 3.5 to muon asymmetry spectra are presented in Figure 3.12. The muon precession frequency, ν_μ, in the ordered phase is shown in Figure 3.12(a). This is proportional to the sublattice magnetization at the muon site, and was fitted to a function [Bors95]:

$$\nu_\mu(T) = \nu_\mu(0)(1 - (T/T_N))^{\beta_m}. \tag{3.6}$$

Fitting Equation 3.6 to the muon precession frequencies gives $\nu_\mu(0) = 64.2(2)$ MHz corresponding to a field at the muon site of ~ 0.5 T, $T_N = 19.51(1)$ K and $\beta_m = 0.24(1)$. This value of β_m suggests that the system is behaving as a 2D XY magnet [Bram95].

Dipole field calculations were carried out as described in section 2.2 for the

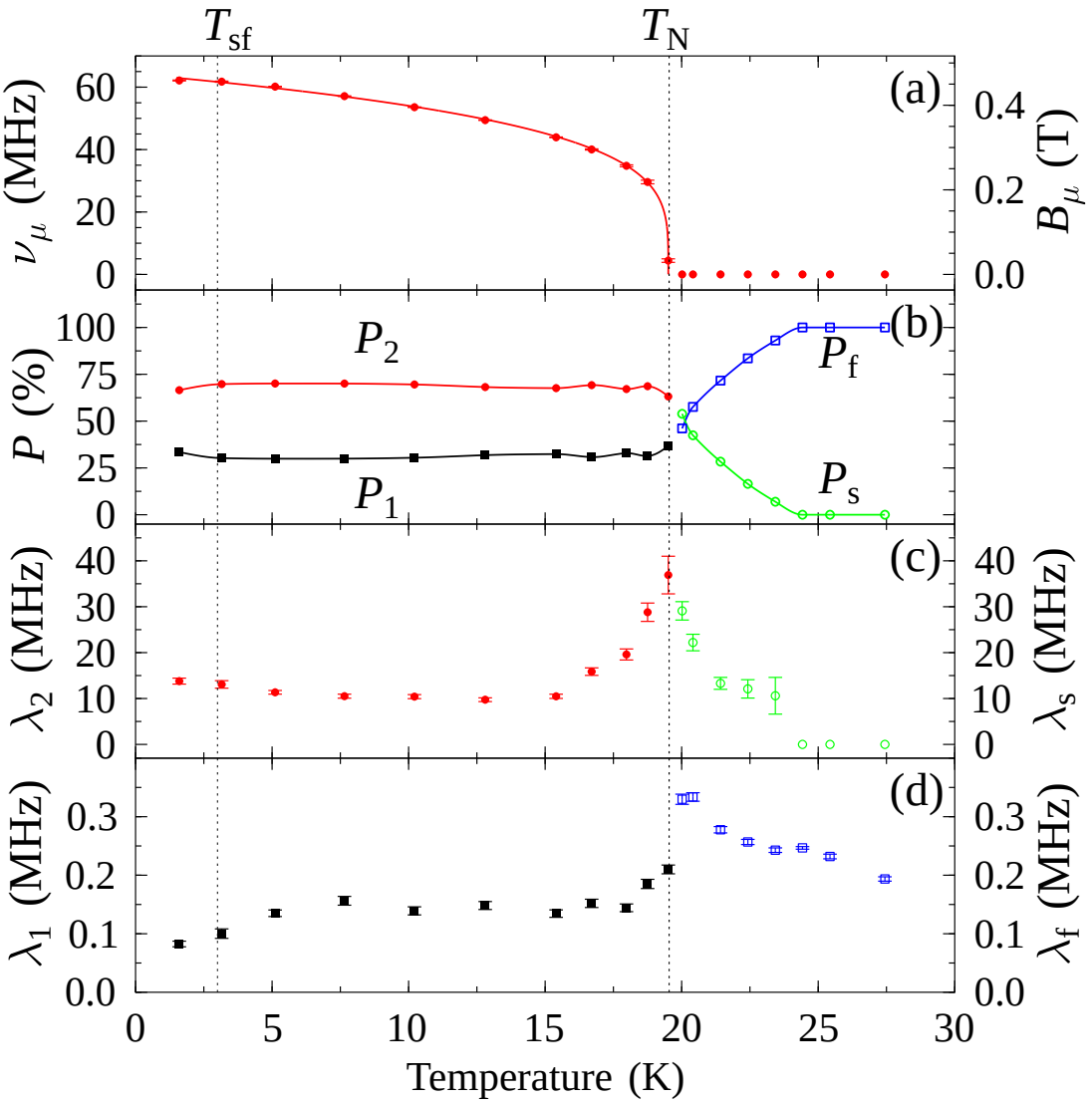

Figure 3.12: Temperature dependence of the parameters determined from fitting data to Equations 3.4 & 3.5: (a) the oscillation frequency, ν_μ, and the internal magnetic field, B_μ, with a fit to Equation 3.6. (b) Amplitudes of the relaxation components P_1 and P_2, and P_f and P_s. (c) Relaxation rates λ_2 and λ_s. (d) Relaxation rates λ_1 and λ_f. The vertical dashed lines indicate temperatures referred to in the text.

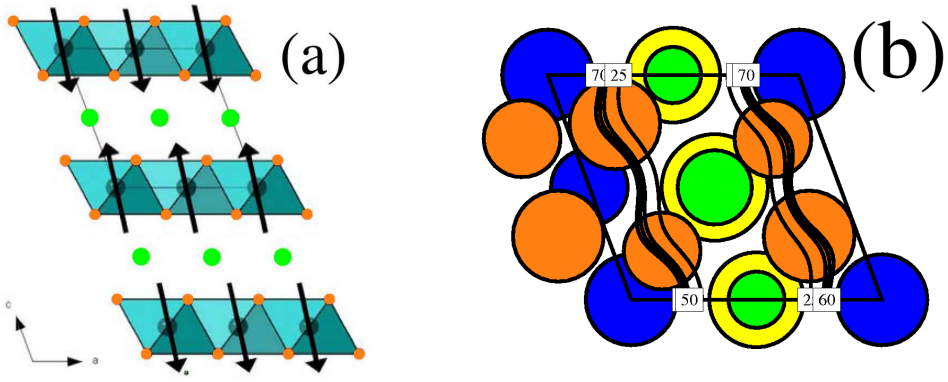

Figure 3.13: (a) Magnetic structure of $NaNiO_2$ derived from neutron powder diffraction measurements viewed along the b-axis. Figure adapted from Ref. [Dari05] (b) Example of the results from dipole field calculations described in the text, plotted in the ab plane with a fractional c co-ordinate of 0.23. The observed zero temperature precession frequency of 64.2 MHz corresponds to sites between oxygen ions, away from the positive ions. In both panels, sodium ions are green, nickel ions are blue, and oxygen ions are orange.

magnetic structure reported by Darie *et al.* [Dari05], obtained using neutron powder diffraction. This structure is shown in Figure 3.13(a). At 4 K, the magnetic moments are aligned at an angle of $100(2)^\circ$ to the a-axis in the ac plane with no moment along the b-axis, this being A-type AF ordering. Calculating over $\sim 10^4$ unit cells gave results as exemplified in Figure 3.13(b). The muon precession frequency of 64.2 MHz corresponds to sites lying in between oxygen ions and away from the positive Na^+ and Ni^{3+} ions, that is in regions of high electron density [Mesk04], and shows that the μSR results are consistent with the reported magnetic structure. These calculations also suggest that the muon precession frequency is insensitive to small deviations from this magnetic structure and any slight inequivalency could be masked by the significant linewidth plotted in Figure 3.12(c).

3.7 $NaNiO_2$ conclusions

Our muon-spin rotation, heat capacity and magnetic susceptibility data determine $T_N = 19.5$ K, in agreement with the values previously reported [Bong66, Kemp90, Chap00a]. The sublattice magnetization follows a power law as a function of temperature that shows strong two-dimensionality in the magnetic ordering. The

B–T phase diagram presented in Figure 3.10 shows that the boundary of the AF ordered phase also tends smoothly to T_N.

In relation to the peak just above T_{sf} in the magnetic susceptibility, the formation of a true spin glass is excluded by the observation of muon precession down to 1.6 K. The most plausible interpretation of this feature is a slowing of spin fluctuations around T_{sf}. It is also possible that a small concentration of oxygen vacancies, each with two associated Ni^{2+} impurity spins for charge balance, exists within the NiO_6 layers. These would weakly couple with one another with a separate energy scale to the bulk Ni^{3+} spins, and given their larger spin could account for such an artifact in the magnetic susceptibility. This artifact is unlikely to be related to stacking frustration. We note that extrapolating the dynamic linear scaling relation to the muon time window suggests a maximum in the dynamic relaxation rate λ_1 should be observed around 7 K, and a broad maximum of low amplitude is just detectable at this temperature (Figure 3.12(d)).

The presence of two exponential relaxation components above T_N (see Equation 3.5) suggests that short-range magnetic order persists over a small temperature range of ~ 5 K above T_N. The fluctuations in the magnetic field producing the faster relaxing component, λ_s, are two orders of magnitude slower than those producing the slowly relaxing component, λ_f. P_s decreases with increasing temperature up to 24 K, showing that the ratio of slow to fast dynamic relaxation is decreasing. Above this temperature the muon relaxation is that expected for a system in the fast-fluctuation regime. The slow spin relaxations observed in the frequency dependence of the ac susceptibility above 25 K are not within the muon time window so are not observed. The observation of two components in the muon relaxation below 24 K, together with a changing frequency dependence of the ac susceptibility, suggest a model of coalescing magnetic clusters forming well above T_N. On cooling below ~ 50 K, ferromagnetic clusters form within the NiO_6 layers and there will be weak coupling between layers. As the volume fraction of clusters increases with decreasing temperature, the coupling of clusters between layers becomes more significant. This is seen in the increase in the frequency dependence of the ac susceptibility until it reaches a maximum at ~ 25 K, suggesting that slowly fluctuating short-range order occurs at this temperature. Between ~ 25 K and T_N the magnetic clusters coalesce, seen in the decrease of χ' and χ'', effectively increasing the registry between planes. The fluctuations in this temperature range are relatively slow, leading to the P_s component of the

muon relaxation, and would appear static within the neutron time window. This perhaps explains the (0,0,1/2) antiferromagnetic Bragg peaks persisting above T_N, as reported by Lewis *et al.* [Lewi05], which would then result from the coalescing clusters of ordered spins.

In conclusion, $NaNiO_2$ shows the onset of long-range magnetic order at $T_N = 19.5$ K, with the dependence of the sublattice magnetization on temperature appropriate for a 2D XY magnet. The slowing of spin fluctuations above T_{sf} is evident in the ac magnetic susceptibility data. At temperatures just above T_N there is evidence of short-range order and of magnetic clusters persisting within a paramagnetic phase above this temperature.

3.8 $LiNiO_2$ and the effect of Mg-doping

The most extensively studied of the layered nickelates is undoubtedly $LiNiO_2$, but this has not yet led to a clear understanding of its magnetic properties. The proposed magnetic ground states listed below are remarkably varied (see Reynaud *et al.* [Reyn01]):

- Quantum spin liquid [Hira85],
- Spin glass [Reim93, Yama96, Cort96, Bajp97],
- Frustrated antiferromagnet [Hiro91, Reim93, Roug96, Barr98],
- Gapless quantum disordered state [Kita98],
- Orbital frustration [Daré03].

As well as these specific states, other studies have suggested combinations of these [Vern04, Reit05] though it must be noted that many of their conclusions have been based on experimental results which were not replicated by later measurements. This motivates the production of high-quality, stoichiometric samples, with as low a concentration of Ni^{2+} ions on the Li sites as possible, also desirable for the use of $LiNiO_2$ as a battery anode material [Pere96].

$LiNiO_2$ has previously been studied using μSR. Yamaura *et al.* [Yama96] quote an unpublished μSR study by Prof. Y. J. Uemura and Dr. K. M. Kojima that found Ni spins fluctuating down to 20 mK. Chatterji *et al.* [Chat05] found a rise in the zero field relaxation rate at around 10 K suggestive of spin freezing, but their low

temperature longitudinal field measurements clearly indicated the influence of the spin dynamics, showing the system to be gapless.

Most theoretical studies have assumed that $LiNiO_2$ does not orbitally order like $NaNiO_2$, maintaining the rhombohedral structure shown in the left panel of Figure 3.1 instead of undergoing a Jahn-Teller distortion. These have been called into question by an x-ray study made by Rougier *et al.* [Roug95] and the more recent neutron diffraction study of Chung *et al.* [Chun05]. Both studies found distortions consistent with a local $C2/m$ structure. The latter study suggested Ni orbitals are arranged in trimers around oxygen sites, rather than the collinear orbital ordering of $NaNiO_2$. This would produce strain fields sufficient to prevent long range orbital ordering.

The question of whether exceptionally small defect concentrations are capable of destroying long range orbital order or seed the local orbital ordering is not clear, and the influence this would have on the magnetic properties has not been investigated theoretically. Some general arguments have been made by Petit *et al.* [Peti06], noting that while Ni^{2+} ions occupying Li sites are not Jahn-Teller active, a distribution of them within the NiO_2 layer could affect the orbital ordering. Their effect on the magnetic interactions might well be more significant, however, since they would change the relative strength of the inter- and intra-layer exchange pathways, a point discussed by Lewis *et al.* [Lewi05].

The possibility of doping $LiNiO_2$ to decrease the proportion of ions on the wrong site has been widely investigated (for a list of examples see [Holz05]). Here we investigate the effect that Mg doping has on $LiNiO_2$, since replacing Ni with Mg should help stabilize the lithium ions on their crystallographic sites [Poui00]. These samples have been characterized by magnetic measurements and ESR, and the results of those experiments will be reported elsewhere [Bond08]. μSR acts as a local probe of magnetic ordering and spin dynamics, both of which are key to identifying the properties of $LiNiO_2$ and in section 3.9 I present the results of experiments on both a nominally pure and close to stoichiometric sample and a 5 % Mg doped sample and discuss the results in section 3.10.

3.9 μSR measurements on $LiNiO_2$

Our μSR experiments were carried out using the GPS instrument at the Paul Scherrer Institute (PSI), Villigen, Switzerland, on polycrystalline samples of nom-

inally undoped $LiNiO_2$ and 5 % Mg doped $LiNiO_2$. Samples were provided by Drs S. de Brion and M. Holzapfel and details of the synthesis and other magnetic measurements are to be published [Bond08]. The methodology was as discussed for $NaNiO_2$ and explained in section 2.2. Dipole field calculations carried out for the structurally similar compound $NaNiO_2$ suggest that the muon stopping sites are near the oxygen ions that form the octahedra around the Ni^{3+} ions, as shown in Figure 3.13(b) above.

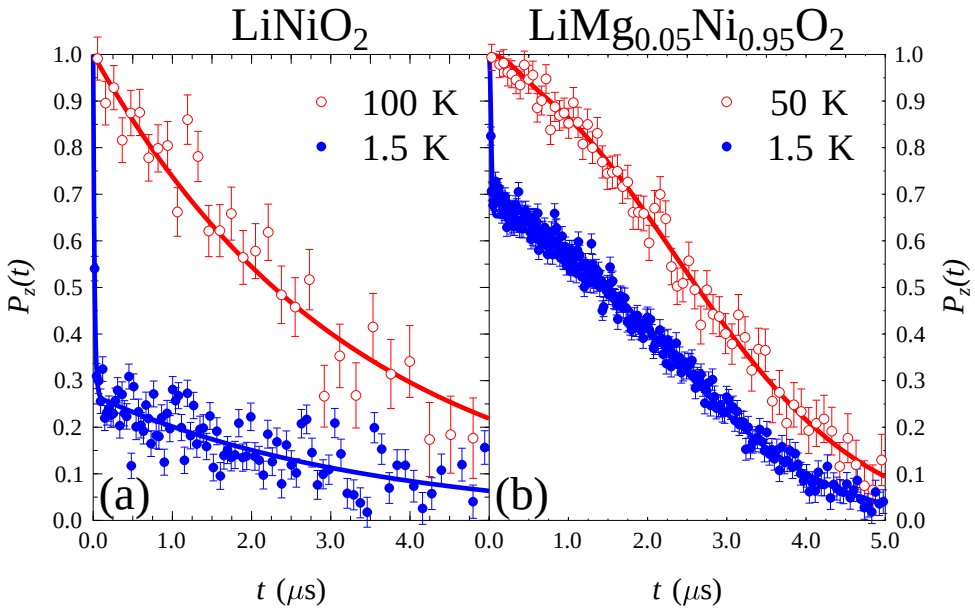

Figure 3.14: Corrected asymmetry data at high and low temperature for: (a) $LiNiO_2$ with fits to Equation 3.7 using the parameters shown in Figure 3.15, and (b) 5 % Mg-doped sample with fits to Equation 3.8 using the parameters shown in Figure 3.16. The data sets have been normalized and a temperature independent background subtracted.

The measured positron asymmetry $A(t)$ was corrected for the non-relaxing background signal resulting from muons stopping in the cryostat and sample holder and normalized to unity. The corrected asymmetry, $P_z(t)$, is plotted in Figure 3.14 for both compounds. It is clear that in both samples there is no spin precession of the implanted muons, which would give rise to coherent oscillations in the asymmetry spectra. Together with the fact that the high and low temperature spectra tend to the same background asymmetry, this is strong evidence for a lack of long range magnetic order in either sample.

From the form of the data we found that in both compounds there were two

components to the relaxing signal at low temperature. These took different forms in the two samples. In $LiNiO_2$ they were both exponential, whereas in the Mg doped specimen both relaxing components were Gaussian. This is indicative of a change in the spin dynamics upon Mg doping.

To model the spin relaxation in the two samples we used the following fitting functions:

$$P_z(t) = P_1 \exp(-\lambda_1 t) + P_2 \exp(-\lambda_2 t), \quad (3.7)$$

$$P_z(t) = P_1 \exp[-(\sigma_1 t)^2] + P_2 \exp[-(\sigma_2 t)^2]. \quad (3.8)$$

Equation 3.7 was used for the $LiNiO_2$ data and Equation 3.8 was used for the 5 % Mg doped sample. The parameters extracted from fitting the raw data are shown in Figure 3.15 ($LiNiO_2$) and Figure 3.16 (5 % Mg).

3.10 $LiNiO_2$ conclusions

Our first result is that the form of the relaxation is different in the two samples. This is particularly clear in the behaviour of the slower relaxing component at high temperature (see Figure 3.14). The exponential relaxation observed in $LiNiO_2$ is characteristic of paramagnetic behaviour with spin fluctuations that are fast relative to the muon time window [Blun99]. This is similar to the behaviour observed at high temperature in $NaNiO_2$ (section 3.6), as we would expect, given the similarity between the two compounds. The previous μSR study of $Li_{0.98}Ni_{1.02}O_2$ found that the high temperature relaxation was essentially Gaussian [Chat05]. For our $LiMg_{0.05}Ni_{0.95}O_2$ sample the high temperature relaxation is well described by a single relaxing component that takes a Gaussian form, as for the sample of Chatterji *et al.* [Chat05], suggesting that they show the same high temperature spin dynamics. The fact that the high temperature relaxation is Gaussian could have two origins, electronic spin fluctuations so fast that only the nuclear spin fluctuations couple to the muon spin, or short-ranged and slowly fluctuating magnetic clusters persisting to high temperature. To distinguish between these possibilities we must examine the change in the form of the data as the temperature is reduced.

Both samples require two relaxing components to describe the low temperature asymmetry data. A stretched exponential $P_z(t) \propto \exp[-(\lambda t)^k]$ [Chat05] provided a somewhat poorer fit to the $LiNiO_2$ data and was not able to describe

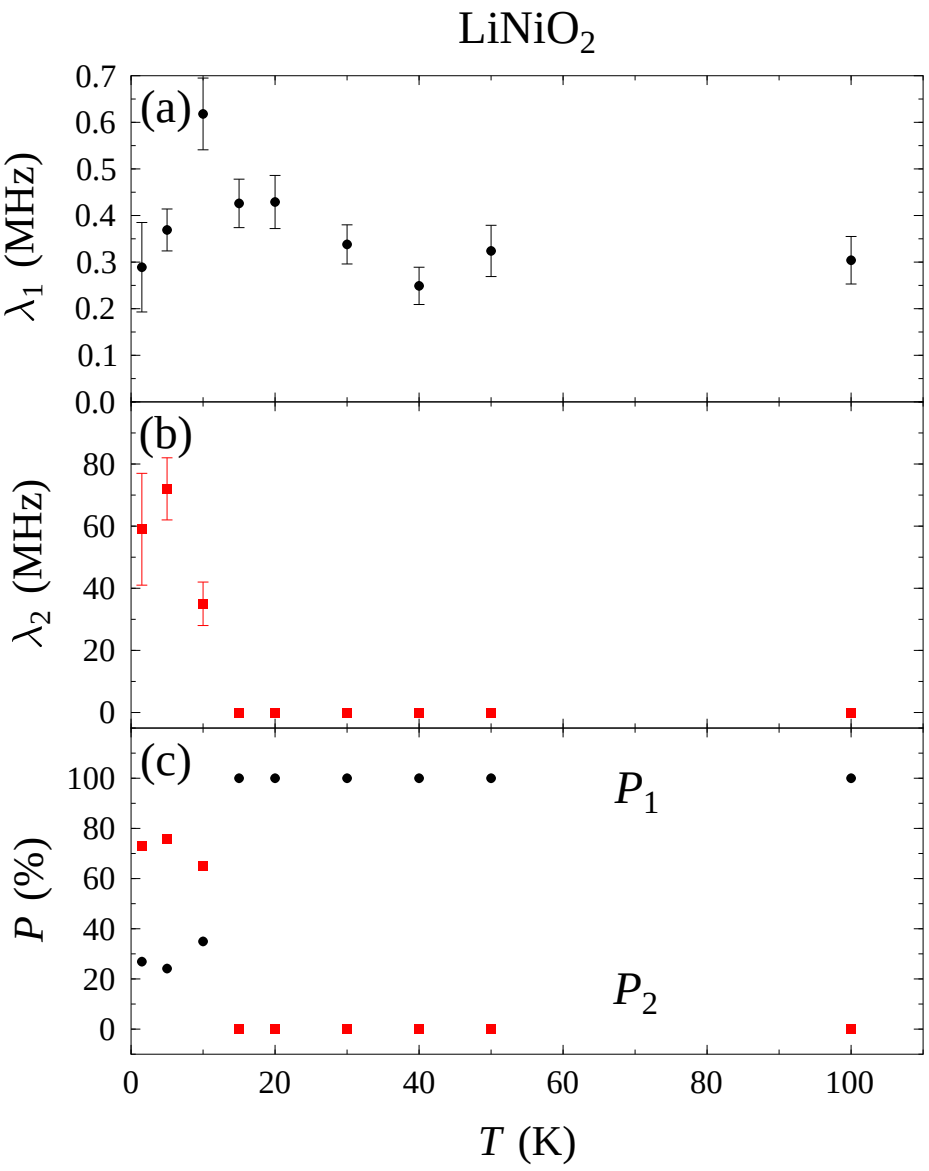

Figure 3.15: Parameters derived from fitting Equation 3.7 to the raw positron asymmetry data for $LiNiO_2$. (a) λ_1 describing the slower relaxing component. (b) λ_2 describing the faster relaxing component. (c) Amplitudes of the relaxation components P_1 and P_2.

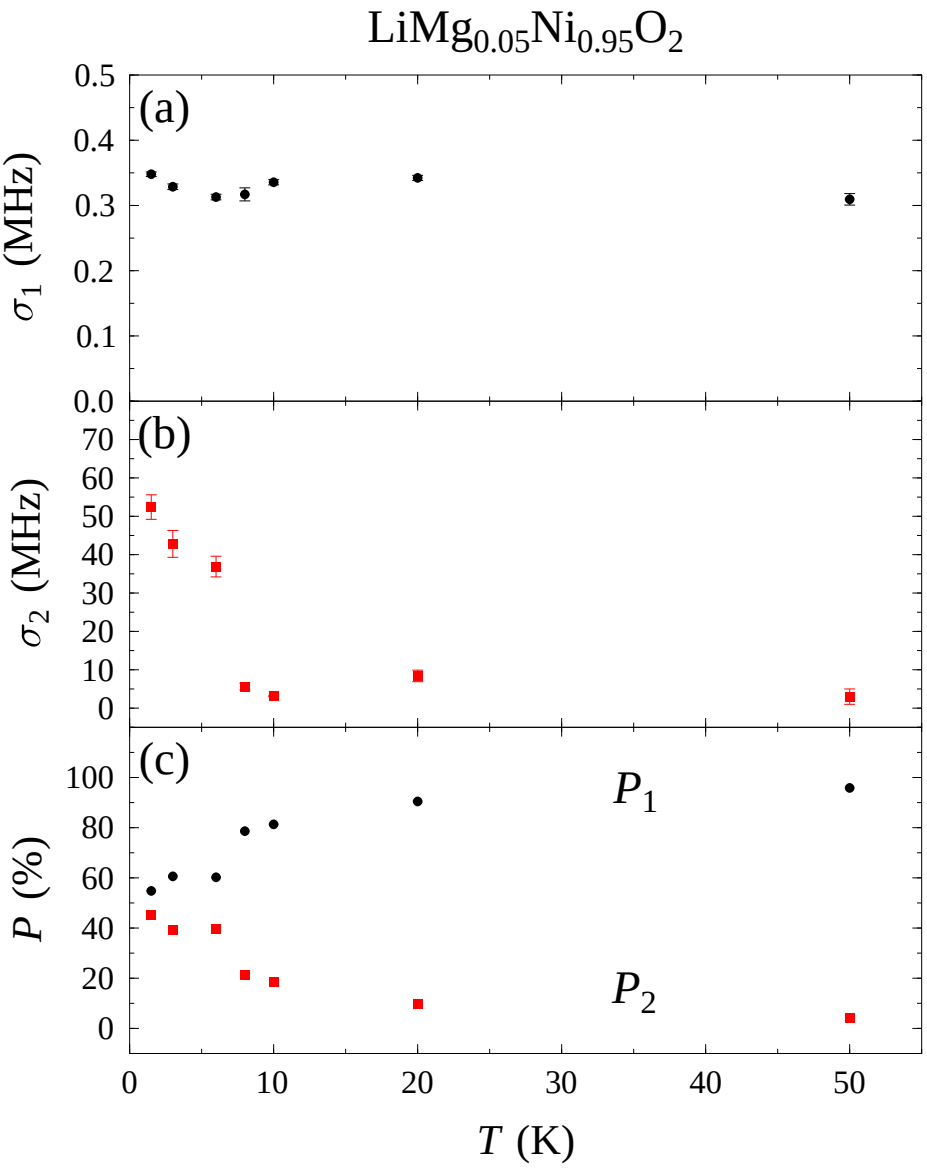

Figure 3.16: Parameters derived from fitting Equation 3.8 to the raw positron asymmetry data for 5 % Mg-doped $LiNiO_2$. (a) σ_1 describing the slower relaxing component. (b) σ_2 describing the faster relaxing component. (c) Amplitudes of the relaxation components P_1 and P_2.

the lower temperature $LiMg_{0.05}Ni_{0.95}O_2$ data correctly. Two relaxing components were successful in describing the muon spin relaxation at temperatures just above T_N in $NaNiO_2$ (section 3.6), with the amplitude of the fast relaxing component increasing as T_N was approached. Coupled with ac susceptibility measurements, this was taken to be evidence for coalescing magnetic clusters preceding the onset of long range magnetic order. In both of the present samples the long range magnetic order never sets in. The form of the fast relaxing components are, however, distinguishable. For $LiNiO_2$, the fast component with amplitude P_2 is exponential, indicating that fluctuations of magnetic fields within the sample slow down, but there is no evidence for static magnetism. The fast relaxation rate λ_2 has a magnitude and temperature dependence similar to the zero field relaxation rate found by Chatterji *et al.* [Chat05]. For $LiMg_{0.05}Ni_{0.95}O_2$ the fast relaxing signal is Gaussian, which is strong evidence for static (but random) magnetism appearing below about 10 K. This could well be associated with defects, probably the Mg doping within the sample. It is likely that the poorer stoichiometry of the sample used by Chatterji *et al.* [Chat05] would give a similar effect and the results seem intermediate between our two samples. The amplitudes of the two components of the fitting functions (Equation 3.7 and Equation 3.8) give information about the volume fraction of the sample where the slower fluctuations (giving rise to the fast relaxing component) originate. In a polycrystalline sample showing long-range magnetic order, the oscillating component of the μSR signal has twice the amplitude of the exponentially relaxing component. If the slowly fluctuating magnetic field or static random magnetic order occupies the full volume of the sample then a similar ratio would be expected. We might therefore expect the fast relaxing signal P_2 to have twice the amplitude of the slower relaxing signal P_1, shown in Figures 3.15(c) and 3.16(c). In the $LiNiO_2$ sample the ratio $P_2 : P_1 \approx 2$ below 10 K, suggesting that the slowly fluctuating magnetic fields occur throughout the whole sample volume. The Gaussian form of the slowly relaxing signal in the 5 % Mg-doped sample prevents us drawing such a conclusion regarding the volume fraction, since static effects cannot relax the longitudinal component of the muon spin, but we note that the amplitude of the fast relaxing signal P_2 increases at low temperature.

From the μSR data we can conclude that Mg-doping has a significant effect on the spin dynamics of $LiNiO_2$. The nominally stoichiometric sample shows slowing down of spin fluctuations throughout the sample as the temperature is

reduced, but there is no evidence of magnetic order. The 5 % Mg-doped sample shows evidence of static random magnetism below around 10 K, suggesting that magnetic clusters nucleate around the Mg dopants.

3.11 Conclusion

In this chapter we have seen the difference between the magnetic properties of $NaNiO_2$ and $LiNiO_2$. Despite their similarity, the non-stoichiometry of $LiNiO_2$ still hinders the determination of its intrinsic magnetic properties. $NaNiO_2$ is less pathological, although the cluster formation above T_N suggests that, even here, there are parts of its behaviour that escape our understanding.

Since the work presented above was completed, there has been extensive effort devoted to understanding the magnetic properties of some newly synthesized layered nickelates with triangular lattices. The compounds $AgNiO_2$ [Sörg05] and Ag_2NiO_2 [Schr02] offer another route to exploring the properties of low-spin Ni^{3+} ions on a triangular lattice, with a different coupling between the layers. The intercalation of water into $NaNiO_2$ has now been achieved [Park06, Park07], analogous to the water intercalation of Na_xCoO_2 that led to superconductivity [Taka03]. In the case of $NaNiO_2$ this appears to lead to a glassy low-temperature magnetic state comparable to that in $NaNiO_2$, but clearly different. Below, I will discuss these results in relation to those on $NaNiO_2$ and $LiNiO_2$ that have been presented above.

A study of rhombohedral $AgNiO_2$ [Kiku99] found a Weiss temperature of $\theta \approx -100$ K, clear evidence of magnetic ordering at $T_N = 28$ K in μSR (three resolved precession frequencies) and magnetic susceptibility measurements, but no magnetic Bragg peaks were observed in polycrystalline neutron diffraction data, which would be a clear indication of long range antiferromagnetic order. This was attributed to the formation of magnetic domains smaller than the coherence length of neutron diffraction. The 2H polytype of $AgNiO_2$ is hexagonal [Sörg05], and has much clearer magnetic properties. The Weiss temperature is $\theta = -107.6$ K and there is a peak in the magnetic susceptibility at 22 K. Neutron powder diffraction has shown that there is a structural transition to a tripled unit cell indicating $\sqrt{3} \times \sqrt{3}$ charge order on the Ni triangular lattice, as opposed to the Jahn-Teller distortion observed in the other layered nickelates [Wawr07]. Zero field heat capacity measurements on a 14 mg pressed pellet of 2H-$AgNiO_2$ [Whee07] are shown

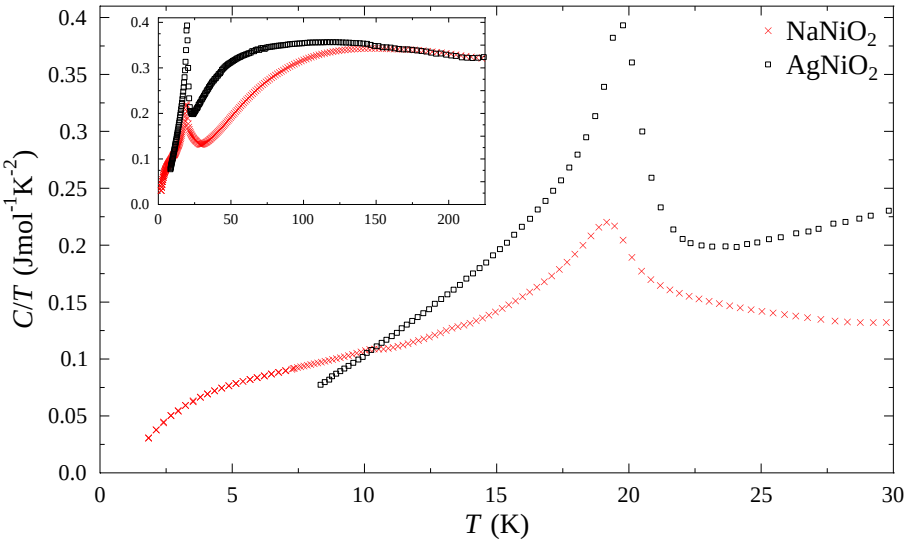

Figure 3.17: Heat capacities of $AgNiO_2$ and $NaNiO_2$ in zero field. The inset shows data between 0 and 225 K. Data taken in collaboration with E. M. Wheeler. [Whee07]

in Figure 3.17, with data on $NaNiO_2$ shown for comparison. We see a sharp peak in the heat capacity at 20 K, significantly sharper than that in $NaNiO_2$, indicating that the magnetic ordering is sharp and suggesting that cluster formation above T_N will be far less significant, a conclusion borne out by measurements of the longitudinal muon relaxation rate [Lanc08]. The lattice contribution also seems to be significantly different, probably due to a lower energy scale for phonons in $AgNiO_2$. The muon relaxation data presented in Figure 2.3(b) shows a far more complicated and interesting temperature dependence than those for either $NaNiO_2$ (Section 3.6) or rhombohedral $AgNiO_2$ [Kiku99]. Parameters extracted from fitting data below T_N to Equation 3.9 are shown in Figure 3.18 [Lanc08].

$$A(t) = \sum_{i}^{6} A_i \exp(-\lambda_i t) \cos(2\pi\nu_i t). \tag{3.9}$$

That six frequencies are needed to describe the muon precession demonstrates the magnetic complexity of this compound. More surprisingly, certain frequencies increase with increasing temperature well below T_N, before falling again close to the transition. This strongly suggests a temperature dependent magnetic structure below T_N. To clarify the reason for this, the frequencies can be compared to the

average precession frequency ν_{av} (Figure 3.18(c)). Since certain frequencies rise and others fall, pairing them as $\nu_1+\nu_6$, $\nu_2+\nu_4$, and $\nu_3+\nu_5$, is seen to give sums that are very close to twice ν_{av}, independent of temperature. This strongly suggests that there are three structurally independent muon stopping sites and that they are also magnetically inequivalent. Further study should lead to a more complete understanding of the magnetic properties of $AgNiO_2$ [Wawr07, Lanc08, Whee07].

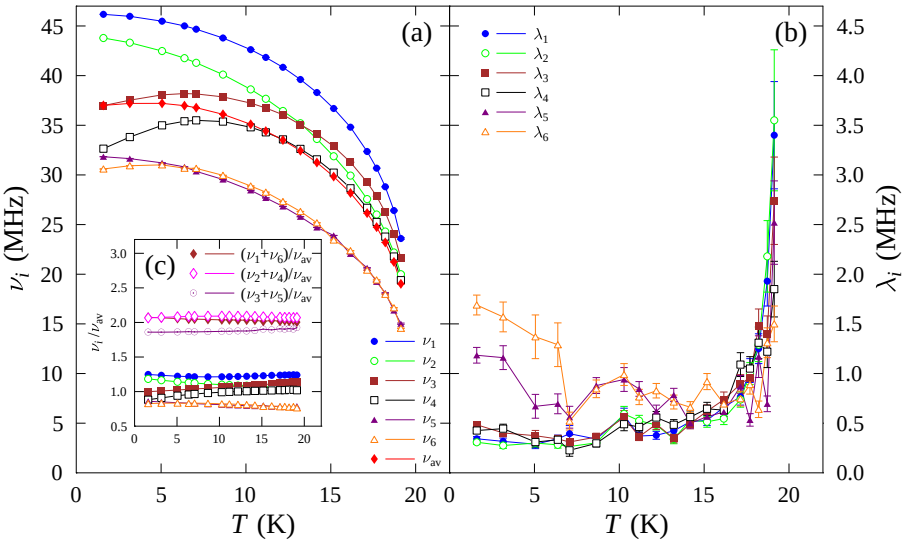

Figure 3.18: Parameters extracted from fitting $AgNiO_2$ μSR data to Equation 3.9 described in the text. (a) Precession frequencies ν_i. (b) Transverse relaxation rates λ_i. (c) Scaled precession frequencies ν_i/ν_{av}. Data from Dr. T. Lancaster. [Lanc08]

Another silver nickelate with a triangular Ni^{3+} lattice is Ag_2NiO_2. This is unusual chemically, since it has $Ag^{\frac{1}{2}+}$ ions lying in between the $(NiO_2)^-$ layers [Schr02]. The magnetic properties show that orbital ordering occurs at $T_s = 260$ K and magnetic ordering at $T_{\mathrm{N}} = 56$ K [Yosh06]. The high temperature $T > T_s$ Weiss temperature is $+10$ K and this changes sign to -33 K below T_s. A μSR study [Sugi06] found evidence for an incommensurate antiferromagnetic ordering below T_{N} with a second transition $T_{\mathrm{m}} \sim 22$ K. The evidence for incommensurate ordering was the distribution of frequencies apparent in the μSR data. Supposing that the muon stopping sites are magnetically equivalent if the ordering is commensurate, which is true within experimental accuracy in $NaNiO_2$ (as discussed in section 3.6 above), observing a distribution of fields means that

the ordering is incommensurate. Given the different structure of Ag_2NiO_2, it is not clear that the muon stopping sites would be magnetically equivalent for commensurate magnetic order, even if they are the same as those in $NaNiO_2$. Nonetheless, observing a change in the field distribution at around 22 K is interesting, given that $T_N = 56$ K. It seems likely that the Ag_2 layers may be stabilizing long range order more effectively than the Na layers in $NaNiO_2$. The magnetic order observed in Ag_2NiO_2 might correspond to a static version of the cluster behaviour observed in $NaNiO_2$. A thorough neutron diffraction study of Ag_2NiO_2 is necessary to clarify the nature of magnetic order in this material.

Analogous to water intercalation in Na_xCoO_2, which leads to superconductivity [Taka03], water can be intercalated between the layers of $NaNiO_2$, leading to a change in the magnetic properties. Two forms have been synthesized: monolayer hydrate (MLH) $Na_{0.3}NiO_2 \cdot 0.7H_2O$ [Park07], and bi-layer hydrate (BLH) $Na_{0.3}NiO_2 \cdot 1.3H_2O$ [Park06]. These show different magnetic properties at low temperature. Using the notation described in section 3.3.3 and analysing the frequency dependence of the temperature of the peak in χ' using Equation 3.3 showed that for BLH $\tau_0 = 4.7 \times 10^{-3}$ s, $z\nu = 4.03$, and $T_{sf} = 4.5$ K, whereas MLH showed no frequency dependence in the temperature of the ac susceptibility maximum. The figures for BLH can be compared with those for $NaNiO_2$: $\tau_0 = 5.4(2) \times 10^{-3}$ s, $z\nu = 8.1(4)$, and $T_{sf} = 3.0(2)$ K. The similarity in the timescale suggests that the origin of this behaviour may be similar in both $NaNiO_2$ and the bi-layer hydrate, but the power law is not the same. Further investigation of these specimens will be necessary before a full comparison with the better characterized layered nickelates described above can be made.

In conclusion, the magnetic properties of the series of layered nickelates $XNiO_2$ show great variety, and while much progress has recently been made in elucidating these properties, open questions still remain that will require improved techniques of both synthesis and characterization.

Chapter 4

Magnetic order in the Mott Insulators $LaTiO_3$ and $YTiO_3$

Contents

Despite their structural simplicity, as exemplified in Figure 4.1, simple perovskite compounds of the form ABX_3 show a wide variety of physical properties, particularly when the simple cubic structure is distorted. Examples of these include:

- Ferroelectricity in $BaTiO_3$ [vonH50, Kwei93],
- Multiferroicity in the rare-earth manganites $GdMnO_3$, $TbMnO_3$, and $DyMnO_3$ [Kimu05] (also observed in hexagonal rare-earth manganites with smaller rare-earth ions),
- Colossal Magnetoresistance in a variety of compounds derived from $LaMnO_3$ [Rami97],
- Superconductivity in $MgCNi_3$ [He01],
- Catalysis of carbon monoxide, unburnt hydrocarbons, and nitrogen oxides to carbon dioxide, water, and nitrogen in vehicle emissions using compounds such as $LaFe_{0.57}Co_{0.38}Pd_{0.05}O_3$ [Nish02].

Changing the ionic radius of the ion on the A site allows the distortion to be controlled and, through this, the physics of these materials can be tuned.

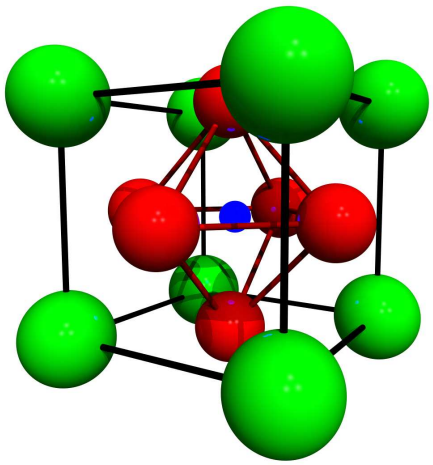

Figure 4.1: The ferroelectric $BaTiO_3$ is a prototypical perovskite compound. Ba^{2+} ions are shown in green, the Ti^{4+} ion is coloured blue, and the O^{2-} ions are red. Both $LaTiO_3$ and $YTiO_3$ represent slightly different distortions of this structure. The structural parameters used to produce this figure come from Ref. [Kwei93].

We can think of the simple perovskite structure as A cations sitting at the centres of a cubic network of BX_6 octahedra, or alternatively as a cubic close-packed AX_3 array with a quarter of the octahedral holes filled by B cations [Wood97a]. The most common means of parametrizing the distortion are the tolerance factor based on the relative sizes of the ions on the A and B sites, and the tilting angles of the BX_6 octahedra relative to the crystal axes. The tolerance factor:

$$t = \frac{R_A + R_X}{\sqrt{2}(R_B + R_X)}, \tag{4.1}$$

uses the ionic radii of the species R_A, R_B, and R_X to parametrize how far the structure is likely to be from the ideal cubic symmetry [Gold26]. We could alternatively consider this to be a relation between the A-X and B-X bond lengths. This approach is limited by the approximation that these systems are entirely ionic, a close approximation in transition metal oxides, and also factors related to the tiling of the octahedra [Zhou05]. For an ideal cubic structure $t = 1$, the perovskite structure is retained for $0.8 \lesssim t < 1$, and hexagonal variants occur for $t > 1$ [John06]. The tilting of the BX_6 octahedra offers another means of describing the distortion to the perovskite structure [Glaz72]. Since we have three principal directions along which the octahedra can be tilted (*abc*), and they can be untilted (^{0}), or tilted in the same ($^+$) or the opposite ($^-$) sense to their neighbour along each direction. All tilting arrangements with no more than two octahedra within the repeated unit can be described within 23 systems [Glaz72]. These allow the space group symmetry to be determined and give a consistent means of transforming between similar crystal systems, particularly useful because many perovskites undergo structural phase transitions without large movements of the ions.

An example of two similar compounds where a small change in the ionic radius causes a significant change in the physical properties are the pair $LaTiO_3$ and $YTiO_3$. These have been studied extensively using a broad variety of techniques, but have not previously been studied using muons. In this chapter I describe such a study, beginning, in section 4.1, with a description of the previous results obtained using other techniques, and the theoretical predictions for their properties. The synthesis of the samples used in this work and the experimental details common to both compounds are explained in section 4.2. The results of the experiments on $LaTiO_3$ and $YTiO_3$ are presented in sections 4.3 and 4.4. Conclusions are drawn

on the results and some suggestions for further work are made in section 4.5.

4.1 Introduction

The two similar perovskite compounds $LaTiO_3$ and $YTiO_3$ have provided a challenging environment in which to test theoretical descriptions of transition metal oxides because they retain the orbital degree of freedom in the t_{2g} state [Solo06] and show a strong coupling between spin and orbital degrees of freedom [Moch04]. Orbital degeneracy, which can lead to phenomena such as colossal magnetoresistance or unconventional superconductivity [Toku00], is present in isolated Ti t_{2g} ions, but is lifted in these compounds [Moch04]. The size of the A^{3+} ion provides one means of tuning the properties of these titanates [Moch04], affecting the Ti-O-Ti bond angles and the exchange interactions along them. This is evident in the difference between the low temperature magnetic structures of these two compounds, observed using neutron diffraction. $LaTiO_3$ is a G-type antiferromagnet [Keim00] below $T_N = 135$ K and has a reduced ordered moment of $\mu_{\text{eff}} \sim 0.5\mu_B$. More recently, a $LaTiO_3$ sample with a slightly higher $T_N = 146$ K was found to have its G-type moment aligned along the a-axis [Cwik03]. $YTiO_3$ orders ferromagnetically [Ulri02] with the spins aligned along the c-axis at $T_C = 27$ K. However, there is a G-type antiferromagnetic component along a, and an A-type component along b.

A recent Raman scattering study [Ulri06] probed the evidence for orbital excitations in the two compounds. It was found that there was a high energy peak in the Raman intensity beyond the range of two phonon excitations. This is strong evidence for orbital excitations due to fluctuations of orbital-exchange bonds, analogous to Raman scattering from magnons in copper oxides. A sizeable deformation of the TiO_6 octahedra in $LaTiO_3$ has been observed using X-ray and neutron diffraction [Cwik03]. This suggests that orbital ordering occurs and there is a splitting in the t_{2g} levels of about 0.24 eV. Similar results were found using spin-resolved photoelectron spectroscopy [Have05], which demonstrated that the crystal field splitting of the t_{2g} levels was in the range $0.12 - 0.30$ eV. This Jahn-Teller distortion is shown in the thermal expansion, heat capacity, electrical transport, X-ray, and optical spectroscopy measurements of Hemberger *et al.* [Hemb03] and the magnetoelastic coupling in the $RTiO_3$ series of compounds has been studied in considerable detail [Koma07]. (R being A^{3+} ions.) Together,

Table 4.1: Structures of $LaTiO_3$ and $YTiO_3$ at 293 K, indexed in the $Pbnm$ space group, taken from Refs. [Cwik03] & [MacL79] respectively. The Ti ions are at $(1/2, 0, 0)$. The tolerance factors t and tilting, notated in the Glazer system, are from Ref. [Wood97b]. The symmetry equivalent sites for each ion are shown in Table 4.2.

Compound	$LaTiO_3$	$YTiO_3$
a (Å)	5.6336(1)	5.316(2)
b (Å)	5.6156(1)	5.679(2)
c (Å)	7.9145(2)	7.611(3)
x_A	0.9916(3)	0.9793(1)
y_A	0.0457(2)	0.0729
z_A	0.25	0.25
x_{O1}	0.0799(3)	0.121(1)
y_{O1}	0.4913(3)	0.458(1)
z_{O1}	0.25	0.25
x_{O2}	0.7096(3)	0.691(1)
y_{O2}	0.2941(3)	0.310(1)
z_{O2}	0.0417(1)	0.058(1)
t	0.95	0.88
Tilting	$a^+a^-a^-$	$a^+a^-a^-$

these results strongly exclude the possibility that an orbital liquid, suggested by Khaliullin and Maekawa [Khal00], forms in $LaTiO_3$. They also show that the orbital moment is significantly reduced, in agreement with both NMR measurements [Kiya03] and the results of X-ray measurements [Keim00]. Orbital ordering in $YTiO_3$ has also been observed directly, using both neutron diffraction [Akim01] and X-ray absorption spectroscopy [Iga04].

It has been shown that the $Y_{1-x}La_xTiO_3$ system [Zhou06] is an itinerant-electron antiferromagnet with no orbital ordering for $x > 0.7$, that an intermediate phase exists for $0.3 < x < 0.7$ with orbital-order fluctuations and ferromagnetic interactions that reduce T_N, and that for $x < 0.3$ the system shows orbital ordering and a ferromagnetic transition. It was suggested that even at $x = 0$ the volume of the orbitally ordered region does not encompass the whole sample.

An NMR study [Itoh99] found magnetic order in both compounds and estimated the Ti moment to be $0.75\mu_B$ in $YTiO_3$. The data showed the internal field at Y sites was 0.857 T and showed that the internal field in $LaTiO_3$ was parallel to the c-axis and cancelled at the La sites. More recent NMR measurements [Iga04] found an internal field at the Ti site in $LaTiO_3$ of 9.2 T. More recent

Table 4.2: Symmetry equivalent positions for the orthorhombic space group $Pbnm$ relevant for $LaTiO_3$ and $YTiO_3$. These values are adapted from those given in Ref. [Hahn95] for $Pnma$ (No. 62). A is the A^{3+} ion, either La or Y. The description given under Site is the multiplicity followed by the Wyckoff letter. These transformations can be used with the structural parameters given in Table 4.1 to generate the crystal structure of the two compounds.

Ion	Site	Equivalent Positions
Ti	$4b$	$1/2,0,0;\ 0,1/2,0;\ 1/2,0,1/2;\ 0,1/2,1/2$
A	$4c$	$x,y,1/4;\ x+1/2,\bar{y}+1/2,3/4;\ \bar{x},\bar{y},3/4;\ \bar{x}+1/2,y+1/2,1/4$
O1	$4c$	$x,y,1/4;\ x+1/2,\bar{y}+1/2,3/4;\ \bar{x},\bar{y},3/4;\ \bar{x}+1/2,\bar{y}+1/2,1/4$
O2	$8d$	$x,y,z;\ x+1/2,\bar{y}+1/2,\bar{z};\ \bar{x},\bar{y},z+1/2;\ \bar{x}+1/2,y+1/2,\bar{z}+1/2;$ $\bar{x},\bar{y},\bar{z};\ \bar{x}+1/2,y+1/2,z;\ x,y,\bar{z}+1/2;\ x+1/2,\bar{y}+1/2,z+1/2$

NMR measurements examined the angular dependence of the electric quadrupole moment in $YTiO_3$ to test theoretical models based on orbital ordering, but found the quadrupole moment is too small to fit in with these models, perhaps due to quantum fluctuations [Kiya05].

Theoretical work on these compounds has focused around the mechanism that selects the ground state from the possible spin and orbital configurations. Models considering the orbitals as quasi-static entities [Cwik03, Moch03, Pava04, Schm05, Solo06] satisfactorily predict the orbital occupation and magnetic ordering. Nevertheless, there remain aspects of the experimental details [Keim00, Ulri02, Ulri06] that cannot be successfully described without including the quantum fluctuations of the orbitals [Khal00, Khal02, Khal03], particularly with regard to the Raman scattering results. With quasi-static orbital occupations, excitations are in the form of well-defined crystal field excitations, whereas if fluctuations are significant, the excitations are collective modes, and it is the latter which are observed by Raman scattering experiments [Ulri06]. The model of an orbital liquid occurring in $LaTiO_3$ [Khal00] predicts a linear term in the heat capacity which is not inconsistent with experimental data [Frit02]. However, the interpretation of this data is not clear, since $LaMnO_3$, which is an orbitally ordered insulator, has a larger linear term in its low temperature heat capacity.

The disparity between theoretical and experimental results in these compounds is primarily related to the orbital properties, for which μSR can only have indirect sensitivity. The justification for a μSR experiment must therefore be centred around questions concerning the magnetic properties that previous neutron stud-

ies would have had less sensitivity to than a μSR experiment and also utilising the well determined magnetic structures to compare our expectations for where muons stop within the structure and the observed precession frequencies. μSR measurements on both $LaTiO_3$ and $YTiO_3$ were used to probe whether the internal magnetic fields have a similar temperature dependence to the magnetic Bragg peaks previously measured [Keim00, Ulri02], whether the magnetic volume fraction extends throughout the system below the ordering transition, and discovering whether the spin dynamics are conventional. The changes in these properties between the two materials illustrate the significance of the changing ionic radius.

4.2 Experimental details

The samples for this study were provided by the groups of Professors Itoh ($LaTiO_3$) and Akimitsu ($YTiO_3$). The $LaTiO_3$ sample was synthesized by arc melting appropriate mixtures of La_2O_3, TiO_2, and Ti in an argon atmosphere [Itoh99]. The properties of $LaTiO_3$ are strongly dependent on the oxygen stoichiometry (see, for examples, Refs. [Ulri06, Zhou06]). To produce a sample as close to the correct stoichiometry as possible, several samples were prepared and the one with the highest $T_N \sim 135$ K, determined by magnetic measurements, was chosen [Itoh]. The $YTiO_3$ was prepared similarly, but using Y_2O_3 instead of La_2O_3, and was determined to be $YTiO_{3+\delta}$ with $\delta \leq 0.05$ and $T_C = 27$ K and a saturation magnetic moment of $0.84\mu_B$/Ti [Akim01, Kuroiwa].

Our μSR experiments on both samples were carried out using the GPS spectrometer at the Paul Scherrer Institute, in zero applied magnetic field (ZF). See section 2.2 for a discussion of the methodology. Examples of the measured asymmetry spectra are presented in Figures 4.2 & 4.5. At low temperature, precession signals are seen in both compounds indicative of long-range magnetic order with two precession frequencies indicating two magnetically inequivalent muon sites. Above their respective transition temperatures the data for both compounds shows exponential relaxation characteristic of a paramagnetic phase. The initial approach to the data analysis for both compounds will be discussed here. After this had been carried out, parameters that were found to be constant within the experimental error were held fixed, and those details will be discussed separately in sections 4.3 and 4.4.

To analyse the data the following equation was used:

$$P_z(t) = P_1 e^{-\lambda_1 t} + P_2 e^{-\lambda_2 t}\cos(2\pi\nu_2 t + \phi_2) + P_3 e^{-\lambda_3 t}\cos(2\pi\nu_3 t + \phi_3). \qquad (4.2)$$

Above the ordering temperature P_2 and P_3 are set equal to zero since no precession is observed. Below the ordering temperature we can take the P_1 term to describe the depolarization of the muon due to fields along its initial spin polarization, and P_2 and P_3 to describe the effect of fields perpendicular to this direction. The difference between ν_2 and ν_3 comes from magnetic inequivalency. To maintain a consistent discussion I will take $\nu_2 > \nu_3$. For both compounds the function:

$$\nu_i(T) = \nu_i(0)(1 - (T/T_c)^{\alpha_i})^{\beta_i}. \qquad (4.3)$$

was used to fit the temperature dependence of each precession frequency $\nu_i(T)$. T_c is the appropriate ordering temperature, α describes the temperature dependence as $T \to 0$, and β is the critical parameter describing the sublattice magnetization close to T_c [Blun01]. We would expect these parameters to be similar for both precession frequencies.

Dipole field calculations were carried out in order to establish whether the observed frequencies were consistent with the calculated fields at plausible muon sites. The methodology was as described in section 2.2 with calculations carried out over 10^4 unit cells. The details specific to each compound will be discussed in conjunction with the experimental results in sections 4.3 and 4.4 below.

Such dipole field calculations have been compared to μSR data in other perovskite compounds. Some of the more thoroughly studied materials have been the rare earth orthoferrites, $R\mathrm{FeO_3}$. The $R = \mathrm{Sm, Eu, Dy, Ho, Y}$, and Er variants were studied by Holzschuh *et al.* [Holz83] and they found that the stable muon site common to all of these compounds was on the mirror plane at $z = 1/4\,(3/4)$, this being the rare earth - oxygen layer, either about 1 or 1.6 Å from the nearest oxygen ion, as would be expected for the $(\mathrm{OH})^-$ analog, $(\mathrm{O}\mu)^-$. This study was followed by others taking a slightly different approach to finding the muon sites [Boek84, Lin86], and these found further plausible sites, albeit apparently metastable ones, neighbouring the rare earth - oxygen layers. Results of these studies have also been applied to orthorhombic nickelates, without precession frequencies to test the hypothesis, but the approach was consistent with phase

separation occurring within magnetically inequivalent layers [Garc95a]. The most immediately relevant example within the literature is $LaMnO_3$ [CeGu01], for which a detailed study showed that the two observed precession frequencies corresponded to two structurally inequivalent muon sites, the lower frequency one within the rare earth - oxygen mirror plane and the higher frequency one at an interstitial site within the Mn-O plane. The latter set of sites require a significant contribution from the contact fields due to the neighbouring oxygen ions, which the dipole field calculations in this chapter do not consider.

4.3 μSR measurements on $LaTiO_3$

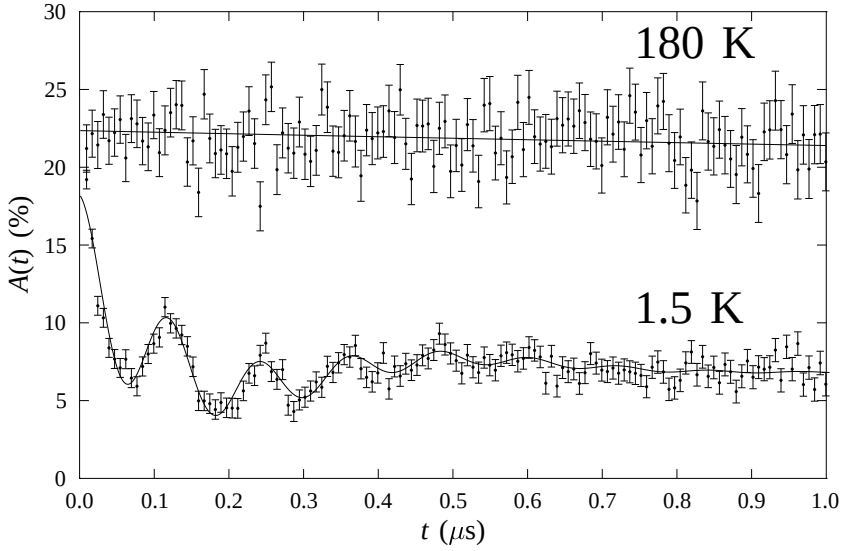

Figure 4.2: Examples of the raw μSR data recorded for $LaTiO_3$ both significantly below and above $T_N \sim 130$ K. The precession is clearly evident in the low temperature data and absent in the high temperature data.

Raw data recorded on $LaTiO_3$ is shown in Figure 4.2. The high temperature data is well described by a single exponential relaxation consistent with fast fluctuating electronic moments in the paramagnetic phase. Muon precession is clearly evident in the ordered phase, as would be expected. The fits shown in Figure 4.2

were to Equation 4.2 with the amplitudes of the two oscillating components set equal, $P_2 = P_3 = 6.5$ %. The precession is rapidly damped in the ordered phase since the linewidth is comparable to the precession frequencies. The amplitude of the two precessing components is close to 2/3 of the relaxing amplitude, suggesting that the sample is ordered throughout its volume. After preliminary fitting showed that they were not significantly different from zero, the phases of the oscillating components, ϕ_2 and ϕ_3, were subsequently fixed equal to zero. The parameters obtained from fitting Equation 4.2 to the asymmetry data applying these constraints are shown in Figure 4.3.

The precession frequencies shown in Figure 4.3(a) are both well defined and follow similar power law behaviours up to T_N. The 130 K data set shows very small precessing amplitudes, around 1/6 of the values at lower temperatures, suggesting that only small regions of the sample order above this temperature. For this reason, 130 K was taken as the bulk T_N value used when fitting Equation 4.3 to the precession frequencies. This value of T_N is quite consistent with the value found by Zhou and Goodenough [Zhou06], and it is conceivable that other magnetic studies may have been strongly affected by small and differently doped regions giving the appearance of a higher T_N. The extracted parameters are shown in Table 4.3. Fixing the amplitudes of $P_1 = 2$ % and $P_2 = P_3 = 6.5$ % proved successful for $T < 130$ K. The linewidths λ_2 and λ_3 are similar at low temperatures, but their values diverge approaching T_N: λ_2 rises, whereas λ_3 falls along with ν_3. The relaxation rate λ_1 is relatively small in the ordered phase and the small value of P_1 below T_N gives rise to the significant error bars. There is a sharp peak in λ_1 at 130 K, consistent with this being the ordering temperature, but the form of the relaxation is complicated at this temperature. Above T_N the relaxation rate falls neatly to a small value, which is again difficult to fit. Measurements at a pulsed muon source where the background is smaller would allow this behaviour to be characterized more precisely.

Dipole field calculations were carried out for the G-type magnetic structure reported in Ref. [Keim00] and shown in Figure 4.4(a), assuming the magnetic moments ($\mu = 0.57\,\mu_B$) are aligned along the a-axis [Cwik03]. Calculations were also carried out assuming alignment along the c-axis. The results are periodic in the c-axis by half the orthorhombic c-axis lattice constant. We would expect the muon sites to lie within the $z = 1/4$ plane, as they do in $LaMnO_3$ [CeGu01]. If the moments are along the c-axis, the only contours corresponding to both observed

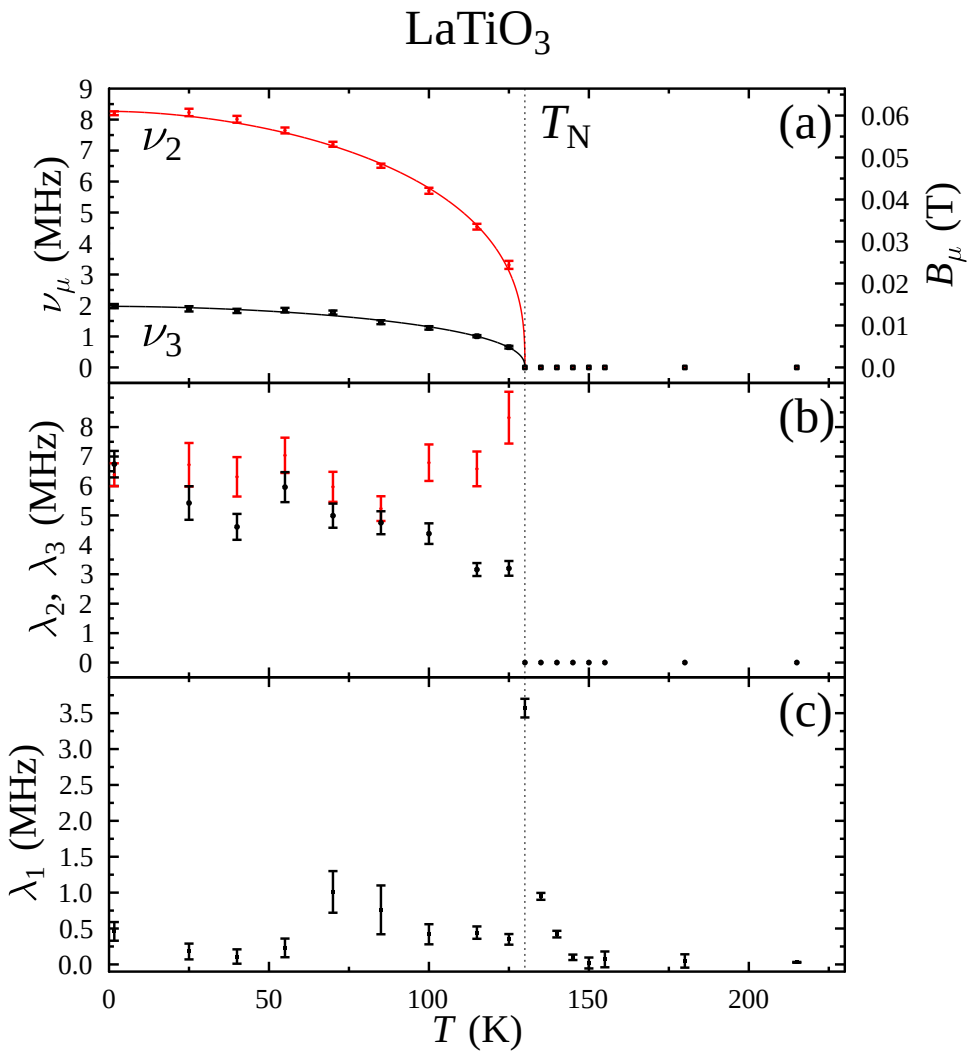

Figure 4.3: Parameters extracted from the raw μSR data on $LaTiO_3$ using Equation 4.2 and setting $P_2 = P_3 = 6.5$ %, as discussed in the text. (a) Precession frequencies ν_2 and ν_3, together with the equivalent magnetic field. (b) Linewidths of the precession frequencies λ_2 and λ_3. (c) Relaxation rate λ_1 for the relaxing component P_1.

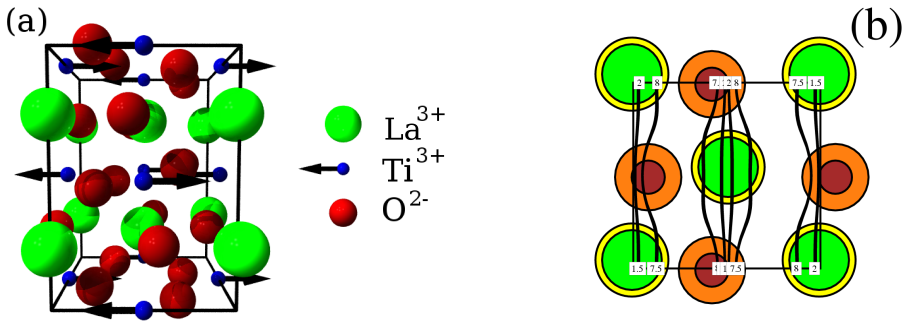

Figure 4.4: (a) Structure of $LaTiO_3$ shown looking along the b-axis. The G-type spin arrangement of the Ti ions is shown assuming the moments are aligned along the a-axis. Structural data was taken from Ref. [Cwik03]. (b) Example of the results from dipole field calculations described in the text, plotted in the ab plane with a fractional c co-ordinate of 0.25. Contours are plotted for frequencies near those observed in the μSR data and plausible sites neighbouring the orange oxygen ions ($r = 1$ Å) can be deduced.

precession frequencies are very closely spaced at points around 0.75 Å from the oxygen ion centres within the plane. For moments aligned along the a-axis the calculations give the results shown in Figure 4.4(b), much more similar to those in $LaMnO_3$. Since we expect the O-μ bond to be around 1 Å, this moment orientation seems far more consistent with the observed precession frequencies. The other possibility is that the muon sites lie within the Ti-O layer. This is far more consistent with moment alignment along the c-axis, since suitable field values are found at sites between oxygen ions. It is more difficult to make precise assignment of muon sites in this case because the field contours are far more closely spaced. While there remains some ambiguity, observing well separated field contours corresponding to previously identified muon sites and apparently equally numbers of plausible muon sites for each frequency, in agreement with the experimental amplitudes, is strong evidence that the moments are aligned along a rather than c, something neutron results have not been able to prove with more certainty [Cwik03]. A μSR study of a single crystal, similar to that of Ref. [CeGu01], might provide the easiest experimental approach sufficient to answer this question.

4.4 μSR measurements on $YTiO_3$

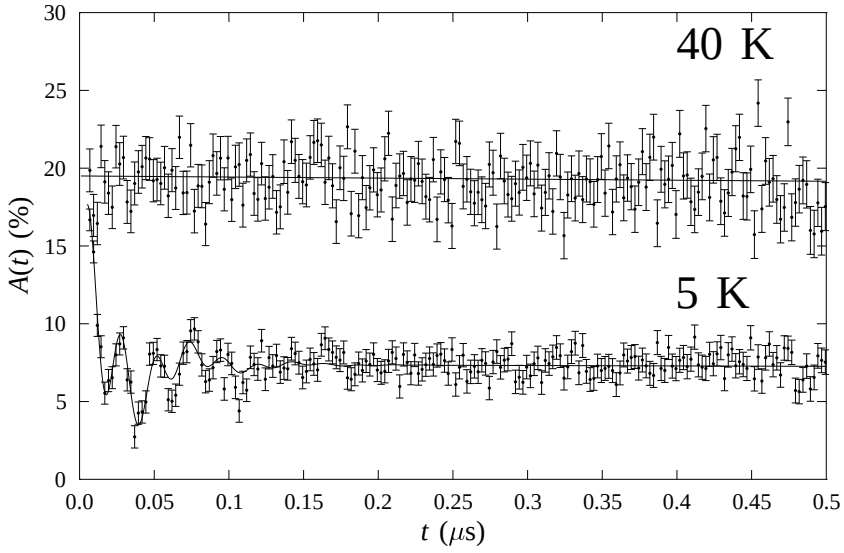

Figure 4.5: Examples of the raw μSR data recorded for $YTiO_3$ both significantly below and above $T_C \sim 27$ K. The precession is clearly evident in the low temperature data and absent in the high temperature data.

Asymmetry spectra recorded on $YTiO_3$ are shown in Figure 4.5. The high temperature data is well described by a single exponentially relaxing component as is typical for paramagnets. Below $T_C \sim 27$ K [Kuroiwa] muon precession is observed, consistent with long range magnetic order developing below this temperature. Preliminary fitting showed that the amplitudes of each component were essentially temperature independent below T_C, and well defined. In subsequent fitting the total relaxing asymmetry was fixed to 16 %. Surprisingly for a polycrystalline sample, the solely relaxing component accounts for only a small proportion of the signal, but this may be due to the small relaxation rate being lost in the background noise in these continuous muon source experiments. Fixing $\lambda_1 = 0.06$ MHz was found to be successful over the whole measured temperature range. Given the similar structures, it might seem likely that the amplitudes of the oscillating components would be very similar, as was the case in $LaTiO_3$, but comparison with the dipole field calculations below suggests that the situation is

not so simple in $YTiO_3$. The initial phase $\phi_2 = -90°$ was independent of temperature and was fixed at this value in subsequent fitting. Such an initial phase offset is generally associated with spin density waves, although the small perturbations to the dominant ferromagnetic structure [Ulri02] (shown in Figure 4.7) could have a similar effect. ϕ_3 was zero within error, and that value was fixed subsequently. The fits to the data shown in Figure 4.5 are to Equation 4.2 with the parameters shown in Figure 4.6.

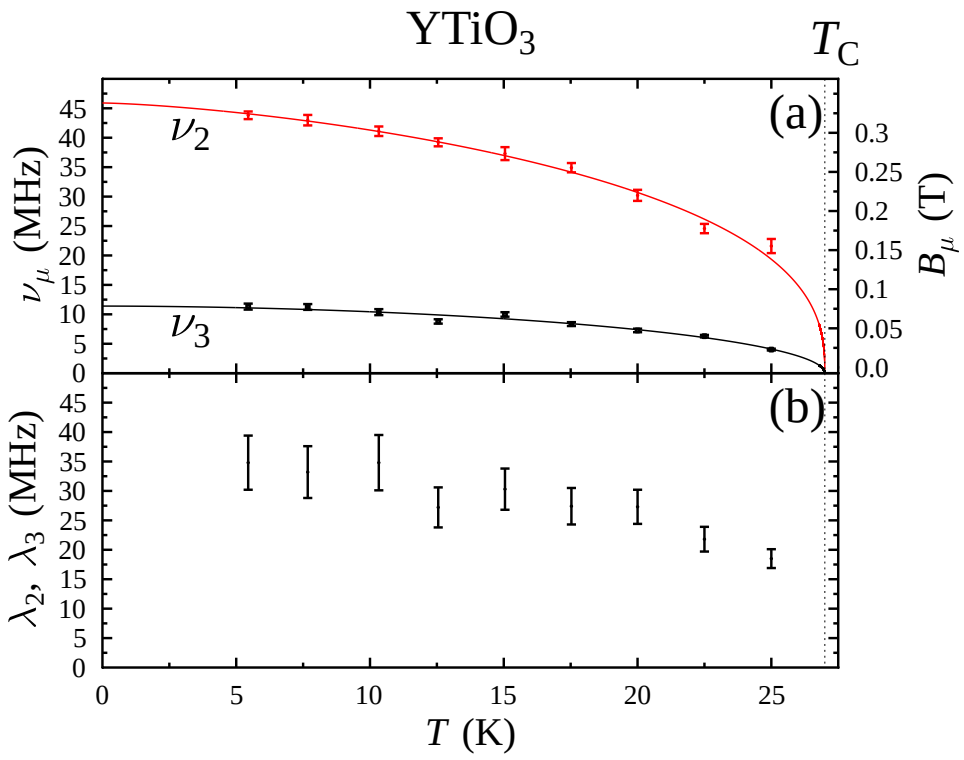

Figure 4.6: Parameters extracted from the raw μSR data on $YTiO_3$ using Equation 4.2 as discussed in the text. (a) Precession frequencies ν_2 and ν_3, together with the equivalent magnetic field. (b) Linewidth of the precession frequencies $\lambda_2 = \lambda_3$.

The two precession frequencies shown in Figure 4.6(a) both follow conventional power laws, with the fits obtained using Equation 4.3 with the parameters presented in Table 4.3. The value of $T_C = 27$ K shown in Figure 4.6 comes from magnetic measurements [Kuroiwa]. Both frequencies are well defined at low temperature, but close to the transition there seems to be more scatter in the values obtained. The linewidths of both components shown in Figure 4.6(b) are large compared to the precession frequencies, such that the oscillations are heavily

damped. Combined with the small size of P_2, this makes fitting ν_2 particularly difficult close to the transition. The linewidths λ_2 and λ_3 were equal within experimental error so were constrained to be equal during subsequent fitting.

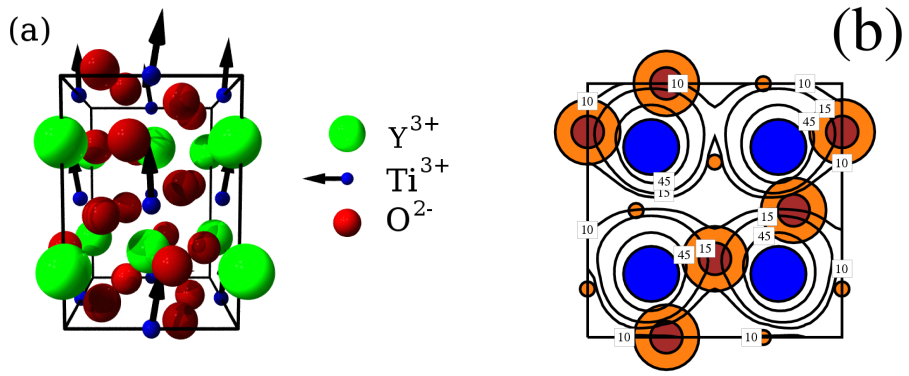

Figure 4.7: (a) Structure of $YTiO_3$ viewed along the b-axis. Structural data was taken from Ref. [MacL79] and the magnetic structure from Ref. [Ulri02]. (b) Example of the results from dipole field calculations described in the text, plotted in the ab plane with a fractional c co-ordinate of 0.43 in the pseudocubic magnetic unit cell (a 45° rotation about c relative to the structure shown in (a) with $\sqrt{2}$ larger a' and b' lattice constants). Contours are plotted for frequencies near those observed in the μSR data and two plausible sites neighbouring the oxygen ions can be deduced.

Dipole field calculations were carried out for the ferromagnetic structure reported in Ref. [Ulri02] and depicted in Figure 4.7(a). Moment values of $(0.106, 0.0608, 0.7034)\,\mu_B$ along the principal axes of the pseudocubic unit cell (a', b', c') were used [Ulri02]. A representative slice through the structure where the contours corresponding to the observed frequencies come near to oxygen ions is shown in Figure 4.7(b). The magnetic fields for this largely ferromagnetic structure are much larger than those in the antiferromagnetic structure of $LaTiO_3$ (Figure 4.4 (b)), in agreement with experiment. As in $LaTiO_3$ the lower frequency component in the signal is consistent with sites within the A - O plane ($z = 1/4$), but there are no sites within this layer that would correspond to the higher frequency observed. The higher frequency component appears consistent with a smaller number of sites between oxygen ions near to or in the $z = 1/2$ layer, but rather closer to the Ti^{3+} ion positions. There are also plausible sites corresponding to the lower frequency within this layer. Because of the small magnetic moments along the a and b-axes the contours are more distorted than those seen in Figure 4.4. Considering the variation of these distortions along the c-axis

leads to a structure not dissimilar to a helically ordered magnet, for these small components. This offers a natural explanation for the significant initial phase offset observed for the higher frequency component of the signal, since it is this frequency that is particularly sensitive to the small moments in the a and b directions. The lower precession frequency will be more dependent on the primary ferromagnetic component in the magnetic structure, and therefore we would not expect such an initial phase offset.

4.5 Conclusion

The μSR results clearly demonstrate intrinsic magnetic order below the expected ordering temperatures in both samples. We are also able to follow the temperature dependence of the (sub)lattice magnetization and show that the behaviour is essentially conventional. The parameters extracted from the precession frequencies shown in Figures 4.3 and 4.6 using Equation 4.3 are shown in Table 4.3.

The parameters α_i in Equation 4.3 describe the behaviour of the precession frequencies as $T \rightarrow 0$. This is normally dominated by spin wave contributions and typically takes values between 1 and 2, with 1.5 being the expectation for classical spin waves [Blun01]. For both materials, neither α_i value is well defined, but lies close to or within this expected range. β_i describes the behaviour close to the transition, determined by critical fluctuations. This parameter is very sensitive to the value chosen for the transition temperature, a process which is difficult in both materials. Given the complicated form of the muon depolarization in $LaTiO_3$ at 130 K, discussed above, it is reasonable to assume that this temperature is a good approximation to T_N. In $YTiO_3$ we must rely on the magnetic susceptibility measurements [Kuroiwa] to obtain $T_C = 27$ K. All but one of the β_i values are significantly below the mean field expectation of 0.5 and lie within the range 0.3-0.4 consistent with 3D critical fluctuations (e.g. 0.346 (3D XY) or 0.369 (3D Heisenberg)) [Peli02]. Fitting to the sum of the two frequencies and fixing $\alpha = 1.5$ leads to $\beta = 0.35(2)$ in $LaTiO_3$ and $\beta = 0.40(2)$ in $YTiO_3$. These values seem reasonable given the relatively isotropic exchange constants in these compounds.

In the context of the dipole field calculations depicted in Figures 4.4 and 4.7 and the previous literature, the sites obtained for the two compounds considered here seem entirely plausible. For both compounds we find a site corresponding to the lower precession frequency in the A - O layer, as in $LaMnO_3$, but the origin

Table 4.3: Parameters extracted from fitting Equation 4.3 to the precession frequencies for $LaTiO_3$ and $YTiO_3$, shown in Figures 4.3 and 4.6 respectively. The ordering temperatures were fixed to the values obtained in magnetic measurements and the error on each fitted parameter is shown in brackets.

Compound	$LaTiO_3$	$YTiO_3$
	$T_N = 130$ K	$T_C = 27$ K
$\nu_2(0)$ (MHz)	8.267 (57)	46 (1)
α_2	1.79 (13)	1.43 (34)
β_2	0.363 (18)	0.382 (43)
$\nu_3(0)$ (MHz)	1.972 (55)	11.4 (6)
α_3	1.80 (38)	1.84 (48)
β_3	0.416 (40)	0.505 (51)

of the higher frequency component is almost certainly different in the two cases. In $LaTiO_3$ the higher frequency sites also appear to be in the rare earth - oxygen layer, and this fits with the equal amplitudes of the two components observed in the μSR signal. Sites near the Ti-O planes seem unlikely on the basis of the calculations. In $YTiO_3$ the higher frequency component cannot be in the Y-O plane if the calculations are correct and the hyperfine coupling is negligible. A more plausible assignment corresponds to sites lying between two oxygen ions and relatively close to the Ti ions, which would explain both the high precession frequency, the relatively small amplitude (since the site would probably be less electrostatically favourable), and also the large initial phase offset consistent with a stronger coupling to the antiferromagnetically coupled moments in the *ab*-plane. Lower frequency sites could also occur in the Ti-O layers, which may contribute to the extra amplitude of the lower frequency component. In both compounds a full site determination would require measurements on single crystals and in applied fields, as was done for the rare earth orthoferrites [Holz83, Boek84, Lin86] and $LaMnO_3$ [CeGu01].

In magnetically ordered polycrystalline samples we would expect the relaxing component to account for around one third of the relaxing asymmetry, owing to the polycrystalline averaging of the effects of the magnetic fields parallel and perpendicular to the muon spin direction. While this is the case in $LaTiO_3$, demonstrating that the magnetic order exists throughout the volume of the sample, in $YTiO_3$ the amplitudes observed do not fit this hypothesis. It seems most likely that the relaxation is sufficiently small to be hidden within the background,

given the measurements were recorded at a continuous muon source. To clearly settle this matter it would be necessary to make measurements at a pulsed muon source, where the background would be negligible.

The results presented in this chapter have confirmed previous reports of the magnetic properties of both $LaTiO_3$ and $YTiO_3$. Unlike the case of $NaNiO_2$ described in Chapter 3, these compounds have been the subject of extensive study using neutron diffraction and are more suitable for that technique. The further information available from μSR experiments can therefore only be marginal, and the μSR experiments are in excellent agreement with the previous neutron results [Keim00, Ulri02]. Nonetheless, this confirmation is worthwhile given the history of sample dependent results and the difficulty of controlling the oxidation state precisely [Ulri06, Zhou06]. Comparison between the precession frequencies observed in $LaTiO_3$ and dipole field calculations strongly favour moment alignment along the a-axis rather than the c-axis, a problem powder neutron diffraction has difficulty resolving [Cwik03]. Using a microscopic probe, rather than a bulk one, gives an independent means of testing the previous results from bulk probes, confirming those results strongly. The other application of these results is in testing the ability of dipole field calculations to reproduce the magnetic field distributions within oxide materials. This is also successful for these materials, where we can note the similarity of the structure and the similarity of the muon sites, while having significantly different magnetic structures. That it is possible to obtain good predictions for the local magnetic fields observed, and even to illustrate the underlying reason behind the initial phase offset observed in $YTiO_3$, is a worthwhile demonstration of the calculations in cases where the magnetic structures are so well defined.

μSR has been previously been used on perovskite compounds exhibiting a great variety of magnetic behaviour, and this will likely continue in future. A natural, and somewhat more specific, extension of the present work would be to investigate the spin-1 analogues of the two compounds discussed in this chapter, $LaVO_3$ and YVO_3. These have attracted almost as much theoretical attention as the two Ti compounds [Solo06], and in YVO_3 we have an example of a relatively unusual and little studied effect, the orbital-Peierls transition [Ulri03]. YVO_3 also has two magnetically ordered phases with significantly different magnetic structures [Ulri03] and would therefore provide an excellent application for the formalism developed within this chapter.

Chapter 5

Spin gaps in Ti^{3+} chains: $NaTiSi_2O_6$ and TiOCl

Contents

Systems of spin-dimers, whether they be isolated, in chains, planes, or within a three-dimensional framework, show a broad variety of physical properties. Examples of these include Bose-Einstein Condensation of magnons in isolated spin-1 dimers [Rüeg03, Seba06, Zapf06], novel structural ordering [Rada02], and magneto-elastic driven [Bray75] or orbitally driven [Schm04] dimerization in chains. In this chapter I describe an investigation of two compounds where spin-1/2 ions are arranged along chains, and form spin-singlet dimers at low temperature. For both these materials the mechanisms leading to dimer formation are unusual, and this is evident in their properties.

The outline of this chapter is as follows: in section 5.1 I describe some of the mechanisms that lead to dimer formation and spin gaps in solids and briefly survey the experimental and theoretical results related to these mechanisms, focusing particularly on the two compounds investigated herein, sodium pyroxene (section 5.1.1) and titanium oxychloride (section 5.1.2). I go on to discuss a simple model in section 5.2 that relates the dimerization of these chain compounds to both magnetic susceptibility and μSR data. This is followed by experimental results on both compounds using magnetic susceptibility (section 5.3) and μSR (section 5.4) techniques. Finally, the results are discussed and compared with each other and suggestions for future work are made in section 5.5.

The majority of this work has previously been published [Bake07].

5.1 Introduction

A number of mechanisms can cause the formation of dimers in the solid state. The first of these to be identified was the Peierls instability [Peie55] where a one dimensional chain with one free electron per lattice point is unstable to the pairing of atoms and the formation of a band gap at the Fermi level, a metal-insulator transition. The energy scale for this process is the Fermi energy and the coupling is between electrons and phonons. Subsequently an analogous effect, now referred to as a spin-Peierls transition, was found in systems with a strong magnetoelastic coupling [Bray75]. The energy scale here is the magnetic exchange constant, J, which is far smaller than E_F, and so the dimerization occurs at a far lower temperature. The canonical spin-Peierls compound $MEM(TCNQ)_2$ in fact shows a Peierls transition at 335 K where the uniform TCNQ chains dimerize, and then a spin-Peierls transition, where these dimers dimerize into a tetramized state, at

18 K [Huiz79]. We can write the spin-Peierls Hamiltonian simply as [Pytt74]:

$$\mathcal{H} = \sum_l J(l, l+1)(\vec{S}_l \cdot \vec{S}_{l+1} - 1/4), \tag{5.1}$$

where $J(l, l+1)$ is given in terms of the atomic displacements $\vec{u}(l)$ as:

$$J(l, l+1) = J + \sum_l [\vec{u}(l) - \vec{u}(l+1)] \cdot \vec{\nabla}_l J(l, l+1). \tag{5.2}$$

As the system dimerizes, alternating exchange constants along the chain pair spins into strongly coupled singlet states with weak coupling between these spin-0 dimers. By re-expressing the above Hamiltonian in terms of phonon creation and annihilation operators, an analogy can be drawn with the 1-D Fröhlich Hamiltonian used in the BCS theory of superconductivity [Bray75], and the spin gap is found to follow the same temperature dependence as the BCS energy gap and the zero temperature limit:

$$2\Delta(T = 0) = 3.53 T_{\mathrm{SP}}, \tag{5.3}$$

where 2Δ is the spin gap and T_{SP} is the spin-Peierls transition temperature. This assumes that the structural deformation is entirely mediated by the magnetoelastic coupling, an assumption that we will see below is not the case in more complicated systems.

Magnetic susceptibility measurements of organic spin-Peierls systems were reported by Bray *et al.* [Bray75] ($TTFCuS_4C_4(CF_3)_4$, $T_{\mathrm{SP}} = 12$ K), and Huizinga *et al.* [Huiz79] ($MEM(TCNQ)_2$, $T_{\mathrm{SP}} = 18$ K). These organic compounds have been joined by inorganic $CuGeO_3$ [Hase93] with a spin-Peierls transition at $T_{\mathrm{SP}} = 14$ K. Below the spin-Peierls transition the magnetic susceptibility falls exponentially, consistent with the formation of spin-singlets. This exponential drop in the susceptibility makes finding the spin gap through magnetic resonance experiments difficult since the signal strength drops accordingly. μSR has been used to probe spin-Peierls systems in the past and benefits from having a relaxation rate which rises as the temperature decreases, therefore showing greater sensitivity in the spin gapped temperature region. Studies of $MEM(TCNQ)_2$ have been reported by Blundell *et al.* [Blun97] and Lovett *et al.* [Love00], the latter study deriving a value for the spin gap from the thermal activation of the muon spin relaxation rate. Pure and Zn-doped $CuGeO_3$ were studied by García-Mũnoz *et al.* [Garc95b] and

the effect of both Si and Zn doping were investigated by Kojima *et al.* [Koji97]. These studies showed that doping can lead to either low temperature spin freezing or antiferromagnetic order, in agreement with theoretical predictions.

Another mechanism that causes dimerization is the distortion of the lattice by orbital interactions. This is particularly significant in systems with partially occupied t_{2g} orbitals such as the Ti^{3+} chains considered below. There are two slightly different processes that have been considered, orbital driven spin-singlet formation and orbital singlet formation. The former has now been observed in a number of systems which will be discussed below, whereas the observation of the latter remains limited to one system, YVO_3 [Ulri03], and there are further possible phases which are yet to be found experimentally.

The more common dimerization process involving orbitals is the formation of spin-singlet dimers, leading to a non-magnetic ground state. This has been discussed for spinels [Khom05, Rada05] (e.g. $CuIr_2S_4$ [Rada02] and $MgTi_2O_4$ [Schm04]), the pyroxene chain compound $NaTiSi_2O_6$ [Hiki04, vWez06], and the layered system $La_4Ru_2O_{10}$ [Khal02, Wu06]. It may also be relevant in $NaTiO_2$, MV_2O_4, and Fe_3O_4 [Khom05]. Qualitatively, we consider orbitals coupling to the lattice through the cooperative Jahn-Teller effect and to spins via superexchange. This gives us an effect which is similar to the magnetoelastic coupling that drives a spin-Peierls transition. The Ti^{3+} ion seems to be a particularly favourable system to exhibit this because the splitting of the active t_{2g} orbitals due to the non-cubic crystal field is smaller than the typical hopping integrals. For the spinel compounds the situation proximate to a metal-insulator transition was considered [Khom05], but one can equally well consider a Mott insulator with strong on-site Coulomb interactions [vWez06], the situation relevant to $NaTiSi_2O_6$.

It must be noted that this approach has now been extended beyond chain like compounds to the bilayer material [Khal02, Wu06] $La_4Ru_2O_{10}$. This undergoes a monoclinic to triclinic structural transition around 160 K accompanied by a significant drop in the magnetic susceptibility. It was originally assumed [Khal02] that this corresponded to a change in the t_{2g} orbital occupation from $t_{2g\uparrow}^3 t_{2g\downarrow}^1$ in the $S = 1$ high temperature phase to $t_{2g\uparrow}^2 t_{2g\downarrow}^2$ in a $S = 0$ low temperature phase. More recent measurements [Wu06] have shown that the Ru^{4+} spin state is unchanged going through the transition. This can be naturally explained in terms of orbital driven dimerization of the $S = 1$ spins.

For chains of integer spins a Haldane gap will be present [Hald83], and this

precludes any low-temperature instability. Examples of these materials where μSR experiments have been carried out include Y_2BaNiO_5 [Koji95b] (including the effect of both Mg and Ca doping), $Ni(C_2H_8N_2)_2NO_2(ClO_4)$ (NENP) [Ster92], and $NiC_2O_42\cdot$(2-methylimidazole) [Fuka99]. These results consistently show an increase in the muon spin relaxation rate as the temperature decreases.

In other materials the mechanism creating the spin gap is more complex. This is particularly true for two-dimensional systems with spin-gaps where chain formation is not apparent. Examples of these include CaV_4O_9 [Tani95, Luke97, Pick97, Jest98], where excitations of plaquettes may be the mechanism creating the spin gap, NaV_2O_5 [Isob96, Fuda99], which has some similarity to ladder compounds, and CaV_2O_5, which is a two-leg spin ladder [Iwas96, Luke97]. Such systems, where the magnetic exchange interactions can be thought of like a ladder, with strong coupling on rungs, weaker coupling between rungs in one perpendicular direction, and the weakest coupling between ladders, also show a spin gap and have been thoroughly investigated using μSR. Examples include: $Sr_2Cu_4O_6$, [Koji95a], $Na_2Co_2(C_2O_4)_3(H_2O)_2$, [Kikk07] and $(CH_3)_2CHNH_3Cu(Cl_xBr_{1-x})_3$. [Sait06] Doping these materials often leads to magnetic order. Another type of spin gapped system is the spin ring, such as Cu_3WO_6 [Fuda02], where low temperature spin freezing is observed and a thermally-activated muon-spin relaxation rate allows the spin gap to be probed.

There are also systems where dimers exist independent of temperature, such as $TlCuCl_3$ [Rüeg03], $BaCuSi_2O_6$ [Seba06], or $NiCl_2$-$4SC(NH_2)_2$ [Zapf06]. In these cases, the dimers are antiferromagnetically coupled in low magnetic fields and the system is paramagnetic, but the application of strong magnetic fields above a critical field H_{c1} turns these dimers into spin-triplets arranged into an ordered magnet. This has been the subject of considerable interest, since the transition at $H_{c1}\,(T=0)$ is a quantum critical point.

I now go on to discuss the literature describing the two title compounds: $NaTiSi_2O_6$ and TiOCl.

5.1.1 Introduction to $NaTiSi_2O_6$

$NaTiSi_2O_6$ is part of the alkali metal pyroxene family of compounds including jadeite and kunzite [Isob02], but unlike most members of this family does not show a Néel ordered ground state at low temperature. The Ti^{3+} ions are arranged

along chains parallel to the c-axis. SiO_4 tetrahedra lie between the chains giving a weak interchain coupling. Figure 5.1 shows the structure projected along the a-axis. The chains are observed to dimerize at 210 K [Isob02, Nino03, Redh03], changing the space group from the high-temperature $P\bar{1}$ to the low-temperature $C2/c$, and giving two different Ti^{3+} - Ti^{3+} distances in the low temperature phase. Accompanying the structural change, the magnetic susceptibility [Isob02] is found to drop sharply below the transition, consistent with the formation of dimers, and follows a thermally-activated behaviour with a spin gap $\Delta \sim 500$ K at low temperature. Above the transition, the susceptibility is well described by a Bonner-Fisher curve, as would be expected for a magnetic chain [Bonn64]. Phonon anomalies measured using Raman scattering [Kons04, Popo05] are consistent with the dimerization being driven by an orbital ordering at $T_{OO} = 210$ K, below which the system is condensed in one of two possible orbitally ordered spin-singlet states, breaking translational symmetry.

Figure 5.1: The structure of $NaTiSi_2O_6$ shown looking along the a-axis. The Ti^{3+} ions are surrounded by oxygen octahedra and are arranged along chains parallel to the c-axis. Figure from Ref. [Redh03].

Far more theoretical work has been carried out on $NaTiSi_2O_6$ than experimen-

tal, since it provides a candidate system on which to test models of the orbital-Peierls transition. I begin by outlining the prevailing theoretical viewpoint, followed by an earlier, seemingly erroneous model. Hikihara and Motome [Hiki04] considered a spin-orbital-lattice coupled model and performed numerical simulations and a mean-field analysis. Similar methods have subsequently been employed by van Wezel and van den Brink [vWez05, vWez06] and Streltsov *et al.* [Stre06]. Van Wezel and van den Brink [vWez06] used the following Hamiltonian to describe the system:

$$\mathcal{H}_{ST} = 4J \sum_{<ij>} S_i \cdot S_j [T_i^z T_j^z + \frac{(-1)^i}{2}(T_i^z + T_j^z) + \frac{1}{4}]. \tag{5.4}$$

T_i^z are pseudospin operators parametrizing the orbital occupation, with $T^z = +1/2$ corresponding to $|xy\rangle$ occupation and $T^z = -1/2$ corresponding to $|yz\rangle$. The chain like geometry of these systems, limiting us to direct $\mathrm{Ti}-\mathrm{Ti}$ hopping, reduces the orbital problem to the Ising-like case. The ground state of this simplified model is ferro-orbital and has an energy per dimer of $-3J/4$. This is depicted in Figure 5.2. The model displays a phase transition associated with orbital ordering, above which is a dynamic Jahn-Teller phase. Below the transition we have a spin-Peierls like state with one of the two orbitals occupied and spin-singlets in neighbouring atoms. An improved model [vWez06] considers a superexchange term and also a crystal field term that acts against spin-singlet formation, but it was found that the orbitally-assisted Peierls transition was stable against a non-zero crystal field. From this model it is possible to reproduce the high and low temperature variation of the magnetic susceptibility [Hiki04, vWez06], although Hikihara and Motome's numerical simulations suggested that short-range correlations enhancing the spin-singlet fluctuations are present around the transition at T_{OO}, and these decrease the magnetic susceptibility. It also possible to fit the numerical simulations of the magnetic susceptibility with an Arrhenius form, and these suggest $2\Delta \sim 650\mathrm{K}$ [Hiki04].

An alternative picture for $NaTiSi_2O_6$ was proposed by Popović *et al.* [Popo04, Popo06], where a composite $S = 1$ Haldane chain with spin triplet dimers of ferromagnetically coupled Ti^{3+} spins would form at T_{OO}. This was on the basis of spin polarized generalized gradient approximation calculations, the results of which are not reproduced using other methods, and may well exclude relevant correlations that would invalidate the result obtained [Hiki04, Stre06, vWez06].

Figure 5.2: Orbital and spin arrangement in $NaTiSi_2O_6$. The spin-singlets are circled and the occupied orbitals are shown in blue. Strangely, there is evidence that the spin-singlets are on the longer bond in the dimerized chain. From Ref. [vWez06].

Motivating our study has been the possibility of making a measurement that could clearly distinguish between the theoretically proposed ground states for the system, as well as attempting to measure the magnitude of the spin gap. To achieve this magnetic susceptibility and μSR experiments were carried on samples provided by Dr M. Isobe and Prof. Y. Ueda of the Institute for Solid State Physics, University of Tokyo. These were powder samples prepared as in Ref. [Isob02].

5.1.2 Introduction to TiOCl

The state of the literature on TiOCl is, perhaps, the opposite of that for $NaTiSi_2O_6$. There have been many experimental studies, particularly within the last five years, but comparatively little theoretical work. Here I will discuss the experimental studies first, and then move on to describe the theoretical work on this compound.

The structure of TiOCl is composed of TiO bilayers within the *ab* plane, well separated by Cl^- ions. This is shown in Figure 5.3. At low temperature the chains of Ti^+ ions along the *b*-axis dimerize with their spins coupled by direct exchange. Below $T_{c1} = 67$ K the dimerization is commensurate with the lattice [Shaz05], but between T_{c1} and $T_{c2} = 91$ K the chains are incommensurately dimerized [Shaz05, Krim06, Schö06]. This is further complicated by the observation of commensurate lattice fluctuations that coexist with the incommensurately dimerized phase between T_{c1} and T_{c2} and persist up to a temperature $T^* \sim 130$ K [Clan07].

Figure 5.3: The structure of TiOCl shown looking along the b-axis. The Ti^{3+} ions form chains parallel to the b-axis. Figure from Ref. [Schö06].

The magnetic properties of TiOCl were studied by Wilson *et al.* [Wils87], and then Beynon and Wilson [Beyn93], who included a study of scandium-doping, with the intention of comparing the system to the high-T_c cuprates. After subtraction of a Curie tail the susceptibility was found to be nearly independent of temperature. These measurements were repeated by Seidel *et al.* [Seid03] for both pure and Sc-doped specimens, and their results did not reproduce the earlier data. Their results are, however, in excellent agreement with subsequent measurements published in later reports [Kata03, Rück05]. The susceptibility follows a Bonner-Fisher curve at high temperature, despite the quasi-2D structure, with $J = 660$ K, and this one-dimensional model describes the data very well down to around 130 K. There is a clear point of inflection at around 91 K (depending on the sample) and the susceptibility falls very steeply at 67 K. Below 67 K the

susceptibility is dominated by the Curie tail from impurities within the sample and subtracting this gives a nearly temperature independent susceptibility due to the Van Vleck paramagnetism and the diamagnetism of the ionic shells.

The heat capacity of TiOCl shows two peaks at the transitions T_{c1} and T_{c2}, with a surprisingly small amount of entropy released at the two transitions (~ 0.1 R), although the total magnetic heat capacity does reach the expected $R \ln 2$ for a spin-1/2 system at high temperatures. The lattice contribution is dominant at all temperatures [Hemb05, Rück05]. There is good evidence for the magnetic contribution persisting up to $T^* \sim 130$ K and this fits in well with the pseudogap picture arising from the structural fluctuations and behaviour of the magnetic susceptibility.

The pseudogap in TiOCl may be thought of in terms of a reduced density of states just below the Fermi surface, in analogy with a similar phase occurring in high-T_c superconductors, and develops below a temperature $T^* \sim 130$ K.

Possibly the best evidence for the onset of the pseudogap comes from unpublished NMR measurements made by Imai and Chou in 2003 [Imai03]. These are particularly difficult due to the small natural abundances of ^{47,49}Ti and the small nuclear gyromagnetic ratios. Nevertheless, this study found a peak in $1/T_1T$ at $T^* \sim 130$ K and clear features at T_{c1} and T_{c2}. The spin gap was found, using the thermal activation of $1/T_1T$ at low temperature, to be $E_g = 430 \pm 60$ K. This enormous spin gap, $2E_g/k_{\mathrm{B}}T_{c1,2} \sim 10 - 15$, compared with the value (3.53, see Equation 5.3) expected for a canonical spin-Peierls system, has been taken to be evidence of the remarkable properties of TiOCl. It is necessary to include a cautionary note with regard to this result. In the conventional units, the activation energy measured by an NMR (or μSR) experiment is actually 2Δ, not Δ as these authors assumed [Ehre77]. (The details of this will discussed in relation to the μSR analysis in section 5.4.) This reduces the relative size of the gap by a factor of two, so it is still larger than would be expected for a canonical spin-Peierls system, but not to the same extent.

Another means of probing the pseudogap, and orbital behaviour in TiOCl, is through optical spectroscopy. The infrared optical properties show that below 200 K the effective dimensionality of the system decreases from two to one and there is a characteristic energy scale of 430 K associated with the pseudogap [Caim04]. This value of $2\Delta = 430$ K is also confirmed by Raman scattering [Lemm04]. Infrared transmittance measurements have also been re-

ported [Rück05]. Applying pressure suggested that an insulator-to-metal transition, apparent in infrared transmittance and reflectance spectra, occurred at a pressure of around 12 GPa [Kunt06].

ESR measurements have been reported [Kata03, Zakh06] and these have shown that the lowest lying orbital excitation has an energy of $\Delta_{\mathrm{ESR}} \sim 0.3$ eV and the orbital ground state is non-degenerate. The drop of the spin susceptibility below T_{c1} is in agreement with the static susceptibility measurements and T_{c2} is evident as a crossover in the ESR linewidths along the three crystallographic axes.

Thermal expansion measurements show two sharp features at T_{c1} and T_{c2}, the former being sharp and symmetric, therefore suggesting that it is a first-order phase transition, and that the feature at T_{c2} resembles a glass transition [Rück05].

An ARPES study of TiOCl [Hoin05] confirmed the quasi-one-dimensional nature of the electronic structure along the b-axis, as is apparent in the above reports, and gave strong evidence against phonon-induced orbital fluctuations being the reason that TiOCl has such an unconventional spin-Peierls transition.

Seidel *et al.* [Seid03] carried out local-density-approximation (LDA) calculations that showed that the electronic structure is essentially one dimensional. These were augmented by density functional theory calculations that confirmed their results and without the correct inclusion of intersite correlations suggest that the ground state should be subject to strong orbital fluctuations [Saha04, Crac06]. Calculations including the intersite correlations have been carried out more recently [Saha07] and these compare well with the recent ARPES measurements [Hoin05] and suggest that fluctuations of Ti-Ti dimers should occur well above the commensurate dimerization occurring at T_{c1} [Clan07]. LDA+U calculations have been carried out to elucidate the phonon spectrum and agree satisfactorily with experiment [Pisa05]. Cluster calculations were carried out to aid interpretation of optical measurements [Rück05] and agree with other determinations of the smallest orbital excitation energy [Pisa05, Crac06].

The sample for our experiments was provided by the group of Prof. R. Claessen at the University of Würzburg and his collaborators at that institution and at the University of Augsburg, in particular Dr M. Hoinkis. The sample was synthesized according to the method described by Schäfer *et al.* [Schä58], and was in the form of many small crystalline platelets ($\sim$ 1 mm square, $\sim$ 50 μm thick) that were not aligned for any of the experiments detailed below.

5.2 Deducing the temperature dependence of the spin gap

The purpose of this section is to discuss how the temperature dependence and magnitude of the spin gap in unconventional systems can be deduced from the temperature dependence of the dimerization, thereby giving a prediction which can be tested against experimental data in the following sections (5.3 and 5.4). This is done under the assumption that the coupling along the chain is well described by a one-dimensional model. Firstly, I will describe a simple model to relate the spin gap to the dimerization through the alternation of the exchange constants along the chain. This is sufficient to describe $NaTiSi_2O_6$, since the dimerization along the chains has already been reported [Redh03]. I then describe a simple method of deducing the dimerization along the chains in TiOCl from the intensity of the X-ray superstructure reflection along the chain direction. Together, these give predictions that can be tested against the experimental data reported below.

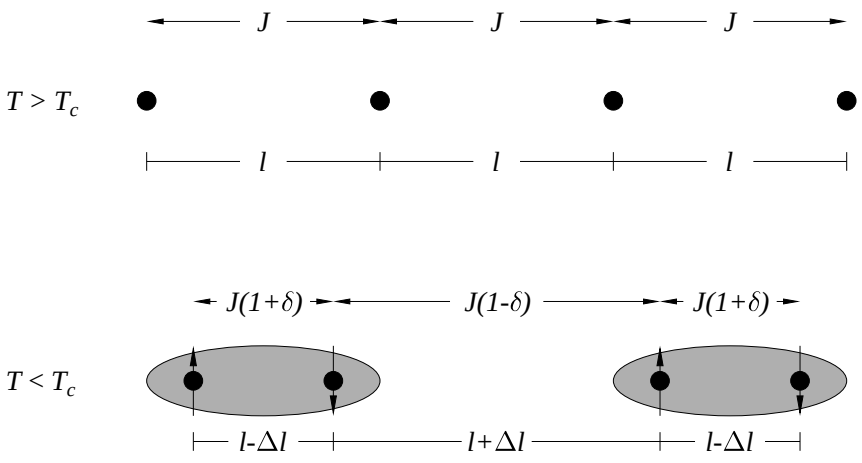

Figure 5.4: Exchange constants in spin chains above and below the structural phase transition T_c. δ describes the alternation in the exchange constants and Δl describes the structural dimerization.

The first step in modelling the dependence of the spin gap, 2Δ, on temperature

is to consider how it depends on the dimerization of the system. This was discussed by Cross and Fisher [Cros79] in terms of chains subject to a dimerization δ, illustrated in Figure 5.4. The exchange constants for neighbouring atoms in the chain are then of the form:

$$J_{l,l+1} = J(1 \pm \delta), \tag{5.5}$$

and since the dimerization is small, we can take δ to be proportional to the structural dimerization Δl. Cross and Fisher [Cros79] used this model to find that the spin gap at zero temperature scaled as:

$$\Delta \propto \delta^{2/3}. \tag{5.6}$$

Similar calculations were carried out by Uhrig *et al.* [Uhri99], including logarithmic corrections, and they obtained a power law of 0.65. Comparing these results to the data showed no significant difference in the parameters obtained, so the 2/3 power law will be used hereafter.

As can be seen in Figure 5.5, the lattice constants in $NaTiSi_2O_6$ are nearly independent of temperature below $T_{OO} \sim 200$ K. From this we can conclude that the degree of dimerization will be essentially constant below the structural transition, and we therefore approximate the spin gap below the structural transition as constant:

$$\Delta(T < T_{OO}) = \Delta(T = 0). \tag{5.7}$$

Since the dimerization along the b-axis has not been reported for TiOCl it is necessary to deduce it by other means. The method I will use here uses the intensity of the superstructure reflection $(0, 1.5, 0)$ measured by Krimmel *et al.* [Krim06]. This is shown in Figure 5.6.

We now need to deduce the variation of this X-ray intensity with respect to the structural dimerization. We begin with the structure factor for a general X-ray reflection,

$$S_{hkl} = \sum_n f_n \exp[-2\pi i(hx_n + ky_n + lz_n)]. \tag{5.8}$$

Since we are considering a superstructure reflection, each of the form factors, f_n, will represent one TiOCl unit, so they are all equal, and we will double the unit cell shown in Figure 5.4 for convenience, thereby choosing the $(0, 3, 0)$ reflection in the doubled unit cell. Taking the dimerization to be a small fractional displacement

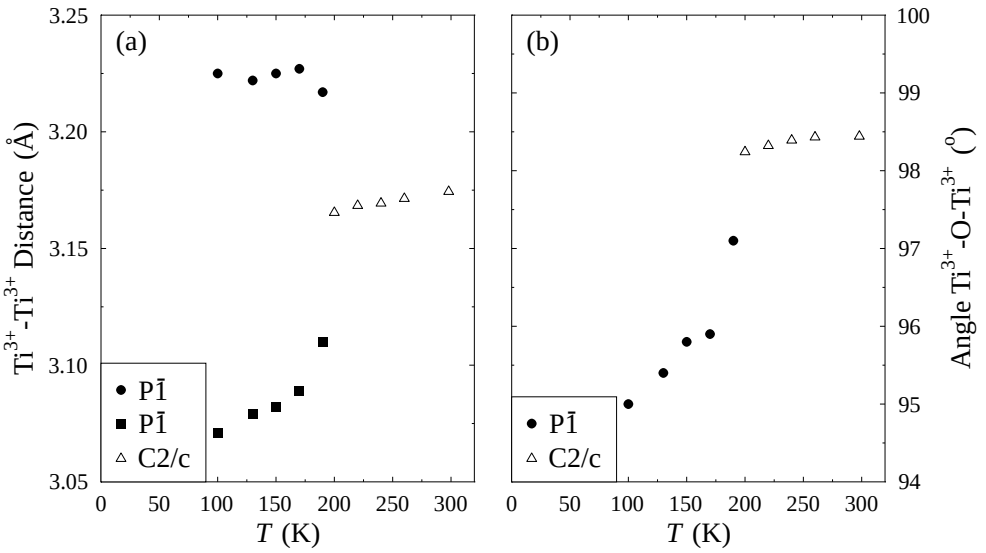

Figure 5.5: Temperature dependence of the Ti^{3+}-Ti^{3+} distance(s) and the angle Ti^{3+}-O-Ti^{3+}. A step change in the distance between Ti^{3+} ions is apparent at the structural transition. Data taken from Redhammer *et al.* [Redh03]

$\delta\,(\propto \Delta l)$ of every other atom along the chain direction, this gives us a structure factor for the $(0, 3, 0)$ reflection of:

$$S_{0,3,0} = f(1 + \exp[-3\pi i(1 + \delta)], \tag{5.9}$$

which we can transform into the measured intensity using $I_{hkl} = |S_{hkl}|^2$. In the limit of small δ, the intensity varies as:

$$I \propto \delta^2. \tag{5.10}$$

Using the above relationship between the degree of dimerization δ and the spin gap Δ (Equation 5.6) we find that:

$$\Delta \propto I^{1/3}. \tag{5.11}$$

This gives the normalized gap value $\Delta(T)/\Delta(0)$ shown in Figure 5.7. Since deriving this model for the case of TiOCl, I discovered that a similar model had been applied to the case of $CuGeO_3$ by Harris *et al.* [Harr94]. By direct measurement of

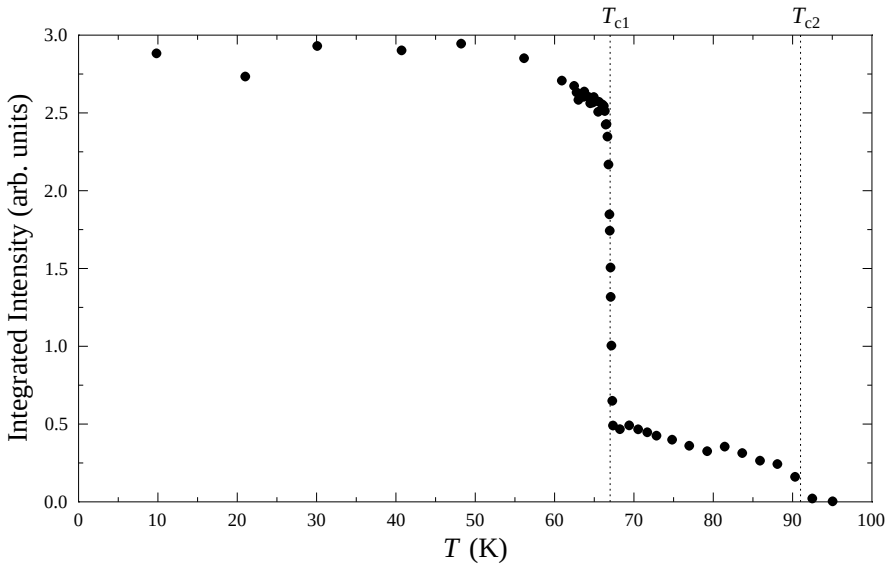

Figure 5.6: Integrated intensity of the superstructure reflection around (0,1.5,0) as a function of temperature. This covers the $(0,1.5,0)$ reflection observed in the commensurate phase, $T < T_{c1}$ and the $(\pm\delta,2-\epsilon,0)$ reflection observed for $T > T_{c1}$. Figure after Ref. [Krim06]. The data were provided by Dr M. Hoinkis.

the lattice constants and also the superlattice reflection they were able to demonstrate the validity of Equation 5.10 for the proportionality between the change in the lattice constant and the intensity of the superstructure reflection, and went on to show that the energy gap followed Equation 5.11. The situation in TiOCl is somewhat more complex, but nevertheless, the agreement with experimental data previously demonstrated for $CuGeO_3$ is encouraging. However, very recent results [Hara07] on lightly Cd-doped $CuGeO_3$ cast some doubt on the conclusions of Harris *et al.*'s study. Specifically, Equation 5.11 was found not to hold, with a non-zero spin gap at T_{SP}. Further investigation will be necessary to establish whether Cd doping has an unusual effect, or whether $CuGeO_3$ is exceptional, or whether the model of Cross and Fisher is not applicable to these systems.

5.3 Magnetic measurements

Magnetic measurements were made on both compounds using the Reciprocating Sample Option of the SQUID magnetometer as described in section 2.3.1. This

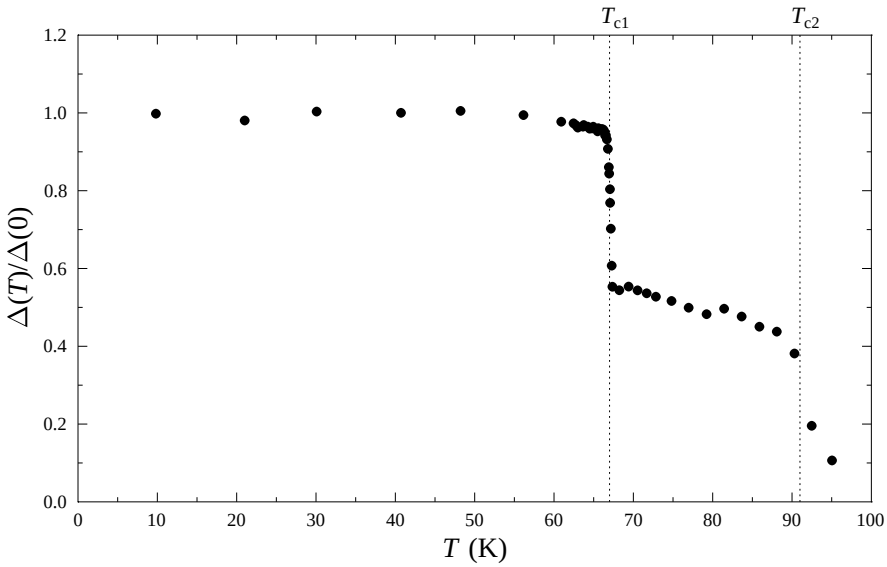

Figure 5.7: Normalized value of the spin gap $\Delta(T)/\Delta(0)$ predicted using Equations 5.9 - 5.11 and the intensity of the $(0, 1.5, 0)$ superstructure reflection reported by Krimmel *et al.* [Krim06] and shown in Figure 5.6.

section describes the results and analyses the data using the models outlined in section 5.2. In the following discussion the thermally activated contribution to the susceptibility will be taken to be:

$$\chi \propto A \exp(-2\Delta/T) \tag{5.12}$$

In order to extract this part of the susceptibility the contribution due to free spins (including impurities) needs to be subtracted. This takes the form of Curie's law $\chi = C/T$. We take the free spins to be spin-1/2, since the Ti^{3+} ions in the chain have that spin, although this may not be a perfect description if the oxidation state of Ti ions near impurities or chain breaks is affected, but it is sufficient to give a simple estimate of the concentration of free spins. Another contribution to the measured susceptibility is the combination of Van Vleck paramagnetism and diamagnetism arising from the sample, χ_0. These give a temperature independent contribution which can be easily subtracted during fitting. The full form fitted to the experimental data was:

$$\chi = A \exp(-2\Delta/k_{\mathrm{B}}T) + \chi_0 + C/T, \tag{5.13}$$

where Δ had the temperature dependence for each compound discussed above in section 5.2. The results of measurements on $NaTiSi_2O_6$ and TiOCl are presented in sections 5.3.1 and 5.3.2 respectively.

5.3.1 Magnetic measurements on $NaTiSi_2O_6$

Isobe *et al.* [Isob02] measured the magnetic susceptibility of $NaTiSi_2O_6$ and found that at high temperature it was well described by a Bonner-Fisher curve [Bonn64], as would be expected for a quasi-one-dimensional chain compound. At a temperature of around 250 K the susceptibility reduces below that expected from the Bonner-Fisher curve and a knee is observed at $T_{OO} = 210$ K. Below T_{OO} the susceptibility is thermally activated and fitting the low-temperature data gave an activation energy of approximately 500 K. The concentration of free spins was found to be < 0.5 %. Our susceptibility measurements were carried out to check that our sample from the μSR experiments detailed below was as synthesized, and to provide data to test models of the susceptibility.

The magnetization of a polycrystalline sample of mass 30 mg was measured in a field of 0.1 T from 2 to 350 K. The results are presented in the form $\chi = M/H$ in Figure 5.8, with the Curie tail subtracted for clarity.

The Curie tail subtracted from original data gave a value for the unpaired spin concentration of 2.10(4) %, somewhat higher than for the sample of Isobe *et al.* [Isob02]. The temperature-independent contribution to the susceptibility was found to be $\chi_0 = 1.21(1) \times 10^{-9}$ m^3 mol^{-1}, consistent with previous data [Isob02]. Taking the spin gap to be independent of temperature proved to be a satisfactory description of the data below 200 K, and fitting the data below this temperature led to a value for the spin gap of $2\Delta = 595(7)$ K. Attempting to fit the data with a mean-field model, as would be expected for a spin-Peierls transition, gave a poorer fit to the data as the maximum temperature in the fitting range tended towards T_{OO}. While the simple model for the thermal activation encapsulated in Equation 5.12 should break down when the temperature approaches the energy scale of the spin gap, the step-like jump in the structural parameters at T_{OO}, shown in Figure 5.5, provides much stronger evidence, compared with the form of the magnetic susceptibility, that this system is not behaving as a canonical spin-Peierls material.

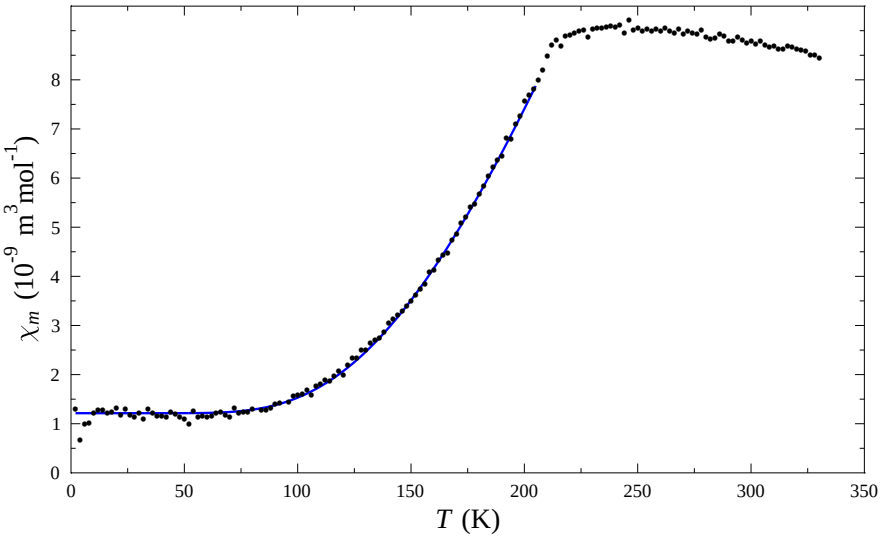

Figure 5.8: The magnetic susceptibility of $NaTiSi_2O_6$ after the subtraction of the Curie law contribution from impurities, as described in the text. The data were fitted according to Equation 5.13, leading to a spin gap $2\Delta = 595(7)$ K, $\chi_0 = 1.21(1) \times 10^{-9}$ m^3 mol^{-1}, and a concentration of unpaired spins $n = 2.10(4)$ %.

5.3.2 Magnetic measurements on TiOCl

The magnetic susceptibility of TiOCl has previously been reported by several authors [Beyn93, Seid03, Kata03, Rück05]. Excepting the first of these reports, the results are in good agreement. At temperatures above 130 K the susceptibility follows a Bonner-Fisher curve [Bonn64], with $J = 660$ K. Features are observed at around $T^* \sim 130$ K and $T_{c2} = 91$ K, followed by a sharp drop at $T_{c1} = 67$ K [Seid03, Kata03, Rück05]. Below T_{c1}, the susceptibility is dominated by the Curie tail and the temperature-independent susceptibility.

Our measurements were made after the μSR experiments described in section 5.4.2 to check that the sample had not degraded. The sample had the same magnetic susceptibility, within the experimental resolution, as it had been when synthesized, so significant degradation was excluded. The sample used was 20 mg of a polycrystalline powder, for which the magnetization was measured as a function of temperature between 2 and 350 K, in a field of 0.1 T. The zero-field cooled RSO measurements presented, after the subtraction of the Curie tail, as $\chi = M/H$ values in Figure 5.9, were repeated both in field cooled RSO measurements and ac

susceptibility measurements cooling in zero field. These measurements were all in good agreement, except that the error bars on the ac susceptibility measurements were far larger, because the small drive field leads to a weak signal.

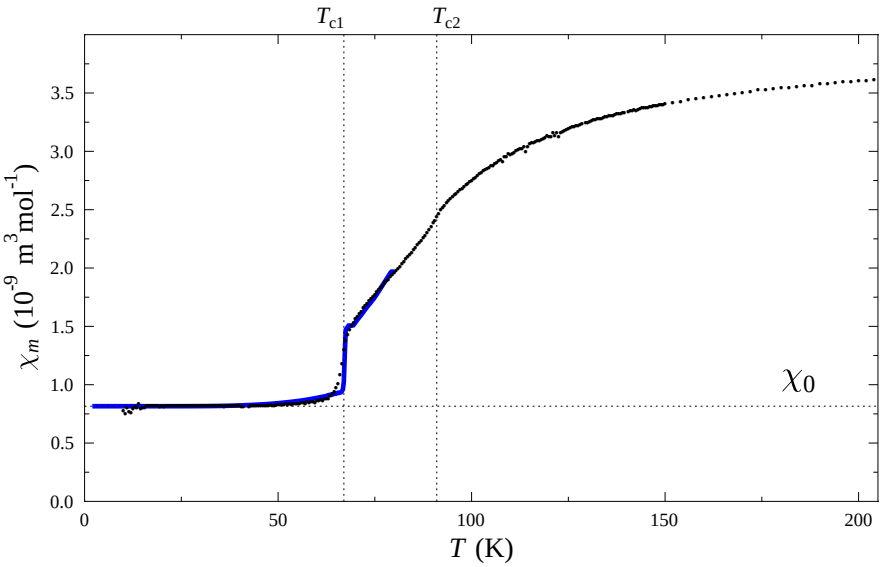

Figure 5.9: The magnetic susceptibility of TiOCl after the subtraction of the Curie law contribution from impurities, as described in the text. The data were fitted according to Equation 5.13 up to 80 K where this model should break down, leading to a spin gap $2\Delta = 270(10)$ K, $\chi_0 = 0.82(1) \times 10^{-9}$ m^3 mol^{-1}, and a concentration of unpaired spins $n = 0.6(1)$ %.

From fits of the experimental data below 80 K, where Equation 5.13 remains valid, the Curie tail was found to correspond to a concentration of unpaired spins $n = 0.6(1)$ %. The temperature independent susceptibility was found to be $\chi_0 = 0.82(1) \times 10^{-9}$ m^3 mol^{-1}. In order to find the magnitude of the spin gap the model described in section 5.2 was used. It is this part of Equation 5.13 which breaks down at around 80 K, because the spin gap ceases to be large compared to the temperature above this temperature [Cros79], hence limiting the range over which Equation 5.13 can be fitted to the data. Fitting the data below 80 K leads to a value of the spin gap at zero temperature of 270(10) K. This model is successful in describing the jump in the magnetic susceptibility at T_{c1}, and the gradient of the susceptibility just above that transition. The fit to the data is shown in Figure 5.9.

5.4 μSR measurements

μSR measurements offer a means of measuring the magnitude of the spin gap in these materials with a microscopic probe, and since no such data had been published on these compounds we were motivated to carry out μSR experiments. The measurements were carried out using two forms of the μSR technique, both described in section 2.2.

Firstly, the form of the relaxation in zero magnetic field (ZF), was measured as a function of temperature from $\sim$ 10 to 340 K. For both compounds the relaxation was well expressed as the product of nuclear moment and electronic moment contributions, as had previously been found to be the case in $MEM(TCNQ)_2$ by Lovett *et al.* [Love00]. In both compounds the nuclear contribution was found to be temperature independent, allowing the thermal activation of the electronic component to be followed as a function of temperature. It must be noted here, however, that the form of the electronic relaxation was different in the two compounds, and this will be discussed in sections 5.4.1 and 5.4.2 below.

We can draw an analogy between NMR measurements and μSR ones in order to determine the spin gap from the thermal activation of the zero-field muon relaxation rate [Love00]. At low temperature, that is below the onset of dimerization, one possible relaxation mechanism is via thermally activated electronic spins fluctuating across the spin gap [Fuda99]. Since we have, in the paramagnetic case, a muon relaxation rate due to electronic spin fluctuations varying as the inverse of the fluctuation rate, $\lambda \propto 1/\nu$, λ increases with decreasing temperature as the electronic fluctuations slow due to the spin gap. For comparison [Ehre77], the nuclear spin flip observed by NMR is accompanied by the scattering of three excitons. Ehrenfreund and Smith [Ehre77] showed that the nuclear relaxation rate T_1^{-1} was of the form:

$$T_1^{-1} \propto \Delta^{-2} D^2(\Delta) D(2\Delta) e^{-2\Delta/k_B T}, \tag{5.14}$$

where Δ is the spin gap and $D(\epsilon)$ is the density of states as a function of the excitation energy ϵ. From this we see that the activation energy is actually 2Δ. It is apparent that for both compounds a second, temperature-independent, relaxation process dominates at low temperatures. This is seen as the saturation of the electronic relaxation rate at low temperature. Considering an electronic relaxation

rate λ, under the assumption that the distribution of local fields is independent of temperature in the range considered, we can parametrize the temperature dependence using the equation:

$$\lambda(T) = \lambda_0/[1 + A\exp(-2\Delta/T)], \tag{5.15}$$

where A is a constant, λ_0 is the low-temperature relaxation rate, and Δ takes the form described in section 5.2. Since the form of the electronic relaxation is different in the two compounds we use the symbols λ for $NaTiSi_2O_6$ and Λ for TiOCl, solely for differentiating between the two forms of the relaxation.

The second type of measurement carried out used a small magnetic field applied along the axis of the initial muon spin polarization (LF measurements described in section 2.2). The purpose of these measurements was to determine the concentration of unpaired spins in the materials by an alternative means, or alternatively, to check that our model for the electronic depolarization of the muon spin was realistic, since the magnetic susceptibility measurements described in section 5.3 can determine the concentration of unpaired spins far more precisely. We follow the method of Lovett *et al.* [Love00], and assume that the unpaired spins are $S = 1/2$, given the spin of the Ti^{3+} ions, although a defect in a chain would produce two free spins and any impurity creating the defect may itself have a spin, so our value is likely to be an overestimate of the true concentration of defects and impurities. The asymmetry spectra were fitted using the product of a longitudinal field Lorentzian Kubo-Toyabe function [Uemu85]:

$$\begin{aligned} P_z(t, a, B_\mathrm{L}) = 1 \quad &- \quad \frac{a}{\gamma_\mu B_\mathrm{L}} j_1(\gamma_\mu B_\mathrm{L} t)\exp(-at) - \left(\frac{a}{\gamma_\mu B_\mathrm{L}}\right)^2 [j_0(\gamma_\mu B_\mathrm{L} t)\exp(-at) - 1] \\ &- \quad [1 + \left(\frac{a}{\gamma_\mu B_\mathrm{L}}\right)^2] a \int_0^t j_0(\gamma_\mu B_\mathrm{L}\tau)\exp(-a\tau)d\tau, \end{aligned} \tag{5.16}$$

and an exponential function to account for the weak dynamics. In equation 5.16, j_0 and j_1 are spherical Bessel functions and B_L is the flux density of the applied field. We can then follow after Lovett *et al.* in using the expression derived for NMR data by Walstedt and Walker [Wals74] to estimate the concentration of unpaired spins, n [Love00]. Taking the field width in the longitudinal field

Kubo-Toyabe function to be a, we have:

$$a = \frac{2\pi\mu_0\mu_B g_\mu g_d S_d m_e n}{9\sqrt{3}m_\mu\hbar}. \tag{5.17}$$

For simplicity, we take the dimensionless magnetic moments of both the defect and the muon to be $g_d = g_\mu = 2$, and take the spin of the defect $S_d = 1/2$. This approach is consistent with that used in the magnetic measurements described above (Section 5.3).

Having described the common elements of the μSR measurements on these two compounds I will describe the specifics of each case, firstly for $NaTiSi_2O_6$ in section 5.4.1 and then for TiOCl in section 5.4.2.

5.4.1 μSR measurements on $NaTiSi_2O_6$

μSR measurements on $NaTiSi_2O_6$ were carried out using the MuSR and ARGUS spectrometers at the ISIS pulsed muon facility. The samples were polycrystalline powders of mass ~ 0.2 g, placed inside silver foil packets greased to the cold finger of the spectrometer cryostat. This gives a weak background relaxation which was subtracted in the data analysis (Section 2.2).

Zero field measurements were made at temperatures between 15 and 340 K using the MuSR spectrometer at ISIS. The raw data are presented in Figure 5.10, with fits to the functional form:

$$A(t) = A(0)\exp[-(\sigma t)^2]\exp(-\lambda t) + A_{BG}, \tag{5.18}$$

which describes the data successfully over the whole of the measured temperature range. The Gaussian term describes the muon relaxation due to fluctuating nuclear moments and fitting this as a free parameter over the whole temperature range showed that the rate could be fixed as $\sigma = 0.06$ MHz. The exponential relaxation is due to the fluctuating electronic moments, and this is thermally activated according to Equation 5.15. Neither the initial or background asymmetry varies with temperature, which, combined with the lack of coherent muon precession, is strong evidence excluding the presence of long range magnetic order in this compound.

As can be seen in Figure 5.11, λ is essentially independent of temperature below 100 K and then falls as the temperature increases. There is no major

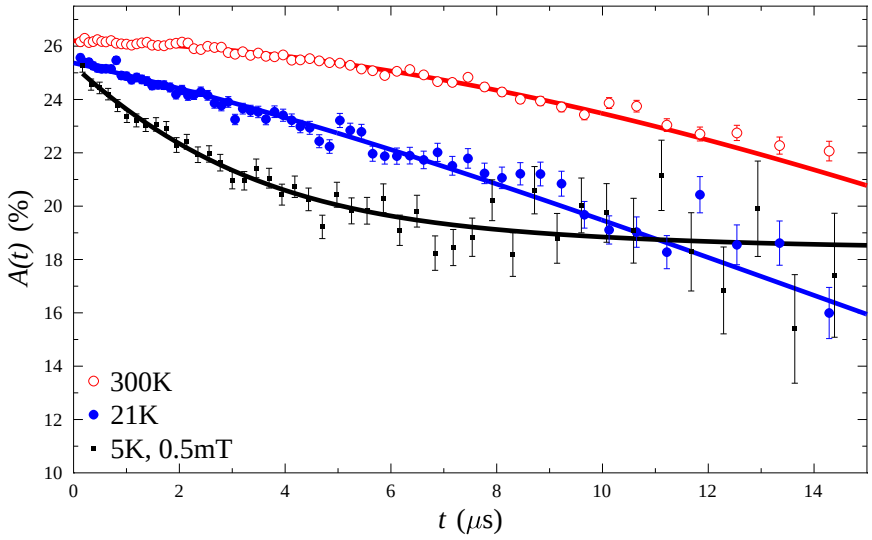

Figure 5.10: Examples of muon decay asymmetry data in $NaTiSi_2O_6$. The zero field data shown for 300 and 21 K is fitted according to Equation 5.18 and the longitudinal field data is fitted to the product of Equation 5.16 and an exponential relaxation, as described in the text.

change in either λ or σ at T_{OO}, which suggests that the size of the local field at the muon site does not change dramatically at this temperature, as it should do if a composite Haldane chain formed at the structural transition [Popo04]. The smooth variation of λ through T_{OO} may be due to the effects of short range correlations enhancing spin-singlet fluctuations near the transition. Fitting the λ values for $T < T_{OO}$ leads to a value for the spin gap of $2\Delta = 700 \pm 100$ K.

Longitudinal field measurements were made on the same sample used for the zero field measurements using the ARGUS spectrometer at the RIKEN-RAL pulsed muon facility. The concentration of unpaired spins at low temperature was extracted following the method described above in section 5.4. Data were collected at 5 K in an applied field of $B_L = 0.5$ mT, shown in Figure 5.10, and were fitted to obtain a field width $a = 0.14(6)$ MHz, which leads, with application of Equation 5.17, to a concentration of unpaired spins $n = 1.7(3)$ %. Data collected in larger fields, $B_L \geq 5$ mT, were found to have a similar field width but significantly larger errors in the fitted parameters, and were therefore less suitable for extraction of the concentration of unpaired spins.

For $NaTiSi_2O_6$ we are able to parametrize the data from both techniques us-

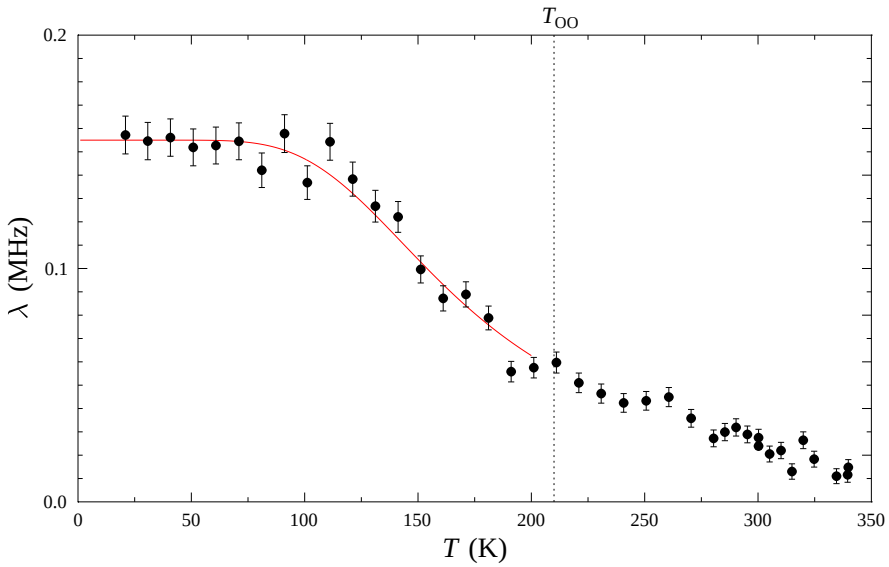

Figure 5.11: Electronic relaxation rate λ in $NaTiSi_2O_6$, extracted from the raw data using Equation 5.18. The red line is a fit to Equation 5.15 and leads to $2\Delta = 700(100)$ K.

ing the assumption of constant dimerization. The two techniques agree reasonably well in the value of the spin gap, $2\Delta = 700(100)$ K, and we can compare this to the transition temperature of $T_{OO} = 210$ K using the mean-field result [Bray75]. We find that the value of the gap fits the mean-field relation very well, consistent with the dimerization being driven by a spin-Peierls mechanism. However, the predicted gap value for an orbital-Peierls transition ($\Delta \sim J$) [Stre06] is also in excellent agreement with our value, as are the predictions of Hikihara and Motome [Hiki04]. From the magnitude of the spin gap we cannot distinguish between the two possible mechanisms for the transition in this material. That there is no significant change in the relaxation rate at T_{OO} is unlikely to be compatible with the formation of Haldane chains at this temperature, since the field at the muon site should change significantly, changing the relaxation rate. Measurements of the orbital occupation will be necessary to make a decisive conclusion as to the mechanism.

5.4.2 μSR measurements on TiOCl

All the μSR measurements on TiOCl were made using the MuSR spectrometer at the ISIS pulsed muon facility (Section 2.2). As for $NaTiSi_2O_6$, the polycrystalline sample of mass ~ 0.2 g was enclosed in a silver packet, as quickly as possible to avoid excess contact with air, and attached to the cold finger of a CCR. Measurements were made in zero field at temperatures between 20 and 340 K.

The temperature range between 30 K and 100 K was measured three times in zero field to provide sufficient data points in the thermally activated region. Each time this was done cooling in zero field. The results were consistent with one another. Representative data sets from low and high temperature measurements are shown in Figure 5.12. The thermal activation is clearly apparent with a significantly larger relaxation rate in the low temperature data set. In zero field we can parametrize the muon relaxation in terms of a product function representing nuclear and electronic contributions to the relaxation. Initially the function, Equation 5.18, used for the $NaTiSi_2O_6$ data were used, but it was clear that this described the low temperature data poorly. High temperature data were dominated by the Gaussian relaxation from the nuclear moments, so a temperature independent Gaussian relaxation of $\sigma = 0.08$ MHz, found at high temperature, was assumed. Preliminary fitting with Equation 5.19 showed that it is difficult to fit this satisfactorily at low temperatures, since the electronic relaxation rate becomes very large compared to that from the nuclear fluctuations. No change in the value obtained from the fitting was observed, but the error in σ becomes significant below T_{c1} for this reason, probably because the electronic relaxation rises so significantly, as can be seen in Figure 5.13. In order to obtain a satisfactory fit to the low temperature data a different form, compared to $NaTiSi_2O_6$, was used after preliminary analysis showed that it was providing significantly improved fits to the data below T_{c1}. The most consistent means of fitting the data used a square root exponential, as would be expected for a dilute distribution of electronic spins [Uemu85]. The product of these Gaussian and square-root exponential functions gives:

$$A(t) = A(0)\exp[-(\sigma t)^2]\exp(-\sqrt{\Lambda t}) + A_{\mathrm{BG}}, \tag{5.19}$$

which was used to fit the TiOCl across the entire temperature range.

The results from fitting Equation 5.19 to the measured asymmetry data are

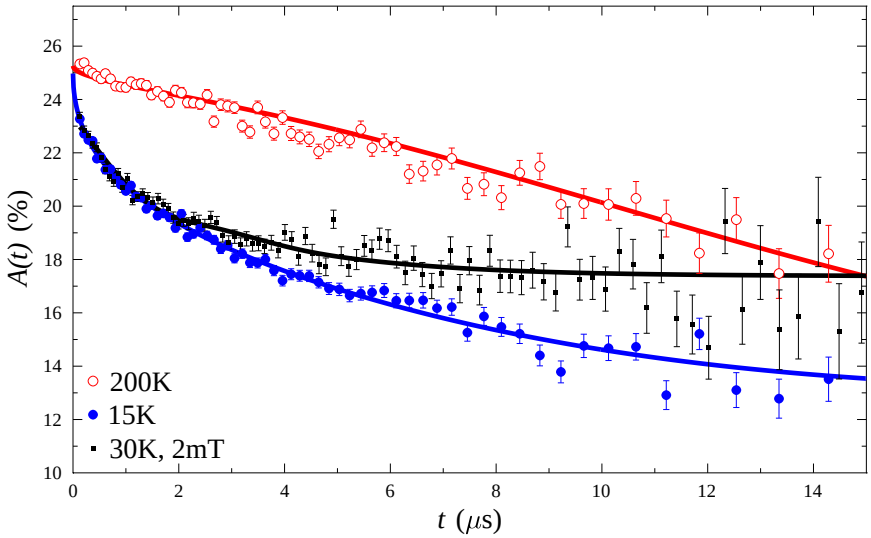

Figure 5.12: Examples of muon decay asymmetry data in TiOCl. The zero field data shown at 200 and 15 K is fitted according to Equation 5.19 and the longitudinal field data is fitted to the product of Equation 5.16 and an exponential relaxation, as described in the text.

presented in Figure 5.13. At high temperature the relaxation rate is constant and small. No significant features are observed at either T^* or T_{c2}, which is perhaps surprising given the clear evidence for these transitions in NMR data [Imai03]. Below T_{c2} the relaxation rate rises slowly with decreasing temperature, until at T_{c1} it rises sharply, tending to a constant value below ~ 30 K. The sharp rise below T_{c1} fits with the model (Equation 5.15) used to analyse the relaxation rate data in $NaTiSi_2O_6$. A temperature-independent slow fluctuation dominates the low temperature data, before thermally activated fluctuations become dominant at intermediate temperature, until the dimerization transition is reached and we see the paramagnetic fluctuations dominating the signal. In TiOCl, we use the form derived in section 5.2 for the gap, as was compared with the magnetic susceptibility data in section 5.3.2. This model has a smaller domain of validity for the μSR data, as can be seen from the fitted line plotted in Figure 5.13. While successful below T_{c1}, there is no step observed in the data at T_{c1}, which this model predicts.

The concentration of unpaired spins at low temperature was extracted following the method described above in section 5.4. Data were collected in an applied field of $B_L = 2$ mT, shown in Figure 5.12, and was fitted to obtain a field width

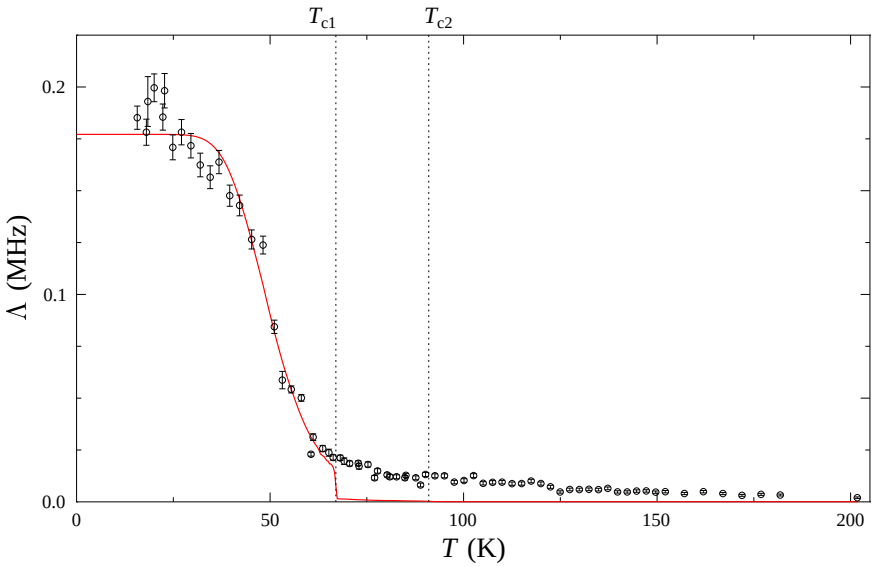

Figure 5.13: Electronic relaxation rate Λ in TiOCl, extracted from the raw data using Equation 5.19. The red line is a fit to Equation 5.15 below T_{c1} and leads to $2\Delta = 440(60)$ K. It must be noted that the temperature dependence of the gap shown in Figure 5.7 does not describe the data correctly above T_{c1}, as discussed in the text.

$a = 0.41(4)$ MHz, which leads, with application of Equation 5.17 to a concentration of unpaired spins $n = 1.1(2)$ %. Data collected in larger fields, $B_{\mathrm{L}} \leq 5$ mT, were found to have a similar field width but marginally larger errors in the fitted parameters, and were therefore less suitable for extraction of the concentration of unpaired spins. The field width was found to be essentially constant below T_{c1}, and then dropped sharply above T_{c1}, below the limit where the value of a (see Equation 5.17) could be reliably extracted.

For TiOCl, our model based on the measured dimerization gives a consistent description of the form of both data sets. The μSR measurements show a sharp, thermally activated increase in the muon relaxation rate below $T_{c1} = 67$ K. Fitting the data below T_{c1} leads to a value of the spin gap of $2\Delta = 440(60)$ K. We also attempted a different parametrization for the data which assumes the spin fluctuations are fast compared with the distribution of magnetic fields, as is the case in $NaTiSi_2O_6$. Fitting Equation 5.18 to the asymmetry data, and the λ values to a simple activation, $\lambda \propto \exp(2\Delta/T)$, leads to $2\Delta = 420(40)$ K. However, Equation 5.18 fails to describe the raw data at temperatures lower than 10 K below

T_{c1}, so this method is less satisfactory for measuring the spin gap. The method only works over such a limited range because of the large gap relative to T_{c1} and the width of the magnetic field distribution. Above T_{c1} other spin fluctuation processes come into play on the μSR timescale, and since there is negligible variation in the μSR relaxation rate, we can no longer compare it to the model. It must be noted that the model based on the structural dimerization only fits the μSR data in the temperature region where the dimerization is constant. There are two obvious possibilities for this discrepancy. There is a decrease in the width of the field distribution at T_{c1}, evident in the longitudinal field measurements, which would change the relation between Λ and the fluctuation rate, or it may be that a separate energy scale which is independent of temperature below T_{c1} is relevant, but only affects the muon depolarization once the dimerization is complete and structural fluctuations lose their importance.

By comparison, fitting the magnetic susceptibility data is much more successful just above T_{c1}; we can describe the jump in the susceptibility at the transition and also the behaviour up to 80 K, where the magnitude of the spin gap becomes comparable to the temperature. The gap 2Δ measured by μSR agrees with those measured using other techniques [Imai03, Lemm04, Caim04] and, via naive application of the mean-field theory of the SP transition, corresponds to $T_{\mathrm{SP}} = 2\Delta/3.53 = 125(10)$ K. Intriguingly, this estimate of T_{SP} is close to the temperature where pseudogap formation has been proposed [Imai03, Lemm04, Caim04]. A similar application of the mean-field theory to our value of 2Δ obtained from susceptibility yields $T_{\mathrm{SP}} \approx 75$ K which lies between T_{c1} and T_{c2}. These results may suggest different energy scales associated with the pseudogap and the dimerization, illustrating the complex nature of TiOCl. Further investigation of this system, using other techniques, may illuminate this issue.

5.5 Conclusion

In conclusion, a consistent means of describing both magnetic susceptibility and μSR measurements on spin gapped systems in terms of the dimerization has been presented. Using both these techniques, we have obtained values for the spin gaps in both $NaTiSi_2O_6$ and TiOCl, as well as determining the concentration of unpaired spins in each material. Our results are summarized in Table 5.1. We see that both techniques give consistent results for the concentration of un-

Table 5.1: Parameters derived from μSR and magnetic susceptibility data, χ. The spin gap, 2Δ, the concentration of unpaired spins, n, and $T_{\rm mf} = 2\Delta/3.53$, the temperature at which mean-field theory estimates that the SP transition should occur, given the value of 2Δ.

Parameter	Technique	$NaTiSi_2O_6$	TiOCl
2Δ (K)	μSR	700(100)	440(60)
2Δ (K)	χ	595(7)	270(10)
n (%)	μSR	1.7(3)	1.1(2)
n (%)	χ	2.10(4)	0.6(1)
$T_{\rm mf}$ (K)	μSR	200(25)	125(10)
$T_{\rm mf}$ (K)	χ	168(5)	76(3)

paired spins, supporting our model for the muon depolarization. The values of the spin gaps are not in such good agreement, with the μSR values being a little larger than those from the susceptibility measurements, perhaps because the muon data may include the effect of some other relaxation process not accounted for in Equation 5.15, or the magnetic susceptibility model does not include the effect of fluctuations. For $NaTiSi_2O_6$ the disagreement in the value of the spin gap between the two techniques is within the statistical error, and so the results must be considered consistent with one another. The disagreement in TiOCl is far larger than the statistical errors and is likely to be significant, possibly due to separate energy scales for the structural dimerization and the pseudogap formation. Our measurements also demonstrate the complementary information that can be discovered about spin-gapped materials by investigating both their microscopic and bulk properties.

Looking forward, there remains much to be explained in the physics of Ti chain compounds. While the experimental investigations of $NaTiSi_2O_6$ have proved consistent with interpretation in terms of an orbitally assisted Peierls transition, examples of this behaviour are rare, and finding further systems that display it will add significantly to the understanding of this mechanism. In terms of μSR experiments, a detailed study of $MgTi_2O_4$ is called for. This was attempted at ISIS in late 2006, but problems with the proton beam prevented a full experiment being carried out. The results suggested that a complete study could be carried out at ISIS in future and would provide a similar amount of information to the cases considered above. One of the ways the spin-Peierls transition has been approached

in inorganic compounds such as $CuGeO_3$ has been through doping the chains with non-magnetic ions, Zn, and doping the side chains with Si. An example of this form of investigation was presented by Kojima *et al.* [Koji97]. Taking a similar approach to compounds showing orbital assisted Peierls transitions has yet to be attempted. This might provide interesting insights into the mechanism of the transition and produce novel magnetic phases.

TiOCl remains somewhat enigmatic. Inelastic neutron scattering experiments might be able to shine considerable light on the excitation spectrum and clear up the discrepancy between the energy scales found in this work, and also clarify the origin of the structural excitations observed by Clancy *et al.* [Clan07]. The effect of cation substitution, Sc, V, on TiOCl has already been considered [Beyn93, Seid03], and μSR work is likely to show interesting results. Given the similarity between the structure of TiOCl and high-temperature superconductors such as those described in Chapter 6, interest has been expressed in charge doping the TiO layers with alkaline metals and also in intercalation. Both of these avenues may lead to new and interesting physical properties in systems closely related to TiOCl.

Chapter 6

Effect of tuning the interlayer spacing of high-T_C superconductors

Contents

6.1 Introduction

Since their discovery in 1986 [Bedn86], the high temperature superconductors based on copper oxide layers have been the subject of considerable work in both experimental and theoretical condensed matter physics, solid state chemistry, and materials science [Pool00]. The structure of such a material is shown in Figure 6.1 (Left). Despite the huge amount of work on the subject, there remain many theoretical questions concerning the mechanism underlying the superconductivity in these materials [Legg06, Zaan06]. To investigate these questions, many approaches have been attempted. The dome-like dependence of the superconducting critical temperature T_c on the doping was identified at an early stage [Pres91]. At some critical doping, $p \sim 0.05$ holes per Cu, superconductivity develops from an insulating state. With increasing doping T_c rises in the underdoped regime, and peaks at the optimal doping, $p_{\rm opt} = 0.16$ holes per Cu. Further increasing the doping reduces T_c in the overdoped regime until at $p \sim 0.27$ holes per Cu, the material enters a metallic phase without superconductivity. The schematic phase diagram of a hole-doped cuprate material is shown in Figure 6.1 (Right). As well as the superconducting phase, antiferromagnetism is observed at small dopings up to high-temperature. This may also coexist with the superconducting phase at intermediate doping [Brew88, Weid89, Sann04, Savi05]. At temperatures above T_c, underdoped materials exhibit what is referred to as 'pseudogap' behaviour, as if the superconducting state is present, but has not gained phase coherence [Xu00]. Isotope effects [Khas04], pressure dependence (both hydrostatic and chemical) [Schi92, Gao94], and the number of CuO_2 layers in each superconducting block [Scot94] have also been shown to be key in determining T_c. Another means of looking for trends common to groups of compounds, or separating them, is to find scaling relations between experimental parameters [Binn92]. This is useful in cases where theoretical models can find the dependence of one parameter on another, but not their absolute magnitude. A recent example of this is the Homes scaling between the bulk superfluid density of a superconductor and the product of T_c and the dc conductivity at T_c [Home04]. A number of possible origins for this scaling relation have been proposed [Home04, Tall06], but it breaks down severely in overdoped cuprates [Tall06] and does not apply to molecular superconductors [Prat05]. Such scaling relations will be discussed in more detail in section 6.4.

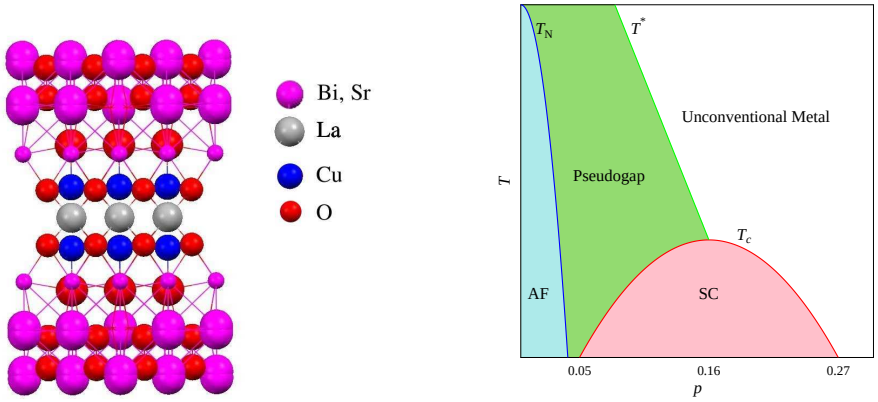

Figure 6.1: (Left) Structure of Bi2212 showing the double copper-oxygen layers separated by a Ca layer. The structural parameters used for this diagram come from Ref. [Mich94]. (Right) Schematic version of the notional phase diagram of hole-doped cuprate superconductors. The phases marked SC and AF are superconducting and antiferromagnetic respectively.

Cuprate superconductors[1] are notable for having a highly anisotropic structure with CuO_2 planes bounded by charge reservoirs such as Sr-O, and intermediate layers that separate the superconducting blocks. This is shown in Figure 6.1 (Left), using Bi2212 (notionally $Bi_2Sr_2CaCu_2O_8$) as an example. The CuO_2 planes are the key locus of superconductivity [Legg06], and it is natural to consider how the superconducting properties depend on the properties of the layers themselves [Emer95, Casa02] and the coupling between them [Whea88, Legg96, Ande98]. To investigate this it is desirable to change the separation between the CuO_2 planes in a controlled manner and measure the superconducting properties. The majority of high-T_c materials have an average CuO_2 layer spacing of 6 ± 1 Å and there are few examples where the layer spacing is significantly outside this range [Uemu97, Pool00]. We must therefore seek ways of changing the layer spacing in a controlled manner. One method of changing the layer spacing is to make multilayers of a superconducting material interspersed by

[1]Hereafter, cuprate superconductors will be referred to by abbreviated forms of their chemical formulae. Two forms are in common use, and are more convenient for different families of cuprates. 1) The form X1234, where X is the first element in the chemical formula, and the numbers are the numbers of each element in the chemical formula, excluding oxygen. The number of Cu ions is the final number, which normally equates to the number of CuO_2 planes in each block, except for compounds where there are also CuO chains. 2) The form ABCD, where each letter is the first letter of the elemental symbols in the chemical formula.

its non-superconducting analogue [Tris90]. This is effective in changing the layer spacing and can be a well controlled process, but the coupling between the superconducting and non-superconducting layers distorts the superconducting layers from their pristine structure, complicating the effect of the increased layer spacing. An alternative method was found for Bi based cuprate superconductors in the 1990's, exploiting the fact that neighbouring Bi-O layers can be used as cleavage planes [Xian90, Choy94, Choy98]. Using chemical intercalation it was found that the average spacing between CuO_2 planes could be increased by a factor of up to three [Choy98]. This process will be described in more detail in section 6.2, since these samples form the basis of this work.

To describe the superconducting properties of a compound we are interested in more than the superconducting critical temperature, T_c. It is also important to consider the length scales relating to superconductivity [Anne04]. The first length scale of interest describes how far the magnetic field penetrates into the superconductor, the London penetration depth,

$$\lambda = \sqrt{\frac{m^*}{\mu_0 n_s e^2}}, \tag{6.1}$$

where m^* is the effective mass of the electrons and n_s is the density of superconducting electrons. Inverting Equation 6.1 shows that if we can measure $1/\lambda^2$ we can deduce the superfluid density n_s/m^*. The second length scale we can consider is the size of the Cooper pairs of superconducting electrons, the Pippard coherence length ξ. Within BCS theory this is simply related to the ratio of the Fermi velocity v_F and the superconducting energy gap Δ as:

$$\xi = \frac{\hbar v_\mathrm{F}}{\pi \Delta}. \tag{6.2}$$

The ratio of these two length scales, $\kappa = \lambda/\xi$, is very informative in categorizing the superconducting phenomena exhibited by a material, because it describes the energetics of magnetic field penetration near the surface of the superconductor. For $\kappa < 1/\sqrt{2}$, we have a Type I superconductor where magnetic field penetration occurs around the edges of the sample, or around domains analogous to those in a magnetic material. For the materials considered in this chapter, the other case, $\kappa > 1/\sqrt{2}$, is of interest. This is referred to as Type II superconductivity. At low fields, $H < H_{c1}$, the material is perfectly diamagnetic, like a Type I

superconductor, but between the lower critical field H_{c1} and the upper critical field H_{c2} it is energetically favourable to allow vortices of magnetic flux to penetrate through the material forming a mixed state. Above H_{c2} the material reenters the normal state. The vortices arrange themselves into a periodic vortex lattice, generally triangular, although square lattices are also observed [Anne04]. We can also relate the length scales to the critical fields of a Type II superconductor as:

$$H_{c1} = \frac{\Phi_0}{4\pi\mu_0\lambda^2}\ln\left(\frac{\lambda}{\xi}\right), \tag{6.3}$$

$$H_{c2} = \frac{\Phi_0}{2\pi\mu_0\xi^2}, \tag{6.4}$$

where Φ_0 is the magnetic flux quantum, and we can consider all the length scales to be functions of temperature [Anne04]. The third length we must consider is the mean free path of electrons in the normal state, l. (In the superconducting state $l \to \infty$.) This is compared to the coherence length ξ. If $l \gg \xi$, the superconductor is considered to be in the clean limit, or if $l \ll \xi$ it is in the dirty limit. The difference between the two cases can influence how we extract the other length scales λ and ξ from experimental data, and this will be discussed below.

μSR has been an effective probe of superconductivity [Soni00], particularly in high-T_c materials, because it offers a direct means of measuring the distribution of magnetic fields in the vortex lattice, which leads to a means of extracting the superfluid density of the material. The details of this will be discussed in section 6.3. Using μSR to measure the superfluid density was exploited by Uemura to define two scaling relations soon after high-T_c materials were discovered. The first of these relates the bulk superfluid density of cuprate superconductors and their critical temperature [Uemu89], and the second relates the critical temperature and the Fermi temperature, which for quasi-2D materials is proportional to the density of electrons in each layer [Uemu91]. Another piece of information that can be extracted from the distribution of fields in the vortex lattice is the different ordered and disordered phases that occur in different temperature and magnetic field regimes. The study of this behaviour in the Bi2212 system using μSR has been particularly extensive [Hars92, Hars93, Lee93, Lee95, Lee97, Aege98, Lee98a], from initial observations that the form of the field distribution changed in different field regimes to characterization of the different ordered and disordered phases as a function of the angle of the applied magnetic field relative to the CuO_2 planes.

The ordering of the vortex lattice can also be investigated using Small Angle Neutron Scattering [Forg90, Cubi93], approaching the problem in reciprocal space rather than real space, and the techniques are complementary.

Relative to Bi2212, Bi2201 has been poorly studied using μSR. Early measurements were made by Weber *et al.* [Webe91], finding a significantly reduced superfluid density compared to the expectation from the Uemura plot [Uemu89]. Further measurements were not reported until Russo *et al.* made a thorough study of a variety of dopings and compared ceramic and single-crystal samples [Russ07]. The later measurements gave superfluid densities much closer to the Uemura trend.

In this chapter I will describe the results of μSR measurements on a series of Bi-based high-T_c superconductors, systematically investigating how the superfluid density changes as a function of the layer spacing and making some initial measurements probing the ordered and disordered regions of the vortex lattice B - T phase diagram. Section 6.2 describes the samples used in these measurements and how they were synthesized. In section 6.3 I describe the experimental methodology and then experiments looking for magnetic order and/or radical states in an intercalated superconductor (section 6.3.1), experiments measuring the superfluid density in polycrystalline samples (section 6.3.2), and measurements on mosaics of intercalated single crystals in section 6.3.3. After reviewing the results of these experiments in section 6.3.4 I move on to discuss these results in relation to literature values by placing them on previously described scaling plots in section 6.4. The information gained from the experiments and how the results fit into current pictures of high-temperature superconductivity are discussed in section 6.5, together with suggestions for further work.

6.2 Intercalated superconductors

Perhaps the most familiar example of intercalation is the occurrence of February 29^{th} in each leap year, intercalation being the addition of an additional day, days, or month into the ordinary or normal year. Chemists have borrowed this term to describe the process of placing guest species into empty lattice sites within a host material [OHar96]. These reactions can be represented as:

$$x\{\text{Guest}\} + \square_x[\text{Host}] \rightleftharpoons \{\text{Guest}\}_x[\text{Host}], \tag{6.5}$$

where □ are empty lattice sites within the host material [OHar96]. The earliest example of intercalation chemistry is probably the production of porcelain in China around 600-700 AD, intercalating alkali metal ions into kaolin, but systematic intercalation was first reported in 1840 with the reaction of sulphuric acid and graphite [OHar96]. Graphite intercalation compounds have remained a primary area of interest within this branch of chemistry, particularly with regard to superconductivity [Hann65, Well05, Kim07].

A wide variety of intercalated superconductors have been synthesized, since the guest species often perturbs the geometry or electronic structure of the host, which can have such effects as disrupting charge density waves or doping the material [OHar96]. The host can be either superconducting or non-superconducting before intercalation. Some examples of intercalated superconductors include:

- Graphite intercalation compounds, firstly with lighter alkali metals in the form C_8A ($A = K, Rb, Cs$) [Hann65], then later with heavy alkaline metals in the form C_6A ($A = Ca, Sr, Yb$) [Well05, Kim07]. ($T_c \lesssim 12$ K).
- TaS_2, $NbSe_2$, NbS_2, $SnSe_2$, intercalated with organic groups such pyridine [OHar96]. ($T_c \lesssim 6$ K).
- $Li_{0.5}ZrSe_2$, $Rb_{0.5}MoS_2$ [OHar96]. ($T_c \lesssim 7$ K)
- Alkali doped fullerides A_3C_{60} ($A = Na, K, Rb, Cs$ and variants) [Heba91, Ross95]. ($T_c \lesssim 45$ K)
- Layered nitrides LiZrNCl [Yama96] and LiHfNCl [Yama98]. ($T_c \lesssim 26$ K)
- Water-intercalated sodium cobaltate $Na_xCoO_2 \cdot yH_2O$ [Taka03]. ($T_c \lesssim 5$ K)

One could also consider molecular superconductors such as BETS and ET salts [Prat05] to be intercalated materials, since the anions lie between layers of the organic molecules.

Since the intercalated superconductors above are all low-temperature superconductors, and the high-temperature superconductors have a layered structure that suggests intercalation might be feasible, the challenge of intercalating a cuprate superconductor was soon pursued. The first success was reported by Xiang *et al.* [Xian90], with the intercalation of iodine into Bi2212. They were able to increase the *c*-axis length by 23 % with iodine layers in between every superconducting block and maintain a critical temperature of $T_c = 80$ K, less than

10 K below the T_c of their pristine Bi2212 starting material. The Bi-Sr-Ca-Cu-O system is particularly suited to intercalation because there is a cleavage plane between double [Bi-O] planes. The next significant increase in the c-axis length in intercalated Bi2212 was achieved by Choy *et al.* [Choy94], with the intercalation of HgI_2. This increases the length of the c-axis by 47 % and again causes only a slight decrease in T_c. The intercalation process is shown schematically in Figure 6.2.

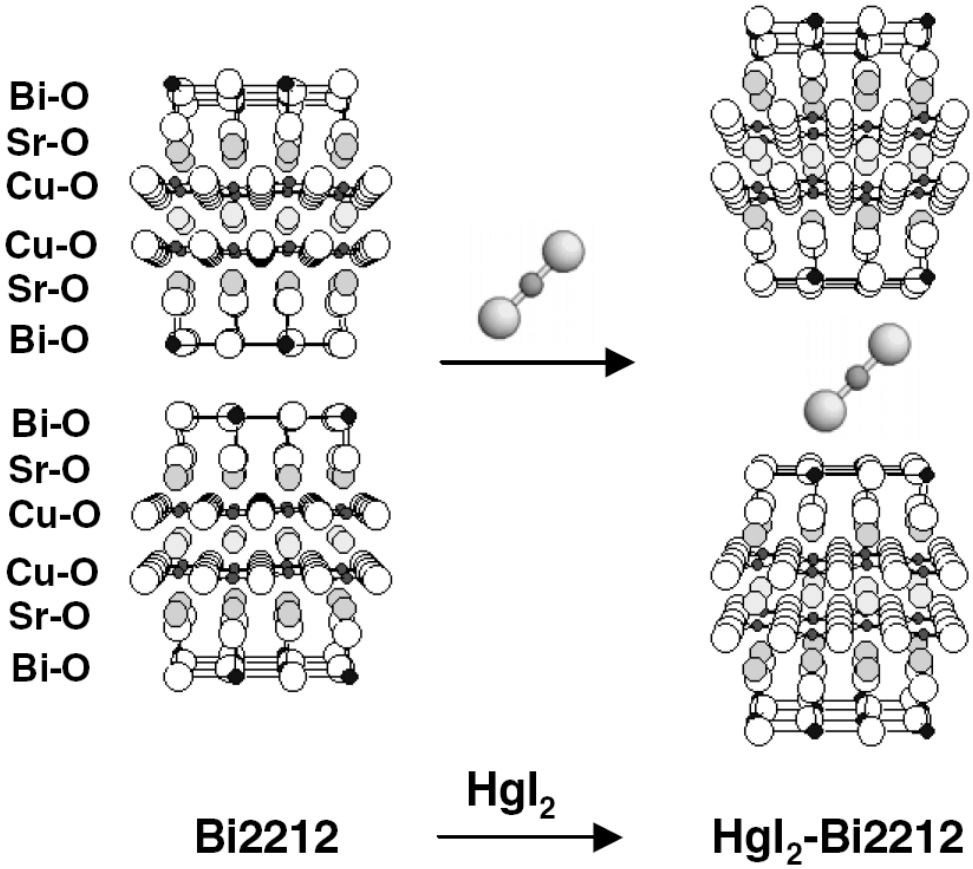

Figure 6.2: Schematic diagram showing the intercalation process described in the text. The Bi-O planes are cleaved and then the intercalant, in this case HgI_2, is inserted between the recombined layers. After Ref. [Kwon05].

To increase the spacing between superconducting blocks further required the intercalation of larger guest species. This was achieved by Choy *et al.* [Choy98] by intercalating organic chains of the form $[(Py - C_nH_{2n+1})_2HgI_4]$ into Bi2212 and Bi2201. Again, the guest species sits between each of the superconducting blocks, inclined at an angle of around 20° to the c-axis, and the average spacing between

CuO_2 planes can be increased by a factor of up to 3. It was shown that despite the dramatic increase in the interlayer spacing, T_c remained essentially constant. Using X-ray diffraction and high-resolution electron microscopy it was shown that the superconducting blocks remained pristine and were regularly spaced. The samples are air-stable.

The starting materials for the synthesis were $Bi_2Sr_{1.6}La_{0.4}CuO_x$ (Bi2201) and $Bi_2Sr_{1.5}Ca_{1.5}Cu_2O_y$ (Bi2212), where the Sr ion is partially substituted by the La ion or Ca ion to obtain single-phase samples. To intercalate the organic chains into these compounds the following synthesis was used [Choy98]. HgI_2 was intercalated into the starting materials by heating them together in a vacuum-sealed Pyrex tube [Choy94]. The intercalation of the organic chains used a solvent-mediated reaction between the HgI_2 intercalates and alkylpyridinium iodide (Py-$C_nH_{2n+1}I$) ($n = 1$ & 8), obtained by reacting alkyliodide with 1 M equivalent of pyridine in diethyl-ether solvent. The HgI_2 intercalates were mixed with two excess reactants of Py-$C_nH_{2n+1}I$, to which a small amount of dried acetone (0.5 ml per 1 g of the mixture) was added. Each solvent-containing mixture was reacted in a closed ampoule at 40° C for 6 hours and washed with a solvent blend of acetone and diethyl-ether (1 : 1 volumetric ratio) to remove the excess reactant of Py-$C_nH_{2n+1}I$. The resulting products were dried in vacuum. Electron probe microanalysis and elemental analysis was used to determine chemical formulae of $[(\text{Py-}C_nH_{2n+1})_2HgI_4]_{0.35}Bi_2Sr_{1.6}La_{0.4}CuO_x$ [(Py-$C_nH_{2n+1})_2HgI_4$-Bi2201] and $[(\text{Py-}C_nH_{2n+1})_2HgI_4]_{0.35}Bi_2Sr_{1.5}Ca_{1.5}Cu_2O_y$ [(Py-$C_nH_{2n+1})_2HgI_4$-Bi2212]. These are identical to the nominal compositions within the experimental error, showing that the host lattice is not chemically modified after the intercalation [Choy98].

Once it had been demonstrated that organic compounds could be intercalated into Bi2212, the next challenge was to intercalate guest species that might have a functional effect on the superconductor. A system where evidence for such an effect has been observed is the compound $[(Me_3S)_2HgI_4]_{0.34}Bi_2Sr_{1.5}Ca_{1.5}Cu_2O_y$ [$(Me_3S)_2HgI_4$-Bi2212] [Kwon02, Kwon04]. Trimethyl-sulfonium iodide, Me_3SI, is a paramagnetic organic radical and from dc magnetic susceptibility and electron paramagnetic resonance measurements it has been suggested [Kwon04] that this has a magnetic transition at around 20 K. The synthesis route is similar to that described above.

Despite their radically changed geometrical properties, relatively few characterization measurements have been carried out on these samples beyond

Table 6.1: Structural and superconducting properties of the samples investigated [Choy98, Kwon04]. The average CuO_2 layer spacing is denoted by $\bar{c}$ and the values of T_c will depend strongly on the doping of the samples.

Compound	$\bar{c}$ (Å)	Expected T_c (K)
Bi2212	7.72	78
HgI_2-Bi2212	11.32	68
$((Me_3S)_2HgI_4)$-Bi2212	14.02	82
$(PyC_1H_3HgI_4)$-Bi2212	13.86	82
$(PyC_8H_{17}HgI_4)$-Bi2212	19.17	82
Bi2201	13	26
HgI_2-Bi2201	20	22
$(PyC_1H_3HgI_4)$-Bi2201	23	27

their structure, X-ray absorption spectra, and magnetic susceptibility [Choy98, Kwon02, Kwon04]. This therefore justifies making a systematic study of their superfluid density as a function of the spacing between the layers in both intercalated Bi2212 and Bi2201 specimens.

6.3 Experiments on intercalated superconductors

In this section I describe the experiments that were carried out on a variety of intercalated superconductors, probing possible magnetic ordering, muonic radical formation, superfluid density variation with layer spacing, and the behaviour of the magnetic vortex lattice. Before continuing to describe the details of the experiments that were carried out, I list the samples that were used and their properties measured by previous studies. The samples used were prepared by Drs S.-J. Kwon and S. J. Kim following the synthesis described in section 6.2 above, and their magnetic properties were consistent with the previous measurements published regarding these materials [Choy98, Kwon02, Kwon04]. The notional structural and superconducting properties are presented in Table 6.1. Slight variations from these T_c values are likely due to the possibility of producing differently doped specimens, but the structural properties should not be affected.

The remainder of this section is split up according to the type of experiment carried out and the form of the samples used. In section 6.3.1, I describe experiments carried out in the longitudinal geometry described in section 2.2, testing for magnetic ordering or organic radical states in $((Me_3S)_2HgI_4)$-Bi2212, since

this system offers the opportunity to test for the previously reported magnetism and also a reference organic intercalant to test for muonic radical states. Sections 6.3.2 and 6.3.3 discuss transverse field measurements (Section 2.2) of the superfluid density of this series of intercalated superconductors. The experimental methodology and data analysis is included in the respective sections.

6.3.1 Searching for magnetic order or radical states in intercalated superconductors

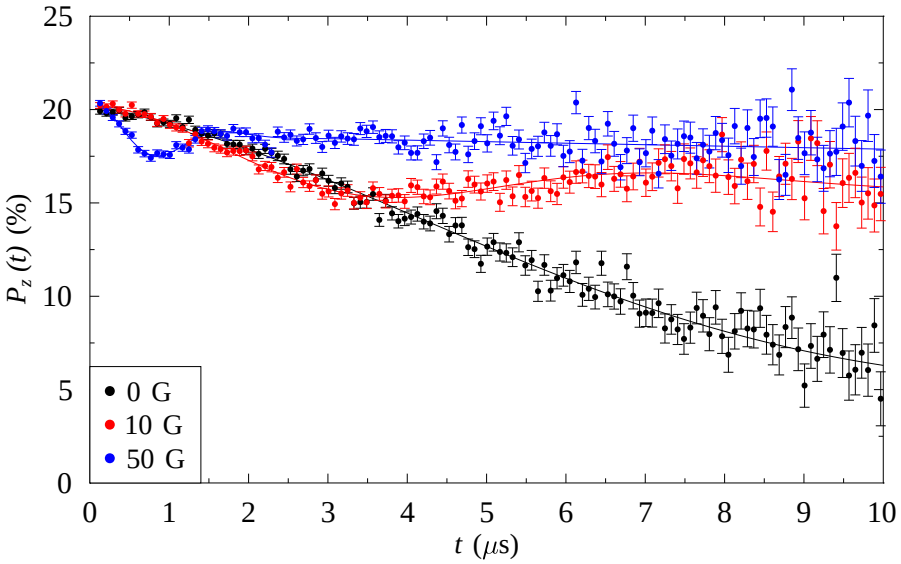

Figure 6.3: Zero-field data and longitudinal field data recorded at 15 K in the indicated longitudinal fields for $((Me_3S)_2HgI_4)$-Bi2212. The fitted functions are Equations 6.6 and 6.7 described in the text.

Evidence for short range magnetic order is seen in a number of cuprate superconductors [Brew88, Weid89, Sann04, Savi05], but not Bi2212 [Savi05]. One of our samples of intercalated superconductor, $((Me_3S)_2HgI_4)$-Bi2212, shows some evidence for a magnetic transition in SQUID measurements [Kwon05]. This could make a significant difference to the superconducting properties and/or the muon relaxation rate used to extract the superfluid density. In order to obtain useful results from TF measurements on this sample we need to exclude the possibility that magnetic ordering occurs in this sample. This can be done by making measurements of the muon relaxation rate in zero applied field (ZF) (Section 2.2).

Magnetic ordering would be seen in a significant change in the relaxation rate or initial and final asymmetries, or in muon precession. Another possible source of error in the TF measurements would be the formation of muonic radicals in the intercalated samples. These might produce a significant and complicated field dependence in the measured asymmetry, complicating the analysis of the TF data. This can be probed by examining how the muon relaxation changes as a function of an applied longitudinal field (LF) (Section 2.2). To examine these possibilities both ZF and LF measurements were carried out on samples of Bi2212 and $((Me_3S)_2HgI_4)$-Bi2212. The former is a control sample, since it does not show evidence for magnetic ordering [Savi05] and has no organic radicals. $((Me_3S)_2HgI_4)$-Bi2212 has a paramagnetic organic radical intercalant, and SQUID measurements suggested that this may have changed the magnetic properties at low temperature [Kwon05].

These experiments were carried out using the MuSR spectrometer at the ISIS pulsed muon facility in its longitudinal configuration (Section 2.2). For both samples the experimental procedure was similar: each sample was mounted on a silver plate and then cooled from well above the superconducting T_c to the base temperature of the CCR cryostat, around 15 K. A zero field run was taken at 15 K before the field scan at 15 K was recorded in increasing field values up to 0.2 T. The magnetic field was removed and zero applied field was returned using the compensation coils within the spectrometer. The zero field temperature scan then proceeded in steps up to temperatures well above T_c. This was not an ideal experimental procedure, since the samples are superconducting, and some flux was trapped in the samples at low temperature. This was evident in a significantly increased relaxation rate in the μSR spectra at 15 K recorded after the field was removed. The effect persists up to around 50 K. Such runs are excluded from the analysis below. Despite this, the objective of these ZF experiments was still achieved, since we can still compare the first base temperature run against the zero field data well above T_c, and the LF data is independent of this issue.

The fitting functions used for these data were Equation 6.6 for the ZF data and Equation 6.7 for the LF data. These are products of a Gaussian Kubo Toyabe function [Haya79], which should provide an adequate description of the static random nuclear dipole moments with a Gaussian distribution width Δ/γ_μ, a longitudinal field at the muon site of B_L, and an exponential relaxation, of rate λ, modelling the dynamically fluctuating electronic moments. Using an exponen-

tial relaxation in this way is rather crude compared to considering the effect of dynamic fluctuations numerically, but since we are searching for changes in the parameters as a function of temperature or field, this approach is sufficient. It must also be noted that, as shown in Figure 6.3, these fitting functions provide an excellent description of the raw data in modest fields.

$$P_z(t) = [\frac{1}{3} + \frac{2}{3}(1-\Delta^2 t^2)\exp(-\Delta^2 t^2)]\exp(-\lambda t). \quad (6.6)$$

$$P_z(t) = \{1 - \frac{\Delta}{\gamma_\mu B_\mathrm{L}} j_1(\gamma_\mu B_\mathrm{L} t)\exp(-\Delta t) - \left(\frac{\Delta}{\gamma_\mu B_\mathrm{L}}\right)^2 [j_0(\gamma_\mu B_\mathrm{L} t)\exp(-\Delta t) - 1] - [1 + \left(\frac{\Delta}{\gamma_\mu B_\mathrm{L}}\right)^2]\Delta \int_0^t j_0(\gamma_\mu B_\mathrm{L}\tau)\exp(-\Delta\tau)d\tau\}\exp(-\lambda t). \quad (6.7)$$

Comparing the relaxation rates shown in Figure 6.4(a) shows that there is a significant difference in the absolute values of the relaxation rate, λ, between the two specimens, but neither shows a strong temperature dependence. That there is little temperature dependence is good evidence for a lack of magnetic ordering (as do the other fitting parameters), and the change in the absolute value could either be due to different backgrounds because the quantity of sample was rather different in the two cases (due to the relative difficulty of making intercalated samples), or perhaps because the paramagnetic organic radical marginally decreases the characteristic timescale of the paramagnetic fluctuations. This effect should be limited to slightly changing the background width observed in the TF measurements described below. The width of the magnetic field distribution at muon sites plotted in Figure 6.4(b) is almost identical in the two samples, and has a weak temperature dependence. This suggests that the magnetic environment of the muon stopping sites in these two samples is almost identical, meaning that the TF measurements on different intercalates should generally have similar background widths. The lack of temperature dependence is further evidence against any magnetic ordering. The values of the relaxing (A_r) and background (A_bg) asymmetries are shown in Figure 6.4(c). Neither of these changes significantly with temperature and the values are similar in the two samples. For these parameters, differences are likely to be due to either difference amounts of sample or organic radical states which will be tested for by the LF measurements. The key result from these parameters is the lack of temperature dependence in either parameter, which could have signalled magnetic ordering. From the zero field re-

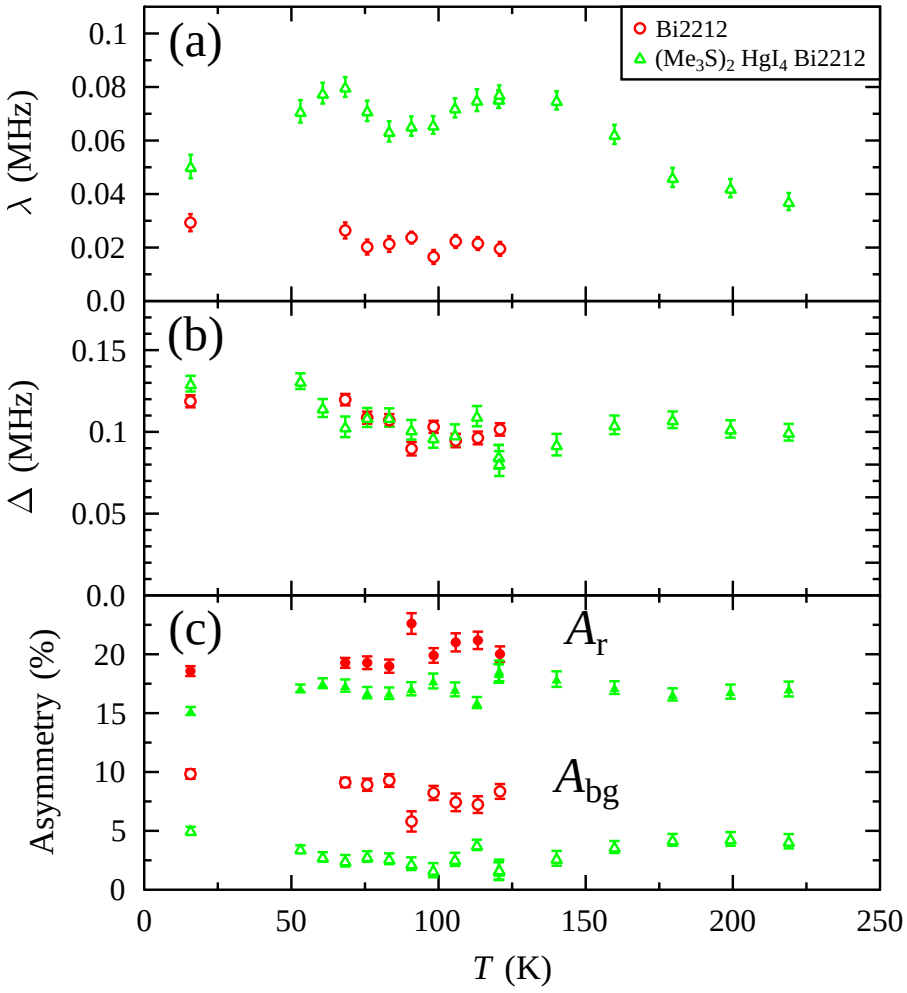

Figure 6.4: Parameters extracted from fitting Equation 6.6 to data recorded on $\mathrm{Bi2212}$ and $((\mathrm{Me_3S})_2\mathrm{HgI_4})$-$\mathrm{Bi2212}$ in zero magnetic field. (a) Relaxation rate λ. (b) Field distribution width Δ. (c) Values of the asymmetry components, A_r describing the relaxing component, and A_bg.

sults, we can conclude that the muon stopping sites are similar in the two samples and no magnetic ordering occurs. They strongly suggest that any effect of the paramagnetic radical on the TF results will be negligible.

The longitudinal field results shown in Figure 6.5 were measured in a series of fields at 15 K. Measurements were taken up to a field of 2000 G (0.2 T), but Equation 6.7 does not successfully describe the data above 200 G (20 mT), due to the lack of relaxing asymmetry to constrain the fitting parameters once the fluctuations are decoupled. The longitudinal field was found to be consistently less than the applied field, which fits with a diamagnetic response of the sample within the superconducting phase. Above 200 G (10 mT) an exponential relaxation of the form $A_0 \exp(-\lambda t) + A_{\mathrm{bg}}$ proved sufficient to describe the data and the values of the initial asymmetry and the relaxation rate λ shown in Figure 6.5 from these higher fields are from exponential fits.

The relaxation rate λ rises gradually from the zero field value as the field is increased, probably describing the increased damping of the Kubo-Toyabe function as the field increases, and this is what prevents reliable fitting using Equation 6.7 at higher fields. Given this effect, useful information cannot be drawn from this parameter.

The width of the field distribution, Δ, rises smoothly and a similar way for both compounds, showing once more that the magnetic environment at the muon stopping sites is quite similar in these two compounds. The rise is probably related to the changing magnetic field distribution in the superconductor vortex lattice and the widths are comparable to those observed in Figure 6.8 below. Beyond the fact that the behaviour is similar in the two compounds, little information can be extracted from this parameter. We may also be seeing effects due to λ and Δ trading off in the fitting procedure.

While the size of the samples may have a small effect on the apparent initial asymmetry, the values of ~ 30 % for Bi2212 and ~ 20 % for $(Me_3S)_2HgI_4$-Bi2212 show that we must include another, significant, contribution from rapid depolarization of muons implanted into the intercalant layers. This might be expected to rise with the intercalated volume fraction, and the variation of the initial asymmetries in TF measurements (section 6.3.2) bore this out. We can therefore think of two types of stopping sites, ones within the superconducting blocks which are likely to be very similar to those in any other cuprate material, and sites within the intercalant layers.

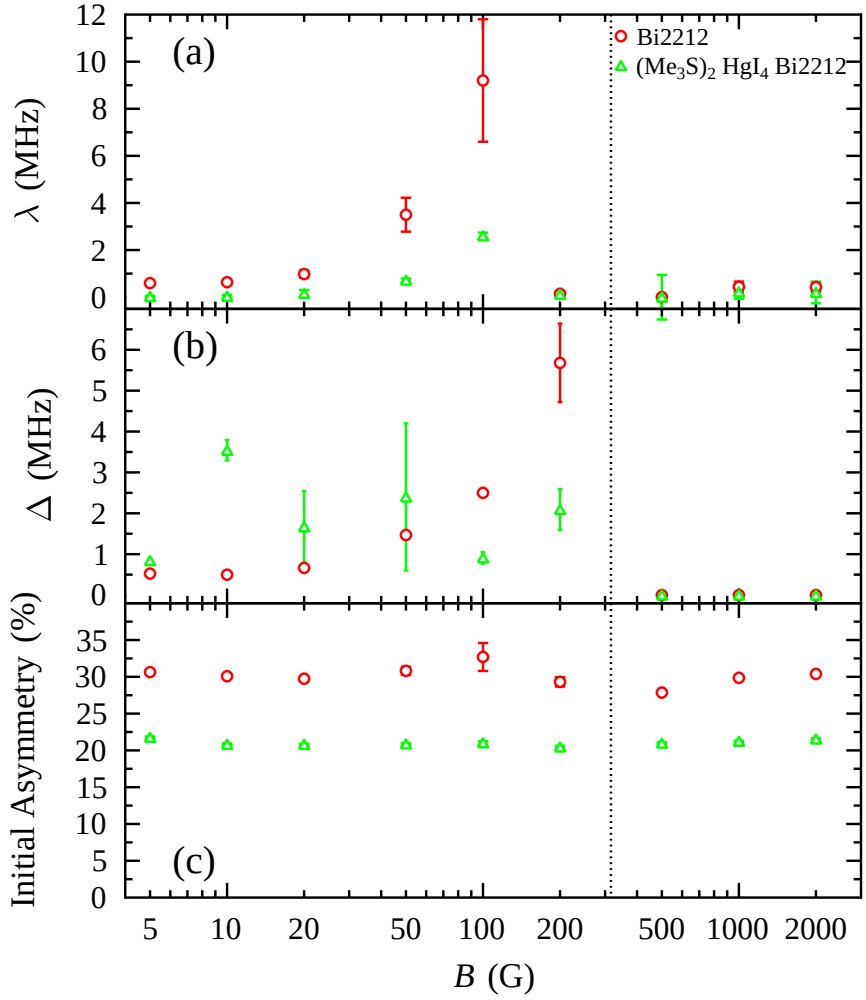

Figure 6.5: Parameters derived from fitting Equation 6.7 to data recorded on Bi2212 and $(Me_3S)_2HgI_4$-Bi2212 at 15 K in the specified magnetic fields, up to 200 G. The relaxation rate and initial asymmetry values above 200 G were fitted to an exponential $A_0 \exp(-\lambda t)$ because Equation 6.7 did not satisfactorily describe the high field data, as discussed in the text. (a) Relaxation rate λ. (b) Field distribution width Δ. (c) Initial asymmetry.

The next question we must address is what effect the muon sites within the intercalant layers will have in TF measurements. On the basis of the LF measurements, we can safely conclude that the answer is that there will be no effect, save for the reduced initial asymmetry. The reasoning for this is that there are no significant dips in the initial asymmetry as a function of applied field within the measured field range, as would signal resonant states formed by the muon in the organic intercalant [Rodu99], and also that the variation of λ and Δ is similar in the two materials, hence the magnetic fields at the muon stopping sites in the superconducting blocks must be similar. Any second order effects are likely to be hidden within the systematic errors of the experiment, such as field dependence in α or the background count rates. These will be excluded by the TF fitting procedure, and so we can carry out and interpret the TF measurements in the normal manner.

6.3.2 Transverse field experiments on polycrystalline intercalated Bi2212 and Bi2201

The primary aim of the measurements on these samples was to determine how the superfluid density of intercalated superconductors changes as a function of the changing layer spacing. To accomplish this it is necessary to carry out TF μSR measurements as a function of both temperature and applied magnetic field. Experiments were carried out using the MuSR spectrometer at ISIS and GPS at PSI. The former provides higher data rates and allows reliable measurements to be carried out in small magnetic fields, but the pulse width at ISIS (see section 2.2) limits the maximum transverse field that could be applied. Experiments using GPS verified a small proportion of the ISIS data and extended the data set to higher magnetic fields for a smaller number of samples.

For each data set presented below a high temperature background run was recorded after the magnet had stabilized to the desired field at a temperature more than 25 % above the sample T_c. This sets the initial amplitudes and phases of signals from each detector for use in the data analysis. After taking the high temperature background data set the sample was cooled to the lowest temperature required for the series of measurements in question, and then measurements were taken on warming, with a temperature stable to within 0.5 K for all measurements. The cryostats used depended on which spectrometer was being used,

and what temperature range was required. At GPS the standard He flow cryostat (section 2.2) was used for all of these measurements. The three detectors perpendicular to the initial muon spin polarization (Up, Down, and Right, since the spin rotator was used) were used in data analysis. At ISIS the MuSR CCR was used for all measurements on polycrystalline Bi2212-based samples and an Oxford Instruments Variox ^{4}He cryostat was used for the Bi2201 measurements, since temperatures well below 20 K were required. The 64 detectors of the MuSR spectrometer were grouped into 8 opposing groups appropriate for the rotated operation of the spectrometer. Experiments were carried out in four separate batches. The first set of measurements were carried out on Bi2212, HgI_2-Bi2212, and $(Me_3S)_2HgI_4$-Bi2212, in June 2005 on the MuSR spectrometer at ISIS. Measurements on the $PyC_1H_3HgI_4$-Bi2212 and $PyC_8H_{17}HgI_4$-Bi2212 specimens were carried out using the GPS spectrometer at PSI in June 2006, together with further measurements on Bi2212. Measurements on the Bi2201 based samples were carried out at ISIS in September 2006, but problems with the particle accelerator reduced the available beamtime significantly. These measurements were repeated and completed at PSI in August 2007. Samples were prepared for each new set of experiments and where experiments were repeated, it was done using the previous samples of the required composition.

The primary method of data analysis [Pratt] was based on the approach taken by Weber *et al.* [Webe93], where the field distributions were calculated for magnetic fields applied at different angles relative to the CuO_2 planes, and a polycrystalline average of these distributions was taken to provide a field distribution that could be fitted numerically. The field distributions used were those calculated by Brandt [Bran03]. The distribution widths obtained were checked using Maximum Entropy methods [Rain94] and simpler Gaussian assumptions for the field distributions, as Uemura *et al.* [Uemu89] had used. The agreement between the different methods of analysis was generally very good. The effect on the transverse polarization, $P_x(t)$, of the implanted muons due to the distribution of magnetic fields within the vortex lattice, $p(B)$, takes the form:

$$P_x(t) = \int_0^\infty p(B)\cos(\gamma_\mu B t + \phi)dB, \tag{6.8}$$

where ϕ is a phase offset due to the experimental geometry of a pair of detectors, which can be determined in the high-temperature phase.

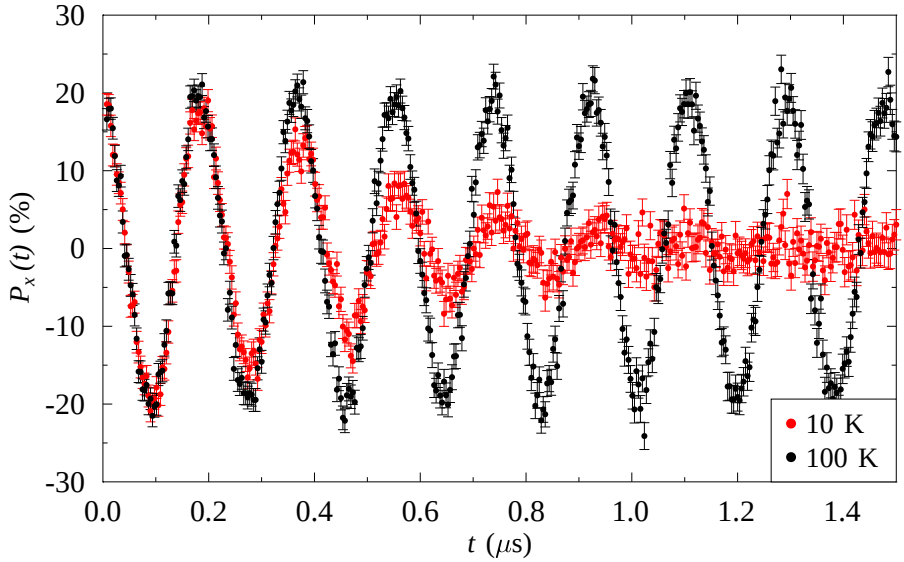

Figure 6.6: Examples of both high and low temperature transverse field data recorded on a polycrystalline sample of Bi2212 using the GPS spectrometer. The slight depolarization in the high temperature data comes from randomly orientated nuclear magnetic moments, whereas the strong dephasing in the low temperature data results from the distribution of magnetic field in the Abrikosov vortex lattice.

Measurements were taken as a function of temperature in fixed fields, primarily 50 G (5 mT), and also as a function of field, with each point representing a separate field cooling at the indicated field to the base temperature of the cryostat used. Examples of the transverse field data are shown in Figure 6.6 with the high temperature 100 K data set showing a very small Gaussian damping of the oscillations and the low temperature 10 K data set showing the strong damping and dephasing effect of the distribution of magnetic fields within the vortex lattice.

Constant field results are shown in Figure 6.7 for constant fields of 50 G (5 mT). Figure 6.7 (a) shows the temperature dependence of the width of the field distribution $B_{\rm rms}$ arising from superconducting vortex lattice and any background relaxation. Figure 6.7 (b) shows the shift of the peak frequency of the distribution from the applied field measured at high temperature in the normal state. Considering the polycrystalline field distributions calculated from the single crystal field distributions reported by Brandt [Bran03, Pratt], there should be no shift in polycrystalline samples. That one is observed in the samples prepared for the first set of experiments, and no others, suggests that the preparation of these sam-

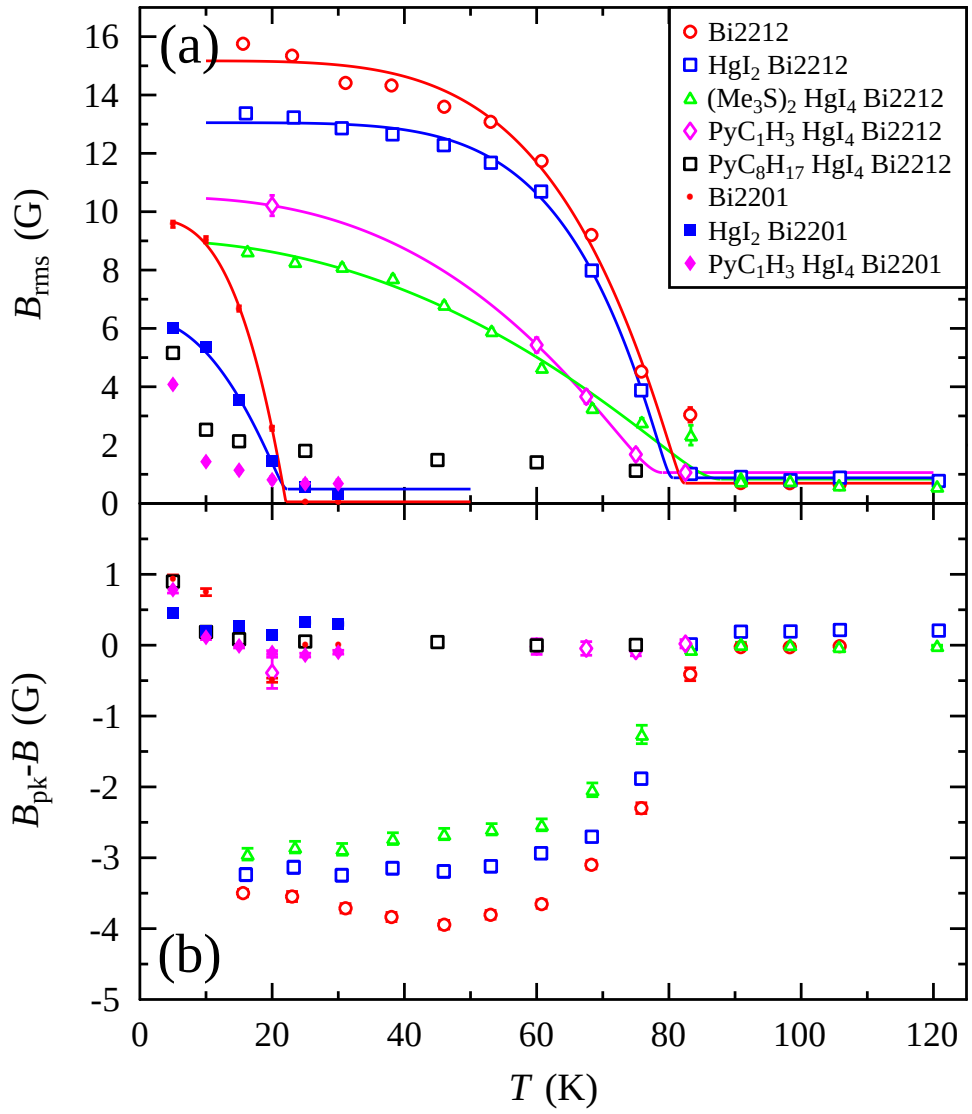

Figure 6.7: Transverse field results for both Bi2212 and Bi2201 samples. (a) $B_{\rm rms}$ fitted using an assumption that the field distribution is that of a highly anisotropic polycrystalline superconductor. The lines are fits to Equation 6.9 over the ranges shown with the parameters shown in Table 6.2. (b) Shift of the peak frequency of the signal from the superconductor, $B_{\rm pk}$, from the applied field. Bi2212, and both HgI_2 and $(Me_3S)_2HgI_4$ intercalated samples show a significant diamagnetic shift, probably due to partial alignment of the crystallites in these samples. The shifts observed in the other samples are within the experimental resolution.

Table 6.2: Fitted parameters extracted from the transverse field data shown in Figure 6.7 by fitting the temperature dependent $B_{\rm rms}$ values to Equation 6.9. The fitting is done in quadrature. It is not possible to fit either the $(PyC_8H_{17}HgI_4)$-Bi2212 or the $(PyC_1H_3HgI_4)$-Bi2201 data in this way because of the vortex lattice breaking up well below T_c.

Compound	T_c (K)	$B_{\rm rms}(0)$ (G)	n	$B_{\rm bg}$ (G)
Bi2212	82.4 ± 1.5	15.2 ± 0.5	4.6 ± 0.6	0.7 ± 0.2
HgI_2-Bi2212	80.6 ± 0.6	13.0 ± 0.3	5.7 ± 0.4	0.88 ± 0.08
$((Me_3S)_2HgI_4)$-Bi2212	88 ± 3	9.0 ± 0.6	2.1 ± 0.3	0.70 ± 0.09
$(PyC_1H_3HgI_4)$-Bi2212	79.0 ± 0.1	10.4 ± 0.1	2.60 ± 0.01	1.06 ± 0.01
$(PyC_8H_{17}HgI_4)$-Bi2212	*	*	*	*
Bi2201	22.1 ± 0.2	9.8 ± 0.3	3.0 ± 0.2	0.06 ± 0.03
HgI_2-Bi2201	22.3 ± 0.5	6.3 ± 0.5	2.1 ± 0.3	0.5 ± 0.3
$(PyC_1H_3HgI_4)$-Bi2201	*	*	*	*

ples is likely to have resulted in a partially aligned powder. This means that the field distributions calculated for the polycrystalline average will be a less successful approximation of the true distribution. Fourier transforms of the data using standard fast Fourier transform and maximum entropy approaches were used to verify the widths obtained from these time domain fits, and reasonable agreement was found at low field. (Complications found at higher fields will be discussed in conjunction with the field dependence results below.) The temperature dependence of $B_{\rm rms}$ has contributions from the vortex lattice and also the background depolarization, largely due to Cu nuclear moments. These two contributions can be extracted from the temperature dependence of $B_{\rm rms}$ using Equation 6.9. This form is based on the two-fluid model where $n = 4$, but allowing n to vary allows the variety of temperature dependences observed in cuprates to be described consistently, and compared to literature values [Zimm95]. The fitting needs to be done in quadrature because this is how the convolution of the two distributions produces the observed width. These considerations leave us with the function:

$$B_{\rm rms}^2(T) = B_{\rm rms}^2(0)[1 - (T/T_c)^n]^2 + B_{\rm bg}^2, \tag{6.9}$$

to describe the temperature dependence of $B_{\rm rms}$ in constant field. The results of fitting this form to the data shown in Figure 6.7 are presented in Table 6.2. The parameter n describing the curvature of the temperature dependence can be seen

to vary between 2 and 6, a slightly wider range than previous results on a variety of other polycrystalline cuprates [Zimm95], but remains well defined for all samples. That the background value $B_{\rm bg}$ is around 1 G for all the Bi2212 specimens also agrees with previous results [Webe93, Zimm95], and fits in with the description that the relevant muon stopping sites in these intercalated specimens appear to be similar to those in unintercalated specimens, although not proving that they are the same, as suggested by the ZF and LF results (section 6.3.1). The parameter of greatest interest, $B_{\rm rms}(0)$, decreases smoothly with increasing layer spacing in both the Bi2212 and Bi2201 series.

The exceptions to this well defined behaviour occur for the largest intercalant in each series, ($PyC_8H_{17}HgI_4$)-Bi2212 and ($PyC_1H_3HgI_4$)-Bi2201. Examining Figure 6.7, we see that the temperature dependence of $B_{\rm rms}$ in both these samples does not follow the smooth power-law decrease observed in all the other samples. Both show a reasonable, compared with the other samples, value of $B_{\rm rms}$ at the lowest temperature, but there is a sharp drop to slightly more than the background value at a temperature well below T_c. Such a sharp decrease in $B_{\rm rms}$ has previously been observed in single crystal samples of Bi2212 [Lee93], but far closer to T_c. This drop is associated with the motional narrowing caused by thermal fluctuations of the vortex lattice at small superfluid densities close to T_c. For the large intercalate samples it seems likely that a similar mechanism is at work, since the superfluid density is lower anyway, and thermal fluctuations would become significant at a smaller fraction of T_c. Comparison of data taken on Bi2212, $PyC_1H_3HgI_4$-Bi2212, and $PyC_1H_3HgI_4$-Bi2212 in higher applied fields found no evidence of the temperature at which the drop occurred depending on the applied magnetic field, but this temperature decreased with increasing layer spacing. This may be because the measurements are in the high-field regime where the vortex lattice melting is field independent [Blat96]. I discuss why the vortex lattice of the samples with the largest layer spacing breaks up at such a low temperature in section 6.3.4 below.

The results of measurements of the linewidth $B_{\rm rms}$ as a function of the applied field are shown in Figure 6.8. Each data point represents the difference between a high-temperature background measurement used to fix the relaxing amplitudes and phases of the signal, and a low-temperature measurement at the base temperature of 20 K for all Bi2212 samples, apart from ($PyC_8H_{17}HgI_4$)-Bi2212, where 5 K data were used, and 5 K for all Bi2201 samples. The counting statistics for both

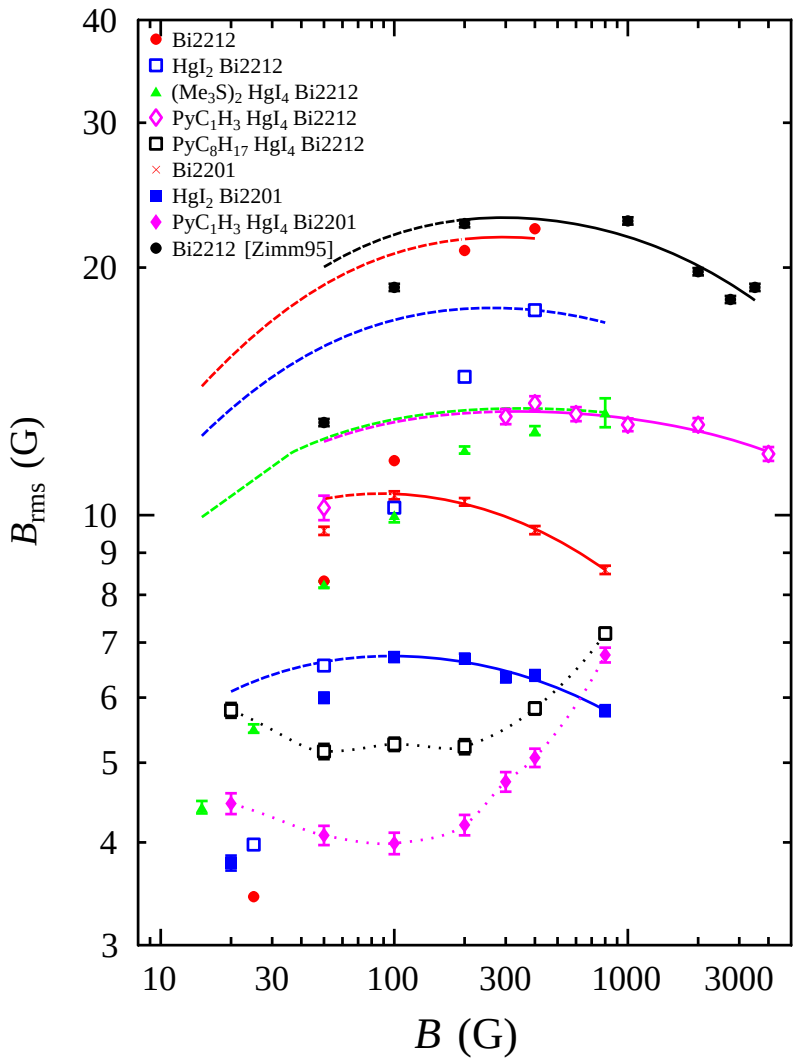

Figure 6.8: $B_{\rm rms}$ fitted using an assumption that the field distribution is that of a highly anisotropic polycrystalline superconductor as discussed in the text, except for the Bi2212 (red) and HgI_2-Bi2212 (blue) data, where Maximum Entropy analysis was used. The solid lines show the ranges used for the fitting to extract λ and ξ, with dashed lines showing the extrapolation of this field dependence to lower field and dotted lines guiding the eye for the two compounds where fitting was not possible. The Bi2212 (black) data come from Ref. [Zimm95].

runs are kept the same and it was ensured that the sample had cooled to a stable base temperature before the data analysed here were recorded. The background width B_{bg} has not been subtracted in the figure, but previous studies suggest that it will be independent of the applied field [Zimm95], so the background values obtained at 50 G and listed in Table 6.2 were used in analysis.

The Bi2212 data (black) from Ref. [Zimm95] were analysed using the assumption that the field distribution due to the vortex lattice is Gaussian. For the Bi2212 (red) and HgI_2-Bi2212 (blue) data the time-domain analysis described above showed anomalously large values of B_{rms}, as was found in Fourier transforms of the data. Fitting using the Gaussian approximation and Maximum Entropy analysis showed more reasonable values, and the latter are shown in Figure 6.8.

We can use the field dependence of B_{rms} to extract values of λ and ξ following the method of Brandt [Bran03], adapted for the polycrystalline case. This is done by taking a polycrystalline average of the values expected for different orientations of the highly anisotropic superconducting crystallites. We can take the contribution to B_{rms} from crystallites with their CuO_2 (ab) planes at angles θ to the magnetic field direction as:

$$B_{\mathrm{rms}}^2 \propto \frac{1}{\lambda^4} \propto \left(\cos^2\theta + \frac{\sin^2\theta}{\gamma^2}\right), \tag{6.10}$$

where $\gamma = \lambda_c/\lambda_{ab}$. Taking the angular average of this function leads to the expression:

$$B_{\mathrm{rms}}^2 \propto \frac{1}{\lambda^4} \propto \left(\frac{2}{3} + \frac{1}{3\gamma^2}\right). \tag{6.11}$$

It has previously been noted that Bi2212 crystals in the doping range considered here have a value of $\gamma \gtrsim 55$ [Mart92], so the contribution from the second term will be negligible, and therefore it has been neglected in further analysis.

The results of fitting the B_{rms} values to this form of the field dependence are shown in Figure 6.8, with the parameter values and fitting ranges shown in Table 6.3. It is immediately apparent that the expected field dependence only describes the high-field data adequately, and the low-field values decrease far more sharply than predicted. This is a particular problem for the samples that were only measured at ISIS, due to the pulse width limiting the upper measurement field (section 2.2). For these data, values of ξ were used from the more extensively measured samples with similar B_{rms} values, as shown in Table 6.3. It was found

that the value of λ depended weakly on the value of ξ chosen, and this possibility is included in the error determined for λ. The peak value of $B_{\rm rms}$ is known to take a value independent of ξ [Bran03], so assuming the value of ξ is similar to this, the conventional method used for analysing values of $B_{\rm rms}$ when the field dependence is small or not fully explored. The breakdown of the model at low fields is disappointing in the context of the ISIS results. It is most likely to arise from the anisotropic magnetization and the distribution of demagnetizing factors in the differently aligned crystallites [Webe93]. This is a complex issue, and more information on the microscopic structure of the samples would be needed before a more conclusive approach to this low-field behaviour could be made. (Some progress in this direction has previously been attempted, e.g. [Webe93, Russ07].)

The $B_{\rm rms}$ values of the ($PyC_8H_{17}HgI_4$)-Bi2212 and ($PyC_1H_3HgI_4$)-Bi2201 samples have a significantly different field dependence to those of the other samples, and also the model prediction. While obtaining quantitative information about the values of λ and ξ for these samples seems unlikely, due to the vortex lattice breakup, we can still consider the qualitative aspects of the observed field dependence of $B_{\rm rms}$. Given the measurements were recorded only slightly below the breakup temperature, it is likely that they significantly underestimate $B_{\rm rms}(T = 0)$. The sharp rise in $B_{\rm rms}$ around 500 G may be due to the magnetic field breaking up the vortex lattice, in a similar manner to that observed in pristine Bi2212 [Lee95].

Considering the λ and ξ values shown in Table 6.3, we see that the λ values for the two pristine samples of Bi2212 fall within the range found by other studies (see Ref. [Zimm95] and references therein), as does the value for Bi2201 [Russ07]. The values of ξ also seem within a reasonable range for values determined by μSR [Blat94, Soni98], although studies of H_{c2} generally suggest smaller values (e.g. Ref. [Pals88]). More interesting is the trend in the values of λ, since we can compare this with the Uemura plots of T_c against $n_s/m^* \propto \lambda^{-2}$ and $T_{\rm F} \propto \bar{c}/\lambda^2$. We note that there is no systematic variation in T_c with changing layer spacing and the random variation due to differing doping is small, so we can look for trends in λ directly. Since λ increases with increasing layer spacing n_s/m^* is clearly falling, without any change in T_c, suggesting that the bulk superfluid density is not the parameter controlling T_c. The question now becomes one of finding how the superfluid density falls as the layer spacing increases. This is shown in Figure 6.11 (Left) A simple guess is to assume that the superfluid density in each

Table 6.3: Fitted parameters extracted from the transverse field data shown in Figure 6.8 by fitting the field dependent $B_{\rm rms}$ values to the numerical model of Brandt [Bran03], corrected for the effects of polycrystalline averaging, over the indicated range. The fitting is done in quadrature. Values of ξ marked † were held fixed due to a lack of high-field data. The parameter $\bar{c}/\lambda^2$ gives a measure of the superfluid density within each plane and has units 10^{-6} Å^{-1}. It is not possible to fit either the $(PyC_8H_{17}HgI_4)$-Bi2212 or the $(PyC_1H_3HgI_4)$-Bi2201 data in this way because of the vortex lattice breaking up well below T_c.

Compound	$B_{\rm bg}$ (G)	Range (G)	λ (Å)	ξ (Å)	$\bar{c}/\lambda^2$
Bi2212					
Pristine	0.7	200-400	2060 (70)	60†	1.82(6)
Pristine [Zimm95]	1.88	200-3500	2000 (60)	60 (10)	1.93(6)
HgI_2	0.88	400-400	2300 (100)	60†	2.1(1)
$((Me_3S)_2HgI_4)$	0.70	400-800	2700 (80)	30†	1.92(6)
$(PyC_1H_3HgI_4)$	1.06	300-4000	2710 (70)	30 (10)	1.89(5)
Bi2201					
Pristine	0.06	100-800	2900 (80)	125 (25)	1.55(4)
HgI_2	0.5	100-800	3700 (100)	100 (20)	1.45(4)

CuO_2 layer is constant, which would make $\bar{c}/\lambda^2$ constant in each family. As can be seen in the right-hand column of Table 6.3, this is a reasonable description of the data. I will return to this matter and discuss the consequences of these results in section 6.4.2.

6.3.3 Experiments on single crystals of intercalated Bi2212

The distribution of magnetic fields in single crystals of pristine Bi2212 has been extensively studied using μSR [Hars93, Lee93, Lee95, Lee97, Aege98, Lee98a]. These studies have shown that the form of the magnetic field can be used to deduce not only the superfluid density, but also the ordering of the vortex lattice at different temperatures, magnetic fields, and under the effect of disorder. While techniques such as Small Angle Neutron Scattering (SANS) or flux decoration are well suited to investigating the structure of the vortex lattice, microscopic probes such as NMR or μSR allow the field distribution to be measured directly and microscopically [Bran88]. The advantage of measuring the field distribution at a microscopic level is that information about the disordered vortex liquid phase can be obtained [Lee93]. Bulk probes such as magnetization or ac susceptibility can

often give information about the boundary between phases with different ordering, but give little insight into the underlying microscopic processes. Of the possible microscopic techniques, μSR is more suitable than NMR for investigating the superconducting vortex lattice because the bulk of samples can be investigated, as well as the surface, allowing the use of much larger crystals which decreases the effect of pinning. The ordered vortex lattice gives an asymmetric distribution of magnetic fields [Bran88] and transitions between different ordered or disordered phases [Blat94] can be seen as changes in the width and/or asymmetry parameters of the field distribution (e.g. [Lee93]).

During the course of this work, small single crystals ($< 3 \times 2$ mm^2) of Bi2212 intercalated with either I_2 or HgI_2 became available. While in principle most of the single crystal studies described above could be repeated, the need to use a mosaic of crystallites with unknown homogeneity may limit how much information could be obtained. For this reason a more limited study was carried out. In terms of the polycrystalline data described in section 6.3.2, two pieces of information that could be obtained from single crystal data are of primary importance, namely the asymmetry of the line shape and the width of the field distribution at low temperature. The former tells us whether an ordered vortex lattice occurs at low temperature, justifying the assumption that the superfluid density can be obtained from the data, and the latter corroborates the fitting procedure used for the polycrystalline data. The sizes of the crystallites for the two intercalants was similar, so HgI_2 intercalated crystallites were chosen for the experiments because of their larger interlayer spacing, and also to give a direct comparison to the polycrystalline data.

Experiments were carried out using the MuSR spectrometer at ISIS for a temperature scan from 5–90 K in a magnetic field of 50 G (5 mT) and using GPS at PSI for a temperature scan from 10–100 K in a field of 400 G (40 mT). The mosaic of crystallites was laid out on their flat faces upon a leaf of silver foil (thickness 25 μm) using vacuum grease. The mosaic was realigned between experiments to optimise for the smaller beam spot at PSI. The form of the asymmetry data is similar to that shown in Figure 6.6, except that there is no angular averaging of the field distribution. To obtain the field distribution the Maximum Entropy procedure implemented in the WiMDA software package [Prat00] was used. A description of the methodology is given in Ref. [Rain94]. Deadtime correction is considered for the ISIS data and steady backgrounds are fitted for the PSI data

(section 2.2). In both cases, the phases used for all data sets are fitted for the highest temperature data set, measured in the normal state, and an apodization time of 4.4 μs was used to decrease the weighting of the data at longer times, which are subject to a greater statistical error.

The results of the maximum entropy analysis are shown as a function of internal field and temperature in Figures 6.9 (50 G) and 6.10 (400 G). At high temperature we see that the field distributions are Gaussian, with a width of around 1 G due to nuclear moments, in excellent agreement with the polycrystalline data. The T_c value in these crystallites should be around 80 K. At the lowest temperatures the distribution becomes more asymmetric, with more spectral weight below the applied field than above, as we would expect from the previous studies described above and the theoretical predictions (e.g. [Lee93, Bran03]). The width of the magnetic field distribution is normally found by evaluating the moments of the spectra resulting from the maximum entropy analysis. Analysing the 400 G data in this way gives $B_{\rm rms} \sim 7.5$ G, far lower than the corresponding polycrystalline value of $B_{\rm rms} \sim 18$ G. This simple analysis breaks down because the background forms a large part of the low temperature signal, due to the sample being mounted on silver rather than hematite. Fitting the maximum entropy spectra with two Gaussian functions showed that the width at low temperature was approximately 13 G, in reasonable agreement with the polycrystalline value. The single crystal value may be lower by ~ 5 G because of a smaller contribution to the width from pinning or the slightly different method of analysis used here. The value of $B_{\rm rms}$ remains approximately constant up to around 40 K and then drops slightly before a sharp drop to around 2.8 G at 70 K and 1.4 G above 80 K. The sharp drop near 70 K and the more symmetric Gaussian like field distribution above this temperature strongly suggests that a vortex liquid phase forms just below T_c, as previous results would lead us to expect [Lee93]. At 50 G, the results are similar, with a low temperature width of around 10 G, slightly smaller than the polycrystalline value, and a similar temperature dependence.

Improving the data analysis to subtract and deconvolve the background signal would allow significantly more information to be drawn from the present data. The width and asymmetry of the lineshape could then be extracted in a similar way to previous studies (e.g. Ref. [Lee93]), allowing a more direct comparison with their results. Larger intercalated crystals would allow the experiments presented in this section to be extended significantly. This is a problem inherent in the preparation

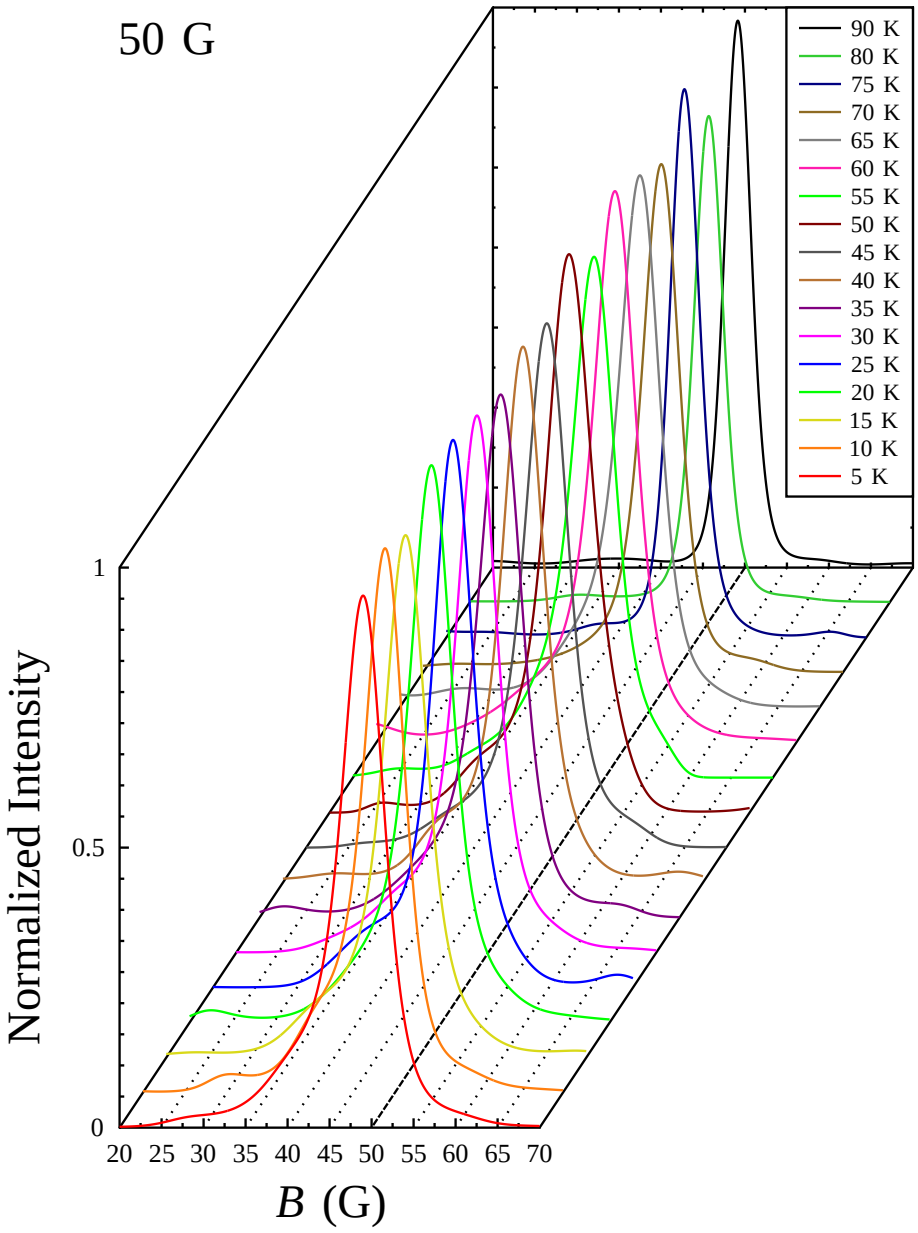

Figure 6.9: Maximum entropy spectra for 50 G transverse field data in a $HgI_2Bi2212$ crystal mosaic recorded using the MuSR spectrometer at ISIS at a series of separate temperatures. All spectra have been normalized to their peak value. The applied field is shown by the dashed line.

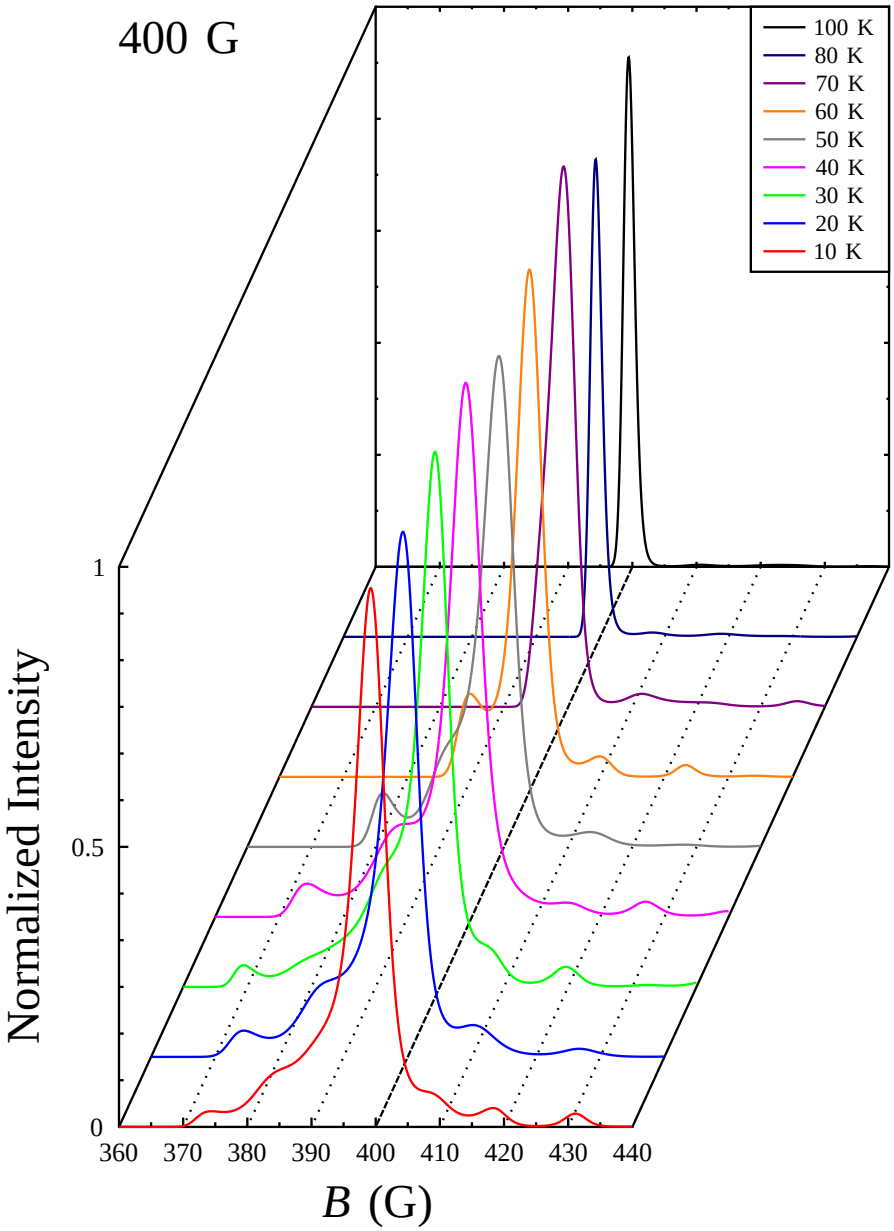

Figure 6.10: Maximum entropy spectra for 400 G transverse field data in a $HgI_2Bi2212$ crystal mosaic recorded using the GPS apparatus at PSI, for a series of separate temperatures. The applied field is shown by the dashed line.

of intercalated specimens, since the intercalation reaction relies on a large surface area of the host material. Nonetheless, the layer spacing is a particularly relevant parameter in the physics of the vortex lattice, and detailed measurements of the ordered and disordered vortex phases are likely to provide new and significant information about the interactions between the vortices. Sufficiently large intercalated single crystals might allow Small Angle Neutron Scattering measurements to directly measure the length scales of the vortex lattice, providing a check of these measurements, and possibly extending them.

6.3.4 Experimental conclusions

The experiments carried out in the longitudinal geometry conclusively excluded the possibility of intercalant induced magnetic order. They also demonstrated that while the intercalant does decrease the initial asymmetry of the precession signal, there are no resonances in the field range where experiments were carried out, so this is a field independent effect that will not affect the parameters of interest in the TF experiments. The measurements on the mosaic of small crystallites of HgI_2 intercalated Bi2212 showed that in both measured fields the low temperature field distributions took the asymmetric form expected for an ordered vortex lattice. This gives strong support to using the widths obtained from the polycrystalline measurements to extract a value of the superfluid density. There is also some evidence that the vortex lattice breaks up close to T_c, seen in a narrower and more symmetric lineshape.

Measuring the temperature dependence of each polycrystalline sample in the relatively small field of 50 G demonstrated that $B_{\rm rms}$ in all bar two of our samples showed a conventional variation with temperature, further supporting the view that the vortex lattice is ordered at low temperature. We also see a steady decrease in $B_{\rm rms}$ with increasing layer spacing. The two exceptions to this are the samples with the largest interplane spacing of the Bi2212 and Bi2201 series. For the samples where $B_{\rm rms}$ followed the conventional temperature dependence, it was also possible to show that in higher fields the field dependence was also conventional, allowing λ and ξ to be deduced from the data, and estimates of λ to be drawn from the lower field data. The lower field data suggests that the demagnetizing factors not included in the model become significant, and prevent the lowest field data points being compared with the model for the field dependence.

The values of λ obtained show a remarkably consistent trend for both the Bi2212 and Bi2201 specimens, with the superfluid density in each CuO_2 layer remaining constant despite the significant change in the separation between the superconducting blocks. This will be compared with the behaviour seen in other superconductors in the next section. Using this result, we can now approach the question of why the temperature and field dependence of $B_{\rm rms}$ in $(PyC_8H_{17}HgI_4)$-Bi2212 and $(PyC_1H_3HgI_4)$-Bi2201 is exceptional. Our first assumption is that the superfluid density in each CuO_2 layer remains similar to that in the other members of each series, and so we can take $\bar{c}/\lambda^2 \sim 1.95$ (Bi2212) and ~ 1.5 (Bi2201). We must then consider what the mechanisms coupling vortices will be, and previous results suggest that both electromagnetic coupling and Josephson coupling will be relevant [Blat96, Lee97]. Vortex lattice breakup due to thermal fluctuations overwhelming electromagnetic coupling should occur at a temperature [Clem91]:

$$T_b^{em} = \frac{\phi_0^2 \bar{c}}{32 k_{\rm B} \mu_0 \pi^2 \lambda^2}, \tag{6.12}$$

if Josephson coupling can be neglected. λ is the in-plane value measured above and the constants have their usual meanings. Putting in the above values of $\bar{c}/\lambda^2$ gives $T_b^{em}(\text{Bi2212}) \simeq 14$ K and $T_b^{em}(\text{Bi2201}) \simeq 11$ K, in reasonably good agreement with the observed narrowing in the $(PyC_8H_{17}HgI_4)$-Bi2212 and $(PyC_1H_3HgI_4)$-Bi2201 samples. However, these temperatures would also be the relevant ones throughout each series of samples. This would suggest that Josephson coupling must be relevant in stabilizing the vortex lattice to higher temperature in samples with smaller interlayer spacings, which may explain the different power laws describing the temperature variation of $B_{\rm rms}$, as thermal breakup would be less well defined in polycrystalline samples. From this we can conclude that the low temperature data points used for the field dependence measurements are representative of an ordered vortex lattice. The present data do not provide sufficient information to quantify the relative significances of electromagnetic and Josephson coupling in the samples with intermediate layer spacing. There is also some possibility that applying the magnetic field at all angles to the CuO_2 planes, because the samples are polycrystalline, complicates the issue further [Aege98]. Previous work on the pristine material has suggested that it is close to the point where Josephson coupling is no longer relevant [Lee95]. Our results are consistent with that. Despite the fact we can show that the breakup in the samples with the largest layer spac-

ing occurs above the temperature at which we measured $B_{\mathrm{rms}}(B)$, we do not have sufficient information to model the unusual field dependences in these samples. This may be better addressed by measurements on single crystal samples.

In the following section I go on to describe the scaling relations that have previously been introduced to describe the trends in various superconducting parameters, allowing the trend observed in the penetration depth of these samples to be compared with previous data on a wide range of superconducting materials.

6.4 Scaling relations

6.4.1 Introduction to scaling relations

In many fields, ranging through all the natural sciences, a convenient means of testing theoretical models describing phenomena, particularly when the phenomena under investigation are complex, is to find trends relating different observed quantities. Examples of this are seen in seismology (the frequency and magnitude of earthquakes is related by the Gutenberg-Richter law [Gute41]), hydrology (Horton's four laws relating the properties of drainage basins [Stra05]), allometries in biology (Kleiber's Law relating metabolic rate to the mass of an organism $q \propto M^{0.75}$ [Schm84]), and within the critical region around continuous phase transitions [Binn92]. These laws take the form of power-laws between measured properties and provide initial tests for simplified theoretical descriptions of these phenomena. In simple terms, they generally arise from properties of the system in question being scale-invariant [Binn92], and often give insights into the processes underlying the observed behaviour, notably so with allometries in biology.

Scaling relations have provided a significant spur to theoretical work trying to ascertain the mechanism(s) underlying high-temperature superconductivity. Shortly after the advent of high-temperature superconductors, Uemura's μSR group made measurements of the superfluid density in a large number of the newly synthesized compounds. Bringing these results together led to a scaling relation $T_c \propto n_s/m^*$ (assuming the proportionality between the muon relaxation rate σ and the superfluid density n_s/m^*) [Uemu88, Uemu89]. This held for underdoped materials up to optimal doping, but for overdoped samples either T_c saturates while n_s/m^* increases in systems such as YBCO, or both T_c and n_s/m^* fall along a different line to the underdoped relation [Nied93]. The linear trend in

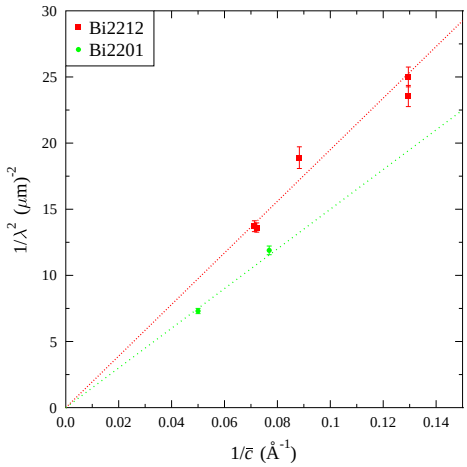

Figure 6.11: (Left) Variation of the superfluid density ($\propto 1/\lambda^2$) for the Bi2212 and Bi2201 samples of section 6.3.2 with the inverse of their interlayer spacing. The lines are $\propto 1/\bar{c}$ and are drawn as guides to the eye. (Right) Uemura scaling between T_c and T_F originally identified in Ref. [Uemu91]. The line marked T_B represents the Bose-Einstein condensation temperature. This version of the plot comes from Ref. [Uemu06] and a further updated subset of these parameters is presented in Figure 6.13.

the underdoped samples is however suggestive that there is a common behaviour between different materials in this doping region. It was noted that the conventional weak-coupling limit description of superconductivity does not predict this and also $T_c \propto n_s/m^*$ implies that $T_c \propto n_{s2d}/m^*$, given the small range of interlayer spacings (6 ± 1 Å) in the compounds studied [Uemu89]. Since these compounds are planar, $n_{s2d} \propto \epsilon_F$, where ϵ_F is the Fermi energy of a non-interacting Fermi gas (of electrons). The proportionality $T_c \propto \epsilon_F$ could originate from energy of the boson mediating the interaction being comparable to or higher than ϵ_F [Uemu89].

Exploring this further required more data, and in 1991 a further paper was published, considering a wider range of materials [Uemu91]. The resulting plot is shown in Figure 6.11 (Right). The scaling between T_c and ϵ_F was demonstrated to occur in both quasi-2D and 3D compounds, and over a range of transition temperatures $0.5 < T_c < 130$ K and Fermi temperatures ($T_F = \epsilon_F/k_B$) $10 < T_F < 100000$ K derived from the μSR data. Data lie in a broad band along the linear trend $T_c \propto T_F$, about 10 times lower than the equivalent Bose-Einstein condensation temperature, assuming the Cooper pairs would undergo such a transition, or roughly 50 times smaller than the Fermi temperature [Uemu91]. Elemen-

tal superconductors such as Nb and Pb lie well to the right of the trend line, having a much larger carrier density and relatively low T_c [Uemu91]. Emery and Kivelson derived a theoretical model for superconductors with small superfluid density, such as cuprates or molecular superconductors, where phase fluctuations of the order parameter determine T_c [Emer95]. The energy scale in this model, which should be proportional to T_c, is proportional to the superfluid density n_s/m^*, multiplied by a length scale relevant to the phase fluctuations. In materials such as the cuprates and molecular superconductors this should correspond to the layer spacing, since this is larger than the in-plane coherence length. Doing so effectively gives the in-plane superfluid density n_{s2d}/m^* so this prediction fits with the scaling behaviour observed by Uemura *et al.* [Uemu91]. More recent theoretical models have also been able to reproduce the Uemura scaling in certain limits, examples being Kopp and Chakravarty's work on the implications of the doping dependent insulator-superconductor quantum phase transition [Kopp05] and Casas *et al.*'s study of the effect of phase fluctuations using a significantly different model to that of Emery and Kivelson [Casa02].

Recent work [Zuev05, Brou06] has shown departures from the linear Uemura scaling in underdoped Y123 in both thin-film and high-quality single-crystal samples. The most detailed study of strongly underdoped Y123 thin-films included data from both thick ($\sim$ 40-unit-cell) and thin (2-unit-cell) samples [Hete07]. Thin samples showed both the 2D Kosterlitz-Thouless-Berezinski transition [Kost73], as a sharp drop in $\lambda^{-2}(T)$ and a linear scaling between T_c and $\lambda^{-2}(0)$, in agreement with Uemura scaling. Thick samples showed the $T_c \propto \sqrt{\lambda^{-2}(0)}$ scaling previously seen in thicker films and high-quality single-crystals [Zuev05, Brou06]. Franz and Iyengar [Fran06] employed a $(3+1)XY$ model to calculate the superfluid density of strongly underdoped cuprates close to the quantum critical point between the superconducting and insulating phases. They were able to show that it fitted the experimentally derived $T_c \propto (n_s/m^*)^{1/2}$, as Casas *et al.* [Casa02] and Kopp and Chakravarty [Kopp05] had done using different models.

In 2004, Homes *et al.* [Home04] reported another, more general, scaling relation between the superfluid density and the product of the dc conductivity at T_c and T_c, applying to both cuprates and elemental superconductors: $\rho_s \propto \sigma_{\mathrm{dc}} T_c$. This applied to both the *ab*-plane and *c*-axis properties of the cuprate superconductors, independent of their doping. The proportionality constant was defined within about 20 %, sufficient to include all the data presented. This success is startling, certainly

compared to the variations seen in the Uemura plots. Since its publication, however, other authors have noted that the success of this scaling relation is less general than originally proposed. For a broader range of cuprates, particularly those which are significantly overdoped, Tallon *et al.* [Tall06] showed that the Homes relation broke down severely. They were also able to suggest four possible causes for the observed scaling behaviour: marginal Fermi-liquid behaviour, Josephson coupling, dirty-limit superconductivity, and unitary impurity scattering. One of the surprising successes of Uemura's scaling relations [Uemu89, Uemu91] is their apparent applicability to a broad range of compounds. Pratt and Blundell considered whether Homes scaling encompasses molecular superconductors [Prat05]. They concluded that it did not. Molecular superconductors follow a supralinear trend on the Uemura plot and have a nearly constant product of σ_{dc} and T_c, independent of ρ_s, and therefore lie on a vertical line in Homes' plot [Prat05]. This simplicity could come from quite different physics in the molecular superconductors, possibly dominated by one parameter such as the ratio of intermolecular overlap t to on-site correlation U [Nam07].

In summary, scaling relations provide a simple means of comparing experimental data on a variety of topics, showing similarities or differences, and providing a foothold for theoretical modelling of the phenomena in question. I now go on to place the results of the μSR experiments described in this chapter in the context of the two scaling relations previously derived by Uemura and collaborators [Uemu89, Uemu91], showing that the structural tuning produced by intercalation leads to a straightforward change in the superconducting properties, as well as putting other recent results into a new context.

6.4.2 How results on intercalated superconductors fit into the picture

The extensive study of Type-II superconductors carried out using μSR over the last three decades provides a body of data with similar experimental systematics and errors. While the penetration depths derived from μSR measurements are generally considered a lower bound, since broadening of the frequency distribution due to effects such as pinning is not always considered, the way the experiments are carried out and data is analysed has been consistent over this period [Soni00]. (Motional narrowing of the vortex lattice due to thermal fluctuations or muon

hopping generally has a more identifiable effect on the data.) The experimental method is essentially that described above, although the layout of detectors and alignment of samples can vary. Data analysis for polycrystalline samples is normally done assuming that the distribution of fields is Gaussian (giving a damping of the precession signal $\exp(-\sigma^2 t^2/2)$) [Soni00], which is a moderately successful description if only relative values of λ are of interest. This model breaks down severely in single crystals and its limits can even be detected in thorough measurements of polycrystalline samples. More recently, detailed analysis of the lineshape observed in single crystals has become commonplace, leading to better agreement in λ values between μSR and other techniques [Soni00].

The method used to analyse the data of section 6.3.2 is more similar to that used for single crystals, and we must therefore find a means of comparing our λ values, and those from single crystal measurements, with the σ values common for polycrystalline samples and used in Uemura's scaling relations [Uemu89, Uemu91]. A commonly used approximation [Uemu91], following after the work of Pincus *et al.* [Pinc64], is to take:

$$\sigma = \left(\frac{2700\,\text{Å}}{\lambda}\right)^2 \text{ MHz}. \tag{6.13}$$

Using a Gaussian relaxation envelope without the factor of 1/2 leads to a correspondingly different value of σ, which has been corrected for below. Where studies have given values of σ and its definition, those values have been used directly; those studies where λ values have been given have been included using Equation 6.13. For pristine Bi2212, Equation 6.13 leads to a value of $\sigma = 1.72$ MHz for our λ value of 2000 Å, almost within the statistical error of the value of 1.84 MHz obtained from direct fitting. The situation in Bi2201 is less satisfactory, since the value of σ expected from Equation 6.13 is nearly twice as large as that derived from direct fitting. This would suggest that the Gaussian envelope truncates some of the field distribution (probably on the high-field side [Soni00]).

A number of studies have collated μSR results on cuprate and other forms of Type-II superconductors in the past, primarily Refs. [Uemu89, Uemu91, Hars92, Prat05, Uemu06], and their results have largely been included below. For further compounds a literature search was carried out. Structural information needed to produce Figure 6.13 was gained from papers reporting μSR results, references on the sample preparation cited within those papers, tables of structural data [Pool00], or from works on the structure of material with similar composi-

Table 6.4: Sources of μSR data for the compounds included in the scaling analysis.

Compound	Source(s)
Bi2212	[Uemu89, Zimm95]
Tl1212	[Uemu89]
Y124	[Shen98]
Y123	[Hars92, Bern96]
Hg1212	[Fabr99]
$(Tl_{2/3}Bi_{1/3})212$	[Aoua98]
$La_{2-x}Sr_xCuO_4$	[Hars92, Pana99]
Hg1201	[Uemu97]
Bi2201	[Webe91, Russ07]
Tl2201	[Nied93]
$Na_xCoO_2 \cdot yH_2O$	[Hige04, Kani04]
$Li_x(Zr/Hf)(THF)NCl$	[Ito04]
Molecular Superconductors (MS)	[Prat05]
MgB_2	[Serv04, Serv06]

tion. The sources of μSR data are shown in Table 6.4.

The Uemura plot shown in Figure 6.12 plots the critical temperatures of a broad range of superconductors against the Gaussian damping rate σ defined above. Since this is a plot of two measured parameters, no assumptions other than consistent methodology are required to make this plot. For the Bi2212 samples the value of σ comes from Equation 6.13 and the λ values in Table 6.3, and these give reasonable agreement with the direct fitting. For $(PyC_8H_{17}HgI_4)$-Bi2212, where the field dependence could not be fitted, the σ value comes from fitting the 400 G dataset with two Gaussian damped precession components. In Bi2201, the truncation of the field distribution due to the Gaussian approximation appears to be significant, so values from direct fitting were used for all three points. The trend in the λ values is very similar, as can be seen in Figure 6.11 (Left), but the effective σ values are approximately twice as large.

The primary result of this Uemura plot was the trend line shown in Figure 6.12. It is clear that our samples depart from this trend in a consistent and systematic way as the average layer spacing increases. This result is quite independent of the absolute value of σ or λ^{-2}, since it is also repeated when considering the latter, as the right-hand column of Table 6.3 effectively shows. To make any comment on the physics that can be drawn from this plot, we must consider what σ corresponds

Figure 6.12: Uemura plot of T_c vs. $\sigma \propto n_s/m^*$ showing the position of the results from section 6.3.2 on samples of pristine and intercalated $\mathrm{Bi2212}$ (squares) and $\mathrm{Bi2201}$ (circles). The colours are chosen to match those in Figures 6.7 and 6.8. The figure is drawn after Refs. [Uemu89, Uemu06].

to. The naïve assumption would be:

$$\sigma \propto B_{\mathrm{rms}} \propto n_s/m^*. \tag{6.14}$$

This assumes the clean limit, where the mean free path l is much greater than the coherence length ξ, which has been found to be an excellent description in high-T_c materials. Correcting for the effects of a shorter mean free path (the dirty limit) Equation 6.14 reads:

$$\sigma \propto B_{\mathrm{rms}} \propto \frac{n_s}{m^*}\frac{1}{1+\xi/l}. \tag{6.15}$$

The structural regularity of the intercalated materials seen in electron micrographs [Choy98] would suggest we are in the clean limit, as do the near constant values of $\bar{c}/\lambda^2$, which would require a fortuitous change in ξ/l as $\bar{c}$ increases. However, neither of these can be considered conclusive. There is, unfortunately, a paucity of transport data on intercalated high-T_c materials, but the two studies that have been carried out, on I_2 and HgI_2 intercalated samples, suggest that the low-temperature properties of the CuO_2 layers are unaffected [Xian92, Lee98b]. Together these justify analysing the results shown in Figure 6.12 in terms of the clean limit, as for other high-T_c materials.

The original interpretation of the $T_c \propto n_s/m^*$ trend [Uemu89] was that it signalled the strong two-dimensionality of the cuprate superconductors, with $T_c \propto \epsilon_{\mathrm{F}}$. If this is true, then the deviation from the trend shown by our samples is entirely expected, but with the ability to change the layer spacing in these samples we can separate two-dimensional from three-dimensional behaviour. Doing this shows that the correlation between bulk superfluid density, n_s/m^*, and T_c breaks down if the layer spacing is changed, so it cannot be the parameter controlling T_c. One might consider the possibility of the 3D superfluid density within each superconducting block being the relevant parameter, but this would still leave 2D physics dominant.

To find out whether the density of superconducting carriers related to each CuO_2 plane gives a clearer trend in T_c, I now relate the results from intercalated superconductors to the second trend Uemura identified, between T_c and n_{s2D}/m^* [Uemu91]. These parameters are plotted for a wide range of layered superconductors in Figure 6.13, together with certain power laws that seem effective in describing certain groups of compounds. To maintain a consistent methodology with previous results, the λ value derived from the Gaussian depolarization

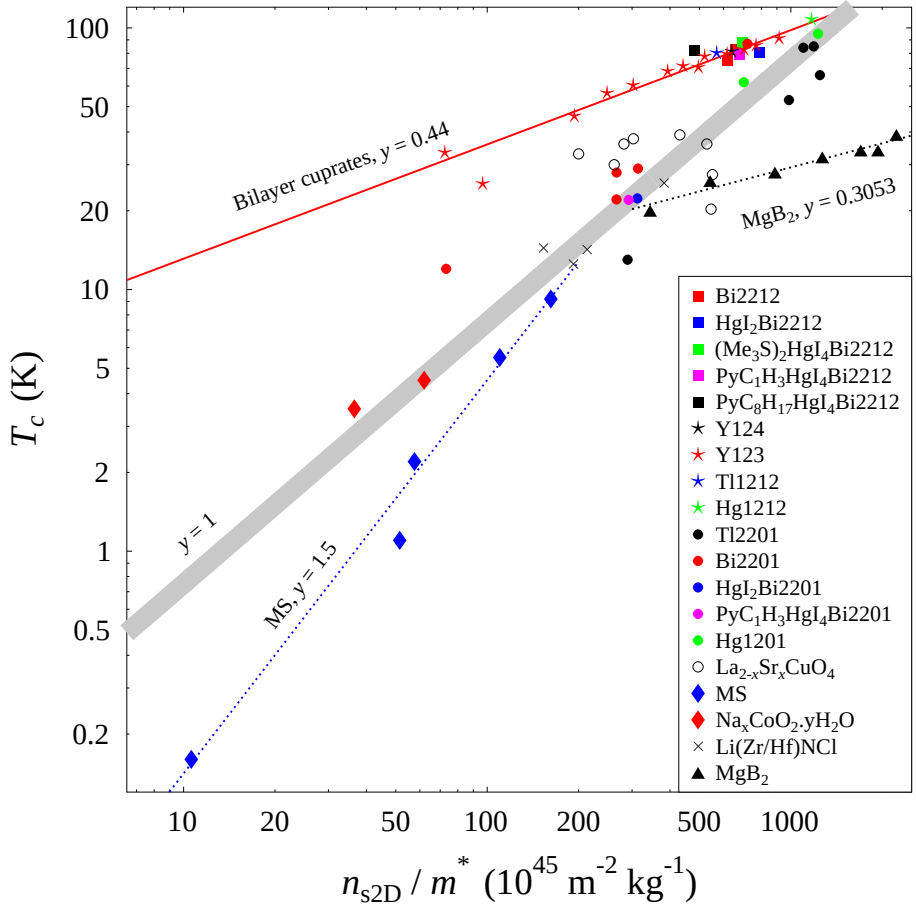

Figure 6.13: Uemura plot of T_c vs. n_{s2d}/m^* for a variety of layered superconductors. n_{s2d}/m^* is proportional to the Fermi energy for these quasi-two-dimensional systems. The derivation of n_{s2d}/m^* and sources for the data are discussed in the text. The red, blue, and black lines are fits to bilayer cuprate, molecular superconductor, and MgB_2 data, respectively. The grey line is a guide to the eye. A version of this plot in terms of the Fermi temperature, which covers a broader range of samples and a larger parameter range, is presented in Figure 6.11(Left) [Uemu91, Uemu06].

rate σ was used in calculating the superfluid density in each layer, n_{s2D}/m^*. For this analysis I have limited myself to compounds which have a layered structure, since the comparison between the layered compounds and more three-dimensional materials has been widely discussed [Uemu91, Uemu06] and we have a more direct comparison with the intercalated specimens. A rough trend of $T_c \propto n_{\mathrm{s2D}}/m^*$ is shown as a broad grey line in Figure 6.13. This line runs through the maximum $T_c(n_{\mathrm{s2D}}/m^*)$ values for all the families of superconductors considered, except MgB_2. The most comprehensively studied family of compounds in this plot are the bilayer cuprates, particularly Y123. Because of the large number of data points in this family, it is possible to fit a power law:

$$T_c \propto \left(\frac{n_{\mathrm{s2D}}}{m^*}\right)^y, \tag{6.16}$$

to these points. The value of $y = 0.44(3)$ is obtained fitting over all the bilayer cuprate values. A similar power law dependence, albeit for n_s/m^*, has been found in experiments on Y123 thin films ($y = 0.43(7)$) [Zuev05]. It is also possible to fit all the quasi-2D molecular superconductors with a single power law, $y = 1.5(1)$ as observed previously for n_s/m^* [Prat05]. Plotting the MgB_2 values on this graph shows that they occupy a different region of the plot to the cuprates, high superfluid density but low critical temperature, as might be expected from their other properties. It is apparent that they also show a power law scaling between these parameters, which fitting determined to be $y = 0.31(3)$, as opposed to the $y = 1/2$ previously proposed for n_s/m^* [Schn07]. The behaviour seen in the overdoped cuprates does not clearly fit on a single power law, neither do similar power laws describe the overdoped cuprates in each family. The behaviour within this doping range has received less attention in μSR studies so it is not possible to draw conclusions on the scaling behaviour for overdoped materials.

6.4.3 Conclusions that can be drawn from new scaling plots

In the two scaling plots, Figures 6.12 and 6.13, we see that no single trend is sufficient to describe all the data. Limits to both general trends had been identified in the past, so this merely confirms those observations. That a particular scaling trend does not describe all available data should not be seen as a failure, since distinguishing different mechanisms underlying the phenomena under investigation can rely on this. The significant feature is the way in which the data

departs from the general trends. In Figure 6.11 (Left) we see that the bulk superfluid density, n_s/m^*, of the intercalated samples falls linearly with the increased layer spacing. We also demonstrated that there are no significant changes in T_c as the layer spacing changes. The trend $T_c \propto n_s/m^*$ therefore cannot adequately describe our data. In fact, we can make the stronger statement that the bulk superfluid density n_s/m^* cannot be the only parameter controlling T_c. Moving our attention to Figure 6.13, certain patterns emerge that include the data from the intercalated samples. We can describe these patterns in terms of power laws in the form of Equation 6.16 as described above. It is interesting to note that the values of the power y are close to ratios of small integers ($y = 1, 1/2, 1/3, 3/2$). The sublinear $T_c \propto (n_{\mathrm{s2D}}/m^*)^{1/2}$ trend seems to repeat for underdoped materials in the single and bi-layer cuprate families, and is also consistent with the underdoped $Na_xCoO_2 \cdot yH_2O$ data. This would strongly suggest that the mechanisms of superconductivity in each of these families have strong similarities. The highest T_c values observed in each family lie close to a common $T_c \propto n_{\mathrm{s2D}}/m^*$ trend, except MgB_2, which shows an entirely separate $T_c \propto (n_{\mathrm{s2D}}/m^*)^{1/3}$ trend. I now identify some theoretical models which have predicted appropriate trends in the superfluid density and may offer some insight into the mechanism underlying the superconductivity.

The linear $T_c \propto n_{\mathrm{s2D}}/m^*$ trend was the first to be identified [Uemu89, Uemu91], and has therefore received the most theoretical attention. Emery and Kivelson [Emer95] suggested that thermal fluctuations of the phase of the superconducting order parameter would account for this. They derived an equation for the temperature, $T_\theta^{\max}$, at which thermal fluctuations would break up superconducting phase coherence:

$$T_\theta^{\max} = A\frac{\epsilon_0 c^2 a}{4e^2}\frac{n_s}{m^*}, \tag{6.17}$$

where A is a coupling constant and a is a length scale characterizing the size of the fluctuating region, identified with the interlayer spacing for organics and cuprates. The parameter A was suggested to be within the range 0.9 (vanishingly small interlayer coupling) and 2.2 (isotropic 3D). If the length scale a is identified with the interlayer spacing $\bar{c}$ [Emer95], the grey trend line plotted in Figure 6.13 is approximately $T_\theta^{\max}/T_c = 2.7$. $T_\theta^{\max}/T_c$ was found to be in the range 0.7-$\sim$ 4 [Emer95], consistent with the appearance of fluctuating superconductivity above T_c, the pseudogap region [Xu00, Nam07]. An alternative means of deriving

a linear relationship between T_c and n_s for a two-dimensional system relies on the scaling of these parameters near a doping-dependent Quantum Critical Point (QCP) [Kopp05, Fran06]:

$$T_c \propto n_s(0)^{z/(z+d-2)}, \tag{6.18}$$

where z is the quantum dynamical critical exponent [Hohe77] (quite different from its thermal equivalent) and d is the spatial dimensionality. If $d = 2$, we have the desired linear relation for an effectively two-dimensional superfluid density.

The three dimensional case of Equation 6.18, where z will be between 1 and 2, gives a power $1/2 \leq y \leq 2/3$, close to the observed power law $y = 0.44(3)$. Schneider [Schn07] suggested an alternative origin for a square root power law, based on BCS scaling. It was further suggested that the hyperscaling relation of Equation 6.18 would not be appropriate for modelling 3D quantum superconductor-metal phase transitions, since the upper critical dimension is $d = 2$. It is puzzling that these methods predict a power law for the scaling between T_c and the bulk superfluid density matching the observed power law describing the scaling between the superfluid density in each layer and T_c. Since the results in intercalated superconductors show that the superfluid density within each superconducting block is the constant parameter, rather than the bulk superfluid density, it is difficult to reconcile these results. One possibility may be that there is a bulk superfluid density within the blocks, and this appears similar to the superfluid density in each layer as the layer spacing changes. The thin-film results on 2 unit cell thick Y123 [Hete07] suggest that the physics is two-dimensional in this case, so this description is probably unhelpful. Alternatively, it may be necessary to reinterpret the superfluid density considered in these scaling relations.

The two groups of compounds that do not fall within the theoretical framework above are MgB_2, where $y \sim 1/3$, and the molecular superconductors, where $y = 1.5(1)$. Kopp and Chakravarty suggested that y might be larger than one in overdoped superconductors, and it is possible that the molecular superconductors might have some similarity in their superconducting mechanism that causes this agreement [Kopp05]. A model offering a consistent framework that could include all the power laws observed in Figure 6.13 was proposed by Casas *et al.* [Casa02]. They considered a gas of pre-formed Cooper pairs as bosons that condensed at T_c. The N_B bosons have a mass m_B and an dispersion relation $\epsilon(K) = C_s K^s$ with $s > 0$ and C_s a constant. The system has a dimensionality d such that

$n_B = N_B/L^d$. Their simpler model, excluding the effects of the background fermions (unpaired electrons) predicts:

$$T_c \propto (n_B)^{s/d}, \tag{6.19}$$

where the constant of proportionality can be derived in terms of numerical and physical constants, and $T = 0$ for $s > d$. If the dispersion relation is linear then we would get appropriate power laws for the quasi-two-dimensional underdoped cuprates and hydrated $NaCoO_2$, and also for the quasi-three-dimensional MgB_2. This model cannot predict any power law with $y > 1$, so cannot describe the molecular superconductors. The full model, including the unpaired electrons, does not lead to such a simple power law scaling, but does give T_c values of the correct magnitude for the underdoped cuprates [Casa02]. While having certain promising characteristics, this model does not currently provide sufficient information to allow a satisfactory test against experiment.

Although certain trends relating the two-dimensional superfluid density within each layer to T_c can be identified, it is not currently possible to unambiguously relate these trends to a theoretical model that can clearly identify more than the characteristics of the mechanism underlying the superconductivity in these materials. Nonetheless, these trends are well defined, and including results from intercalated superconductors strongly justifies thinking in terms of the physics of the layers. It is hoped that this interpretation may provide an alternative means of considering previously identified scaling trends and a grouping of different superconducting families helpful in elucidating their superconducting mechanisms.

6.5 Conclusion

The detailed conclusions of this chapter are contained in sections 6.3.4 and 6.4.3. It remains to note here that the experiments on intercalated superconductors verified that reliable results could be obtained for the superfluid density of these materials as the interlayer spacing was increased by a factor of around 2. These results clearly demonstrated that the previously identified trend relating T_c and the bulk superfluid density n_s/m^* did not offer a plausible description of intercalated specimens, where the bulk superfluid density fell proportionately to the increase in the interlayer spacing but T_c was unchanged. Considering the super-

fluid density to be constant within each layer and proportional, in some way, to T_c gives a satisfactory description of the intercalated superconductors. Plotting the T_c values for a broad range of samples against their two-dimensional superfluid density leads to a number of power laws appropriate for different families of compounds, and to distinguishing underdoped and overdoped materials in each family. It is not possible to conclusively assign theoretical explanations for these power laws, although similar power laws have been derived from a number of models.

While the variation of the bulk superfluid density as a function of layer spacing has clearly been established by this work, this trend could be verified using other techniques, such as microwave measurements or Small Angle Neutron Scattering (SANS). The difficulty in doing such experiments, as with most possible extensions to this work, lies in the preparation of larger intercalated single crystals, particularly for SANS. With such samples, μSR experiments could make a far more detailed study of the order-disorder transitions in the vortex lattice. Since our results on polycrystalline samples with the largest layer spacings strongly suggest that Josephson coupling between vortices is no longer relevant, it is conceivable that suitable intercalated single crystal specimens might allow measurements of vortex lattice behaviour in a situation where electromagnetic coupling completely dominates Josephson coupling. There are certain experimental systematics in polycrystalline samples, particularly the effect of demagnetizing factors on the width of the field distribution in low magnetic fields, that were too complicated to be dealt with in this work. A detailed study of the microscopic structure of intercalated polycrystallites using neutron scattering might be a first step towards treating this problem quantitatively, since the angular distribution of crystallites could be measured directly.

This chapter has reported a detailed study of the effect of a geometrical change to the structure of high-T_c superconductors without strongly affecting the properties of the cuprate layers. Intercalation chemistry is notable for its flexibility in tuning the properties of materials. The possibility of intercalating a guest species that would have a functional effect on the cuprate layers remains an enticing prospect. While we were able to exclude that for the paramagnetic radical described above, the possibility remains that functional nanostructures including superconducting cuprate layers could be produced in future. The properties of such materials could provide an even richer combination of physical phenomena than those materials described in the present investigation.

Bibliography

[Abra61] A. Abragam, *The principles of nuclear magnetism*, (Clarendon Press, Oxford, 1961).

[Abra70] A. Abragam and B. Bleaney, *Electron paramagnetic resonance of transition metal ions*, (Clarendon Press, Oxford, 1970).

[AlsN01] J. Als-Nielsen and D. F. McMorrow, *Elements of modern X-ray physics*, (Wiley, New York, 2001).

[Ande84] P. W. Anderson, *Basic Notions of Condensed Matter Physics*, (Benjamin/Cummings, Menlo Park, California, 1984).

[Balc89] E. Balcar and S. W. Lovesey, *Theory of magnetic neutron and photon scattering*, (Clarendon Press, Oxford, 1989).

[Bedn86] J. G. Bednorz and K. A. Müller, *Z. Phys. B* **64**, 189 (1986).

[Blun01] S. J. Blundell, *Magnetism in Condensed Matter Physics*, (OUP, Oxford, 2001).

[Borz07] R. A. Borzi, S. A. Grigera, J. Farrell, R. S. Perry, S. J. S. Lister, S. L. Lee, D. A. Tennant, Y. Maeno, A. P. Mackenzie, *Science* **315**, 214 (2007).

[Brew94] J. S. Brewer, in *Encyclopedia of Applied Physics* **11**, 23 (VCH Publishers, Inc., 1994).

[Chai95] P. M. Chaikin and T. C. Lubensky, *Principles of Condensed Matter Physics*, (CUP, Cambridge, 1995).

[Cox92] P. A. Cox, *Transition metal oxides: an introduction to their electronic structure and properties*, (Clarendon Press, Oxford, 1992).

[Garw57] R. L. Garwin, L. M. Lederman and M. Weinrich, *Phys. Rev.* **105**, 1415 (1957).

[Hore95] P. J. Hore, *Nuclear Magnetic Resonance*, (OUP, Oxford, 1995).

[Kitt96] C. Kittel, *Introduction to solid state physics*, (7^{th} ed., Wiley, New York, 1996).

[Lanc06] T. Lancaster, S. J. Blundell, M. L. Brooks, P. J. Baker, F. L. Pratt, J. L. Manson, C. P. Landee, and C. Baines, *Phys. Rev. B* **73**, 020410(R) (2006).

[Love84] S. W. Lovesey, *Theory of neutron scattering from condensed matter*, Vols. 1 & 2, (Clarendon Press, Oxford, 1984).

[Luke98] G. M. Luke, Y. Fudamoto, K. M. Kojima, M. I. Larkin, J. Merrin, B. Nachumi, Y. J. Uemura, Y. Maeno, Z. Q. Mao, Y. Mori, H. Nakamura, and M. Sigrist, *Nature* **394**, 558 (1998).

[Pine63] D. Pines, *Elementary excitations in solids : lectures on phonons, electrons and plasmons*, (W. A. Benjamin, New York, 1963).

[Prat05] F. L. Pratt and S. J Blundell, *Phys. Rev. Lett.* **94**, 097006 (2005).

[Rami97] A. P. Ramirez, *J. Phys.: Condens. Matter* **9**, 8171 (1997).

[Rao98] C. N. R. Rao and B. Raveau, *Transition metal oxides: structure, properties, and synthesis of ceramic oxides*, (2nd ed., Wiley-VCH, New York, 1998).

[Snyd01] J. Snyder, J. S. Slusky, R. J. Cava, and P. Schiffer, *Nature* **413**, 48 (2001).

[Squi78] G. L. Squires, *Introduction to the theory of thermal neutron scattering*, (Cambridge University Press, Cambridge, 1978).

[Uemu89] Y. J. Uemura, G. M. Luke, B. J. Sternlieb, J. H. Brewer, J. F. Carolan, W. N. Hardy, R. Kadono, J. R. Kempton, R. F. Kiefl, S. R. Kreitzman, P. Mulhern, T. M. Riseman, D. Ll. Williams, B. X. Yang, S. Uchida, H. Takagi, J. Gopalakrishnan, A. W. Sleight, M. A. Subramanian, C. L. Chien, M. Z. Cieplak, G. Xiao, V. Y. Lee, B. W. Statt, C. E. Stronach, W. J. Kossler, and X. H. Yu, *Phys. Rev. Lett.* **62**, 2317 (1989).

[Uemu91] Y. J. Uemura, L. P. Le, G. M. Luke, B. J. Sternlieb, W. D. Wu, J. H. Brewer, T. M. Riseman, C. L. Seaman, M. B. Maple, M. Ishikawa, D. G. Hinks, J. D. Jorgensen, G. Saito, and H. Yamochi, *Phys. Rev. Lett.* **66**, 2665 (1991).

[Whit79] G. K. White, *Experimental techniques in low-temperature physics*, (Clarendon Press, Oxford, 1979).

Chapter 2

[Abel99] R. Abela, A. Amato, C. Baines, X. Donath, R. Erne, D. C. George, D. Herlach, G. Irminger, I. D. Reid, D. Renker, G. Solt, D. Suhi, M. Werner, and U. Zimmermann, *Hyp. Int.* **120/121**, 575 (1999).

[Amat06] A. Amato, *GPS User Guide* (2006).
http : //lmu.web.psi.ch/facilities/gps/User_Guide_version_march_2006.pdf

[Bake08] P. J. Baker, P. D. Battle, S. J. Blundell, F. Grandjean, T. Lancaster, G. J. Long, S. E. Oldham, and T. J. Prior, *Phys. Rev. B* **77**, 134405 (2008).

[Benn04] G. W. Bennett *et al.*, *Phys. Rev. Lett.* **92**, 161802 (2004).

[Blun99] S. J. Blundell, Contemp. Phys. **40**, 175 (1999).

[Brew86] J. H. Brewer, S. R. Kreitzman, D. R. Noakes, E. J. Ansaldo, D. R. Harshman, and R. Keitel, *Phys. Rev. B* **33**, 7813 (1986).

[Brew94] J. S. Brewer, in *Encyclopedia of Applied Physics* **11**, 23 (VCH Publishers, Inc., 1994).

[Chap84] J. Chappert, *Principles of the μSR Technique*, in: J. Chappert and R. I. Grynszpan (eds.): *Muons and Pions in Materials Research*, Amsterdam (1987).

[Chit07] D. B. Chitwood, T. I. Banks, M. J. Barnes, S. Battu, R. M. Carey, S. Cheekatmalla, S. M. Clayton, J. Crnkovic, K. M. Crowe, P. T. Debevec, S. Dhamija, W. Earle, A. Gafarov, K. Giovanetti, T. P. Gorringe, F. E. Gray, M. Hance, D. W. Hertzog, M. F. Hare, P. Kammel, B. Kiburg, J. Kunkle, B. Lauss, I. Logashenko, K. R. Lynch, R. McNabb, J. P. Miller, F. Mulhauser, C. J. G. Onderwater, C. S. Özben, Q. Peng, C. C. Polly, S. Rath, B. L. Roberts, V. Tishchenko, G. D. Wait, J. Wasserman, D. M. Webber, P. Winter, and P. A. Żołnierczuk, *Phys. Rev. Lett.* **99**, 032001 (2007).

[Cox87] S. F. J. Cox, *J. Phys. C* **20**, 3187 (1987).

[Dalm97] P. Dalmas de Reotier and A. Yaouanc, *J. Phys.: Condens. Matter* **9**, 9113 (1997).

[Eato99] G. H. Eaton and S. H. Kilcoyne, in *Muon Science: Muons in Physics, Chemistry and Materials*, eds. S. L. Lee, S. H. Kilcoyne, and R. Cywinski, *Proceedings of the Fifty First Scottish Universities Summer School in Physics*, (IoP Publishing, Bristol, 1999).

[Evan06] M. Evangelisti, F. Luis, L. J. de Jongh, and M. Affronte, *J. Mater. Chem.* **16**, 2534 (2006).

[Garw57] R. L. Garwin, L. M. Lederman and M. Weinrich, *Phys. Rev.* **105**, 1415 (1957).

[GPSWeb] http : //lmu.web.psi.ch/facilities/gps/gps.html

[Hill05] A. D. Hillier, P. J. C. King, S. P. Cottrell, and J. S. Lord, *The MuSR User Guide* (ISIS Facility, CCLRC Rutherford Appleton Laboratory, 2005).
http : //www.isis.rl.ac.uk/muons/musr/MuSRManual.pdf

[Hwan97] J. S. Hwang, K. J. Lin, and C. Tien, *Rev. Sci. Instrum.* **68**, 94 (1997).

[Jami06] B. Jamieson, R. Bayes, Yu. I. Davydov, P. Depommier, J. Doornbos, W. Faszer, M. C. Fujiwara, C. A. Gagliardi, A. Gaponenko, D. R. Gill, P. Gumplinger, M. D. Hasinoff, R. S. Henderson, J. Hu, P. Kitching, D. D. Koetke, J. A. Macdonald, R. P. MacDonald, G. M. Marshall, E. L. Mathie, R. E. Mischke, J. R. Musser, M. Nozar, K. Olchanski, A. Olin, R. Openshaw, T. A. Porcelli, J.-M. Poutissou, R. Poutissou, M. A. Quraan, N. L. Rodning, V. Selivanov, G. Sheffer, B. Shin, T. D. S. Stanislaus, R. Tacik, V. D. Torokhov, R. E. Tribble, and M. A. Vasiliev, *Phys. Rev. D* **74**, 072007 (2006).

[Lanc07] T. Lancaster, S. J. Blundell, P. J. Baker, M. L. Brooks, W. Hayes, F. L. Pratt, J. L. Manson, M. M. Conner, J. A. Schlueter, and C. P. Landee, *Phys. Rev. Lett.* **99**, 267601 (2007).

[Lanc08] T. Lancaster, S. J. Blundell, P. J. Baker, M. L. Brooks, W. Hayes, F. L. Pratt, R. Coldea, T. Sörgel, and M. Jansen, *Phys. Rev. Lett.* **100**, 017206 (2008).

[Lars03] F. K. Larsen, E. J. L. McInnes, H. El Mkami, J. Overgaard, S. Piligkos, G. Rajaraman, E. Rentschler, A. A. Smith, G. M. Smith, V. Boote, M. Jennings, G. A. Timco, R. E. P. Winpenny, *Angew. Chem. Int. Ed.* **42**, 101 (2003).

[Lash03] J. C. Lashley, M. F. Hundley, A. Migliori, J. L. Sarrao, P. G. Pagliuso, T. W. Darling, M. Jaime, J. C. Cooley, W. L. Hults, L. Morales, D. J. Thoma, J. L. Smith, J. Boerio-Goates, B. F. Woodfield, G. R. Stewart, R. A. Fisher, and N. E. Phillips, *Cryogenics* **43**, 369 (2003).

[Lee99] *Muon Science: Muons in Physics, Chemistry and Materials*, eds. S. L. Lee, S. H. Kilcoyne, and R. Cywinski, *Proceedings of the Fifty First Scottish Universities Summer School in Physics*, (IoP Publishing, Bristol, 1999).

[Mans07] J. L. Manson *et al.*, (unpublished).

[MPMS90] *MPMS Hardware User's Manual*, (Quantum Design, 1990).

[MPMS99] *Magnetic Property Measurement System: Reciprocating Sample Option User's Manual*, (Quantum Design, 1999).

[MuSRWeb] http : //www.isis.rl.ac.uk/muons/musr/

[Naga03] K. Nagamine, *Introductory Muon Science*, (Cambridge University Press, 2003).

[PPMS00] *Physical Property Measurement System: Hardware Manual*, (Quantum Design, 2000).

[Prat00] F. L. Pratt, *Physica B* **289**, 710 (2000).
http : //www.isis.rl.ac.uk/muons/data_analysis/wimda/index.htm

[Prat07] F. L. Pratt, P. J. Baker, S. J. Blundell, T. Lancaster, M. A. Green, and M. Kurmoo, *Phys. Rev. Lett.* **99**, 017202 (2007).

[Part06] Review of Particle Physics, *J. Phys. G: Nucl. Part. Phys.* **33**, 1 (2006).

[Sche85] A. Schenck, *Muon Spin Rotation Spectroscopy*, Bristol (1985).

[Schw75] R. E. Schwall, R. E. Howard, and G. R. Stewart, *Rev. Sci. Instrum.* **46**, 1054 (1975).

[Soni02] J. E. Sonier, *Muon Spin Rotation/Relaxation/Resonance (μSR) Brochure*,
http : //musr.org/intro/musr/muSRBrochure.pdf, (2002).

Chapter 3

[Ande73] P. W. Anderson, *Mater. Res. Bull.* **8**, 153 (1973).

[Bajp97] A. Bajpai and A. Banerjee, *Phys. Rev. B* **55**, 12439 (1997).

[Bake05] P. J. Baker, T. Lancaster, S. J. Blundell, M. L. Brooks, W. Hayes, D. Prabhakaran, and F. L. Pratt, *Phys. Rev. B* **72**, 104414 (2005).

[Bake06] P. J. Baker, T. Lancaster, S. J. Blundell, M. L. Brooks, W. Hayes, D. Prabhakaran, and F. L. Pratt, *Physica B* **374-375**, 47 (2006).

[Barr98] A. L. Barra, G. Chouteau, A. Stepanov, and C. Delmas, *J. Mag. Magn. Mat.* **177-181**, 783 (1998).

[Bond08] M. Bonda *et al.*, (manuscript in preparation).

[Bong66] P. F. Bongers and U. Enz, *Sol. Stat. Commun.* **4**, 153 (1966).

[Bors95] F. Borsa, P. Carreta, J. H. Cho, F. C. Chou, Q. Hu, D. C. Johnston, A. Lascialfari, D. R. Torgeson, R. J. Gooding, N. M. Salem, and K. J. E. Vos, *Phys. Rev. B* **52**, 7334 (1995).

[Bram95] S. T. Bramwell, P. C. W. Holdsworth, and M. T. Hutchings, *J. Phys. Soc. Japan* **64**, 3066 (1995).

[Chap00a] E. Chappel, M. D. Núñez-Regueiro, F. Dupont, G. Chouteau, C. Darie, and A. Sulpice, *Euro. Phys. J. B* **17**, 609 (2000).

[Chap00b] E. Chappel, M. D. Núñez-Regueiro, G. Chouteau, O. Isnard, and C. Darie, *Euro. Phys. J. B* **17**, 615 (2000).

[Chat05] T. Chatterji, W. Henggeler, C. Delmas, *J. Phys.: Condens. Matter* **17**, 1341 (2005).

[Chun05] J.-H. Chung, Th. Proffen, S. Shamoto, A. M. Ghorayeb, L. Croguennec, W. Tian, B. C. Sales, R. Jin, D. Mandrus, and T. Egami, *Phys. Rev. B* **71**, 064410 (2005).

[Cold03] R. Coldea, D. A. Tennant, and Z. Tylczynski, *Phys. Rev. B* **68**, 134424 (2003).

[Coll97] M. F. Collins and O. A. Petrenko, *Can. J. Phys.* **75**, 605 (1997).

[Cort96] M. Corti, S. Marini, A. Rigamonti, V. Massarotti, and D. Capsoni, *J. Appl. Phys.* **79**, 6621 (1996).

[Daré03] A.M. Daré, R. Hayn, and J.L. Richard, *Europhys. Lett.* **61**, 803 (2003).

[Dari05] C. Darie, P. Bordet, S. de Brion, M. Holzapfel, O. Isnard, A. Lecchi, J. E. Lorenzo, and E. Suard, *Euro. Phys. J. B* **43**, 159 (2005).

[Dyer54] L. D. Dyer, B. S. Borie Jr., and G. P. Smith, *J. Am. Chem. Soc.* **76**, 1499 (1954).

[Godd05] P. A. Goddard, P. J. Baker, S. J. Blundell, and J. Singleton, *National High Magnetic Field Laboratory 2005 Research Report*, p.255.

[Good58] J. B. Goodenough, D. G. Wickham, and W. J. Croft, *J. Phys. Chem. Solids* **5**, 107 (1958).

[Hira85] K. Hirakawa, H. Kadowaki, and K. Ubukoshi, *J. Phys. Soc. Japan* **54**, 3526 (1985).

[Hiro91] K. Hirota, Y. Nakazawa, and M. Ishikawa, *J. Phys.: Condens. Matter* **3**, 4721 (1991).

[Hohe77] P. C. Hohenberg and B. I. Halperin, *Rev. Mod. Phys.* **49**, 435 (1977).

[Holz04] M. Holzapfel, S. de Brion, C. Darie, P. Bordet, E. Chappel, G. Chouteau, P. Strobel, A. Sulpice, and M. D. Núñez-Regueiro, *Phys. Rev. B* **70**, 132410 (2004).

[Holz05] M. Holzapfel, C. Darie, P. Bordet, E. Chappel, M.-D. Núñez-Regueiro, S. Diaz, S. de Brion, G. Chouteau and P. Strobel, *Solid State Sciences* **7**, 497 (2005).

[Kemp90] J. P. Kemp, P. A. Cox, and J. W. Hodby, *J. Phys.: Condens. Matter* **2**, 6699 (1990).

[Kiku99] H. Kikuchi, H. Nagasawa, M. Mekata, Y. Fudamoto, K. M. Kojima, G. M. Luke, Y. J. Uemura, H. Mamiya, and T. Naka, *Hyp. Int.* **120-121**, 623 (1999).

[Kita98] Y. Kitaoka, T. Kobayashi, A. Koda, H. Wakabayashi, Y. Niino, H. Yamakage, S. Taguchi, K. Amaya, K. Yamaura, M. Takano, A. Hirano and R. Kanno, *J. Phys. Soc. Japan* **67**, 3703 (1998).

[Koba00] S. Kobayashi, S. Mitsuda, and K. Prokes, *Phys. Rev. B* **63**, 024415 (2000).

[Lewi05] M. J. Lewis, B. D. Gaulin, L. Filion, C. Kallin, A. J. Berlinsky, H. A. Dabkowska, Y. Qiu, and J. R. D. Copley, *Phys. Rev. B* **72**, 014408 (2005).

[Mesk04] H. Meskine and S. Satpathy, *J. Appl. Phys.* **97**, 10A314 (2004).

[Mydo93] J. A. Mydosh, *Spin glasses: an experimental introduction*, (Taylor & Francis, London, 1993).

[Ogie85] A. T. Ogielski, *Phys. Rev. B* **32**, 7384 (1985).

[Park06] S. Park, K. Kang, W.-S. Yoon, A. R. Moodenbaugh, L. H. Lewis, and T. Vogt, *Sol. Stat. Commun.* **139**, 60 (2006).

[Park07] S. Park, W.-S. Yoon, and T. Vogt, *Sol. Stat. Commun.* **142**, 75 (2007).

[Pere96] J. P. Peres, C. Delmas, A. Rougier, M. Broussely, F. Perton, P. Biensan, and P. Willman, *J. Phys. Chem. Solids* **57**, 1057 (1996).

[Peti06] L. Petit, G. M. Stocks, T. Egami, Z. Szotek, and W. M. Temmerman, *Phys. Rev. Lett.* **97**, 146405 (2006).

[Poui00] C. Pouillerie, L. Croguennec, P. Biensan, P. Willmann, and C. Delmas, *J. Electrochem. Soc.* **147**, 2061 (2000).

[Reim93] J. N. Reimers, J. R. Dahn, J. E. Greedan, C. V. Stager, G. Liu, I. Davidson, and U. von Sacken, *J. Solid State Chem.* **102**, 542 (1993).

[Reit05] A. J. W. Reitsma, L. F. Feiner, and A. M. Oleś, *New J. Phys.* **7**, 121 (2005).

[Reyn01] F. Reynaud, D. Mertz, F. Celestini, J.-M. Debierre, A. M. Ghorayeb, P. Simon, A. Stepanov, J. Voiron, and C. Delmas, *Phys. Rev. Lett.* **86**, 3638 (2001).

[Roug95] A. Rougier, C. Delmas, and A. V. Chadwick, *Sol. Stat. Commun.* **94**, 123 (1995).

[Roug96] A. Rougier, C. Delmas, and G. Chouteau, *J. Phys. Chem. Solids* **57**, 1101 (1996).

[Sale04] B. C. Sales, R. Jin, K. A. Affholter, P. Khalifah, G. M. Veith, and D. Mandrus, *Phys. Rev. B* **70**, 174419 (2004).

[Schr02] M. Schreyer and M. Jansen, *Angew. Chem. Int. Ed.* **41**, 643 (2002).

[Sörg05] T. Sörgel and M. Jansen, *Z. Anorg. Allg. Chem.* **631**, 2970 (2005).

[Sugi06] J. Sugiyama, Y. Ikedo, K. Mukai, J. H. Brewer, E. J. Ansaldo, G. D. Morris, K. H. Chow, H. Yoshida, and Z. Hiroi, *Phys. Rev. B* **73**, 224437 (2006).

[Taka03] K. Takada, H. Sakurai, E. Takayama-Muromachi, F. Izumi, R. A. Dilanian, and T. Sasaki, *Nature* **422**, 53 (2003).

[Torn99] S. Tornow, O. Entin-Wohlman, and A. Aharony, *Phys. Rev. B* **60**, 10206 (1999).

[Vern04] F. Vernay, K. Penc, P. Fazekas, and F. Mila, *Phys. Rev. B* **70**, 014428 (2004).

[Wawr07] E. Wawrzyńska, R. Coldea, E. M. Wheeler, I. I. Mazin, M. D. Johannes, T. Sörgel, M. Jansen, R. M. Ibberson, and P. G. Radaelli, *Phys. Rev. Lett.* **99**, 157204 (2007).

[Whee07] E. M. Wheeler, (private communication).

[Yama96] K. Yamaura, M. Takanoa, A. Hiranob, and R. Kanno, *J. Solid State Chem.* **127**, 109 (1996).

[Yosh06] H. Yoshida, Y. Muraoka, T. Sorgel, M. Jansen, and Z. Hiroi, *Phys. Rev. B* **73**, 020408 (2006).

Chapter 4

[Akim01] J. Akimitsu, H. Ichikawa, N. Eguchi, T. Miyano, M. Nishi, and K. Kakurai, *J. Phys. Soc. Japan* **70**, 3475 (2001).

[Blun01] S. J. Blundell, *Magnetism in Condensed Matter Physics*, (OUP, Oxford, 2001).

[Boek84] C. Boekema, R. L. Lichti, and K. J. Rüegg, *Phys. Rev. B* **30**, 6766 (1984).

[CeGu01] M. Cestelli Guidi, G. Allodi, R. De Renzi, G. Guidi, M. Hennion, L. Pinsard, and A. Amato, *Phys. Rev. B* **64**, 064414 (2001).

[Cwik03] M. Cwik, T. Lorenz, J. Baier, R. Müller, G. André, F. Bourée, F. Lichtenberg, A. Freimuth, R. Schmitz, E. Müller-Hartmann, and M. Braden, *Phys. Rev. B* **68**, 060401 (2003).

[Frit02] V. Fritsch, J. Hemberger, M. V.Eremin, H.-A. Krug von Nidda, F. Lichtenberg, R. Wehn, and A. Loidl, *Phys. Rev. B* **65**, 212405 (2002).

[Garc95a] J.L. García-Muñoz, P. Lacorre, and R. Cywinski, *Phys. Rev. B* **51**, 15197 (1995).

[Glaz72] A. M. Glazer, *Acta Cryst. B* **28**, 3384 (1972).

[Gold26] V. M. Goldschmidt, *Naturwissenschaften*, **14**, 477 (1926).

[Hahn95] *International Tables of Crystallography, Volume A: Space-Group Symmetry*, Fourth, Revised Edition, ed. T. Hahn, (Kluwer Academic Publishing, Dordrecht, 1995).

[Have05] M. W. Haverkort, Z. Hu, A. Tanaka, G. Ghiringhelli, H. Roth, M. Cwik, T. Lorenz, C. Schüßler-Langeheine, S. V. Streltsov, A. S. Mylnikova, V. I. Anisimov, C. de Nadai, N. B. Brookes, H. H. Hsieh, H.-J. Lin, C. T. Chen, T. Mizokawa, Y. Taguchi, Y. Tokura, D. I. Khomskii, and L. H. Tjeng, *Phys. Rev. Lett.* **94**, 056401 (2005).

[He01] T. He, Q. Huang, A. P. Ramirez, Y. Wang, K. A. Regan, N. Rogado, M. A. Hayward, M. K. Haas, J.S. Slusky, K. Inumara, H. W. Zandbergen, N. P. Ong, and R. J. Cava, *Nature* **411**, 54 (2001).

[Hemb03] J. Hemberger, H.-A. Krug von Nidda, V. Fritsch, J. Deisenhofer, S. Lobina, T. Rudolf, P. Lunkenheimer, F. Lichtenberg, A. Loidl, D. Bruns, and B. Büchner, *Phys. Rev. Lett.* **91**, 066403 (2003).

[Holz83] E. Holzschuh, A. B. Denison, W. Kündig, P. F. Meier, and B. D. Patterson, *Phys. Rev. B* **27**, 5294 (1983).

[Iga04] F. Iga, M. Tsubota, M. Sawada, H. B.Huang, S. Kura, M. Takemura, K. Yaji, M. Nagira, A. Kimura, T. Jo, T. Takabatake, H. Namatame, and M. Taniguchi, *Phys. Rev. Lett.* **93**, 257207 (2004); *Phys. Rev. Lett.* **97**, 139901(E) (2006).

[Itoh99] M. Itoh, M. Tsuchiya, H. Tanaka, and K. Motoya, *J. Phys. Soc. Japan* **68**, 2783 (1999).

[Itoh] M. Itoh, (private communication).

[John06] M. Johnsson and P. Lemmens, *Crystallography and Chemistry of Perovskites*, in *Handbook of Magnetism and Advanced Magnetic Media*, ed. H. Kronmüller, (John Wiley and Sons, New York, 2006). condmat/0506606

[Keim00] B. Keimer, D. Casa, A. Ivanov, J. W. Lynn, M. v. Zimmermann, J. P. Hill, D. Gibbs, Y. Taguchi, and Y. Tokura, *Phys. Rev. Lett.* **85**, 3946 (2000).

[Khal00] G. Khaliullin and S. Maekawa, *Phys. Rev. Lett.* **85**, 3950 (2000).

[Khal02] G. Khaliullin and S. Okamoto, *Phys. Rev. Lett.* **89**, 167201 (2002).

[Khal03] G. Khaliullin and S. Okamoto, *Phys. Rev. B* **68**, 205109 (2003).

[Kimu05] T. Kimura, G. Lawes, T. Goto, Y. Tokura, and A. P. Ramirez, *Phys. Rev. B* **71**, 224425 (2005).

[Kiya03] T. Kiyama and M. Itoh, *Phys. Rev. Lett.* **91**, 167202 (2003).

[Kiya05] T. Kiyama, H. Saitoh, M. Itoh, K. Kodama, H. Ichikawa, and J. Akimitsu, *J. Phys. Soc. Japan* **74**, 1123 (2005).

[Koma07] A. C. Komarek, H. Roth, M. Cwik, W.-D. Stein, J. Baier, M. Kriener, F. Bourée, T. Lorenz, and M. Braden, *Phys. Rev. B* **75**, 224402 (2007).

[Kuroiwa] S. Kuroiwa, (private communication).

[Kwei93] G. H. Kwei, A. C. Lawson Jr., S. J. L. Billinge, and S. W. Cheong, *J. Phys. Chem.* **97**, 2368 (1993).

[Lin86] T. K. Lin, L. Lichti, C. Boekema, and A. B. Denison, *Hyp. Int.* **31**, 475 (1986).

[MacL79] D. A. MacLean, H.-N. Ng, and J. E. Greedan, *J. Solid State Chem.* **30**, 35 (1979).

[Moch03] M. Mochizuki and M. Imada, *Phys. Rev. Lett.* **91**, 167203 (2003).

[Moch04] M. Mochizuki and M. Imada, *New J. Phys.* **6**, 154 (2004).

[Nish02] Y. Nishihata, J. Mizuki, T. Akao, H. Tanaka, M. Uenishi, M. Kimura, T. Okamoto, and N. Hamada, *Nature* **418**, 164 (2002).

[Pava04] E. Pavarini, S. Biermann, A. Poteryaev, A. I. Lichtenstein, A. Georges, and O. K. Andersen, *Phys. Rev. Lett.* **92**, 176403 (2004).

[Peli02] A. Pelissetto and E. Vicari, *Phys. Rep.* **368**, 549 (2002).

[Rami97] A. P. Ramirez, *J. Phys.: Condens. Matter* **9**, 8171 (1997).

[Schm05] R. Schmitz, O. Entin-Wohlman, A. Aharony, A. B. Harris, and E. Müller-Hartmann, *Phys. Rev. B* **71**, 144412 (2005); *Phys. Rev. B* **76**, 059901(E) (2007).

[Solo06] I. V. Solovyev, *Phys. Rev. B* **74**, 054412 (2006).

[Toku00] Y. Tokura and N. Nagaosa, *Science* **288**, 462 (2000).

[Ulri02] C. Ulrich, G. Khaliullin, S. Okamoto, M. Reehuis, A. Ivanov, H. He, Y. Taguchi, Y. Tokura, and B. Keimer, *Phys. Rev. Lett.* **89**, 167202 (2002).

[Ulri03] C. Ulrich, G. Khaliullin, J. Sirker, M. Reehuis, M. Ohl, S. Miyasaka, Y. Tokura, and B. Keimer, *Phys. Rev. Lett.* **91**, 257202 (2003).

[Ulri06] C. Ulrich, A. Gössling, M. Grüninger, M. Guennou, H. Roth, M. Cwik, T. Lorenz, G. Khaliullin, and B. Keimer, *Phys. Rev. Lett.* **97**, 157401 (2006).

[vonH50] A. von Hippel, *Rev. Mod. Phys.* **22**, 221 (1950).

[Wood97a] P. M. Woodward, *Acta Cryst. B* **53**, 32 (1997).

[Wood97b] P. M. Woodward, *Acta Cryst. B* **53**, 44 (1997).

[Zhou05] J.-S. Zhou and J. B. Goodenough, *Phys. Rev. Lett.* **94**, 065501 (2005).

[Zhou06] H. D. Zhou and J. B. Goodenough, *Phys. Rev. B* **71**, 184431 (2006).

Chapter 5

[Bake07] P. J. Baker, S. J. Blundell, F. L. Pratt, T. Lancaster, M. L. Brooks, W. Hayes, M. Isobe, Y. Ueda, M. Hoinkis, M. Sing, M. Klemm, S. Horn, and R. Claessen, *Phys. Rev. B* **75**, 094404 (2007).

[Beyn93] R. J. Beynon and J. A. Wilson, *J. Phys.: Condens. Matter* **5**, 1983 (1993).

[Blun97] S. J. Blundell, F. L. Pratt, P. A. Pattenden, M. Kurmoo, K. H. Chow, S. Takagi, Th. Jestädt, and W. Hayes, *J. Phys.: Condens. Matter* **9**, L119 (1997).

[Bonn64] J. C. Bonner and M. E. Fisher, *Phys. Rev.* **135**, A640 (1964).

[Bray75] J. W. Bray, H. R. Hart Jr., L. V. Interrante, I. S. Jacobs, J. S. Kasper, G. D. Watkins, S. H. Wee, and J. C. Bonner, *Phys. Rev. Lett.* **35**, 744 (1975).

[Caim04] G. Caimi, L. Degiorgi, N. N. Kovaleva, P. Lemmens, and F. C. Chou, *Phys. Rev. B* **69**, 125108 (2004).

[Clan07] J. P. Clancy, B. D. Gaulin, K. C. Rule, J. P. Castellan, and F. C. Chou, *Phys. Rev. B* **75**, 100401 (2007).

[Crac06] L. Craco, M. S. Laad, and E. Müller-Hartmann, *J. Phys.: Condens. Matter* **18**, 10943 (2006).

[Cros79] M.C. Cross and D.S. Fisher, *Phys. Rev. B* **19**, 402 (1979).

[Ehre77] E. Ehrenfreund and L.S. Smith, *Phys. Rev. B* **16**, 1870 (1977).

[Fuda99] Y. Fudamoto, K. M. Kojima, M. I. Larkin, G. M. Luke, J. Merrin, B. Nachumi, Y. J. Uemura, M. Isobe, and Y. Ueda, *Phys. Rev. Lett.* **83**, 3301 (1999).

[Fuda02] Y. Fudamoto, I. M. Gat, M. I. Larkin, J. Merrin, B. Nachumi, A. T. Savici, Y. J. Uemura, G. M. Luke, K. M. Kojima, M. Hase, T. Matsuda, and K. Uchinokura, *Phys. Rev. B* **65**, 174428 (2002).

[Fuka99] A. Fukaya, S. Ohira. I. Watanabe, M. Hagiwara and K. Nagamine, *Hyp. Int.* **120-121**, 619 (1999).

[Garc95b] J.L. García-Muñoz, M. Suaaidi, and B. Martinéz, *Phys. Rev. B* **52**, 4288 (1995).

[Hald83] F. D. M. Haldane, *Phys. Lett.* **93A**, 464 (1983).

[Hara07] S. Haravifard, K. C. Rule, H. A. Dabkowska, B. D. Gaulin, Z. Yamani, and W. J. L. Buyers, *J. Phys.: Condens. Matter* **19**, 436222 (2007).

[Harr94] Q. J. Harris, Q. Feng, R. J. Birgeneau, K. Hirota, K. Kakurai, J. E. Lorenzo, G. Shirane, M. Hase, K. Uchinokura, H. Kojima, I. Tanaka, and Y. Shibuya, *Phys. Rev. B* **50**, 12606 (1994).

[Hase93] M. Hase, I. Terasaki, and K. Uchinokura, *Phys. Rev. Lett.* **70**, 3651 (1993).

[Hemb05] J. Hemberger, M. Hoinkis, M. Klemm, M. Sing, R. Claessen, S. Horn, and A. Loidl, *Phys. Rev. B* **72**, 012420 (2005).

[Hiki04] T. Hikihara and Y. Motome, *Phys. Rev. B* **70**, 214404 (2004); *Phys. Rev. B* **72**, 179902(E) (2005).

[Hoin05] M. Hoinkis, M. Sing, J. Schäfer, M. Klemm, S. Horn, H. Benthien, E. Jeckelmann, T. Saha-Dasgupta, L. Pisani, R. Valenti, and R. Claessen, *Phys. Rev. B* **72**, 125517 (2005).

[Hors03] P. Horsch, G. Khaliullin, and A. M. Oleś, *Phys. Rev. Lett.* **91**, 257203 (2003).

[Huiz79] S. Huizinga, J. Kommandeur, G. A. Sawatzky, B. T. Thole, K. Kopinga, W. J. M. de Jongh, and J. Roos, *Phys. Rev. B* **19**, 4723 (1979).

[Imai03] T. Imai and F.C. Chou, cond-mat/0301425 (unpublished).

[Isob96] M. Isobe and Y. Ueda, *J. Phys. Soc. Japan* **65**, 1178 (1996).

[Isob02] M. Isobe, E. Ninomiya, A. N. Vasil'ev, and Y. Ueda, *J. Phys. Soc. Japan* **71**, 1423 (2002).

[Iwas96] H. Iwase, M. Isobe, Y. Ueda, H. Yasuoka, *J. Phys. Soc. Japan* **65**, 2397 (1996).

[Jest98] Th. Jestädt, R. I. Bewley, S. J. Blundell, W. Hayes, B. W. Lovett, F. L. Pratt, and R. C. C. Ward, *J. Phys.: Condens. Matter* **10**, L259 (1998).

[Kata03] V. Kataev, J. Baier, A. Möller, L. Jongen, G. Meyer, and A. Freimuth, *Phys. Rev. B* **68**, 140405(R) (2003).

[Kikk07] A. Kikkawa, K. Katsumata, Z. Honda, I. Watanabe, T. Suzuki, and T. Matsuzaki, *J. Phys. Soc. Japan* **76**, 023707 (2007).

[Khal02] P. Khalifah, R. Osborn, Q. Huang, H. W. Zandbergen, R. Jin, Y. Liu, D. Mandrus, and R. J. Cava, *Science* **297** 2237 (2002).

[Khom05] D. I. Khomskii and T. Mizokawa, *Phys. Rev. Lett.* **94**, 156402 (2005).

[Koji95a] K. Kojima, A. Keren, G. M. Luke, B. Nachumi, W. D. Wu, Y. J. Uemura, M. Azuma, and M. Takano, *Phys. Rev. Lett.* **74**, 2812 (1995).

[Koji95b] K. Kojima, A. Keren, L. P. Le, G. M. Luke, B. Nachumi, W. D. Wu, Y. J. Uemura, K. Kiyono, S. Miyasaka, H. Takagi, and S. Uchida, *Phys. Rev. Lett.* **74**, 3471 (1995).

[Koji97] K. M. Kojima, Y. Fudamoto, M. Larkin, G. M. Luke, J. Merrin, B. Nachumi, Y. J. Uemura, M. Hase, Y. Sasago, K. Uchinokura, Y. Ajiro, A. Revcolevschi, and J.-P. Renard, *Phys. Rev. Lett.* **79**, 503 (1997).

[Kons04] M.J. Konstantinović, J. van den Brink, Z. V. Popović, V. V. Moshchalkov, M. Isobe, and Y. Ueda, *Phys. Rev. B* **69**, 020409(R) (2004).

[Krim06] A. Krimmel, J. Strempfer, B. Bohnenbuck, B. Keimer, M. Hoinkis, M. Klemm, S. Horn, A. Loidl, M. Sing, R. Claessen and M. von Zimmermann, *Phys. Rev. B* **73**, 172413 (2006).

[Kunt06] C. A. Kuntscher, S. Frank, A. Pashkin, M. Hoinkis, M. Klemm, M. Sing, S. Horn, and R. Claessen, *Phys. Rev. B* **74**, 184402 (2006).

[Lemm04] P. Lemmens, K. Y. Choi, G. Caimi, L. Degiorgi, N. N. Kovaleva, A. Seidel, and F. C. Chou, *Phys. Rev. B* **70**, 134429 (2004).

[Love00] B. W. Lovett, S. J. Blundell, F. L. Pratt, T. Jestadt, W. Hayes, S. Tagaki and M. Kurmoo, *Phys. Rev. B* **61**, 12241 (2000).

[Luke97] G. M. Luke, Y. Fudamoto, K. M. Kojima, M. Larkin, J. Merrin, B. Nachumi, S. Sinawi, Y. J. Uemura, M. J. P. Gingras, M. Sato, S. Taniguchi, M. Isobe, and Y. Ueda, cond-mat/9709123 (unpublished).

[Nino03] E. Ninomiya, M. Isobe, Y. Ueda, M. Nishi, K. Ohoyama, H. Sawa, and T. Ohama, *Physica B* **329-333**, 884 (2003).

[Peie55] R. E. Peierls, *Quantum Theory of Solids* (Oxford University Press, London, 1955).

[Pick97] W. E. Pickett, *Phys. Rev. Lett.* **79**, 1746 (1997).

[Pisa05] L. Pisani and R. Valenti, *Phys. Rev. B* **71**, 180409(R) (2005).

[Popo04] Z. S. Popović, Ž. V. Šljivančanin, and F. R. Vukajlović, *Phys. Rev. Lett.* **93**, 036401 (2004).

[Popo05] Z. V. Popović, M. J. Konstantinović, V. N. Popov, A. Cantarero, Z. Dohčevic-Mitrović, M. Isobe, and Y. Ueda, *Phys. Rev. B* **71**, 224302 (2005)

[Popo06] Z. S. Popović, Ž. V. Šljivančanin, and F. R. Vukajlović, *Phys. Rev. Lett.* **96**, 249702 (2006).

[Pytt74] E. Pytte, *Phys. Rev. B* **10**, 4637 (1974).

[Rada02] P. G. Radaelli, Y. Horibe, M. J. Gutmann, H. Ishibashi, C. H. Chen, R. M. Ibberson, Y. Koyama, Y.-S. Hor, V. Kiryukhin, and S.-W. Cheong, *Nature* **416**, 155 (2002).

[Rada05] P. G. Radaelli, *New J. Phys.* **7**, 53 (2005).

[Redh03] G. J. Redhammer, H. Ohashi, and G. Roth, *Acta Cryst.* **B59**, 730 (2003).

[Rück05] R. Rückamp, J. Baier, M. Kriener, M. W. Haverkort, T. Lorenz, G. S. Uhrig, L. Jongen, A. Möller, G. Meyer, and M. Grüninger *et al.*, *Phys. Rev. Lett.* **95**, 097203 (2005).

[Rüeg03] Ch. Rüegg, N. Cavadini, A. Furrer, H.-U. Güdel, K. Krämer, H. Mutka, A. Wildes, K. Habicht, and P. Vorderwisch, *Nature* **423**, 62 (2003).

[Saha04] T. Saha-Dasgupta, R. Valentí, H. Rosner, and C. Gros, *Europhys. Lett.* **67**, 63 (2004).

[Saha07] T. Saha-Dasgupta, A. Lichtenstein, M. Hoinkis, S. Glawion, M. Sing, R. Claessen, and R. Valentí, *New J. Phys.* **9**, 380 (2007).

[Sait06] T. Saito, A. Oosawa, T. Goto, T. Suzuki, and I. Watanabe, *Phys. Rev. B* **74**, 134423 (2006).

[Schä58] H. Schäfer, F. Wartenpfuhl, and E. Weise, *Z. Anorg. Allg. Chem.* **295**, 268 (1958).

[Schm04] M. Schmidt, W. Ratcliff II, P. G. Radaelli, K. Refson, N. M. Harrison, and S. W. Cheong, *Phys. Rev. Lett.* **92**, 056402 (2004).

[Schö06] A. Schönleber, S. van Smaalen, and L. Palatinus, *Phys. Rev. B* **73**, 214410 (2006).

[Seba06] S. E. Sebastian, N. Harrison, C. D. Batista, L. Balicas, M. Jaime, P. A. Sharma, N. Kawashima, and I. R. Fisher, *Nature* **441**, 617 (2006).

[Seid03] A. Seidel, C. A. Marianetti, F. C. Chou, G. Ceder, and P. A. Lee, *Phys. Rev. B* **67**, 020405(R) (2003).

[Shaz05] M. Shaz, S. van Smaalen, L. Palatinus, M. Hoinkis, M. Klemm, S. Horn, and R. Claessen, *Phys. Rev. B* **71**, 100405(R) (2005).

[Ster92] B. J. Sternlieb, L. P. Le, G. M. Luke, W. D. Wu, Y. J. Uemura, T. M. Riseman, J. H. Brewer, Y. Ajiro and M. Mekata, *J. Mag. Magn. Mat.* **104-107**, 801 (1992).

[Stre06] S.V. Streltsov, O. A. Popova, and D. I. Khomskii, *Phys. Rev. Lett.* **96**, 249701 (2006).

[Tani95] S. Taniguchi, T. Nishikawa, Y. Yasui, Y. Kobayashi, M. Sato, T. Nishioka, M. Kontani, and K. Sano, *J. Phys. Soc. Japan* **64**, 2758 (1995).

[Uemu85] Y. J. Uemura, T. Yamazaki, D. R. Harshman, M. Senba, and E. J. Ansaldo, *Phys. Rev. B* **31**, 546 (1985).

[Uhri99] G. S. Uhrig, F. Schönfeld, M. Laukamp, E. Dagotto, *Euro. Phys. J. B* **7**, 67 (1999).

[vWez05] J. van Wezel and J. van den Brink, *J. Mag. Magn. Mat.* **290-291**, 318 (2005).

[vWez06] J. van Wezel and J. van den Brink, *Europhys. Lett.* **75**, 957 (2006).

[Wals74] R.E. Walstedt and L.R. Walker, *Phys. Rev. B* **9**, 4857 (1974).

[Wils87] J. A. Wilson, C. Maule, P. Strange, and J. N. Tothill, *J. Phys. C* **20**, 4159 (1987).

[Wu06] Hua Wu, Z. Hu, T. Burnus, J. D. Denlinger, P. G. Khalifah, D. G. Mandrus, L.-Y. Jang, H. H. Hsieh, A. Tanaka, K. S. Liang, J. W. Allen, R. J. Cava, D. I. Khomskii, and L. H. Tjeng, *Phys. Rev. Lett.* **96**, 256402 (2006).

[Zakh06] D. V. Zakharov, J. Deisenhofer, H.-A. Krug von Nidda, P. Lunkenheimer, J. Hemberger, M. Hoinkis, M. Klemm, M. Sing, R. Claessen, M. V. Eremin, S. Horn, and A. Loidl, *Phys. Rev. B* **73**, 094452 (2006).

[Zapf06] V. S. Zapf, D. Zocco, B. R. Hansen, M. Jaime, N. Harrison, C. D. Batista, M. Kenzelmann, C. Niedermayer, A. Lacerda, and A. Paduan-Filho, *Phys. Rev. Lett.* **96**, 077204 (2006).

Chapter 6

[Aege98] C. M. Aegerter, J. Hofer, I. M. Savić, H. Keller, S. L. Lee, C. Ager, S. H. Lloyd, and E. M. Forgan, *Phys. Rev. B* **57**, 1253 (1998).

[Ande98] P. W. Anderson, *Science* **279**, 1196 (1998).

[Anne04] J. F. Annett, *Superconductivity, Superfluids and Condensates*, (OUP, Oxford, 2004).

[Aoua98] T. Aouraroun and Ch. Simon, *Phys. Rev. B* **58**, 11692 (1998).

[Bae96] M.-K. Bae, M.-S. Kim, S.-I. Lee, N.-G. Park, S.-J. Hwang, D.-H. Kim, and J.-H. Choy, *Phys. Rev. B* **53**, 12416 (1996).

[Barf88] W. Barford and J. M. F. Gunn, *Physica C* **156**, 515 (1998).

[Bedn86] J. G. Bednorz and K. A. Müller, *Z. Phys. B* **64**, 189 (1986).

[Bern95] C. Bernhard, Ch. Niedermayer, U. Binninger, A. Hofer, Ch. Wenger, J. L. Tallon, G. V. M. Williams, E. J. Ansaldo, J. I. Budnick, C. E. Stronach, D. R. Noakes, and M. A. Blankson-Mills, *Phys. Rev. B* **52**, 10488 (1995).

[Bern96] C. Bernhard, J. L. Tallon, C. Bucci, R. De Renzi, G. Guidi, G. V. M. Williams, and Ch. Niedermayer, *Phys. Rev. Lett.* **77**, 2304 (1996).

[Binn92] J. J. Binney, N. J. Dowrick, A. J. Fisher, and M. E. J. Newman, *The theory of critical phenomena* (OUP, Oxford, 1992).

[Blat94] G. Blatter, M. V. Feigel'man, V. B. Geshkenbein, A. I. Larkin, and V. M. Vinokur, *Rev. Mod. Phys.* **66**, 1125 (1994).

[Blat96] G. Blatter, V. Geshkenbein, A. Larkin, and H. Nordborg, *Phys. Rev. B* **54**, 72 (1996).

[Bran88] E. H. Brandt, *Phys. Rev. B* **37**, 2349 (1988); *J. Low Temp. Phys.* **73**, 355 (1988).

[Bran95] E. H. Brandt, *Rep. Prog. Phys.* **58**, 1465 (1995).

[Bran03] E. H. Brandt, *Phys. Rev. B* **68**, 054506 (2003).

[Brew88] J. H. Brewer, E. J. Ansaldo, J. F. Carolan, A. C. D. Chaklader, W. N. Hardy, D. R. Harshman, M. E. Hayden, M. Ishikawa, N. Kaplan, R. Keitel, J. Kempton, R. F. Kiefl, W. J. Kossler, S. R. Kreitzman, A. Kulpa, Y. Kuno, G. M. Luke, H. Miyatake, K. Nagamine, Y. Nakazawa, N. Nishida, K. Nishiyama, S. Ohkuma, T. M. Riseman, G. Roehmer, P. Schleger, D. Shimada, C. E. Stronach, T. Takabatake, Y. J. Uemura, Y. Watanabe, D. Ll. Williams, T. Yamazaki, and B. Yang, *Phys. Rev. Lett.* **60**, 1073 (1988).

[Brou06] D. M. Broun, P. J. Turner, W. A. Huttema, S. Özcan, B. Morgan, R. Liang, W. N. Hardy, and D. A. Bonn, cond-mat/0509223.

[Casa02] M. Casas, M. de Llano, A. Puente, A. Rigo, and M. A. Solís, *J. Phys. Chem. Solids* **63**, 2365 (2002).

[Choy94] J.-H. Choy, N. G. Park, S. J. Hwang, D. H. Kim, and N. H. Hur, *J. Am. Chem. Soc.* **116**, 11564 (1994).

[Choy98] J.-H. Choy, S.-J. Kwon, and G.-S. Park, *Science* **280**, 1589 (1998).

[Clem91] J. R. Clem, *Phys. Rev. B* **43**, 7837 (1991).

[Cubi93] R. Cubitt, E. M. Forgan, G. Yang, S. L. Lee, D. McK. Paul, H. A. Mook, M. Yethiraj, P. H. Kes, T. W. Li, A. A. Menovsky, Z. Tarnawski, and K. Mortensen, *Nature* **365**, 407 (1993).

[Emer95] V. J. Emery and S. A. Kivelson, *Nature* **374**, 434 (1995).

[Fabr99] L. Fàbrega, A. Calleja, A. Sin, S. Piñol, X. Obradors, J. Fontcuberta, and P. J. C. King, *Phys. Rev. B* **60**, 7579 (1999).

[Forg90] E. M. Forgan, D. McK. Paul, H. A. Mook, P. A. Timmins, H. Keller, S. Sutton, and J. S. Abell, *Nature* **343**, 735 (1990).

[Fran06] M. Franz and A. P. Iyengar, *Phys. Rev. Lett.* **96**, 047007 (2006).

[Gao94] L. Gao, Y. Y. Xue, F. Chen, Q. Xiong, R. L. Meng, D. Ramirez, C. W. Chu, J. H. Eggert, and H. K. Mao, *Phys. Rev. B* **50**, 4260 (1994).

[Gute41] B. Gutenberg and C. F. Richter, *Geological Society of America Special Papers* **34**, 1 (1941).

[Hann65] N. B. Hannay, T. H. Geballe, B. T. Matthias, K. Andres, P. Schmidt, and D. MacNair, *Phys. Rev. Lett.* **14**, 225 (1965).

[Hars92] D. R. Harshman and A. P. Mills Jr., *Phys. Rev. B* **45**, 10684 (1992).

[Hars93] D. R. Harshman, E. H. Brandt, A. T. Fiory, M. Inui, D. B. Mitzi, L. F. Schneemeyer, and J. V. Waszczak, *Phys. Rev. B* **47**, 2905 (1993).

[Haya79] R. S. Hayano, Y. J. Uemura, J. Imazato, N. Nishida, T. Yamazaki, and R. Kubo, *Phys. Rev. B* **20**, 850 (1979).

[Heba91] A. F. Hebard, M. J. Rosseinsky, R. C. Haddon, D. W. Murphy, S. H. Glarum, T. T. M. Palstra, A. P. Ramirez, and A. R. Kortan, *Nature* **350**, 600 (1991).

[Hete07] I. Hetel, T. R. Lemberger, and M. Randeria, *Nature Physics* **3**, 700 (2007).

[Hige04] W. Higemoto, K. Ohishi, A. Koda, S. R. Saha, R. Kadono, K. Ishida, K. Takada, H. Sakurai, E. Takayama-Muromachi, and T. Sasaki, *Phys. Rev. B* **70**, 134508 (2004).

[Home04] C. C. Homes, S. V. Dordevic, M. Strongin, D. A. Bonn, R. Liang, W. N. Hardy, S. Komiya, Y. Ando, G. Yu, N. Kaneko, X. Zhao, M. Greven, D. N. Basov, T. Timusk, *Nature* **430**, 539 (2004).

[Ito04] T. Ito, Y. Fudamoto, A. Fukaya and I. M. Gat-Malureanu, M. I. Larkin, P. L. Russo, A. Savici, Y. J. Uemura, K. Groves, R. Breslow, K. Hotehama, S. Yamanaka, P. Kyriakou, M. Rovers, G. M. Luke, and K. M. Kojima, *Phys. Rev. B* **69**, 134522 (2004).

[Kani04] A. Kanigel, A. Keren, L. Patlagan, K. B. Chashka, P. J. C. King, and A. Amato, *Phys. Rev. Lett.* **92**, 257007 (2004).

[Khas04] R. Khasanov, A. Shengelaya, E. Morenzoni, K. Conder, I. M. Savic, and H. Keller, *J. Phys.: Condens. Matter* **16**, S4439 (2004).

[Kim07] J. S. Kim, L. Boeri, J. R. O'Brien, F. S. Razavi, and R. K. Kremer, *Phys. Rev. Lett.* **99**, 027001 (2007).

[Kopp05] A. Kopp and S. Chakravarty, *Nature Physics* **1**, 53 (2005).

[Kost73] J. M. Kosterlitz and D. J. Thouless, *J. Phys. C: Solid State Phys.* **6**, 1181 (1973).

[Kwon02] S.-J. Kwon, J. H. Choy, D.-Y. Jung, and P. V. Huong, *Phys. Rev. B* **66**, 224510 (2002).

[Kwon04] S.-J. Kwon and D.-Y. Jung, *Sol. Stat. Commun.* **130**, 287 (2004).

[Kwon05] S.-J. Kwon, Y. H. Lee, J. H. Choy, and S. J. Kim, *Supercond. Sci. Technol.* **18**, 470 (2005).

[Lee93] S. L. Lee, P. Zimmermann, H. Keller, M. Warden, I. M. Savíc, R. Schauwecker, D. Zech, R. Cubitt, E. M. Forgan, P. H. Kes, T. W. Li, A. A. Menovsky, and Z. Tarnawski, *Phys. Rev. Lett.* **71**, 3862 (1993).

[Lee95] S. L. Lee, M. Warden, H. Keller, J. W. Schneider, D. Zech, P. Zimmermann, R. Cubitt, E. M. Forgan, M. T. Wylie, P. H. Kes, T. W. Li, A. A. Menovsky, and Z. Tarnawski, *Phys. Rev. Lett.* **75**, 922 (1995).

[Lee97] S. L. Lee, C. M. Aegerter, H. Keller, M. Willemin, B. Stäuble-Pümpin, E. M. Forgan, S. H. Lloyd, G. Blatter, R. Cubitt, T. W. Li, and P. Kes, *Phys. Rev. B* **55**, 5666 (1997).

[Lee98a] S. L. Lee, C. M. Aegerter, S. H. Lloyd, E. M. Forgan, C. Ager, M. B. Hunt, H. Keller, I. M. Savíc, R. Cubitt, G. Wirth, K. Kadowaki, and N. Koshizuka, *Phys. Rev. Lett.* **81** 5209 (1998).

[Lee98b] J. H. Lee, G.-T. Kim, Y. W. Park, J.-H. Choy, S.-J. Hwang, and W. Lee, *Chin. J. Phys.* **36**, 316 (1998).

[Legg96] A. J. Leggett, *Science* **274**, 587 (1996).

[Legg06] A. J. Leggett, *Nature Physics* **2**, 134 (2006).

[Lian06] R. Liang, D. A. Bonn, and W. N. Hardy, *Phys. Rev. B* **73**, 180505(R) (2006).

[Mart92] J. C. Martínez, S. H. Brongersma, A. Koshelev, B. Ivlev, P. H. Kes, R. P. Griessen, D. G. de Groot, Z. Tarnavski, and A. A. Menovsky, *Phys. Rev. Lett.* **69**, 2276 (1992).

[Mich94] C. Michel, D. Pelloquin, M. Hervieu, and B. Raveau, *J. Solid State Chem.* **112**, 362 (1994).

[Nam07] M.-S. Nam, A. Ardavan, S. J. Blundell, J. A. Schlueter, *Nature* **449**, 584 (2007).

[Nied93] Ch. Niedermayer, C. Bernhard, U. Binninger, H. Glückler, J. L. Tallon, E. J. Ansaldo, and J. I. Budnick, *Phys. Rev. Lett.* **71**, 1764 (1993).

[OHar96] D. O'Hare, *Inorganic Intercalation Compounds* in *Inorganic Materials*, eds. D. W. Bruce and D. O'Hare, (John Wiley & Sons Ltd., Chichester, 1996).

[Pals88] T. T. M. Palstra, B. Batlogg, L. F. Schneemeyer, R. B. van Dover, and J. V. Waszczak, *Phys. Rev. B* **38**, 5102 (1988).

[Pana99] C. Panagopoulos, B. D. Rainford, J. R. Cooper, W. Lo, J. L. Tallon, J. W. Loram, J. Betouras, Y. S. Wang, and C. W. Chu, *Phys. Rev. B* **60**, 14617 (1999).

[Pinc64] P. Pincus, A. C. Gossard, V. Jaccarino, and J. H. Wernick, *Phys. Lett.* **13**, 31 (1964).

[Pool00] *Handbook of Superconductivity*, ed. C.P. Poole, Jr., (Academic Press, San Diego, 2000).

[Prat05] F. L. Pratt and S. J Blundell, *Phys. Rev. Lett.* **94**, 097006 (2005).

[Pratt] F. L. Pratt, (*private communication*).

[Pres91] M. R. Presland, J. L. Tallon, R. G. Buckley, R. S. Liu, and N. E. Flower, *Physica C* **176**, 95 (1991).

[Rain94] B. D. Rainford and G. J. Daniell, *Hyp. Int.* **87**, 1129 (1994).

[Rodu99] E. Roduner, in *Muon Science: Muons in Physics, Chemistry and Materials*, eds. S. L. Lee, S. H. Kilcoyne, and R. Cywinski, *Proceedings of the Fifty First Scottish Universities Summer School in Physics*, (IoP Publishing, Bristol, 1999).

[Ross95] M. J. Rosseinsky, *J. Mater. Chem.* **5**, 1497 (1995).

[Russ07] P. L. Russo, C. R. Wiebe, Y. J. Uemura, A. T. Savici, G. J. MacDougall, J. Rodriguez, G. M. Luke, N. Kaneko, H. Eisaki, M. Greven, O. P. Vajk, S. Ono, Y. Ando, K. Fujita, K. M. Kojima, and S. Uchida, *Phys. Rev. B* **75**, 054511 (2007).

[Sann04] S. Sanna, G. Allodi, G. Concas, A. D. Hillier, and R. De Renzi, *Phys. Rev. Lett.* **93**, 207001 (2004).

[Savi05] A. T. Savici, A. Fukaya, I. M. Gat-Malureanu, T. Ito, P. L. Russo, Y. J. Uemura, C. R. Wiebe, P. P. Kyriakou, G. J. MacDougall, M. T. Rovers, G. M. Luke, K. M. Kojima, M. Goto, S. Uchida, R. Kadono, K. Yamada, S. Tajima, T. Masui, H. Eisaki, N. Kaneko, M. Greven, and G. D. Gu, *Phys. Rev. Lett.* **95**, 157001 (2005).

[Schi92] J. S. Schilling and S. Klotz, in *Physical Properties of High Temperature Superconductors III*, ed. D. M. Ginsberg, (World Scientific, Singapore, 1992), p. 59.

[Schm84] K. Schmidt-Nielsen, *Scaling: Why is animal size so important?*, (Cambridge University Press, Cambridge, 1984), pp. 56-74.

[Schn07] T. Schneider, *Quantum Superconductor-Metal Transition in* Al*,* C *doped* MgB_2 *and overdoped Cuprates?*, in *High Tc Superconductors and Related Transition Metal Oxides: Special Contributions in Honor of K. Alex Müller on the Occasion of His 80th Birthday*, eds. A. Bussmann-Holder and H. Keller, (Springer, Berlin, 2007); cond-mat/0702468.

[Scot94] B. A. Scott, E. Y. Suard, C. C. Tsuei, D. B. Mitzi, T. R. McGuire, B.-H. Chen, and D. Walker, *Physica C* **230**, 239 (1994).

[Serv04] S. Serventi, G. Allodi, R. De Renzi, G. Guidi, L. Romanò, P. Manfrinetti A. Palenzona, Ch. Niedermayer, A. Amato, and Ch. Baines, *Phys. Rev. Lett.* **93**, 217003 (2004).

[Serv06] S. Serventi, G. Allodi, R. De Renzi, L. Romanò, P. Manfrinetti A. Palenzona, A. Amato, and Ch. Baines, *Physica B* **374-375**, 235 (2006).

[Shen98] A. Shengelaya, C. M. Aegerter, S. Romer, H. Keller, P. W. Klamut, R. Dybzinski, B. Dabrowski, I. M. Savic, and J. Klamut, *Phys. Rev. B* **58**, 3457 (1998).

[Soni98] J. E. Sonier, (PhD Thesis, University of British Columbia, 1998).

[Soni00] J. E. Sonier, J. H. Brewer, and R. F. Kiefl, *Rev. Mod. Phys.* **72**, 769 (2000).

[Stra05] A. H. Strahler and A. N. Strahler, *Physical Geography: Science and Systems of the Human Environment*, 3rd edition, (John Wiley & Sons, Hoboken, N.J., 2005), pp. 522 & 523.

[Taka03] K. Takada, H. Sakurai, E. Takayama-Muromachi, F. Izumi, R. A. Dilanian, and T. Sasaki, *Nature* **422**, 53 (2003).

[Tall06] J. L. Tallon, J. R. Cooper, S. H. Naqib, and J. W. Loram, *Phys. Rev. B* **73**, 180504(R) (2006).

[Tris90] J.-M. Triscone, Ø. Fischer, O. Brunner, L. Antognazza, A. D. Kent, and M. G. Karkut, *Phys. Rev. Lett.* **64**, 804 (1990).

[Uemu88] Y. J. Uemura, V. J. Emery, A. R. Moodenbaugh, M. Suenaga, D. C. Johnston, A. J. Jacobson, J. T. Lewandowski, J. H. Brewer, R. F. Kiefl, S. R. Kreitzman, G. M. Luke, T. Riseman, C. E. Stronach, W. J. Kossler, J. R. Kempton, X. H. Yu, D. Opie, and H. E. Schone, *Phys. Rev. B* **38**, 909 (1988).

[Uemu89] Y. J. Uemura, G. M. Luke, B. J. Sternlieb, J. H. Brewer, J. F. Carolan, W. N. Hardy, R. Kadono, J. R. Kempton, R. F. Kiefl, S. R. Kreitzman, P. Mulhern, T. M. Riseman, D. Ll. Williams, B. X. Yang, S. Uchida, H. Takagi, J. Gopalakrishnan, A. W. Sleight, M. A. Subramanian, C. L. Chien, M. Z. Cieplak, G. Xiao, V. Y. Lee, B. W. Statt, C. E. Stronach, W. J. Kossler, and X. H. Yu, *Phys. Rev. Lett.* **62**, 2317 (1989).

[Uemu91] Y. J. Uemura, L. P. Le, G. M. Luke, B. J. Sternlieb, W. D. Wu, J. H. Brewer, T. M. Riseman, C. L. Seaman, M. B. Maple, M. Ishikawa, D. G. Hinks, J. D. Jorgensen, G. Saito, and H. Yamochi, *Phys. Rev. Lett.* **66**, 2665 (1991).

[Uemu97] Y. J. Uemura, *Physica C* **282-287**, 194 (1997).

[Uemu06] Y. J. Uemura, *Physica B* **374-375**, 1 (2006).

[Webe91] M. Weber and A. Amato and P. Birrer and V. N. Duginov, V. G. Grebinnik, F. N. Gygax, S. Kaputsa, B. F. Kirillov, E. Lippelt, H. Malleta, V. G. Olshevsky, A. V. Pirogov, V. Yu. Pomjakushin, A. N. Ponomarev, A. Schenck, V. G. Storchak, and V. A. Zhukov, *Supercond. Sci. Technol.* **4**, S403 (1991).

[Webe93] M. Weber, A. Amato, F. N. Gygax, A. Schenck, H. Malleta, V. N. Duginov, V. G. Grebinnik, A. B. Lazarev, V. G. Olshevsky, V. Yu. Pomjakushin, S. N. Shilov, V. A. Zhukov, B. F. Kirillov, A. V. Pirogov, A. N. Ponomarev, V. G. Storchak, S. Kaputsa, and J. Bock, *Phys. Rev. B* **48**, 13022 (1993).

[Weid89] A. Weidinger, Ch. Niedermayer, A. Golnik, R. Simon, E. Recknagel, J. I. Budnick, B. Chamberland, and C. Baines, *Phys. Rev. Lett.* **62**, 102 (1989).

[Well05] T. E. Weller, M. Ellerby, S. S. Saxena, R. P. Smith, and N. T. Skipper, *Nature Physics* **1**, 39 (2005).

[Whea88] J. M. Wheatley, T. C. Hsu, and P. W. Anderson, *Nature* **333**, 121 (1988).

[Xian90] X. D. Xiang, S. McKernan, W. A. Vareka, A. Zettl, J. L. Corkill, T. W. Barbee III, and M. L. Cohen, *Nature* **348**, 145 (1990).

[Xian92] X.-D. Xiang, W. A. Vareka, A. Zettle, J. L. Corkill, M. L. Cohen, N. Kijima, and R. Gronsky, *Phys. Rev. Lett.* **68**, 530 (1992).

[Xu00] Z. A. Xu, N. P. Ong, Y. Wang, T. Kakeshita, and S. Uchida, *Nature* **406**, 486 (2000).

[Yama96] S. Yamanaka, H. Kawaji, K. Hothama, M. Ohashi, *Adv. Mater.* **9**, 771 (1996).

[Yama98] S. Yamanaka, K. Hotehama, and H. Kawaji, *Nature* **392**, 580 (1998).

[Zaan06] J. Zaanen, S. Chakravarty, T. Senthil, P. Anderson, P. Lee, J. Schmalian, M. Imada, D. Pines, M. Randeria, C. Varma, M. Vojta, and M. Rice, *Nature Physics* **2**, 138 (2006).

[Zimm95] P. Zimmermann, H. Keller, S. L. Lee, I. M. Savić, M. Warden, D. Zech, R. Cubitt, E. M. Forgan, E. Kaldis, J. Karpinski, and C. Krüger, *Phys. Rev. B* **52**, 541 (1995).

[Zuev05] Y. Zuev, M. S. Kim, and T. R. Lemberger, *Phys. Rev. Lett.* **95**, 137002 (2005).

List of Publications

- Thermodynamic and magnetic properties of the layered triangular magnet $NaNiO_2$,
  P. J. Baker, T. Lancaster, S. J. Blundell, M. L. Brooks, W. Hayes, D. Prabhakaran, and F. L. Pratt, *Phys. Rev. B* **72**, 104414 (2005).

- Thermodynamic and magnetic properties of the layered triangular magnet $NaNiO_2$,
  P. J. Baker, T. Lancaster, S. J. Blundell, M. L. Brooks, W. Hayes, D. Prabhakaran, and F. L. Pratt, (*Proceedings of the 10th International Conference on Muon Spin Rotation, Relaxation, and Resonance*, Oxford, 2005.) *Physica B* **374-375**, 47 (2006).

- Magnetic order in the quasi-one-dimensional spin-1/2 molecular chain compound copper pyrazine dinitrate,
  T. Lancaster, S. J. Blundell, M. L. Brooks, P. J. Baker, F. L. Pratt, J. L. Manson, C. P. Landee, and C. Baines, *Phys. Rev. B* **73**, 020410(R) (2006).

- Magnetism in the $S = 1$ frustrated antiferromagnet $GeNi_2O_4$ studied using implanted muons,
  T. Lancaster, S. J. Blundell, D. Prabhakaran, P. J. Baker, W. Hayes, and F. L. Pratt, *Phys. Rev. B* **73**, 184436 (2006).

- Muon-spin relaxation study of the spin-1/2 molecular chain compound $Cu(HCO_2)_2(C_4H_4N_2)$,
  T. Lancaster, S. J. Blundell, M. L. Brooks, P. J. Baker, F. L. Pratt, J. L. Manson, and C. Baines, *Phys. Rev. B* **73**, 172403 (2006).

- Kagome staircase compounds $Ni_3V_2O_8$ and $Co_3V_2O_8$ studied with implanted muons,
  T. Lancaster, S. J. Blundell, P. J. Baker, D. Prabhakaran, W. Hayes, and F. L. Pratt, *Phys. Rev. B* **75**, 064427 (2007).

- Muon spin relaxation measurements on the dimerized spin-1/2 chains $NaTiSi_2O_6$ and TiOCl,
  P. J. Baker, S. J. Blundell, F. L. Pratt, T. Lancaster, M. L. Brooks, W. Hayes, M. Isobe, Y. Ueda, M. Hoinkis, M. Sing, M. Klemm, S. Horn, and R. Claessen, *Phys. Rev. B* **75**, 094404 (2007).

- Magnetic order in the $S = 1/2$ two-dimensional molecular antiferromagnet copper pyrazine perchlorate $Cu(Pz)_2(ClO_4)_2$,
  T. Lancaster, S. J. Blundell, M. L. Brooks, P. J. Baker, F. L. Pratt,

J. L. Manson, M. M. Conner, F. Xiao, C. P. Landee, F. A. Chaves, S. Soriano, M. A. Novak, T. P. Papageorgiou, A. D. Bianchi, T. Herrmannsdörfer, J. Wosnitza, and J. A. Schlueter, *Phys. Rev. B* **75**, 094421 (2007).

- Magnetism in Geometrically Frustrated $YMnO_3$ Under Hydrostatic Pressure Studied with Implanted Muons,
  T. Lancaster, S. J. Blundell, D. Andreica, M. Janoschek, B. Roessli, S. N. Gvasaliya, K. Conder, E. Pomjakushina, M. L. Brooks, P. J. Baker, D. Prabhakaran, W. Hayes, and F. L. Pratt, *Phys. Rev. Lett.* **98**, 197203 (2007).

- Magnetism in the high-T_c analogue Cs_2AgF_4 studied with muon-spin relaxation,
  T. Lancaster, S. J. Blundell, P. J. Baker, W. Hayes, S. R. Giblin, S. E. McLain, F. L. Pratt, Z. Salman, E. A. Jacobs, J. F. C. Turner, and T. Barnes, *Phys. Rev. B* **75**, 220408(R) (2007).

- Chiral-like critical behavior in the antiferromagnet cobalt glycerolate,
  F. L. Pratt, P. J. Baker, S. J. Blundell, T. Lancaster, M. A. Green, and M. Kurmoo, *Phys. Rev. Lett.* **99**, 017202 (2007).

- A muon-spin relaxation study of multiferroic $BiMnO_3$,
  T. Lancaster, S. J. Blundell, P. J. Baker, F. L. Pratt, W. Hayes, I. Yamada, M. Azuma, and M. Takano, *J. Phys.: Condens. Matter* **19**, 376203 (2007).

- μSR as a probe of anisotropy in low-dimensional molecular magnets,
  S. J. Blundell, T. Lancaster, F. L. Pratt, P. J. Baker, M. L. Brooks, C. Baines, J. L. Manson, and C. P. Landee, (*Proceedings of QuBS2006*, Tokai, August 2006) *J. Phys. Chem. Solids* **68**, 2039 (2007).

- Muon-fluorine entangled states in molecular magnets,
  T. Lancaster, S. J. Blundell, P. J. Baker, M. L. Brooks, F. L. Pratt, W. Hayes, J. L. Manson, M. M. Conner, and J. A. Schlueter, *Phys. Rev. Lett.* **99**, 267201 (2007).

- Anomalous temperature evolution of the internal magnetic field distribution in the charge-ordered triangular antiferromagnet $AgNiO_2$,
  T. Lancaster, S. J. Blundell, P. J. Baker, M. L. Brooks, W. Hayes, F. L. Pratt, R. Coldea, T. Sörgel, and M. Jansen, *Phys. Rev. Lett.* **100**, 017206 (2008).

- Magnetism and orbitally driven spin-singlet states in Ru oxides,
  S. J. Blundell, T. Lancaster, P. J. Baker, W. Hayes, F. L. Pratt, T. Atake, D. S. Rana, and S. K. Malik, *Phys. Rev. B* **77**, 094424 (2008).

- Synthesis and characterization of two metallic spin-glass phases of $FeMo_4Ge_3$,
  P. J. Baker, P. D. Battle, S. J. Blundell, F. Grandjean, T. Lancaster, G. J. Long, S. E. Oldham, and T. J. Prior, *Phys. Rev. B* **77**, 134405 (2008).